



**HAL**  
open science

# Caractérisation expérimentale et prédiction de la formabilité d'un alliage d'aluminium en fonction de la température et de la vitesse de déformation

Xingrong Chu

► **To cite this version:**

Xingrong Chu. Caractérisation expérimentale et prédiction de la formabilité d'un alliage d'aluminium en fonction de la température et de la vitesse de déformation. Autre. INSA de Rennes, 2013. Français. NNT : 2013ISAR0004 . tel-00910093

**HAL Id: tel-00910093**

**<https://theses.hal.science/tel-00910093>**

Submitted on 27 Nov 2013

**HAL** is a multi-disciplinary open access archive for the deposit and dissemination of scientific research documents, whether they are published or not. The documents may come from teaching and research institutions in France or abroad, or from public or private research centers.

L'archive ouverte pluridisciplinaire **HAL**, est destinée au dépôt et à la diffusion de documents scientifiques de niveau recherche, publiés ou non, émanant des établissements d'enseignement et de recherche français ou étrangers, des laboratoires publics ou privés.

Thèse



**THESE INSA Rennes**  
sous le sceau de l'Université européenne de Bretagne  
pour obtenir le titre de  
**DOCTEUR DE L'INSA DE RENNES**  
Spécialité : Génie Mécanique

présentée par  
**Xingrong CHU**  
**ECOLE DOCTORALE : SDLM**  
**LABORATOIRE : Génie Civil et Génie Mécanique**

**Caractérisation  
expérimentale et prédiction  
de la formabilité d'un  
alliage  
d'aluminium en fonction de  
la température et de la  
vitesse de déformation**

**Thèse soutenue le 20.02.2013**  
devant le jury composé de :

**Sandrine THUILLIER**  
Professeur – UBS Lorient / Présidente du jury  
**Elisabeth MASSONI**  
Maître de Recherche – Cemef, Sophia Antipolis / rapporteur  
**Guillaume RACINEUX**  
Professeur – Ecole Centrale de Nantes / rapporteur  
**Dominique GUINES**  
Maître de conférences – INSA de Rennes / co-encadrant  
**Lionel LEOTOING**  
Maître de conférences – INSA de Rennes / co-encadrant  
**Eric RAGNEAU**  
Professeur – INSA de Rennes / Directeur de thèse

# Caractérisation expérimentale et prédiction de la formabilité d'un alliage d'aluminium en fonction de la température et de la vitesse de déformation

Xingrong CHU



To Xiaoli

To my parents

To all my friends



# Acknowledgements

First and foremost, I would like to express my sincere gratitude to my supervisors, Professor Eric RAGNEAU, Doctors Lionel LEOTOING and Dominique GUINES, for giving me the opportunity to work with a talented research team on such an interesting and rewarding subject. Thank you so much for your patience, continuous encouragement, invaluable insights and excellent instructions for every detail during my PhD study at INSA-Rennes. I have greatly benefited from your supervision style which helps me to think carefully and present logically. Thank you again for all your discussions and guidance!

I would also like to express my sincere appreciation to Professor Sandrine THUILLIER, Professor Elisabeth MASSONI and Professor Guillaume RACINEUX for their time, effort and expert advice as members of my doctoral thesis committee. My special appreciation to Professor Sandrine THUILLIER for serving as chairman of my thesis committee, and again to Professor Elisabeth MASSONI and Professor Guillaume RACINEUX, for their inspiring suggestions and encouraging feedback.

To all my colleagues in PSM team, Chansopheak, Jérémy, Mario, Stéphane, Gaël, Shun ying, Liu wei, Yuan han, Tang liang, ....., thank you very much for all the great conversations and good times we've had. Special thanks to Sylvain Rigaud for his technical support during the experiments.

To my family who has been there for me in every step of the way, and for your love and endless support in all my endeavors.

I greatly acknowledge the financial support for this work provided by China Scholarship Council (CSC), without this help I could not complete this field research.



# Résumé

---

*Les procédés de mise en forme de tôles minces sont très largement répandus dans l'industrie. Néanmoins, l'utilisation de ces procédés est limitée par le niveau de formabilité du matériau formé, notamment dans le cas des alliages d'aluminium. Afin d'améliorer ces limites de formabilité, des procédés de mise en forme à chaud peuvent être envisagés.*

*L'objectif de cette thèse est d'étudier à l'aide d'approches expérimentale et numérique l'effet de la température et de la vitesse de déformation sur la formabilité des tôles en alliage d'aluminium AA5086 et de proposer une modélisation capable de prédire ces effets. Une campagne d'essais a été réalisée sur ce matériau à partir d'un essai d'emboutissage de type Marciniak. Des courbes limites de formage (CLF) ont été établies sur une plage de température allant de l'ambient jusqu'à 200°C et pour des vitesses de déformation allant du quasi-statique à  $2s^{-1}$ . Des effets, positif de la température et négatif de la vitesse de déformation sur la formabilité ont été mis en évidence.*

*La prise en compte des effets de la température et de la vitesse de déformation dans les modèles prédictifs des CLF, qu'ils soient analytiques ou numériques, est à ce jour très limitée. Dans ce travail, un modèle numérique prédictif basé sur la simulation par éléments finis du modèle géométrique de Marciniak et Kuczynski (M-K) est proposé. Les déformations limites obtenues avec de ce modèle sont très sensibles à la description du comportement thermo-viscoplastique du matériau et à la calibration du défaut géométrique pilotant l'apparition de la striction dans le modèle M-K.*

*Des essais de traction uniaxiale réalisés dans les mêmes conditions opératoires que les essais de mise en forme de Marciniak ont permis d'identifier des lois d'érouissage de nature très différentes (rigidifiante, saturante ou mixte). Ces lois conduisent à des prédictions très différentes de la formabilité du matériau pour une valeur donnée du défaut géométrique du modèle EF M-K. Différentes stratégies de calibration de la taille de ce défaut initial ont été envisagées. L'utilisation du point expérimental de la  $CLF_0$  correspondant à des conditions de déformation plane permet de calibrer de manière satisfaisante la valeur de ce défaut. Cette procédure de calibration a été appliquée pour l'ensemble des lois identifiées. Les lois de nature rigidifiante de type Ludwick se sont montrées les plus efficaces alors que les lois saturante de type Voce se sont avérées incapables de prédire la formabilité du matériau pour certaines conditions opératoires. Finalement, il est démontré qu'une valeur constante du défaut géométrique ne peut être retenue pour l'ensemble des conditions opératoires étudiées même si le modèle M-K s'est avéré assez efficace pour représenter l'effet de la température plutôt que celui de la vitesse de déformation.*



# Abstract

---

Sheet metal forming processes are widely used in industry. Nevertheless, the use of these processes is limited by the formability of the considered material, in particular in the case of the aluminium alloys. To improve the formability, warm forming processes can be considered.

The objective of this work is to study by means of both experimental and numerical approaches, the effects of temperature and strain rate on the formability of AA5086 aluminium alloy sheets and to propose a modeling suitable to predict these effects. Experimental tests have been carried out on this material by means of the Marciniak stamping experimental device. Forming limit curves (FLCs) have been established on a temperature range going from ambient temperature to 200°C and on a strain rate range going from quasi-static up to  $2s^{-1}$ . A positive effect of the temperature and a negative effect of the strain rate on the formability limits were highlighted.

To date, very few predictive models of the FLCs taking into account temperature and strain rate effects are proposed in the literature. In this work, in order to predict the experimental temperature and strain rate sensitivities, a predictive model based on the finite element simulation of the Marciniak and Kuczynski (M-K) geometrical model is proposed. The limit strains obtained with this model are very sensitive to the description of the thermo-viscoplastic behavior modeling and to the calibration of the initial geometrical imperfection controlling the onset of the necking.

Thanks to tensile tests carried out for the same operating conditions that those of Marciniak forming tests, several types (power law, saturation and mixed) of hardening laws have been identified. These hardening laws have been implemented in the FE M-K model to obtain numerical limit strains. Very different formability limits have been observed for a given value of the geometrical defect. Several strategies for the calibration of this initial imperfection size have been tested. The use of the experimental point of the  $FLC_0$  corresponding to plane strain condition allows a good calibration of the initial imperfection value. This calibration procedure was carried out for all hardening laws. It is shown that the power law type models such as Ludwick law are more efficient while saturation laws such as Voce law are unable to predict the material formability for some conditions. Finally, it is shown that a constant value of the geometrical defect cannot be used to the whole operating conditions studied even if FE M-K model is shown to be efficient to represent the temperature effect rather than strain rate one.



# Contents

<b>1</b>	<b>Experimental characterization and modeling of sheet metal behavior</b>	<b>5</b>
1.1	Introduction . . . . .	9
1.1.1	Sheet metal forming processes . . . . .	9
1.1.1.1	Traditional sheet forming processes . . . . .	9
1.1.1.2	Innovative sheet forming processes . . . . .	10
1.1.2	Mechanical behavior modeling of metallic sheets . . . . .	12
1.1.2.1	Yield criterion . . . . .	12
1.1.2.2	Flow rule . . . . .	14
1.1.2.3	Hardening law . . . . .	14
1.1.3	Forming limit diagram (FLDs) . . . . .	15
1.2	Experimental characterization . . . . .	15
1.2.1	Flow stress determination . . . . .	16
1.2.1.1	Uniaxial tensile test . . . . .	16
1.2.1.2	Biaxial tension test with cruciform specimen . . . . .	17
1.2.1.3	Bulge test . . . . .	18
1.2.1.4	Shear test . . . . .	19
1.2.1.5	Plane strain compression test . . . . .	20
1.2.2	Yield surface determination . . . . .	21
1.2.2.1	Experimental methods . . . . .	21
1.2.2.2	Yield point definition . . . . .	22
1.2.3	Sheet metal formability . . . . .	23
1.2.3.1	Experimental methods to determine FLDs . . . . .	23
1.2.3.2	Failure criteria . . . . .	26
1.2.3.3	Temperature and strain rate effects on experimental sheet metal formability . . . . .	27
1.3	Rheological modeling of sheet metal . . . . .	28
1.3.1	Phenomenological models . . . . .	28
1.3.1.1	Strain hardening functions . . . . .	28
1.3.1.2	Temperature functions . . . . .	29
1.3.1.3	Strain rate sensitivity functions . . . . .	30
1.3.1.4	Johnson-Cook (JC) model . . . . .	31
1.3.1.5	Khan-Huang (KH), Khan-Huang-Liang (KHL) model . . . . .	31
1.3.1.6	Hollomon - Voce model (H-V) . . . . .	32
1.3.1.7	Modified power law model . . . . .	32

1.3.1.8	Arrhenius equation . . . . .	32
1.3.2	Physical based models . . . . .	33
1.3.2.1	Bodner and Partom (BP) model . . . . .	34
1.3.2.2	Zerilli-Armstrong model (ZA) . . . . .	34
1.3.2.3	Voyiadjis-Abed model (VA) . . . . .	35
1.3.2.4	Rusinek-Klepaczko model . . . . .	35
1.3.2.5	Bergström model . . . . .	36
1.3.3	The yield criteria . . . . .	37
1.3.3.1	Hill 1948 . . . . .	37
1.3.3.2	Hosford 1979 . . . . .	38
1.3.3.3	Barlat 1989 (Yld89) . . . . .	38
1.3.3.4	Banabic-Balan-Comsa (BBC) Yield criteria . . . . .	39
1.3.3.5	Conclusion . . . . .	40
1.4	Predictive models of FLCs . . . . .	40
1.4.1	Analytical models . . . . .	41
1.4.1.1	Hill's criterion . . . . .	41
1.4.1.2	Modified maximum force criterion (MMFC) . . . . .	42
1.4.1.3	Marciniak and Kuczynski (M-K) model . . . . .	42
1.4.2	Theoretical studies of temperature and strain rate sensitivity on FLCs . . . . .	45
1.4.3	Numerical models . . . . .	47
1.4.3.1	Finite element M-K model . . . . .	47
1.4.3.2	Simulation of conventional tests . . . . .	47
1.4.4	Conclusions . . . . .	48
1.5	Conclusions . . . . .	48
<b>2</b>	<b>Investigations on the thermo-elasto-viscoplastic hardening behavior of a</b>	
	<b>5086 aluminium alloy</b>	<b>51</b>
2.1	Introduction . . . . .	55
2.2	Uniaxial tensile test of AA5086 . . . . .	55
2.2.1	Material . . . . .	55
2.2.2	Experimental setup . . . . .	55
2.2.2.1	Specimen . . . . .	55
2.2.2.2	Experimental equipments . . . . .	56
2.2.3	Experimental results . . . . .	56
2.2.4	Discussions . . . . .	57
2.2.4.1	Temperature influence . . . . .	57
2.2.4.2	Strain rate influence . . . . .	57
2.3	Identification methods . . . . .	57
2.3.1	Direct method . . . . .	57
2.3.2	Optimization method . . . . .	61
2.3.2.1	Analytical . . . . .	61
2.3.2.2	Numerical . . . . .	62
2.4	Identification of the rheological parameters for different hardening models . . . . .	63
2.4.1	Initial yield stresses of AA5086 . . . . .	63

2.4.2	Identified hardening models . . . . .	63
2.4.3	Power law hardening models . . . . .	64
2.4.3.1	Ludwick model . . . . .	64
2.4.3.2	KHL model . . . . .	69
2.4.3.3	ZA model . . . . .	73
2.4.4	Saturation type hardening model . . . . .	75
2.4.4.1	Voce_1 model ( $V_1$ model ) . . . . .	75
2.4.4.2	Voce_2 model ( $V_2$ model ) . . . . .	78
2.4.4.3	Voce_3 model ( $V_3$ model ) . . . . .	80
2.4.4.4	Bergström model . . . . .	82
2.4.5	Mixed hardening model (H-V) . . . . .	84
2.5	Conclusions . . . . .	86
<b>3</b>	<b>Experimental investigations of sheet formability under different temperatures and strain rates</b>	<b>89</b>
3.1	Introduction . . . . .	93
3.2	Experimental Marciniak test . . . . .	93
3.2.1	Marciniak heating apparatus . . . . .	94
3.2.2	Specimen geometry . . . . .	95
3.2.3	Image acquisition system . . . . .	97
3.2.4	Strain analyzing . . . . .	99
3.3	Failure criteria to determine the forming limit strains . . . . .	101
3.3.1	Strain increment ratio . . . . .	101
3.3.2	ISO 12004-2 standard . . . . .	102
3.3.3	Time dependent analysis method . . . . .	105
3.3.4	Maximum punch force . . . . .	106
3.3.5	Discussion . . . . .	107
3.4	Temperature and strain rate influence on the formability of AA5086 . . . . .	109
3.4.1	Temperature effect . . . . .	109
3.4.2	Strain rate effect . . . . .	112
3.5	Conclusions . . . . .	114
<b>4</b>	<b>Numerical predictions of AA5086 sheet formability</b>	<b>115</b>
4.1	Introduction . . . . .	119
4.2	Simulation of Marciniak test . . . . .	119
4.2.1	FE Marciniak model . . . . .	119
4.2.1.1	Modeling . . . . .	120
4.2.2	FLCs with FE Marciniak model . . . . .	120
4.2.3	Conclusions . . . . .	122
4.3	Simulation of M-K model . . . . .	123
4.3.1	Presentation of the FE M-K model . . . . .	123
4.3.2	Influence factors of the FE M-K model . . . . .	124
4.3.2.1	Initial imperfection value $f_0$ . . . . .	125
4.3.2.2	Initial inclined groove orientation $\psi_0$ . . . . .	125

---

4.3.2.3	Hardening law . . . . .	126
4.3.2.4	Yield function . . . . .	127
4.4	Determination of FLCs through FE M-K model . . . . .	128
4.4.1	Strategies to calibrate $f_0$ . . . . .	128
4.4.1.1	Calibration at 20°C and 10 mm/s . . . . .	129
4.4.1.2	Calibration at 200°C and 10 mm/s . . . . .	130
4.4.1.3	Conclusions . . . . .	130
4.4.2	FLCs with $f_0$ calibrated from each forming condition . . . . .	131
4.4.2.1	Predicted FLCs from power law type hardening model . . . . .	131
4.4.2.2	Predicted FLCs from saturation type hardening model . . . . .	136
4.4.2.3	Predicted FLCs by mixed type hardening model (H-V) . . . . .	139
4.4.2.4	Conclusions . . . . .	140
4.4.3	Predicted FLCs with a constant calibrated $f_0$ . . . . .	141
4.4.3.1	Temperature influence on the FLCs with a constant $f_0$ . . . . .	141
4.4.3.2	Strain rate influence on the FLCs with constant $f_0$ . . . . .	144
4.4.3.3	Conclusions . . . . .	146
4.5	Conclusions . . . . .	147

# Figures

1.1	Deep cylindrical cup drawing forming process . . . . .	9
1.2	Stretch forming process and equipment . . . . .	10
1.3	Single point incremental sheet forming setup . . . . .	10
1.4	Tube hydroforming process . . . . .	11
1.5	Age forming process . . . . .	12
1.6	A curve of yield locus under plane stress condition . . . . .	13
1.7	Types of hardening . . . . .	14
1.8	Representation of a typical FLD . . . . .	15
1.9	Typical uniaxial tensile stress-strain curve . . . . .	16
1.10	A typical uniaxial tensile specimen . . . . .	17
1.11	Cruciform specimen to determine the flow stress [101] . . . . .	18
1.12	Geometry of the bulge test [36] . . . . .	18
1.13	Comparison of flow stresses obtained with bulge test and uniaxial tensile test	19
1.14	Specimen geometry for double shear test . . . . .	19
1.15	Specimen and device for shear test [10] . . . . .	20
1.16	Schematic view of the plane strain compression test . . . . .	21
1.17	Tensile specimen at an angle $\theta$ from rolling direction . . . . .	21
1.18	Plane strain and simple shear specimen (gray part is clamped) . . . . .	22
1.19	Cruciform specimen for biaxial tension test (in mm) [73] . . . . .	23
1.20	Method to determine the yield point using the stress-strain curve . . . . .	23
1.21	Temperature vs. elongation for standard tensile test piece [67] . . . . .	24
1.22	Out-of-plan and in-plan stretching . . . . .	24
1.23	Warm Nakazima forming test [64] . . . . .	25
1.24	Specimens for tensile test . . . . .	25
1.25	Cruciform specimen for AA5086 [109] . . . . .	26
1.26	Determined FLCs with cruciform specimen for AA5086 [109] . . . . .	26
1.27	Schematic view of Hill's criterion . . . . .	42
1.28	Representation of the M-K model . . . . .	43
1.29	Effect of the initial imperfection factor $f_0$ on the FLCs [105] . . . . .	44
1.30	Comparison of FLCs with different analytical models [105] . . . . .	44
1.31	Comparison of rate sensitivity effect on FLCs between perturbation analysis and M-K model . . . . .	46
1.32	FE M-K model and corresponding boundary conditions [106] . . . . .	47

2.1	Geometry and dimensions of the tensile specimen (dimensions in mm) . . . . .	56
2.2	Grip system used in the tensile tests . . . . .	56
2.3	Force versus displacement curves at different temperatures for each tensile speed	58
2.4	Temperature influence on the flow stresses at different tensile speeds . . . . .	59
2.5	Tensile speed influence on the flow stresses at different temperatures . . . . .	60
2.6	Parameter determination with direct method . . . . .	61
2.7	Principle of the optimization procedure [29] . . . . .	62
2.8	Evolution of the initial yield stresses for AA5086 . . . . .	64
2.9	Identification results of the original Ludwick model . . . . .	66
2.10	Evolution of $K$ and $n$ with temperature for Ludwick model . . . . .	66
2.11	Prediction results with strain rate modified Ludwick model for each tempera- ture . . . . .	67
2.12	Evolution of $K$ and $n$ for Ludwick model with strain rate term . . . . .	68
2.13	Strain rate sensitivity index $m$ at different temperatures . . . . .	68
2.14	Correlation results of proposed Ludwick model with strain level up to 50% . .	69
2.15	Correlation results of the proposed Ludwick model under different temperatures and strain rates . . . . .	70
2.16	Correlation results of the proposed KHL model with strain levels up to 50% .	71
2.17	Correlation results of the proposed KHL model under different temperatures and strain rates . . . . .	72
2.18	Correlation results of the proposed ZA model with strain levels up to 50% . .	73
2.19	Correlation results of the proposed ZA model under different temperatures and strain rates . . . . .	74
2.20	Evolution of $C_1$ and $C_2$ with temperature under different tensile speeds . . . .	76
2.21	Correlation results of $V_1$ model with strain levels up to 50% . . . . .	76
2.22	Correlation results of the proposed $V_1$ model under different temperatures and strain rates . . . . .	77
2.23	Correlation results of $V_2$ model with strain levels up to 50% . . . . .	78
2.24	Correlation results of the proposed $V_2$ model under different temperatures and strain rates . . . . .	79
2.25	Correlation results of $V_3$ model with strain levels up to 50% . . . . .	80
2.26	Correlation results of the proposed $V_3$ model under different temperatures and strain rates . . . . .	81
2.27	Correlation results of the proposed Bergström model with strain levels up to 50% 82	
2.28	Correlation results of the proposed <i>Bergström</i> model under different tempera- tures and strain rates . . . . .	83
2.29	Correlation results of proposed H-V model with strain levels up to 50% . . . .	84
2.30	Correlation results of the proposed H-V model under different temperatures and strain rates . . . . .	85
2.31	Flow stresses predicted by different hardening models with strain level up to 50%. . . . .	87
3.1	Comparison of Nakazima and Marciniak tests . . . . .	93
3.2	Cross section of Marciniak test . . . . .	94

---

3.3	Marciniak heating apparatus . . . . .	95
3.4	Temperature evolutions in the punch and specimen . . . . .	95
3.5	Typical specimen example . . . . .	96
3.6	Different strain paths on the FLC . . . . .	97
3.7	Schema of the acquisition system . . . . .	98
3.8	Experimental acquisition system . . . . .	98
3.9	Specimen painted with a speckle pattern . . . . .	98
3.10	DIC principle . . . . .	99
3.11	Selected zone for correlation analysis . . . . .	100
3.12	Subset dimensions . . . . .	100
3.13	Geometry models for strain calculation . . . . .	100
3.14	Major true strain evolution of different zones . . . . .	101
3.15	Strain increment ratio criterion . . . . .	102
3.16	Cross sections proposed in ISO 12004-2 . . . . .	103
3.17	Profile of major strain distribution . . . . .	103
3.18	Determination of the inner boundary of the fit window . . . . .	104
3.19	Example of inverse fit parabola to determine the limit strains . . . . .	104
3.20	Limit points obtained with ISO 12004-2 and the modified method . . . . .	105
3.21	Time dependent method . . . . .	106
3.22	Force evolution during Marciniak test . . . . .	107
3.23	Equivalent strain distribution into the specimen at different critical times . . . . .	108
3.24	The FLCs of AA5086 at 150°C and 10 mm/s with different failure criteria . . . . .	108
3.25	FLCs of AA5086 under different temperatures and strain rates . . . . .	109
3.26	Limit major strains for the 3 typical strain states at different temperatures and 10 mm/s . . . . .	110
3.27	Limit major strains for the 3 typical strain states at different temperatures and 1 mm/s . . . . .	110
3.28	Limit major strains for the 3 typical strain states at different temperatures and 0.1 mm/s . . . . .	110
3.29	$FLC_0$ at different temperatures and strain rates . . . . .	111
3.30	The FLCs of AA5086 at different temperatures for a forming speed of 10 mm/s . . . . .	111
3.31	The FLCs of AA5086 at different temperatures for a forming speed of 1 mm/s . . . . .	112
3.32	The FLCs of AA5086 at different temperatures for a forming speed of 0.1 mm/s . . . . .	112
3.33	Limit major strains of 3 typical strain states for different strain rates at 150°C . . . . .	113
3.34	Limit major strains of 3 typical strain states for different strain rates at 200°C . . . . .	113
3.35	Strain rate influence on the formability of AA5086 at 150°C . . . . .	113
3.36	Strain rate influence on the formability of AA5086 at 200°C . . . . .	114
4.1	FE Marciniak test model in ABAQUS . . . . .	119
4.2	Example of a specimen shape . . . . .	120
4.3	Specimen mesh in the FE model of the Marciniak test . . . . .	120
4.4	Selected zone of the ISO 12004-2 criterion in the FE Marciniak model . . . . .	121
4.5	Example of inverse fit parabola for FE Marciniak . . . . .	121
4.6	Predicted FLCs obtained by Ludwick model with ISO 12004-2 . . . . .	122

4.7	Predicted FLCs obtained by Voce_1 model with ISO 12004-2 . . . . .	122
4.8	Predicted FLCs with Ludwick model under different strain rates . . . . .	123
4.9	FE MK model in ABAQUS (dimensions in mm) . . . . .	124
4.10	Equivalent plastic strain (PEEQ) distribution in different zones of the FE M-K model . . . . .	124
4.11	Influence of $f_0$ on the FLCs in the FE M-K model . . . . .	125
4.12	FE M-K model with an initial inclined groove . . . . .	126
4.13	FLCs obtained with different initial inclined grooves in FE M-K model . . . . .	126
4.14	Crack in experimental specimens . . . . .	126
4.15	Hardening law influence on the FLCs in FE M-K model . . . . .	127
4.16	Yield function influence on the FLCs in FE M-K model . . . . .	128
4.17	Imperfection value $f_0$ calibration method . . . . .	129
4.18	Comparison of different $f_0$ calibration methods at 20°C and 10 mm/s . . . . .	130
4.19	Comparison of different $f_0$ calibration methods at 200°C and 10 mm/s . . . . .	131
4.20	Predicted FLCs with Hill'48 yield function and Ludwick model . . . . .	132
4.21	Predicted FLCs with Ludwick model . . . . .	133
4.22	Predicted FLCs with KHL model . . . . .	135
4.23	Predicted FLCs with ZA model under 10 mm/s . . . . .	136
4.24	Predicted FLCs by Voce_1 model under 10 mm/s . . . . .	137
4.25	Predicted FLCs by Ludwick model under 10 mm/s . . . . .	137
4.26	Predicted FLCs with Hill'48 yield function and Voce_1 model . . . . .	138
4.27	Predicted FLCs by Voce_3 model at 10 mm/s . . . . .	139
4.28	Predicted FLCs by H-V model at 10 mm/s . . . . .	140
4.29	Predicted FLCs by Ludwick model with $f_0=0.996$ at 10 mm/s . . . . .	142
4.30	$FLC_0$ by Ludwick model with $f_0$ calibrated at different temperatures and at 10 mm/s . . . . .	142
4.31	$FLC_0$ for different $f_0$ values at 10 mm/s . . . . .	143
4.32	$FLC_0$ by Ludwick model with $f_0$ calibrated at different temperatures and at 1 mm/s . . . . .	144
4.33	$FLC_0$ with different values of $f_0$ from Ludwick model at 150°C . . . . .	144
4.34	$FLC_0$ with different values of $f_0$ from Voce_1 model at 150°C . . . . .	145
4.35	$FLC_0$ with different values of $f_0$ by Ludwick model at 200°C . . . . .	145
4.36	$FLC_0$ from Ludwick model with different calibrated $f_0$ at different forming speeds and at 150°C . . . . .	146
4.37	$FLC_0$ from Ludwick model with different calibrated $f_0$ at different forming speeds and at 200°C . . . . .	146

# Tables

1.1	The mechanical parameters needed for different yield functions . . . . .	40
2.1	Chemical components of AA5086 in weight percent (asm.matweb.com) . . . . .	55
2.2	Identification of rheological parameters [29] . . . . .	61
2.3	Initial yield stresses of AA5086 at different temperatures . . . . .	63
2.4	Overview of the different hardening models . . . . .	64
2.5	The values of $K$ and $n$ under different temperatures and tensile speeds . . . . .	65
2.6	Fitting values of $K$ , $n$ and $m$ for each temperature under the three tensile speeds . . . . .	65
2.7	Optimized parameters of the final proposed Ludwick model . . . . .	69
2.8	The fitting parameters of proposed KHL model . . . . .	71
2.9	The fitting parameters of modified ZA model . . . . .	73
2.10	The fitting values $C_1$ and $C_2$ under each forming condition . . . . .	75
2.11	The fitting parameters of $V_1$ model under all forming conditions . . . . .	76
2.12	The fitting parameters of $V_2$ model . . . . .	78
2.13	The fitting parameters of $V_3$ model . . . . .	80
2.14	The fitting parameters of the proposed Bergström model . . . . .	82
2.15	The fitting parameters of proposed H-V model . . . . .	84
3.1	Part dimensions of Marciniak test . . . . .	94
3.2	Temperature parameters in the heating system . . . . .	96
3.3	Specimen dimensions of Marciniak test . . . . .	96
3.4	Configuration parameters in the CMOS camera . . . . .	99
3.5	Forming limit values with different interval times . . . . .	102
3.6	Limit strains obtained by ISO 12004-2 and modified method . . . . .	105
3.7	Limit strain and corresponding instants with different criteria . . . . .	107
4.1	Friction coefficients in contact interactions of the FE model of Marciniak test . . . . .	120
4.2	The parameters of Hill'48 yield function for AA5086 . . . . .	127
4.3	Experimental points and calibrated $f_0$ at 20°C and 10 mm/s . . . . .	129
4.4	Experimental points and calibrated $f_0$ at 200°C and 10 mm/s . . . . .	130
4.5	Experimental values of $FLC_0$ under different forming conditions . . . . .	131
4.6	Calibrated $f_0$ with Ludwick model . . . . .	132
4.7	Calibrated $f_0$ with KHL model . . . . .	134
4.8	Calibrated $f_0$ with ZA model . . . . .	134
4.9	Calibrated $f_0$ with Voce_1 model . . . . .	136

---

4.10	Calibrated $f_0$ with Voce_2 model . . . . .	138
4.11	Calibrated $f_0$ with Voce_3 model . . . . .	139
4.12	Calibrated $f_0$ with Bergström model . . . . .	140
4.13	Calibrated $f_0$ with H-V model . . . . .	140

# Notations

---

<i>DIC</i>	Digital Image Correlation
<i>FLCs</i>	Forming Limit Curves
<i>FLDs</i>	Forming Limit Diagrams
<i>FLC<sub>0</sub></i>	forming limit under plane strain condition
M-K	Marciniak and Kuczynski
$\bar{\epsilon}, \dot{\bar{\epsilon}}$	equivalent strain and equivalent strain rate
$\bar{\epsilon}_p, \dot{\bar{\epsilon}}_p$	equivalent plastic strain and equivalent plastic strain rate
$\bar{\sigma}$	equivalent stress
$\sigma_0$	initial yield stress
$T_m$	material melting temperature
$E$	Young's modulus
$\dot{\epsilon}_0$	reference strain rate
$\psi_0, \psi$	initial and current groove orientation in the M-K model
$f_0, f$	initial and current imperfection factor in the M-K model
$\sigma_{ij}, \epsilon_{ij}$	components of stress and strain tensor
$\beta, \beta_{exp}$	principal strain path and experimental strain path
$\bar{\sigma}_a, \bar{\sigma}_{th}$	athermal and thermal stresses



# Introduction Générale

---

*Les procédés de mise en forme des tôles métalliques sont largement employés dans les cycles de production de biens d'équipement très divers. Dans le domaine des transports notamment, les exigences environnementales et économiques conduisent à une innovation continue tant sur les procédés de fabrication que sur les nuances de matériaux mis en œuvre. Néanmoins, l'utilisation de ces nouvelles nuances peut rapidement être limitée par une faible aptitude à la mise en forme. Cette remarque est notamment valable pour les alliages d'aluminium qui en dépit d'une rigidité spécifique intéressante, d'une bonne résistance à la corrosion ou encore d'un fort potentiel d'assemblage par soudage, présentent généralement une formabilité à température ambiante bien inférieure à celle de la plupart des aciers. La formabilité des alliages d'aluminium peut être améliorée en augmentant la température de mise en forme. Cependant, si ces matériaux sont chauffés, le niveau des vitesses de déformation mis en jeu au sein du procédé peut alors modifier leur comportement mécanique et donc leurs limites de formabilité. L'utilisation d'outils numériques pour optimiser les procédés de mise en forme requiert une connaissance fine du matériau formé afin d'intégrer des modèles de comportement fiables quelles que soient les conditions opératoires considérées. Concernant l'évaluation des limites de formabilité, il est donc essentiel de prendre en compte les effets couplés de la température et de la vitesse de déformation.*

*Le niveau de formabilité des métaux en feuilles est classiquement estimé à partir du tracé de Courbes Limites de Formage (CLF). Malgré de nombreux désavantages, sa simplicité de mise en œuvre lui confère une utilisation relativement large. Le tracé expérimental de CLF en température et à différentes vitesses de déformation reste assez difficile et limite l'obtention de bases expérimentales fiables. De plus, peu de modèles prédictifs des limites de formabilité, qu'ils soient analytiques ou numériques, intègrent les effets de la température et de la vitesse de déformation et surtout proposent une corrélation directe avec des résultats expérimentaux.*

*Beaucoup de modèles prédictifs des courbes limites de formage sont basés sur le modèle classique de Marciniak et Kuczynski (M-K). Ce modèle consiste à incorporer un défaut géométrique dans l'épaisseur d'une plaque afin de favoriser l'apparition d'une striction localisée. L'inconvénient majeur de ce modèle réside dans la grande sensibilité des résultats vis-à-vis de la valeur de ce défaut. De plus, le modèle M-K met généralement en œuvre des comportements élastoplastiques simplistes, pas toujours représentatifs du comportement du matériau étudié. Le manque de précision de ces modèles est donc lié à un calibrage difficile du défaut géométrique et à une modélisation approximative du comportement rhéologique du matériau. Ce dernier point est d'autant plus sensible lorsque l'effet de la température et de la vitesse de déformation doit être intégré au modèle. Les limitations intrinsèques des modèles analytiques classiques ont naturellement orienté le développement des modèles prédictifs vers des formulations plus riches, capables de modéliser des comportements thermo-élasto-viscoplastiques plus réalistes. La méthode des éléments finis (EF) peut répondre à ce besoin et peut s'avérer assez efficace pour détecter l'apparition d'une striction localisée.*

*L'objectif de ce travail est de contribuer à l'étude de l'effet de la température et de la vitesse de déformation sur la formabilité d'un alliage d'aluminium de type 5086. Cette étude sera menée à partir d'une base expérimentale qui permettra ainsi de discuter la validité d'un modèle prédictif suffisamment riche pour prendre en compte les conditions opératoires retenues.*

*Dans le premier chapitre, une revue bibliographique est présentée. Elle porte sur la caractérisation expérimentale et la modélisation du comportement rhéologique et de la formabilité des matériaux métalliques en température et sur une large plage de vitesse de déformation. La dernière partie de ce*

chapitre met en évidence le déficit de modèles prédictifs fiables de courbes limites de formage pour ces conditions.

Dans le deuxième chapitre, le choix d'un modèle de loi d'écrouissage intégrant les effets de la température et de la vitesse de déformation est discuté. Ce choix est d'autant plus difficile lorsque l'identification de ces lois est réalisée à partir d'essais de traction uniaxiale classiques sur une plage de déformation limitée. Parmi toutes les lois présentées dans le chapitre I, huit d'entre elles sont choisies et classifiées suivant trois familles : lois de type puissance, de type saturante et de type mixte. L'identification de ces lois a été menée à partir d'essais de traction uniaxiale sur éprouvettes à section constante pour des vitesses d'essai de 1, 10 et 100 mm/s et pour des températures de 20, 150 et 200°C. Les lois choisies permettent de décrire une grande variété de comportements pour des grandes déformations. Les effets de ces lois sur la prédiction des CLF seront discutés dans le dernier chapitre.

Dans le troisième chapitre, un dispositif de type Marciniak a été retenu pour caractériser la formabilité de l'alliage d'aluminium 5086 pour les conditions opératoires étudiées. La mise en température des éprouvettes se fait par conduction, grâce à des cartouches chauffantes placées à l'intérieur des serre-flans. La mesure des déformations dans le plan de l'éprouvette est assurée par corrélation d'images. Le choix du critère permettant de détecter l'apparition de la striction est discuté grâce à la comparaison des résultats de plusieurs critères. Les essais sont réalisés à température ambiante et pour des températures de 150 et 200°C. Trois vitesses de poinçon sont retenues : 0.1, 1 et 10 mm/s, ces vitesses engendrent les mêmes niveaux de vitesses de déformation mesurés lors des précédents essais de traction. Les courbes limite de formage obtenues montrent un effet certain de la température et de la vitesse de déformation sur la formabilité du matériau étudié.

Dans le quatrième chapitre, une modélisation par la méthode des éléments finis de l'essai de Marciniak développé dans le précédent chapitre est tout d'abord présentée. Ce modèle ne permettant pas une prédiction précise des CLF, le modèle géométrique M-K est alors modélisé par la méthode des éléments finis. Dans un premier temps, l'influence de plusieurs paramètres (valeur du défaut géométrique, loi d'écrouissage et critère de plasticité) est quantifiée. Il est montré que la phase de calibration du défaut géométrique est bien évidemment critique, plusieurs stratégies de calibration sont alors discutées. Finalement, une comparaison des résultats expérimentaux du chapitre précédent avec les prédictions du modèle M-K est réalisée pour toutes les températures et vitesses de déformation testées. La comparaison est menée avec l'ensemble des lois identifiées dans le second chapitre, certaines d'entre elles se sont avérées incapables de prédire la formabilité du matériau pour certaines conditions.

# General introduction

---

Sheet metal forming processes are widely used for the manufacturing of diverse components. In transportation industries, due to the increasing environment and fuel economy requirements, many innovative materials and forming processes have been developed. Aluminium alloys which show good specific stiffness, corrosion resistance and weldability properties are considered as interesting candidates for mass reduction problem. However, their applications are highly limited by their low formability at ambient temperature compared to traditional steels. With innovative warm forming methods, the formability can be greatly improved. However, under warm forming conditions, the forming speed and then strain rate can affect the sheet metal mechanical behavior and formability. Numerical models are often used to optimize the process parameters and require a good knowledge of the material rheological behavior under the tested forming conditions. Hence, to predict the sheet metal formability, it is essential to take into account the coupling effect of temperature and strain rate.

A prevalent tool to assess sheet metal formability is the Forming Limit Diagram (FLD) developed by Keeler and Backofen (1960s). Despite many disadvantages, it is widely used due to its simplicity and it is always the subject of extensive experimental, analytical and numerical studies. The difficulty to obtain experimental Forming Limit Curves (FLCs) at different temperatures and strain rates limits the availability of reliable experimental database. In addition, few analytical or numerical predictive models, taking into account both temperature and strain rate effects, can be found in the literature and comparisons between experimental and predictive results are very seldom.

Based on the Marciniak and Kuczynski (M-K) theory, many works on FLC prediction have been carried out. The analytical M-K model assumes an initial thickness imperfection which leads to the onset of a localized necking. The main disadvantage of the M-K model is that the studied results are greatly dependent on this initial imperfection value. In addition, the hardening models which can be implemented in the M-K model are generally simplistic and are not always representative of the behavior of the material. The difficulty of calibrating the initial imperfection and to use sophisticated behavior models make this analytical model imprecise. This imprecision is much more significant when the temperature and strain rate effects should be considered. The intrinsic limitations of classical analytical predictive models have led to the development of numerical modeling in which advanced formulations able to represent the realistic thermo-elasto-viscoplastic behaviors could be implemented. The FE method can be an interesting alternative in this way and can be an efficient tool to detect the localized necking.

The objective of this work is to investigate the temperature and strain rate effects on the formability of an aluminium alloy AA5086. This study is based on an experimental database which will permit to discuss the validity of a predictive model taking into account these operating conditions.

In Chapter 1, a bibliographical review is presented. It focuses on the experimental characterization and modeling of the rheological behavior and formability of the metallic sheet

at different temperatures and over a wide range of strain rate. The last part of this chapter highlights the lack of reliable FLC predictive models for these forming conditions.

In Chapter 2, the choice of a hardening model able to describe the effects of temperature and strain rate is discussed. This choice can be very difficult when the parameter identification is led with the uniaxial test in which the strain level for an homogeneous deformation is limited. Among all the models presented in Chapter 1, eight hardening models are selected and classified into three types of laws: power, saturation and mixed. The uniaxial tensile tests with constant section specimens are performed at different temperatures (20, 150 and 200°C) and tensile speeds (1, 10 and 100 mm/s). The identified flow stresses from different hardening models up to large strain levels are compared and discussed. The effects of these models on the FLC predictions will be discussed in Chapter 4.

In Chapter 3, an existing Marciniak experimental device is modified to characterize the formability of sheet metal AA5086 under different temperatures (20, 150 and 200°C) and different punch speeds (0.1, 1 and 10 mm/s). These speeds give the same strain rate levels as the ones discussed in the previous tensile tests. The Marciniak specimen is heated by heat conduction through heaters inserted inside the blankholders. The specimen deformation is measured with a high speed camera and Digital Image Correlation (DIC) method. Different criteria are used to determine the limit strain values and discussed. The obtained FLCs show a clear temperature and strain rate effect on the formability of the studied material.

In Chapter 4, a FE Marciniak model corresponding to experimental apparatus is first presented. This model can not give an accurate FLC prediction, and a FE M-K model is then proposed according to the M-K theory. With this FE M-K model, the influence of several parameters (initial imperfection value, hardening model and yield function) is first quantified. The results show that the calibration of the initial imperfection value  $f_0$  is clearly critical. Different geometrical calibration methods are proposed and discussed. Finally, a comparison between experimental results and predictions from the FE M-K model is performed for all the tested temperatures and strain rates. The comparison notably shows that some of the hardening models proposed in Chapter 2 are unsuitable to predict the material formability under certain conditions.

## Chapter 1

# Experimental characterization and modeling of sheet metal behavior



*Dans ce chapitre, une brève présentation des principaux procédés de mise en forme des tôles métalliques minces et de leurs principales spécificités est tout d'abord proposée. On s'intéresse plus particulièrement ici aux différents travaux concernant la mise en forme des alliages d'aluminium. Pour l'ensemble des procédés envisagés, qu'ils soient conventionnels ou innovants, la plage de température dans laquelle l'opération de mise en forme est généralement réalisée ainsi que le niveau des vitesses de déformation rencontrées sont identifiés.*

*L'objectif principal de ce travail est de contribuer à l'amélioration des modèles prédictifs de comportement des tôles métalliques en mise en forme. Dans ce but, les outils nécessaires, d'une part à la modélisation du comportement thermo-viscoplastique et d'autre part à l'évaluation de la formabilité des matériaux métalliques sont succinctement présentés. La calibration de ces modèles, en température et sur une plage de vitesse de déformation donnée, nécessite l'établissement de bases expérimentales fiables. Pour cela, les principaux essais rhéologiques permettant la caractérisation de la surface de charge initiale, de la loi d'érouissage ainsi que des limites de formabilité des tôles métalliques minces sont présentés.*

*Par la suite, une étude bibliographique montre que de nombreux modèles rhéologiques ont été proposés pour traduire le comportement thermo-viscoplastique des tôles minces en mise en forme, tant au niveau de l'érouissage qu'en ce qui concerne la description de la surface de charge initiale du matériau. Les modèles d'érouissage peuvent être classés en deux catégories distinctes selon leur origine : phénoménologique ou physique. Parmi les nombreux modèles de la littérature, les plus représentatifs d'entre-eux ont été retenus pour la suite de ce travail. Ils seront calibrés au chapitre 2 et introduits dans le modèle prédictif proposé au chapitre 4. En ce qui concerne les modèles prédictifs des limites de formabilité, qu'ils soient analytiques ou numériques, peu d'entre eux intègrent les effets de la température et de la vitesse de déformation et surtout proposent une corrélation directe avec des résultats expérimentaux.*



## 1.1 Introduction

Sheet metal forming is very commonly used for producing components of various products in automotive or aeronautic industries. The increasing industrial demands such as reduction cost, reducing production cycle, part performance improvement and complex shapes lead to the development of innovative sheet forming processes and new designed materials, as well as the knowledge of related characterizations. For sheet metal forming process, a final objective is to find a reliable predictive model to optimize the related parameters.

In this chapter, a brief overview of the main sheet metal forming processes and their characteristics is first introduced. The essential tools (hardening law and yield function) that can be used to establish a predictive model for sheet metal are then presented. The experimental methods used to identify these tools are also given. A literature of the different hardening models used to describe the flow stress of the sheet metal is introduced and discussed. This review helps to choose the appropriate hardening models for describing the flow stress of the studied aluminium alloy. Finally, a review of sheet formability predictive models taking into account temperature and strain rate effects is presented.

### 1.1.1 Sheet metal forming processes

Due to new demands of the market, lots of innovative processes are developed. In this part, the traditional and innovative sheet metal processes are briefly introduced.

#### 1.1.1.1 Traditional sheet forming processes

Figure 1.1 shows an example of deep cylindrical cup drawing process, the punch and die are manufactured to be close to the shape of product.

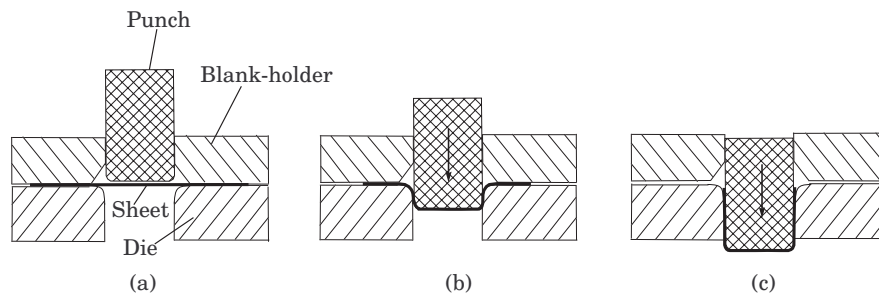


Figure 1.1: Deep cylindrical cup drawing forming process

Figure 1.2 shows another conventional stretch forming process. The sheet metal is stretched bent simultaneously over a die in order to form large contour parts. The sheet is securely gripped along its edges by the gripping jaws which provide the stretching force. The stretch forming is usually combined with other forming techniques to perform the parts with large dimensions (aircraft fuselage).



Figure 1.2: Stretch forming process and equipment

For large-scale part production, traditional processes are economical. They are usually performed at ambient temperature which limits the complexity of the manufactured parts. But with increasing demands of process flexibility, short production cycle or high accuracy dimension control, some innovation techniques have been developed in the last decades.

#### 1.1.1.2 Innovative sheet forming processes

**Incremental sheet forming** The incremental sheet forming technology is a process in which a generic tool profile produces a progressive local plastic deformation in a sheet metal, increasing the formability. This process allows the manufacture of complex parts for small to medium-batch production by moving a spherical-ended indenter over a controlled tool path. This process may be very economical for small batch production, particularly for prototyping. Although it owns many advantages, the long time to form a part, the dedicated machine and the springback caused by the residual stress relaxation are the main disadvantages. An example of single point incremental forming (SPIF) setup combined with cooling-lubrication is shown in Figure 1.3.



Figure 1.3: Single point incremental sheet forming setup

**Hydroforming** Hydroforming uses high pressure hydraulic fluid to expand the sheet metal until it matches the mold. Hydroforming can produce complex parts which are difficult or even impossible with standard solid die stamping. The schematic diagram of tube hydroforming and an example of part are shown in Figure 1.4. By heating the sheet material through the heated hydraulic fluid or with a direct induction heating system, the warm hydroforming

process can be carried out, which improves the formability of materials (e.g. aluminium alloys).

Hydroforming process allows to obtain a good quality part with uniform strain distribution and it is possible to produce the part with complex shapes. A homogeneous and regular pressure is an advantage for the sheet metal drawing ability using hydroforming process.

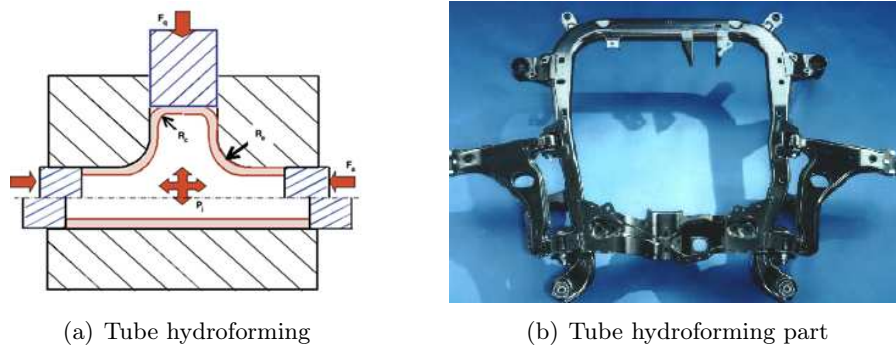


Figure 1.4: Tube hydroforming process

**Warm forming** To improve the poor formability of some metallic alloys, a lot of studies were focused on warm forming processes which significantly increase the formability. They are usually carried out at an intermediate temperature below recrystallization temperature (maximum up to 350°C for aluminium alloys). Under warm forming conditions, the forming speed begins to play an important role. It can affect mechanical behavior of the sheet metal and limit the sheet metal formability. A review of warm forming of aluminum–magnesium alloys about temperature and strain rate effects was introduced in [96]. It was demonstrated that the sheet formability was greatly improved by an uniform temperature increase, but better results are obtained by applying temperature gradients among the sheet, the punch and the blank holder.

**Age forming** Age forming is commonly practiced to improve mechanical strength of the structure and is well known as a low cost process for forming aircraft wing skins. Age forming can be performed on heat treatable alloys of AA 2XXX, 6XXX and 7XXX series. During age forming process, the material is heated to a dedicated temperature (e.g. 150°C for AA7075 [38]) and kept for several hours for aging, creeping and stress relaxation stages. The process usually needs common vacuum bagging and autoclave technologies as shown in Figure 1.5. During autoclave process, the vacuum forces the sheet into the mold.

The main drawback of this process is the springback [43] that occurs during forming which is much larger than that obtained under conventional cold forming condition. To get the required tolerances, it needs a lot of trial-error tests to find the best solution which increases the manufacture cost.

**Superplastic forming** Superplastic Forming (SPF) brings solid crystalline materials, such as titanium, aluminium or magnesium alloys, to a state of superplasticity in which the flow stress of material is low and the elongation can reach ten times of the usual state. In the case of aluminium alloys, superplastic forming is generally carried out at a temperature

close to the alloy solution one (470 - 520°C ) and for low strain rates ( $10^{-3}$  to  $10^{-4}$  s $^{-1}$ ) (www.keytometal.com).

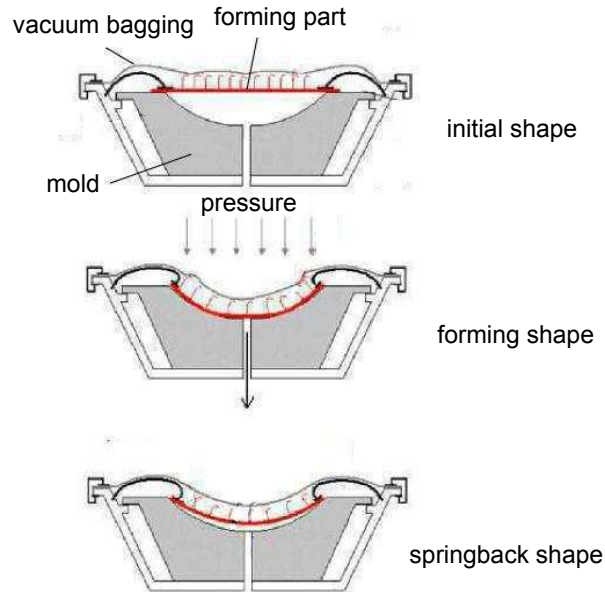


Figure 1.5: Age forming process

For all the innovative processes described above, expensive equipments and the lack of knowledge for the determination of optimum process parameters and tool design limit their applications. To optimize these processes, the simulation method is generally used. But the simulation result depends greatly on the rheological behaviors of the sheet metal under different forming conditions. Generally, the temperature can improve the sheet metal formability and the strain rate also plays an important role. Hence, it is crucial to know the sheet metal rheological behaviors taking into account the temperature and strain rate effects.

### 1.1.2 Mechanical behavior modeling of metallic sheets

The reliability of the simulation process greatly depends on the material constitutive models. Three elements are needed to describe the plastic behavior of a material in a general stress state:

- a yield criterion that defines initial plastic response of the material, expressing a relationship between the stress components when plastic yielding happens.
- a flow rule that gives the relationship between plastic strain increments and stress increments after initiation of plastic deformation.
- a hardening law describing the evolution of yield stress during forming process according to the level of deformation in the material.

#### 1.1.2.1 Yield criterion

For a material, the yield point defines the beginning of plastic deformation. Prior to the yield point, the material deforms elastically which is reversible when the applied stress is

removed. When the stress passes the yield point, non-reversible plastic deformation occurs. The condition under which the plastic flow occurs is known as the yield criterion. The yield criterion surface is usually described by an implicit equation with the form:

$$f(\bar{\sigma}, \sigma_0) = \bar{\sigma} - \sigma_0 \quad (1.1)$$

Where  $\bar{\sigma}$  and  $\sigma_0$  are the equivalent stress and the yield stress from a simple test (tension, compression or shearing). According to different stress states, the function  $f$  may equal to zero (plastic state) or be negative (elastic state). The yield criterion is a mathematical description of a three-dimension surface in the principal stress space. Under plane stress condition (generally admitted for sheet forming process), the yield surface is reduced to a curve in which different strain state points are identified, as shown in Figure 1.6.

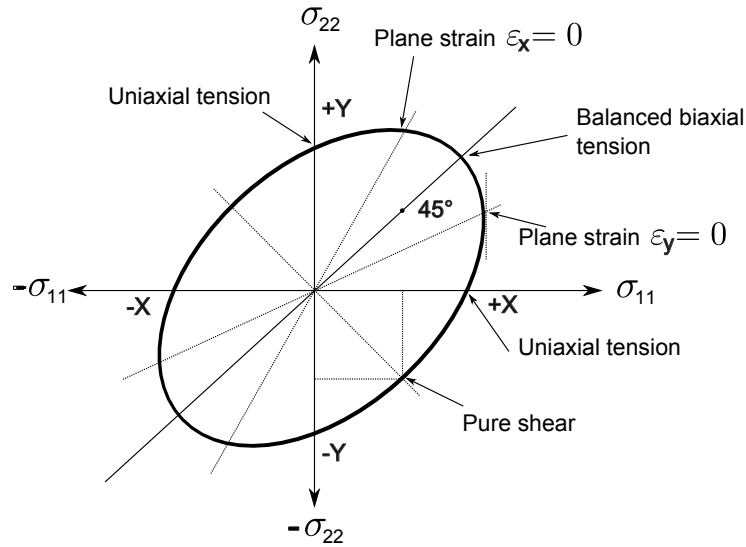


Figure 1.6: A curve of yield locus under plane stress condition

The von Mises yield function is widely used for isotropic materials. It can be written in terms of the general stress state:

$$2\bar{\sigma}^2 = (\sigma_{xx} - \sigma_{yy})^2 + (\sigma_{xx} - \sigma_{zz})^2 + (\sigma_{yy} - \sigma_{zz})^2 + 6(\sigma_{xy}^2 + \sigma_{xz}^2 + \sigma_{yz}^2) \quad (1.2)$$

Where  $\sigma_{xx}$ ,  $\sigma_{yy}$ ,  $\sigma_{zz}$ ,  $\sigma_{xy}$ ,  $\sigma_{xz}$  and  $\sigma_{yz}$  are stress tensor components in an arbitrary orthogonal coordinate set.

In principal stress space, it is reduced to:

$$2\bar{\sigma}^2 = (\sigma_{11} - \sigma_{22})^2 + (\sigma_{11} - \sigma_{33})^2 + (\sigma_{22} - \sigma_{33})^2$$

and under plane stress condition  $\sigma_{33} = 0$  :

$$\bar{\sigma}^2 = \sigma_{11}^2 - \sigma_{11}\sigma_{22} + \sigma_{22}^2$$

Where  $\sigma_{11}$ ,  $\sigma_{22}$  and  $\sigma_{33}$  are the principal stresses.

### 1.1.2.2 Flow rule

For metals, to describe the material behavior under plastic deformation, the associated flow rule is necessary. It can be interpreted that the plastic strain increment vector is normal to the yield surface when the plastic deformation happens. The normality rule can be expressed as :

$$\frac{d\varepsilon_{ij}^p}{dt} = \lambda \frac{\partial f}{\partial \sigma_{ij}} \quad (1.3)$$

Where  $\varepsilon_{ij}^p$  is a plastic strain component,  $\lambda$  is the plastic multiplier coefficient,  $f$  the yield function and  $\sigma_{ij}$  a stress component.

### 1.1.2.3 Hardening law

The hardening law predicts the changes of flow stress according to the plastic strain. Two types of hardening laws are available: isotropic hardening and kinematic hardening. For isotropic hardening, the yield surface remains centered about its initial centerline and expands in size as the plastic strains develop (Figure 1.7(a)). Kinematic hardening assumes that the yield surface remains constant in size and the surface translates in stress space with progressive yielding, as presented in Figure 1.7(b).

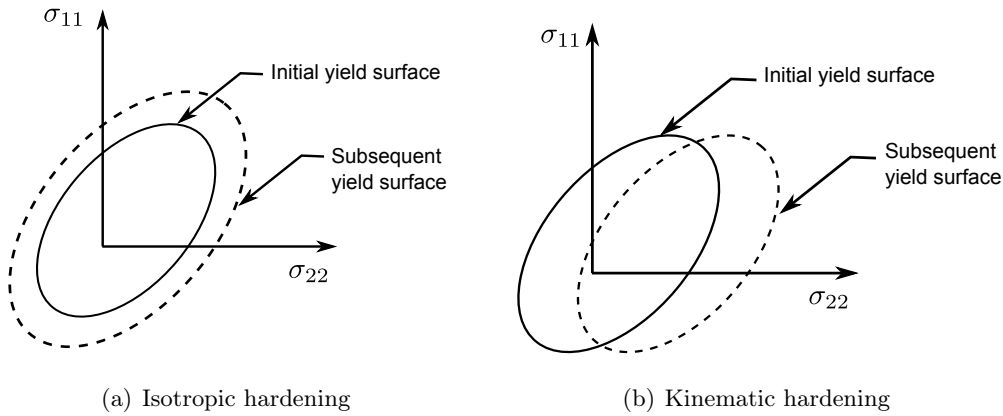


Figure 1.7: Types of hardening

The hardening law is used to describe the strain hardening, thermal softening, temperature and strain rate sensitivities of the material. Two parameters play an important role in describing the material flow stress: strain hardening index ( $n$ ) and strain rate sensitivity index ( $m$ ).

$$n = d(\ln \bar{\sigma}) / d(\ln \bar{\varepsilon}) \quad (1.4)$$

$$m = d(\ln \bar{\sigma}) / d(\ln \dot{\bar{\varepsilon}}) \quad (1.5)$$

Where  $\bar{\varepsilon}$  and  $\dot{\bar{\varepsilon}}$  are equivalent strain and equivalent strain rate, respectively. The strain hardening index  $n$  controls the amount of strain that the material can undergo before strain localization, necking and failure. The value of  $n$  results from a competition between thermal

softening and work hardening. The strain rate sensitivity index  $m$  evolves with temperature, and for some materials, it is also strain rate dependent. With a higher  $m$  value, strain localization in the reduced section is postponed and the formability is enhanced.

Due to combined effects of strain hardening and thermally activated softening, most metallic flow stress curves consist four stages: work hardening stage, transition stage, softening stage and steady stage [61]. In the first stage, the stress increases deeply. The softening phenomenon is induced by the dynamic recovery and dynamic recrystallization. At last, the stress becomes steady when a new balance between softening and hardening is obtained.

### 1.1.3 Forming limit diagram (FLDs)

The sheet metal forming process is usually limited by the onset of localized necking, which leads to early failure. The formability of sheet metal describes its intrinsic ability to be formed into various shapes without failure. Formability depends on many factors like material properties (e.g. strain hardening coefficient, strain rate sensitivity, anisotropy ratio) and process parameters (e.g. strain rate, temperature) [91]. The main tool to evaluate the sheet metal formability is the forming limit diagram (FLD) developed by Keeler and Backofen (1960s).

The FLDs are widely referenced in sheet metal forming field and becomes a standard characteristic in the optimization and controlling of sheet metal forming process. Figure 1.8 shows a typical representation of the FLD. A so-called forming limit curve (FLC) combines the major strain and the minor strain for different strain paths (from uniaxial tension through plane strain to biaxial tension). Strain combinations below the curve are considered to be safe while those above are considered to be failed. The  $FLC_0$  corresponds to the limit point under plane strain condition for which the minor strain equals to 0.

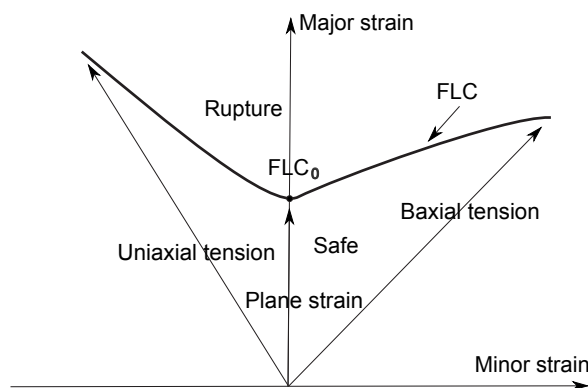


Figure 1.8: Representation of a typical FLD

## 1.2 Experimental characterization

In this part, a review of experimental methods able to determine the flow stress and formability of sheet metal under wide range of temperatures and strain rates is introduced. The different methods are compared and discussed.

### 1.2.1 Flow stress determination

The material flow stress can be obtained by many methods, the general methods include tensile test, bulge test, shear test or compression test.

#### 1.2.1.1 Uniaxial tensile test

Uniaxial tensile test is the most widely used method to determine the flow stress of the sheet metal. The uniaxial tensile test is carried out by applying a longitudinal load at a specific extension rate to a standard tensile specimen until failure. A typical uniaxial tensile stress under different deformation stages is introduced in Figure 1.9. From the stress-strain curve, several values such as the yield strength, Young's modulus and ultimate tensile strength can be obtained.

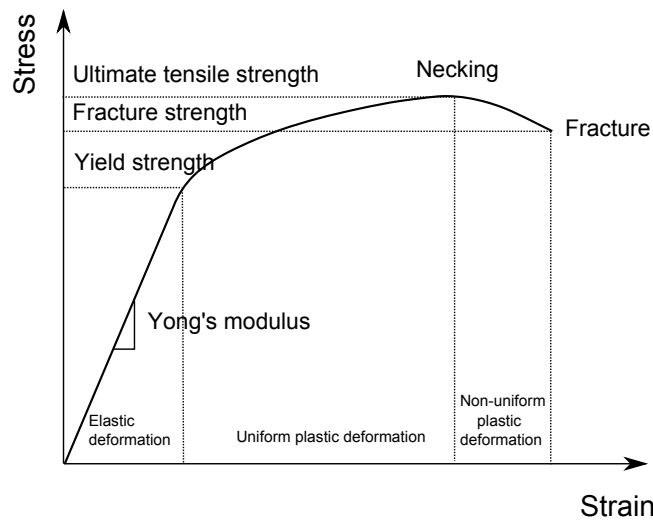


Figure 1.9: Typical uniaxial tensile stress-strain curve

A typical uniaxial tensile test specimen of sheet metals is shown in Figure 1.10. With the results of tensile test, the following values can be calculated:

The engineering stress ( $s$ ):

$$s = F/A_0 \quad (1.6)$$

The engineering strain ( $e$ ):

$$e = \Delta l/l_0 \quad (1.7)$$

The true stress ( $\bar{\sigma}$ ):

$$\bar{\sigma} = F/A \quad (1.8)$$

The true strain ( $\bar{\epsilon}$ ):

$$\bar{\epsilon} = \ln(l/l_0) \quad (1.9)$$

Where  $l_0$  is the initial gauge length,  $w_0$  and  $t_0$  are the initial width and thickness,  $l$  is the current gauge length,  $w$  and  $t$  are the current width and thickness,  $A_0 = w_0 \times t_0$  is the initial cross-section area and  $A = w \times t$  is the current cross-section area. With the uniaxial tensile test with constant area specimen, the flow stress can be determined directly from the equations above. For the uniaxial tensile test with a variable area specimen, high strain rates can be reached.

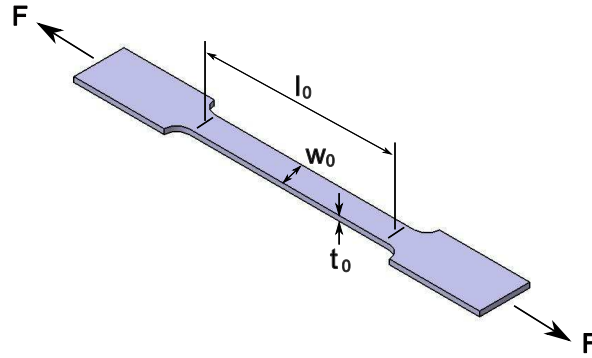


Figure 1.10: A typical uniaxial tensile specimen

Due to the necking phenomenon, the maximum homogeneous strain level obtained by uniaxial tensile test is limited (generally  $< 20\%$ ). Li and Ghosh [57] used the uniaxial tensile test to study the flow stress behaviors of three aluminium alloys, AA5182, AA5754 and AA6111-T4 at different temperatures (20, 200 and 350 °C) and strain rates (0.015, 0.15 and  $1.5 \text{ s}^{-1}$ ). The mechanical behavior of AA5182-O was investigated at temperatures ranging from -120 to 150°C and strain rate from  $10^{-6}$  to  $10^{-1} \text{ s}^{-1}$  by uniaxial tension tests with ASTM tension specimens [83]. Many results have been presented for aluminium alloy characterization in temperature and at different strain rates, the uniaxial tensile test is well adopted for these conditions.

### 1.2.1.2 Biaxial tension test with cruciform specimen

The biaxial tensile test becomes attractive for testing the mechanical behaviors of the sheet metals. Under balanced biaxial stretching mode, more important strain levels can be reached. But, for biaxial tension test, the main difficulty lies in the design of the test cruciform specimen which restricts its application. During the cruciform specimen tension test, many inhomogeneous deformations exist in the central zone. Although specimens of the cruciform type have been investigated quite extensively, there is still no standard geometry [33][46][108].

Moreover, to obtain the localization in the central zone, the section of the central zone is generally not constant, so it is very difficult to obtain directly the stress-strain curves. With two extensometers set on the gage area of the cruciform specimen to measure the strains in rolling and transverse directions, the flow stress of AA5754-O was determined in [101] with a cruciform specimen (Figure 1.11). The obtained maximum strain value was about 10% under different loading ratios. And up to now, little work at different temperatures and strain rates is carried out with cruciform specimen.

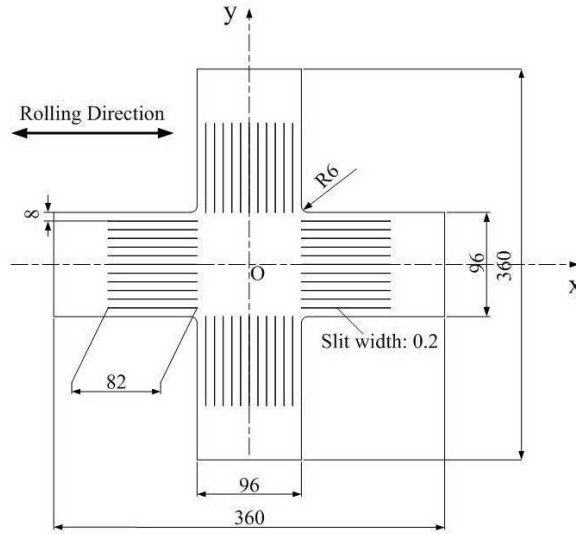


Figure 1.11: Cruciform specimen to determine the flow stress [101]

### 1.2.1.3 Bulge test

Bulge test can determine the material behavior for high strain levels in a biaxial stress mode. Figure 1.12 shows the schematic geometry of a bulge test. The flow stress can be calculated with Eq 1.10.

$$\begin{cases} R_d = \frac{(d_c/2 + R_c)^2 + h_d^2 - 2R_c h_d}{2h_d} \\ t_d = t_0 \left( \frac{1}{1 + (2h_d/d_c)^2} \right)^2 \\ \bar{\sigma} = \frac{pR_d}{2t_d} \\ \bar{\varepsilon} = \ln \left( \frac{t_d}{t_0} \right) \end{cases} \quad (1.10)$$

Where  $p$  is the hydraulic pressure,  $R_c$  is the radius of the fillet of the cavity,  $R_d$  is the radius at the apex of the dome,  $d_c$  is the diameter of the cavity,  $t_d$  is the current sheet thickness at the apex of the dome,  $t_0$  is the initial sheet thickness,  $h_d$  is the dome height.

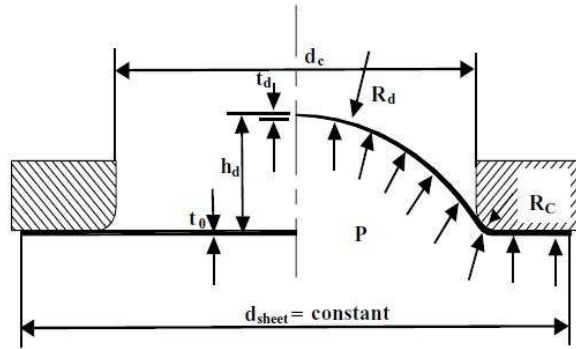


Figure 1.12: Geometry of the bulge test [36]

In bulge test, to calculate the flow stress, some major assumptions are adopted (such as continuous hemispherical bulge shape, thinnest point at apex) which lead to uncertainties in the final result, the influence of these parameters was studied in [21]. With bulge test and

uniaxial tensile test, Gtuscher et al. [36] studied the flow stresses of aluminum killed deep drawing quality (AKDQ) steel and aluminium AA6111. The flow stresses obtained by the two methods are shown in Figure 1.13. The results show that localized necking occurs in a tensile test at the effective strain of about 20% while in bulge test, localized necking occurs at effective strain between 50% (AA6111) and 80% (AKDQ steel). Using hot oil and heaters in the die, Mahabunphachiai and Koç [66] designed a warm hydraulic bulge test setup and studied the flow stresses of AA5052 and AA6061 for a wide range of temperature (room temperature to 400°C) from both tensile and bulge tests. Great difference between the determined flow stresses for the two methods is observed.

For the flow stress determination with bulge test, the advantages are the determined high strain levels and the existed formulations to calculate the flow stress. While the disadvantages lie in the inaccuracy of the low curvature at the beginning of deformation and the related assumptions presented previous.

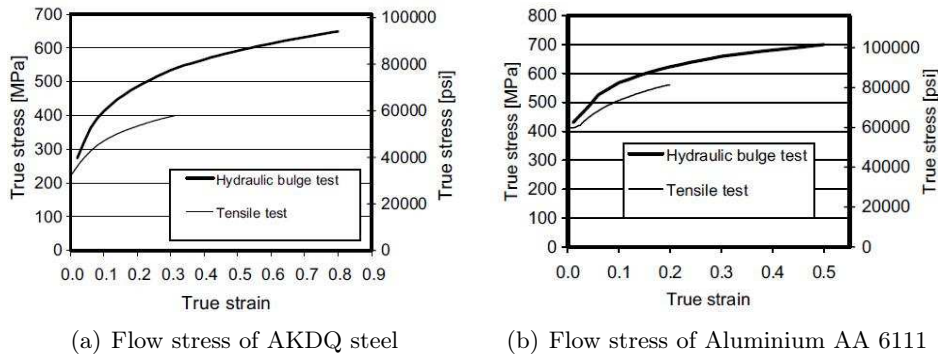


Figure 1.13: Comparison of flow stresses obtained with bulge test and uniaxial tensile test

#### 1.2.1.4 Shear test

Shear test is usually used to obtain shear modulus, elastic limit and shear strength of the material. It can also be used to determine the material flow stress. With a "double shear specimen" (Figure 1.14), the flow stresses of a steel sheet with a typical thickness of 1 mm for a strain rate range between  $10^{-4}$  to  $10^2 \text{ s}^{-1}$  are determined in [85].

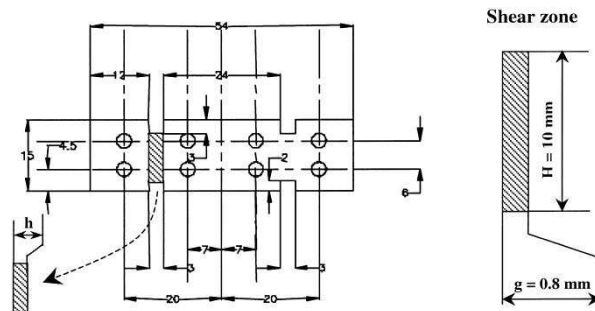


Figure 1.14: Specimen geometry for double shear test

A device for planar simple shear test was designed and performed on a superplastic Al-Mg alloy sheet in [10] as shown in Figure 1.15. Tests were performed under a constant crosshead speed in the range of 0.286 to 2.86 (mm/min) corresponding to the strain rate range of  $10^{-4}$

to  $10^{-2}s^{-1}$  and at a temperature of  $550\text{ }^{\circ}\text{C}$  (specimen surrounded by a clamshell furnace). The result showed that the flow stress for a planar simple shear test was lower than the one for the uniaxial tension test.

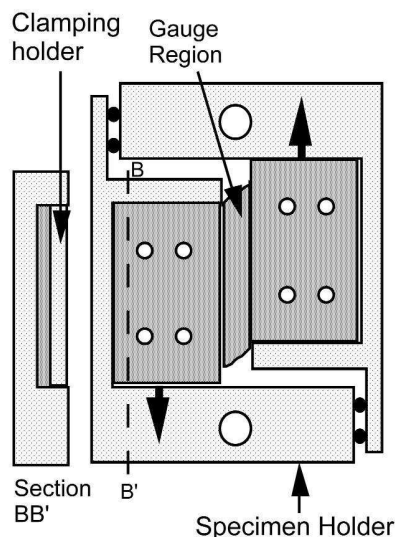


Figure 1.15: Specimen and device for shear test [10]

### 1.2.1.5 Plane strain compression test

The compression test is an alternative solution to obtain stress data at high strain level without interference of necking. A schematic view of a plane strain compression test is shown in Figure 1.16. In the test, for narrow dies, the stress in the longitudinal direction (3) of the strip can be neglected. The specimen dimensions must satisfy the conditions in Eq 1.11.

$$\begin{cases} 2 < \frac{b}{t} < 4 \\ \frac{w}{t} \geq 6 \end{cases} \quad (1.11)$$

With lubricants on the die surface and on the specimen, the test can be carried out. The stress and strain components can be obtained with Eq 1.12 and the respective equivalent strain and stress can be calculated.

$$\begin{cases} \sigma_{11} = \frac{P}{b \cdot w} & \varepsilon_{11} = \ln \frac{t}{t_0} \\ \sigma_{22} = \frac{1}{2}\sigma_{11} & \varepsilon_{22} = 0 \\ \sigma_{33} = 0 & \varepsilon_{33} = -\varepsilon_{11} \end{cases} \quad (1.12)$$

Plane strain compression tests at different testing conditions of elevated temperatures ( $400 - 500^{\circ}\text{C}$ ) and strain rate range of  $0.05 - 1\text{ }s^{-1}$  with the true strain of 1 were studied in [84]. The sample geometry (tool width/sample thickness ratio -  $w/h$ ) influences on the flow stresses of AA6061 were investigated.

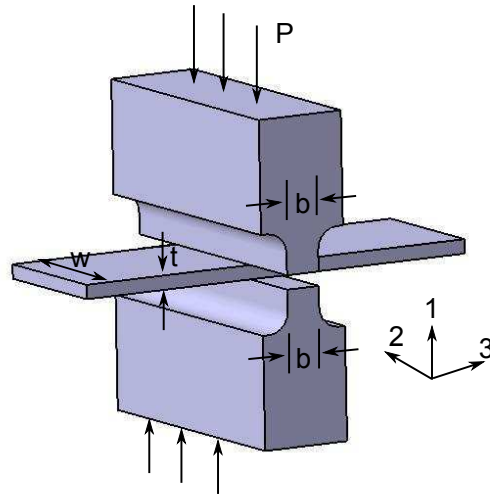


Figure 1.16: Schematic view of the plane strain compression test

## 1.2.2 Yield surface determination

### 1.2.2.1 Experimental methods

For rolled sheet metal, three orthogonal axes can be defined, the rolling direction (RD), the transverse direction (TD) and the normal direction (ND). The rolled sheet usually exhibits an orthotropic symmetry. Hence, four characteristic stress states are selected as reference points to describe a complete yield locus (equi-biaxial point, plane strain point, uniaxial point and pure shear point).

Different mechanical tests are used to obtain the four initial yield points on the yield surface. Uniaxial test is used for determining the uniaxial point. Cruciform and hydraulic bulge tests are proposed to determine the biaxial stress state yield point. Moreover, in cruciform test, with different stress ratios, we can scan the balanced biaxial tension state, plane strain state to the uniaxial tensile state.

For many yield functions, the fitting parameters can be determined through uniaxial tensile tests with the specimens oriented at an angle  $\theta$  from the rolling direction as shown in Figure 1.17.

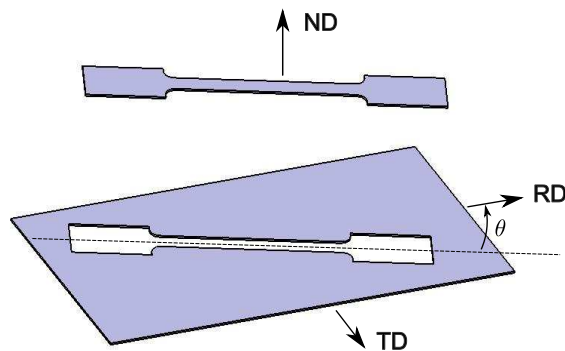


Figure 1.17: Tensile specimen at an angle  $\theta$  from rolling direction

The anisotropy in sheet metals can be quantified through the Lankford strain ratio  $r$ . The  $r_\theta$  value is defined as the ratio of width ( $\varepsilon_{22}$ ) to thickness ( $\varepsilon_{33}$ ) strain in a uniaxial tensile test

with specimen orientation  $\theta$ .

$$r_{\theta} = \frac{\varepsilon_{22}}{\varepsilon_{33}} \quad (1.13)$$

The coefficient of normal anisotropy is determined by:

$$R = \frac{r_0 + 2r_{45} + r_{90}}{4} \quad (1.14)$$

The coefficient of planar anisotropy is determined by:

$$\Delta R = \frac{r_0 + r_{90} - 2r_{45}}{2} \quad (1.15)$$

To calculate the plane strain and pure shear point on the yield surface, a special test specimen is presented in [99] as shown in Figure 1.18. Only the small white area in the middle is the deformed zone. Vertical translation of the upper clamp in an ordinary tensile testing machine gives a plane strain deformation. Horizontal translation of the upper clamp gives a simple shear deformation, in which case an additional bearing must suppress the rotation of the specimen.

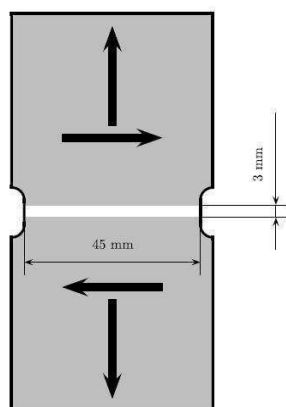


Figure 1.18: Plane strain and simple shear specimen (gray part is clamped)

The effects of strain rate and temperature on the yield locus of magnesium alloy (AZ31) sheet were experimentally investigated by performing biaxial tensile tests, using cruciform specimens, at different temperatures (100, 150, 200, 250 and 300°C) and strain rates ( $10^{-2}$ ,  $10^{-3}$  and  $10^{-4} s^{-1}$ ) in [73]. The results show that the size of yield locus drastically decreases with increasing temperature and decreases with decreasing strain rate. The cruciform specimen used in the test is shown in Figure 1.19.

### 1.2.2.2 Yield point definition

To determine the initial yield point, different methods exist. The prevalent method is the use of stress-strain curve. The point that transits from elastic to plastic is chosen as the yield point. When the transition is not sharp, an offset yield point is defined using a specified small plastic strain (0.2%) based on the stress-strain curve as presented in Figure 1.20. This method is usually applied for high strength steel and aluminum alloys.

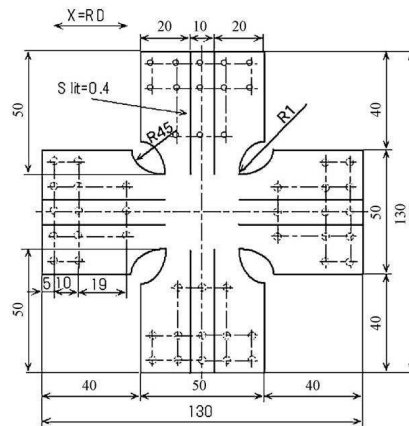


Figure 1.19: Cruciform specimen for biaxial tension test (in mm) [73]

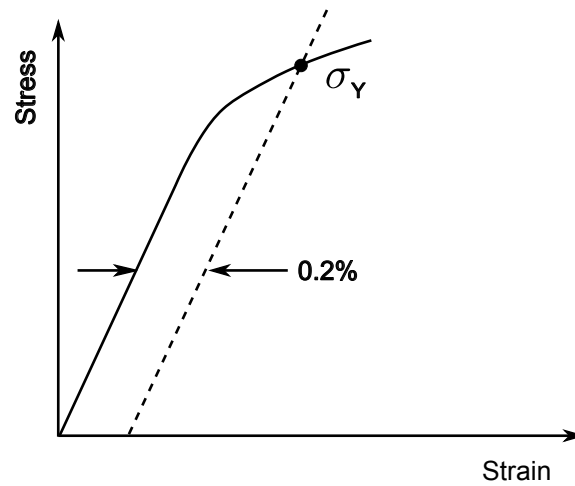


Figure 1.20: Method to determine the yield point using the stress-strain curve

For biaxial stress condition, the yield point can be determined thanks to the concept of equi-plastic work [73]. From experimental uniaxial stress-strain curve, the plastic work dissipated up to the defined yield point can be obtained. The yield point under biaxial stretching can be defined as a point when the plastic work reaches  $W_{0.2\%}$ .

Another method to determine the yield point is using the temperature measurement with an infrared thermocouple [67]. As Figure 1.21 demonstrates, for an elastic tensile deformation, the increase of volume causes a decrease of temperature. The beginning of plastic deformation is identified by a sharp increase of temperature due to the dissipation of plastic work.

### 1.2.3 Sheet metal formability

#### 1.2.3.1 Experimental methods to determine FLDs

For experimental determination of FLDs, the main procedure is to form a number of sheet specimens with varying widths. The specimens are deformed up to fracture and different strain path can be obtained with related strain measurement tools. There are mainly two methods, called the out-of-plane stretching (e.g. Nakazima test) and the in-plane stretching

(e.g. Marciniak test) tests (Figure 1.22). Besides these two basic tests, other methods are also applied.

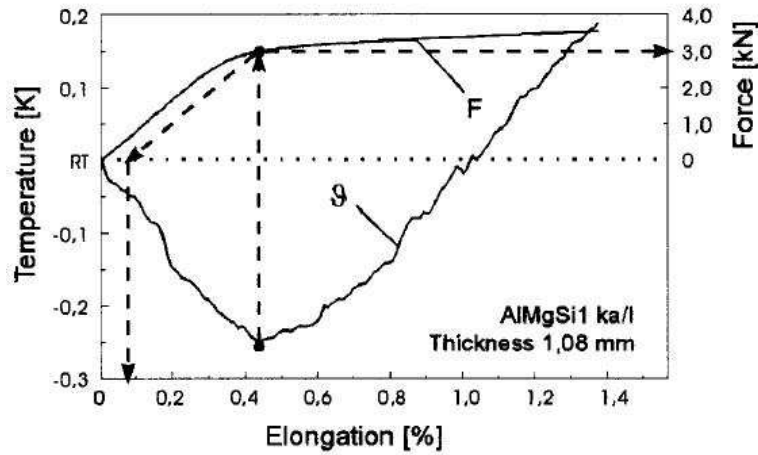


Figure 1.21: Temperature vs. elongation for standard tensile test piece [67]

**1.2.3.1.1 Nakazima and Marciniak tests** In standard ISO 12004-2 [1], Nakazima and Marciniak tests are proposed to determine the Forming Limit Curves (FLCs) of sheet metal materials. The basic idea is to deform a sheet until fracture by applying a load with a punch while the surrounding sheet metal is clamped by a blank holder. Varying the specimen width, different strain paths can be obtained. The critical strain values (prior to failure) are determined and plotted as the FLCs.

The major difference between the two tests is the use of different punch shape as shown in Figure 1.22, a hemispherical punch for Nakazima test and a cylindrical flat punch for Marciniak test. A carrier blank is used in Marciniak test instead of lubrication layers of PE or PTFE in Nakazima test.

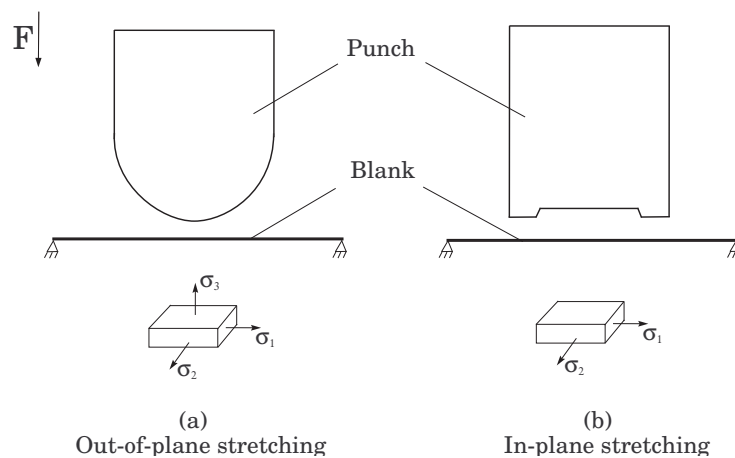


Figure 1.22: Out-of-plan and in-plan stretching

Many works on the formability were carried out with Nakazima and Marciniak tests. The Nakazima punch-stretch test was used in [52] to study the formability of CQ and DP590 at high speeds (forming velocity of 2.3 - 10 m/s, corresponding to the final strain rates of about

65 - 110  $s^{-1}$ ) and room temperature. A Nakazima test is used by Liu [64] to study the FLCs of AZ31-O at different temperatures (100, 200 and 300°C) and different punch velocities (0.1, 0.5 and 5 mm/s). The Nakazima apparatus is shown in Figure 1.23. In their work, the sheet metal was first heated in a furnace and then transferred into the Nakazima test apparatus.



Figure 1.23: Warm Nakazima forming test [64]

The Marciniak test was used by Naka [72] to study the formability of 5083-O sheet at different temperatures (20 - 300°C) and forming speeds (0.2, 20 and 200 mm/min). A Marciniak test was adopted in [79] to determine the FLCs of AZ31 at temperature of 200°C and strain rates of 0.002 and 0.02  $s^{-1}$ .

**1.2.3.1.2 Uniaxial tensile test** Because of its easiness, the uniaxial tensile test can also be used to determine the forming limit strains in the negative minor strain zone. Specimens of different geometries with and without notches are used to obtain different strain paths, as shown in Figure 1.24. With this test, only a partial FLC is plotted.

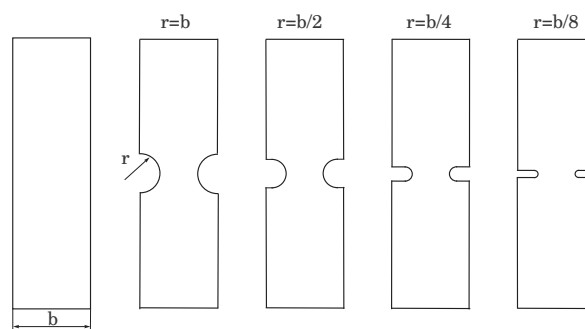


Figure 1.24: Specimens for tensile test

**1.2.3.1.3 Hydraulic bulge test** Hydraulic bulge test can be applied to determine FLDs by means of circular or elliptical dies with different shapes. The most important advantage of this test is the absence of contact, no friction exists in the area of interest. However, this method can be only used to determine the positive minor strain side of FLDs.

**1.2.3.1.4 Biaxial tension test** In biaxial tension test, with different loading displacements, the forming limit points corresponding to different strain paths on the FLCs can be determined. A related work to determine the FLC using biaxial tension test was carried out by Zidane [109] for aluminium AA5086. The cruciform specimen is shown in Figure 1.25 and the determined FLC is shown in Figure 1.26.

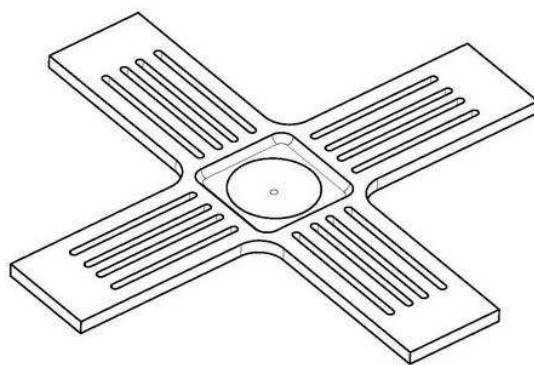


Figure 1.25: Cruciform specimen for AA5086 [109]

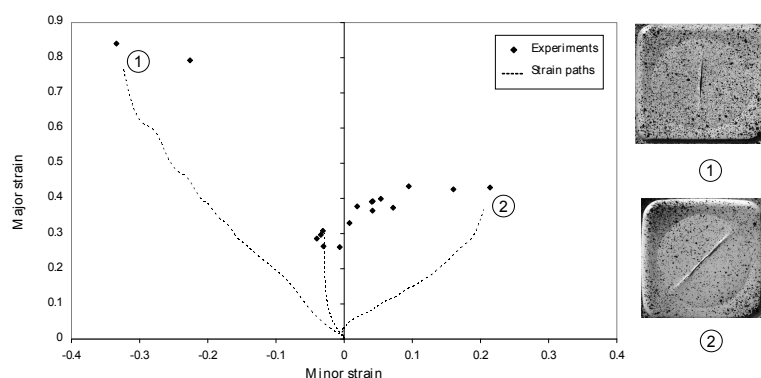


Figure 1.26: Determined FLCs with cruciform specimen for AA5086 [109]

### 1.2.3.2 Failure criteria

In industrial stamping, as mentioned by Aretz [8], the maximum allowable strains are given by localized necking. Many criteria to detect the onset of necking have been already presented in the literature and even if a standard is established, the discussion is still open. The main criteria are given hereafter and they will be discussed in detail in the experimental part of this work.

The equivalent strain increment ratio criterion was first proposed by Marciniak and Kuczynski [68] and is widely used in the M-K theory. Necking is considered to happen when the strain ratio between a reference zone and the necking zone reaches a critical value. Barata Da Rocha et al. [27] proposed a value of 10 for this critical ratio while Banabic et al. [14] suggested a value of 7.

The criterion given by the standard ISO 12004-2 is a spatial one. With the strain distributions of a necked, but not cracked specimen, the major and minor strain values on both

sides of the necked area are used to fit a best inverse polynomial function of second order. The maximum of this function corresponds to the major and minor limit strains.

Recently, a so-called time continuous evaluation method was also proposed by [70] based on a trend analysis of strain rate in the area of necking and subsequent cracking. In the work of Zhang [107], several failure criteria used in the FE simulation are introduced and compared.

### 1.2.3.3 Temperature and strain rate effects on experimental sheet metal formability

In this part, the related research work about temperature and strain rate influence on the FLCs for aluminium alloys is presented.

The effects of forming speed and temperature on the FLCs for AA5083-O sheet were studied by [72] experimentally with a Marciniak test at various forming speeds (0.2 - 200 mm/min) and temperatures (20 to 300°C). It was found that the FLCs were not sensitive to speed at ambient temperature but it increased drastically with decreasing speed at temperature ranging from 150°C to 300°C. The increase of forming temperature elevates the levels of the FLCs.

The formabilities of three aluminium alloys AA5754, AA5182 and AA6111 were studied in [58] by forming a rectangular designed part under temperatures (200 - 350°C) and punch speed of 10 mm/s (strain rate  $1s^{-1}$ ). The FLCs were constructed for all the three aluminium alloys. It was found that the formability increases with increasing forming temperatures. But the formability temperature sensitivity was different for different materials. For AA5754, it exhibited high temperature sensitivity from 250 to 350°C. For AA5182, a high formability increase was observed from 250 to 300°C while low temperature sensitivity was found from 300 to 350°C. For AA6111, it always exhibited a low temperature sensitivity under the tested temperature range.

Palumbo and Tricarico [80] investigated the warm deep drawing process of AA5754-O aluminium alloy using a home designed experimental equipment. With heated blank holder and cooled punch process, they found that the temperature in the blank center had a strong influence on the process feasibility and the material formability.

Test of cup forming of AA2024 were carried out in [102] with flat and hemispherical head punch at different temperatures and punch velocities (170 and 486 mm/s). Results confirmed that the formability of AA2024 could be improved considerably by forming in the vicinity but not in excess of 450°C. The punch velocity also had a strong influence on the formability, it affected the temperature and strain rate distribution. The forming trials suggested an optimum punch velocity existed that would distribute plastic deformation most uniformly over the workpiece, allowing to delay necking for a greater formability.

With the reviews above, the strain rate was shown to have a negative influence on the formability for aluminium alloys, and the formability is generally increased with the increasing temperature, up to 300°C for 5XXX aluminium alloys. Nevertheless a conflict phenomenon were observed in [66] for AA5052, through hydraulic bulge tests, the authors found that AA5052 exhibited poor formability at 200°C.

### 1.3 Rheological modeling of sheet metal

The material constitutive model implementation in these numerical codes, including the hardening law and the yield function, plays an important role. A review of hardening laws and yield functions is introduced below.

In the literature, two kinds of advanced hardening laws called "phenomenological" or "physical" laws incorporating the effects of strain, strain rate and temperature on the material flow stress are usually defined. They are introduced in detail hereafter.

#### 1.3.1 Phenomenological models

The phenomenological models provide a definition of the material flow stresses based on experimental observations. In general, these models present simple expressions, reduced number of material constants and their implementation into Finite Element codes is easy. But due to their empirical characters, their applications can be limited to a range of strain rates and temperatures.

In phenomenological models, the strain, strain rate and temperature effects, are described [28] by a multiplicative formulation:

$$\bar{\sigma}(\bar{\varepsilon}, \dot{\bar{\varepsilon}}, T) = \bar{\sigma}(\bar{\varepsilon}) \cdot v(\dot{\bar{\varepsilon}}) \cdot h(T) \quad (1.16)$$

or an additional one:

$$\bar{\sigma} = \bar{\sigma}(\bar{\varepsilon}, T) + v(\dot{\bar{\varepsilon}}) \quad or \quad \bar{\sigma} = [\bar{\sigma}(\bar{\varepsilon}) + v(\dot{\bar{\varepsilon}})] \cdot h(T) \quad (1.17)$$

Where  $\bar{\sigma}(\bar{\varepsilon})$ ,  $v(\dot{\bar{\varepsilon}})$ ,  $h(T)$  are the strain, strain rate and temperature functions, respectively. For strain rate function, the additional formula is usually applied to high strain rate condition [86] which is not widely adopted for sheet metal forming. The multiplicative formulation is generally used in sheet metal forming process. In the following parts, several prevalent models existing in literature are introduced.

##### 1.3.1.1 Strain hardening functions

The strengthening of a metal during plastic deformation is due to the dislocation movement within the material crystal structure. The general equations used for representing the strain hardening behavior are introduced:

- Hollomon (1945)

$$\bar{\sigma} = K \bar{\varepsilon}^n \quad (1.18)$$

- Swift (1952)

$$\bar{\sigma} = K (\bar{\varepsilon}_p + \varepsilon_0)^n \quad (1.19)$$

- Voce (1948)

$$\bar{\sigma} = B - (B - A) \exp(-n \bar{\varepsilon}_p) \quad (1.20)$$

- Ludwick (1909)

$$\bar{\sigma} = \sigma_0 + K\bar{\varepsilon}_p^n \quad (1.21)$$

- Hartley and Srinivasan (1983)

$$\bar{\sigma} = \sigma_0 + K(\bar{\varepsilon}_p + \varepsilon_0)^n \quad (1.22)$$

- Ludwigson (1971)

$$\bar{\sigma} = K_1\bar{\varepsilon}_p^{n_1} + \exp(K_2 + n_2\bar{\varepsilon}_p) \quad (1.23)$$

Where  $\varepsilon_0$  is the strain at the yield stress ( $\bar{\varepsilon}_p = 0$ ). Some other strain hardening equations have been introduced in [34]. The strain hardening functions introduced above all exhibit a monotonic strain hardening character with the increase of plastic strain except the Voce law whose strain hardening decreases and flow stress arrives at a saturation state with the strain increase.

### 1.3.1.2 Temperature functions

Temperature softening effect can lead to a significant decrease of flow stress, especially in adiabatic forming condition. Several temperature functions have been proposed to describe the temperature effects in [95]:

- Linear model (Hutchison, 1963)

$$h(T) = (1 - \beta(T - T_0)) \quad (1.24)$$

- Power law model 1 (Zuzin et al., 1964; Misaka and Yoshimoto, 1969)

$$h(T) = \left(\frac{T}{T_0}\right)^\beta \quad (1.25)$$

- Power law model 2 (Lubahn and Schnectady, 1947)

$$h(T) = (\alpha)^{\frac{T}{T_0}} \quad (1.26)$$

- Wada et al. model (1978)

$$h(T) = \exp\left(\frac{\beta}{T}\right) \quad (1.27)$$

- Chen et al. model (2008)

$$h(T) = \exp\left[C\left(\frac{T - T_0}{T_m - T_0}\right)^m\right] \quad (1.28)$$

- Johnson-cook model (1983)

$$h(T) = \left[1 - \left(\frac{T - T_0}{T_m - T_0}\right)^m\right] \quad (1.29)$$

- Khan model (2004)

$$h(T) = \left( \frac{T_m - T}{T_m - T_0} \right)^m \quad (1.30)$$

Where  $T_m$  is the melting temperature and  $T_0$  is the reference temperature.

For small temperature range (up to 100°C), no significant difference in the accuracy of Eq 1.24 1.25 1.29 is found in [95]. Generally, Eq 1.29 1.30 1.28 are usually adopted at high temperatures. Compared to Khan model and Exponential model 2, Johnson-cook model cannot be applied to the temperature which is lower than  $T_0$ .

### 1.3.1.3 Strain rate sensitivity functions

To describe the strain rate effect on the flow stress, several functions are proposed.

- Power law model (Norton-Hoff)

$$v(\dot{\epsilon}) = \dot{\epsilon}^m \quad (1.31)$$

- Johnson-Cook model

$$v(\dot{\epsilon}) = \left[ 1 + C \ln \left( \frac{\dot{\epsilon}}{\dot{\epsilon}_0} \right) \right] \quad (1.32)$$

- Cowper-Symond model

$$v(\dot{\epsilon}) = \left[ 1 + \frac{\dot{\epsilon}}{D} \right]^{1/m} \quad (1.33)$$

- Wagoner model

$$v(\dot{\epsilon}) = \left( \frac{\dot{\epsilon}}{\dot{\epsilon}_0} \right)^{m_0 \sqrt{\dot{\epsilon} \dot{\epsilon}_0}^{m_1}} \quad (1.34)$$

- Gavrus et al. [31]

$$v(\dot{\epsilon}) = \arcsin h \left[ \frac{e}{2} \left( \frac{\dot{\epsilon}}{\dot{\epsilon}_0} \right)^m \right] \quad (1.35)$$

Where  $\dot{\epsilon}_0$  is the reference strain rate. The above strain rate functions have different application domains. Johnson-Cook model is frequently used at high strain rates. Cowper-Symonds model is often used at high or intermediate strain rate. The Arcsinh law is proved to be more appropriate at intermediate strain rates than the others, it can reduce to Norton-Hoff model under low strain rate and Johnson-Cook equation under high strain rates as pointed by [31]. Wagoner model is suitable for the material whose strain rate sensitivity index is also strain rate dependent.

After introducing the strain, temperature and strain rate functions above in a unique constitutive equation, the following formulations given hereafter have been proposed in the literature:

### 1.3.1.4 Johnson-Cook (JC) model

Johnson-Cook model is very well known [45], it is described with an effective form taking into strain hardening, strain rate hardening and thermal softening effects.

$$\bar{\sigma} = (A + B\bar{\varepsilon}_p^n) \left[ 1 + C \ln \left( \frac{\dot{\bar{\varepsilon}}}{\dot{\bar{\varepsilon}}_0} \right) \right] \left[ 1 - \left( \frac{T - T_0}{T_m - T_0} \right)^m \right] \quad (1.36)$$

$A$  is the yield stress at reference temperature and reference strain-rate.  $B$ ,  $n$ ,  $C$  and  $m$  are material parameters. For JC model, there is no coupling between strain rate and temperature during plastic deformation. Due to its simplicity and relative few material constants, many modifications of JC model have been proposed [92][62]. This model is generally used for impact or fracture analyze, but rarely applied in sheet metal forming.

### 1.3.1.5 Khan-Huang (KH), Khan-Huang-Liang (KHL) model

With Direct Disc Impact technique to perform the dynamic experiments, Khan and Huang [50] studied the mechanical behavior of 1100 aluminum in the strain rate range from  $10^{-5}$  to  $10^4 s^{-1}$ . After analyzing the experimental results, they proposed a new constitutive model, the KH model, without taking into account temperature effects. The KH model is capable of predicting the strong work-hardening behavior in a large range of strain rate.

- KH model

$$\begin{cases} \bar{\sigma} = g_1(\bar{\varepsilon}_p) g_2(\dot{\bar{\varepsilon}}_p) \\ g_1(\bar{\varepsilon}_p) = \sigma_0 + E_\infty \bar{\varepsilon}_p - a e^{-\alpha \bar{\varepsilon}_p} \\ g_2(\dot{\bar{\varepsilon}}_p) = \frac{1}{\left[ 1 - \frac{\ln(\dot{\bar{\varepsilon}}_p)}{\ln(D_0)} \right]} \end{cases} \quad (1.37)$$

Where  $\sigma_0$ ,  $E_\infty$ ,  $a$ ,  $\alpha$  are material constants,  $D_0$  is fixed to  $10^6$  by the authors.

To incorporate temperature effects, Khan and Liang [51] proposed a viscoplastic model (KHL) for isotropic hardening materials. In the model, strain and strain rate have some coupling effects on the description of work hardening relation.

- KHL model

$$\bar{\sigma} = \left( A + B \left( 1 - \frac{\ln \dot{\bar{\varepsilon}}}{\ln D_0} \right)^{n_1} \bar{\varepsilon}_p^{n_0} \right) e^{c \ln \dot{\bar{\varepsilon}}} \left[ 1 - \left( \frac{T - T_0}{T_m - T_0} \right)^m \right] \quad (1.38)$$

Where  $A$ ,  $B$ ,  $n_1$ ,  $n_0$ ,  $c$ , and  $m$  are material constants. A major feature of this model, unlike the JC model, is that decreasing work hardening with increasing strain rate can be accommodated through the material constants.

- Modified KHL model

The true stress-strain response of AA5082-O was studied by [49] using both tension and compression methods over a wide range of strain-rates ( $10^{-4} s^{-1}$  to  $10^0 s^{-1}$ ) and temperatures (23 - 200°C). A modified KHL constitutive relationship was proposed by the authors. Compared to experimental curves, this model gave a satisfied correlation results for the material mechanical responses under the tested forming conditions.

$$\bar{\sigma} = \left( A \left( \frac{T_m - T}{T_m - T_r} \right)^{m_1} + B \left( 1 - \frac{\ln \dot{\bar{\varepsilon}}}{\ln D_0} \right)^{n_1} \bar{\varepsilon}_p^{n_0} \left( \frac{T_m - T}{T_m - T_r} \right)^{m_2} \right) \left( \frac{\dot{\bar{\varepsilon}}}{\dot{\bar{\varepsilon}}_0} \right)^C \quad (1.39)$$

Where  $B$ ,  $n_1$ ,  $n_0$ ,  $C$ ,  $m_1$ , and  $m_2$  are material constants.  $\dot{\varepsilon}_0 = 1s^{-1}$ .  $A$  is the yield stress of the material at a strain-rate of  $1s^{-1}$  and at room temperature.

### 1.3.1.6 Hollomon - Voce model (H-V)

Sung et al. [95] proposed a new empirical work hardening equation called H-V model.

$$\bar{\sigma} = \bar{\sigma}(\bar{\varepsilon}_p, \dot{\bar{\varepsilon}}, T) = f(\bar{\varepsilon}_p, T) v(\dot{\bar{\varepsilon}}) h(T)$$

$$\begin{cases} f(\bar{\varepsilon}_p, T) = \alpha(T) f_H + (1 - \alpha(T)) f_V \\ \alpha(T) = \alpha_1 - \alpha_2(T - T_0) \\ f_H = K \bar{\varepsilon}_p^n \\ f_V = V(1 - Ae^{-B\bar{\varepsilon}_p}) \end{cases} \quad (1.40)$$

Where  $\alpha_1$ ,  $\alpha_2$ ,  $K$ ,  $n$ ,  $V$ ,  $A$ ,  $B$  are material constants. The functions  $g$  and  $h$  can be chosen from the literature according to different process conditions. The model incorporates a linear combination coefficient  $\alpha(T)$  varying with temperature, which allows the representation of Hollomon behavior for  $\alpha(T) = 1$  and Voce (saturation) behavior for  $\alpha(T) = 0$  or any intermediate case ( $0 < \alpha(T) < 1$ ).

By choosing  $v(\dot{\bar{\varepsilon}}) = \left(\frac{\dot{\bar{\varepsilon}}}{\dot{\varepsilon}_0}\right)^{\gamma_2 + (\gamma_1/2) \log(\dot{\bar{\varepsilon}}/\dot{\varepsilon}_0)}$  and  $h(T) = (1 - \beta(T - T_0))$ , the authors used the proposed model to fit the flow stress behaviors of DP590, DP780 and DP980 steels from a serie of tensile tests at strain rates of  $10^{-3}$  and  $1s^{-1}$  and temperatures of 25, 50 and  $100^\circ\text{C}$ . Good correlation results are obtained.

### 1.3.1.7 Modified power law model

Abedrabbo et al. [2] proposed a modified power law to study the flow stress of AA3003-H111 in a thermo-forming analysis at different temperatures (25 -  $260^\circ\text{C}$ ) and strain rates (0.001, 0.01, 0.05 and  $0.08 s^{-1}$ ). The equation writes:

$$\bar{\sigma}(\bar{\varepsilon}_p, \dot{\bar{\varepsilon}}, T) = K(T) (\bar{\varepsilon}_p + \varepsilon_0)^{n(T)} \left(\frac{\dot{\bar{\varepsilon}}}{\dot{\varepsilon}_0}\right)^{m(T)} \quad (1.41)$$

Where  $K(T)$ ,  $n(T)$ ,  $m(T)$  are fitted according to experimental results as a function of temperature.  $K(T)$  and  $n(T)$  are expressed in a linear expression and  $m(T)$  is expressed in an exponential expression.

The comparison between experimental and simulation results of hemispherical punch test has shown that the developed fully coupled thermo-mechanical model gives an accurate punch load curves at different temperatures (25 -  $204^\circ\text{C}$ ) [3].

### 1.3.1.8 Arrhenius equation

The Arrhenius equation is widely used to describe the flow stress at high temperature. The effects of the temperature and strain rate on the deformation behavior can be represented by Zener-Hollomon parameter ( $Z$ ) in an exponent-type equation. The hyperbolic law in Arrhenius type equation gives better approximations between Zener-Hollomon parameter and stress.

$$\begin{cases} Z = \dot{\varepsilon} \exp\left(\frac{Q}{RT}\right) \\ \dot{\varepsilon} = AF(\bar{\sigma}) \exp\left(-\frac{Q}{RT}\right) \\ F(\bar{\sigma}) = \begin{cases} \bar{\sigma}^n & \alpha\sigma < 0.8 \\ \exp(\beta\bar{\sigma}) & \alpha\sigma > 1.2 \\ [\sinh(\alpha\bar{\sigma})]^n & \text{for all } \bar{\sigma} \end{cases} \end{cases} \quad (1.42)$$

Based on the equations above, Lin et al. [63] used Eq 1.43 to study the deformation behaviors of 2124-T851 aluminium at different temperatures (380 - 470°C) and strain rates (0.01, 0.1, 1 and 10  $s^{-1}$ ) with experimental data obtained from compression test, good correlation results were obtained.

$$\begin{cases} \bar{\sigma} = \frac{1}{\alpha} \ln \left\{ \left(\frac{Z}{A}\right)^{1/n} + \left[\left(\frac{Z}{A}\right)^{2/n} + 1\right]^{1/2} \right\} \\ Z = \dot{\varepsilon} \exp\left(\frac{Q}{RT}\right) \end{cases} \quad (1.43)$$

Where  $R$  is the universal gas constant (8.31  $J \text{ mol}^{-1} K^{-1}$ ).  $Q$  is the activation energy of hot deformation ( $\text{kJ mol}^{-1}$ ).  $A$ ,  $\beta$ ,  $\alpha$ , and  $n$  are material constants.

A similar constitutive model with a hyperbolic sine function was proposed by [26] to study the strain rate and temperature effects on the flow stress of a 30CrMnSiA steel. Good results were obtained between predicted and experimental data under temperatures of 20, 300, 500, 700°C and strain rates of 0.001 and 1  $s^{-1}$ .

### 1.3.2 Physical based models

Different from phenomenological model, the physical based models are derived from the analysis of microstructure evolution and have many physical parameters to be identified from physical experiments. For example, Orwan's equation (Orwan, 1948) was proposed to relate the equivalent plastic strain rate to the density of the mobile dislocation. The details introduction of the related theory can be found in [100].

To deform a metal beyond the elastic limit means to activate and move its dislocation through the crystal. During material plastic deformation, through the lattice, there are two kinds of obstacles that prevent dislocation movement: long-range and short-range barriers. The long-range obstacles are due to the structure of the material and cannot be overcome by introducing thermal energy through the crystal. Therefore they contribute to the flow stress with a component that is non-thermally activated (athermal stress). Meanwhile, the short-range barriers can be overcome by thermal energy [24]. Based on this theory, the flow stress of a material can be additionally decomposed into equivalent athermal stress ( $\bar{\sigma}_a$ ) and equivalent thermal stress ( $\bar{\sigma}_{th}$ ):

$$\bar{\sigma} = \bar{\sigma}_a + \bar{\sigma}_{th} \quad (1.44)$$

This assumption has been proven experimentally and was used by several authors [104][76][89]. For BCC metals, the thermal stress component  $\bar{\sigma}_{th}(\dot{\varepsilon}, T) |_{BCC}$  is independent on plastic strain and the yield stress is strongly temperature and strain rate dependent. While for FCC metals, it depends on the plastic strain  $\bar{\sigma}_{th}(\bar{\varepsilon}, \dot{\varepsilon}, T) |_{FCC}$ , but the yield stress has reduced dependence

on the plastic strain [87].

Based on the above theories, several physical models have been proposed. Due to the many numbers of parameters, their application are limited to some extent. In this part, several current physical models are briefly introduced.

### 1.3.2.1 Bodner and Partom (BP) model

Bodner and Partom [23] presented an internal variable theory constitutive equation to represent elasto-viscoplastic strain hardening behaviors for large deformations and arbitrary loading histories. It is based on the assumption that the total deformation rate consists in elastic and inelastic components. A detail introduction can be found in [60][78].

$$\begin{cases} \dot{\varepsilon}_{ij} = \dot{\varepsilon}_{ij}^e + \dot{\varepsilon}_{ij}^p \\ \dot{\varepsilon}_{ij}^e = \frac{\dot{\sigma}_{ij}}{E} \\ \dot{\varepsilon}_{ij}^p = D_0 \exp \left\{ -\frac{1}{2} \left[ \frac{Z}{\sigma_{ef}} \right]^{2n} \right\} \frac{\sqrt{3}s_{ij}}{\sigma_{ef}} \end{cases} \quad (1.45)$$

Where  $\dot{\varepsilon}_{ij}^e$  and  $\dot{\varepsilon}_{ij}^p$  are the elastic and plastic strain rate components, E represents the Young's modulus,  $D_0$  is the assumed maximum plastic strain rate, Z is a loading history dependent internal or state variable whose evolution is a function of plastic work,  $\sigma_{ef}$  is the effective stress and  $s_{ij}$  is the deviatoric stress.

The BP model was used by Huang and Khan [40] to describe the mechanical behavior of 1100-0 aluminum at large plastic strain within the strain rate range of  $10^{-5}$  to  $10^4 s^{-1}$ . It is pointed out that the work hardening behavior of the BP model is not able to describe the hardening response of this material in the beginning portion of the stress-strain curve.

### 1.3.2.2 Zerilli-Armstrong model (ZA)

Based on the dislocation characteristics and the related thermal activation theory for BCC and FCC metals, Zerilli and Armstrong [104] developed a constitutive model taking into account the strain rate and temperature dependence in a coupling manner.

BCC metals:

$$\bar{\sigma} = \bar{\sigma}_a + B \exp(-\beta T) + A \bar{\varepsilon}_p^n \quad (1.46)$$

$$\beta = \beta_0 - \beta_1 \ln \dot{\varepsilon}$$

FCC metals:

$$\bar{\sigma} = \bar{\sigma}_a + A \bar{\varepsilon}_p^n \exp(-\alpha T) \quad (1.47)$$

$$\alpha = \alpha_0 - \alpha_1 \ln \dot{\varepsilon}$$

Where  $\bar{\sigma}_a$  is the athermal component of stress containing grain size effect.  $A$ ,  $B$ ,  $\beta_0$ ,  $\alpha_0$ ,  $\beta_1$ ,  $\alpha_1$  and  $n$  are material constants. For Z-A BCC model, the work hardening rate is independent of temperature and strain rate. While it is temperature and strain rate dependent for FCC model:

$$\frac{d\bar{\sigma}}{d\bar{\varepsilon}} = An\bar{\varepsilon}^{n-1} (BCC) \quad (1.48)$$

$$\frac{d\bar{\sigma}}{d\bar{\varepsilon}} = An e^{-(\alpha_0 - \alpha_1 \ln \dot{\bar{\varepsilon}})T} \bar{\varepsilon}^{n-1} (FCC) \quad (1.49)$$

### 1.3.2.3 Voyiadjis-Abed model (VA)

Based on Kocks's equation [55] to relate the activation energy to the thermal flow stress, Voyiadjis and Abed [100] proposed physical constitutive equations for BCC and FCC metals.

BCC metals:

$$\bar{\sigma} = \hat{Y} \left( 1 - (\beta_1 T - \beta_2 T \ln \dot{\bar{\varepsilon}})^{1/q} \right)^{1/p} + B\bar{\varepsilon}_p^n + Y_a \quad (1.50)$$

FCC metals:

$$\bar{\sigma} = B\bar{\varepsilon}_p^n \left( 1 - (\beta_1 T - \beta_2 T \ln \dot{\bar{\varepsilon}})^{1/q} \right)^{1/p} + Y_a \quad (1.51)$$

Where  $Y_a$  is the temperature-independent yield stress.  $\hat{Y}$ ,  $p$ ,  $q$ ,  $B$ ,  $n$ ,  $\beta_1$  and  $\beta_2$  are material constants.  $p$  and  $q$  are the constants defining the shape of short-range barrier.  $p$  is fixed to 0.5 and  $q$  is fixed to 1.5 by the authors.  $\beta_1$  and  $\beta_2$  are related to the microstructure physical components.

For VA BCC model, the value of  $\hat{Y}$  is sensitive to the choice of  $p$ . The parameter  $\beta_1$  contains the effects of dislocation density and dislocation distance which represents crucial aspect in controlling the scale effect of the internal deformation behavior. It plays an important role in determining temperature and strain rate behaviors during plastic deformation. The V-A FCC model was used to describe the flow stress of Oxygen Free High Conductivity (OFHC) Copper [100]. Compared to experimental results at different temperatures (20, 200 and 457°C) and strain rates (449, 451 and 464  $s^{-1}$ ), a good prediction by the V-A model was found.

### 1.3.2.4 Rusinek-Klepaczko model

Based on the double shear test data with different strain rates ( $10^{-4}$  to  $10^3 s^{-1}$ ) and some extend on physical considerations, Rusinek and Klepaczko [85] proposed a new semi-phenomenological R-K constitutive model with strain rate sensitivity and temperature effects. Recently, Rusinek et al. [87] presented a modified R-K model for FCC metals with application to OFHC copper as shown:

$$\left\{ \begin{array}{l}
\bar{\sigma} = \frac{E(T)}{E_0} [\bar{\sigma}_a + \bar{\sigma}_{th}] + \bar{\sigma}_{vs} \\
\frac{E(T)}{E_0} = 1 - \frac{T}{T_m} \exp(\theta^* (1 - \frac{T}{T_m})) \\
\bar{\sigma}_a = Y \\
\bar{\sigma}_{th} = \sigma_0^* \langle 1 - \xi_1 \left( \frac{T}{T_m} \right) \log \frac{\dot{\epsilon}_{max}}{\dot{\epsilon}_p} \rangle^{\xi_2} \\
\sigma_0^* = B(\dot{\epsilon}_p, T) \cdot (\dot{\epsilon}_p)^{n(\dot{\epsilon}_p, T)} \\
\left\{ \begin{array}{l}
B(\dot{\epsilon}, T) = B_0 \left[ \left( \frac{T}{T_m} \right) \log \left( \frac{\dot{\epsilon}_{max}}{\dot{\epsilon}_p} \right) \right]^{-\nu} \\
n(\dot{\epsilon}, T) = n_0 \langle 1 - D_2 \left( \frac{T}{T_m} \right) \log \frac{\dot{\epsilon}_p}{\dot{\epsilon}_{min}} \rangle \\
\bar{\sigma}_{vs}(\dot{\epsilon}) = \chi \cdot [1 - \exp(-\alpha \cdot \dot{\epsilon})]
\end{array} \right.
\end{array} \right. \quad (1.52)$$

Where the McCauley operator  $\langle \bullet \rangle = \bullet$  if  $\langle \bullet \rangle \geq 0$  or  $\langle \bullet \rangle = 0$  if  $\langle \bullet \rangle \leq 0$ .  $Y$  is the flow stress of undeformed material,  $E_0$  is the Young modulus at  $T = 0K$ ,  $E(T)$  is the evolution of the modulus as a function of temperature, based on some extent on physical considerations [53].  $\theta^*$  value depends on the material micro-structure. For FCC metals  $\theta^* = 0.9$  and for BCC metals  $\theta^* = 0.6$  in [86].  $B(\dot{\epsilon}_p, T)$  is based on experimental observation [65] and  $n(\dot{\epsilon}, T)$  is inspired from the mobile dislocation density evolution at high strain rates [54].  $n_0$  and  $B_0$  are material constants at  $T = 0K$ .  $\dot{\epsilon}_{max}$  ( $10^7$ ) and  $\dot{\epsilon}_{min}$  ( $10^{-5}$ ) are the maximum and minimum strain rates.  $D_2$ ,  $\nu$ ,  $\xi_1$  and  $\xi_2$  are material constants

$\bar{\sigma}_{vs}$  defines the viscous drag stress component for high strain rate [47], it is active when the strain rate exceeded  $1000s^{-1}$ .  $\chi$  is a material constant and  $\alpha$  represents an effective damping coefficient affecting the dislocation motion. These two parameters can be obtained directly from experiments [35].

The RK model has lots of extensions. A comparison between RK analytical predictions and experimental results of the ES steel flow stresses was studied in [88], a good agreement was obtained for the strain rate range of  $10^{-3}$  to  $130s^{-1}$ . Another extended R-K model was used by [86] to describe the negative strain rate behavior of AA 5083-H116 with experimental data from uniaxial tension tests (including a Split-Hopkinson bar test) at different strain rates (0.00041, 0.51, 3.95, 122 and  $1313s^{-1}$ ) and room temperature. The analytical predictions and the experimental results agreed well with each other under a limited strain level (maximum 20%).

Comparing analytical predictions and experimental results in compression at different strain rates (0.001, 0.1, 4000 and  $8000s^{-1}$ ) and at different temperatures (20, 227, 327, 427, 527 and  $627^\circ C$ ) with constant strain rate ( $4000 s^{-1}$ ) for high strain levels (80%), Rusinek et al. [87] suggested that the RK FCC model was a good alternative to other physically based models for modeling behaviors of FCC metals.

For RK model, a strong coupling of  $\dot{\epsilon}_p - T$  inducing a thermal softening of the material is expressed by the strain hardening exponent  $n(\dot{\epsilon}, T)$ . Complex model expression and many numbers of parameters (9 parameters in RK FCC model) limits its application.

### 1.3.2.5 Bergström model

The original Bergström model was introduced in [19][20]. Based on the decomposition of the flow stress into a dynamic stress (depending on the strain rate and temperature), a term

for describing work hardening (through the evolution of the micro-structure) and a strain and strain rate independent stress, a modified Bergström material model for describing the flow stress of aluminium sheet (AA 5754-O) under different temperatures (100, 175, 250°C) and strain rates (0.002, 0.02  $s^{-1}$ ) is presented in [97]. The predictions well coincided with experimental data obtained from monotonic tensile tests. The iterative formulation of this model and the high numbers of physical parameters limited its application.

An extended Bergström model was presented in [98] to study the prediction of strain distribution of stretch forming parts in LC-steel and AA5182. The results are in better agreement with the measured ones. The extended Bergström model writes as:

$$\bar{\sigma} = \sigma_0 + \Delta\sigma_m \left[ \beta (\bar{\varepsilon}_p + \varepsilon_0) + \left( 1 - e^{-\Omega(\bar{\varepsilon}_p + \varepsilon_0)} \right)^{n'} \right] + \sigma_0^* \left( 1 + \frac{kT}{\Delta G_0} \ln \frac{\dot{\varepsilon}}{\dot{\varepsilon}_r} \right)^{m'} \quad (1.53)$$

Where  $\sigma_0^*$  is the limit dynamic flow stress (dynamic stress at zero thermal activation),  $k$  is the Boltzmann constant ( $8.617 \times 10^{-5}$  eV/K),  $\dot{\varepsilon}_r$  is the limit strain rate for thermally activated movement (fixed to  $10^8$ ),  $\Delta G_0$  is the maximum activation enthalpy.  $\Delta\sigma_m$ ,  $\beta$ ,  $\Omega$ ,  $n'$  and  $m'$  are material constants.

The extended model was also used in [42] to plot the FLD for DC06 and DP600 with M-K modeling and FE Nakazima test simulation, good results were obtained for DC06 with the M-K prediction, FE simulation and experimental results. The modified Bergström model was also adopted by [80] to study the formability of AA5754-O by means of the material Limit Drawing Ratio. Good correlation between the numerical and experimental punch load was obtained.

### 1.3.3 The yield criteria

The application of the advanced yield functions is limited by the high number of anisotropic parameters. The identification of these parameters requires many tests and various experimental setups. Several typical yield functions are introduced hereafter.

#### 1.3.3.1 Hill 1948

The quadratic Hill'48 yield function was the first proposed criterion able to describe the anisotropic behavior of materials. The parameters of this model are usually determined with uniaxial tensile tests at 0°, 45° and 90° with respect to the rolling direction. The criterion is expressed by a quadratic function:

$$2\bar{\sigma}^2 = H (\sigma_{xx} - \sigma_{yy})^2 + F (\sigma_{yy} - \sigma_{zz})^2 + G (\sigma_{zz} - \sigma_{xx})^2 + 2N\sigma_{xy}^2 + 2L\sigma_{yz}^2 + 2M\sigma_{zx}^2 \quad (1.54)$$

In the plane stress condition, the criterion is written as:

$$2\bar{\sigma}^2 = \sigma_{xx}^2 (H + G) + \sigma_{yy}^2 (H + F) - 2H\sigma_{xx}\sigma_{yy} + 2N\sigma_{xy}^2 \quad (1.55)$$

Four parameters must be identified in this criterion:  $H$ ,  $F$ ,  $G$  and  $N$ .

With the rotation matrice, the Lankford coefficient  $r_\theta$  can be calculated:

$$r(\theta) = \frac{\varepsilon_{22}}{\varepsilon_{33}} = \frac{H + (2N - F - G - 4H)(\sin \theta)^2(\cos \theta)^2}{F(\sin \theta)^2 + G(\cos \theta)^2} \quad (1.56)$$

With three uniaxial tensile test data with different angles  $\theta$  (0, 45 and 90°) to the rolling direction, three yield stress values ( $\sigma_0$ ,  $\sigma_{45}$ ,  $\sigma_{90}$ ) and three Lankford coefficients ( $r_0$ ,  $r_{45}$ ,  $r_{90}$ ) can be measured. The following six equations can be written.

$$\begin{cases} r(0) = \frac{H}{G} = r_0 & \frac{\sigma_0}{\sqrt{G+H}} = \sigma_0 \\ r(45) = \frac{N}{F+G} - \frac{1}{2} = r_{45} & \frac{2\sigma_0}{\sqrt{G+F+2N}} = \sigma_{45} \\ r(90) = \frac{H}{F} = r_{90} & \frac{\sigma_0}{\sqrt{F+H}} = \sigma_{90} \end{cases} \quad (1.57)$$

Then, the parameters of the Hill'48 criterion can be determined by the Lankford coefficient:

$$\begin{cases} F = \frac{r_0}{r_{90}(1+r_0)}, & G = \frac{1}{(1+r_0)} \\ H = \frac{r_0}{(1+r_0)}, & N = \frac{(1+2r_{45})(r_0+r_{45})}{2r_{90}(1+r_0)} \end{cases} \quad (1.58)$$

### 1.3.3.2 Hosford 1979

Hosford proposed a yield criterion in 1979, in principal stress space for isotropic material, it writes:

$$|\sigma_{22} - \sigma_{33}|^a + |\sigma_{33} - \sigma_{11}|^a + |\sigma_{11} - \sigma_{22}|^a = 2\sigma_0^a \quad (1.59)$$

For anisotropic material, under plane stress state, it is reduced to:

$$|\sigma_{11}|^a + |\sigma_{22}|^a + R|\sigma_{11} - \sigma_{22}|^a = (R+1)\sigma_0^a$$

Where  $R$  is the normal anisotropy coefficient and  $\sigma_0$  is the yield stress. For Hosford 1979 yield criterion, by fitting the value of the integer exponent  $a$ , it ensures a good approximation of the yield locus compared to experimental data. The author concluded that the best approximation was given by  $a = 6$  for BCC materials and  $a = 8$  for FCC materials.

### 1.3.3.3 Barlat 1989 (Yld89)

Barlat and co-workers proposed a series of yield functions (Yld89, Yld91, Yld94, Yld96 and Yld2000). These yield functions are mainly focused on the description of the plastic deformation of aluminium alloys. The parameters of Yld89 can be determined with uniaxial tensile tests, considering either the yield stress or the  $r$ -value with different angles to the rolling direction. The equi-biaxial yield stress is added in the plane stress version of Yld91. The 'isotropy plasticity equivalent' (IPE) theory proposed by [48] was used in the subsequent models Yld94, Yld96 and Yld2000 [99]. Here, the yield function of Yld89 is introduced, the equivalent stress with a planar anisotropy hypothesis is given by:

$$2\bar{\sigma}^M = a |k_1 + k_2|^M + a |k_1 - k_2|^M + c |2k_2|^M \quad (1.60)$$

Where  $M$  is an integer exponent and the coefficients  $k_1$  and  $k_2$  are given by

$$k_1 = \frac{\sigma_{11} + h\sigma_{22}}{2}; \quad k_2 = \left[ \left( \frac{\sigma_{11} - h\sigma_{22}}{2} \right)^2 + p^2 \sigma_{12}^2 \right]^{1/2} \quad (1.61)$$

$a$ ,  $c$ ,  $h$  and  $p$  are material parameters that can be identified by the following two methods.

The first method needs two uniaxial tensile tests (with the angle  $0^\circ$  and  $90^\circ$ ) and two different types of shear tests:  $\sigma_{12} = \tau_{s1}$  for  $\sigma_{11} = \sigma_{22} = 0$  and  $\sigma_{12} = 0$  for  $\sigma_{22} = -\sigma_{11} = \tau_{s2}$ .

$$\begin{cases} a = 2 - c = \frac{2\left(\frac{\sigma_0}{\tau_{s2}}\right)^M - 2(1+h)^M}{1+h^M - (1+h)^M} \\ h = \frac{\sigma_0}{\sigma_{90}} \\ p = \frac{\sigma_0}{\tau_{s1}} \left( \frac{2}{2a+2^M c} \right)^{1/M} \end{cases}$$

Another identification procedure is based on the Lankford coefficient:

$$\begin{cases} a = 2 - c = 2 - 2\sqrt{\frac{r_0}{1+r_0} \cdot \frac{r_{90}}{1+r_{90}}} \\ h = \sqrt{\frac{r_0}{1+r_0} \cdot \frac{1+r_{90}}{r_{90}}} \end{cases}$$

In this case, the coefficient  $p$  has to be calculated by a numerical procedure (solving a non-linear equation). Some advantages and disadvantages of Yld89 were introduced in [11]. A relative good prediction of the yield locus for aluminium alloys without high anisotropy. As observed, the coefficients of the yield function do not have a direct and intuitive physical significance. The model does not give accurate predictions for the biaxial yield stress and the biaxial coefficient of plastic anisotropy, especially in the case of aluminium alloys exhibiting a pronounced anisotropy. And the model cannot capture simultaneously the planar variation of the uniaxial yield stresses and uniaxial coefficients of plastic anisotropy.

#### 1.3.3.4 Banabic-Balan-Comsa (BBC) Yield criteria

Based on the work of Barlat and Lian (1989), a flexible yield function (BBC 2000) is proposed. It is improved with the version BBC 2002 and BBC 2003. For BBC2002 yield function, the equivalent stress  $\bar{\sigma}$  is defined as:

$$\bar{\sigma} = \left[ a(\Gamma + \Psi)^{2k} + a(\Gamma - \Psi)^{2k} + (1-a)(2\Lambda)^{2k} \right]^{1/2k} \quad (1.62)$$

$k$  is an integer exponent. For BCC materials,  $k = 3$  leads to a satisfactory agreement of the yield locus shape. For FCC materials, the value is 4. The terms  $\Gamma$ ,  $\Psi$ ,  $\Lambda$  are defined as follows for the principal stresses of a plane stress state:

$$\begin{cases} \Gamma = M\sigma_{11} + N\sigma_{22} \\ \Psi = \sqrt{(P\sigma_{11} - Q\sigma_{22})^2 + R^2\sigma_{12}\sigma_{21}} \\ \Lambda = \sqrt{(P\sigma_{11} - S\sigma_{22})^2 + T^2\sigma_{12}\sigma_{21}} \end{cases} \quad (1.63)$$

The use of this model requires the calibration of 8 parameters for a given exponent  $k$ . The flexibility of the function is not always ensured [12] and it may fail in reproducing given experimental data. For this reason, an improved form of the BBC2002 criterion is proposed.

In order to overcome the shortcomings of BBC 2002, the yield function BBC 2003 is

proposed in [12]. In BBC 2003, the terms  $\Gamma$ ,  $\Psi$ ,  $\Lambda$  are defined as follows:

$$\begin{cases} \Gamma = \frac{\sigma_{11} + M\sigma_{22}}{2} \\ \Psi = \sqrt{\frac{(N\sigma_{11} - P\sigma_{22})^2}{4} + Q^2\sigma_{12}\sigma_{21}} \\ \Lambda = \sqrt{\frac{(R\sigma_{11} - S\sigma_{22})^2}{4} + T^2\sigma_{12}\sigma_{21}} \end{cases} \quad (1.64)$$

With BBC2003 model, Banabic and Siegert [16] calculated the yield locus for AA5182-O alloy sheet, good results were obtained compared to experimental data. With Swift hardening law and BBC2003, the theoretical FLC was determined and a good agreement between experimental data was observed. The BBC yield functions (2000, 2003) were applied to AA3003-O aluminium alloy [6]. Good predictions of yield stresses and r-values were observed by BBC2003. The criterion was also applied to predict the FLC with M-K theory and Swift and Voce hardening laws. The results showed that BBC yield criteria could be used for the forming limits predictions for this material.

### 1.3.3.5 Conclusion

For the choice of the yield functions, besides the flexibility, efficiency and accuracy, the identified parameter number should also be taken into consideration. The mechanical parameters needed for the identification of the yield functions are compared in [11] as shown in Table 1.1.

Table 1.1: The mechanical parameters needed for different yield functions

Author, year	$\sigma_0$	$\sigma_{45}$	$\sigma_{90}$	$\sigma_b$	$r_0$	$r_{45}$	$r_{90}$	$r_b$
Hill'48	×				×	×	×	
Horsford79	×				×		×	
Yld89	×				×		×	
BBC2000	×	×	×	×	×	×	×	
BBC2003	×	×	×	×	×	×	×	×

Even if Hill 48 is not well adopted for many materials, especially for aluminium alloys, it is still widely applied due to its simplicity, direct significance of the coefficients and easy of use in commercial finite element codes.

## 1.4 Predictive models of FLCs

Experimental determination of FLCs is a very time consuming procedure which requires specific equipments. Several analytical and numerical predictive models have been proposed to determine the FLCs.

### 1.4.1 Analytical models

The typical analytical models, including Considère's theory, Swift's criterion, Hill's criterion, Ramaekers' criterion, bifurcation theory, perturbation method, modified maximum force criterion (MMFC) and the M-K model, have been summarized in [105]. Hereafter, the Hill's criterion, the MMFC and the M-K theory are introduced briefly.

#### 1.4.1.1 Hill's criterion

Hill [37] developed a general criterion for localized necking in thin sheets under plane stress condition. The theory predicts that localized necking develops along the zero extension direction, known as Hill's zero-extension assumption. The localized necking occurs when the maximum load is reached perpendicular to this zero-extension direction (Figure 1.27), i.e.

$$dF_n = 0$$

With the material incompressibility hypothesis, after some mathematical calculations, the instability condition can be written as:

$$\frac{1}{\bar{\sigma}} \frac{d\bar{\sigma}}{d\bar{\varepsilon}} = \frac{\partial \bar{\sigma}}{\partial \sigma_{11}} + \frac{\partial \bar{\sigma}}{\partial \sigma_{22}} \quad (1.65)$$

With the Levy-Mises flow rule, the Hollomon hardening law, and the assumption of proportional loading, the limit strains can be expressed in a more familiar form:

$$\varepsilon_{11}^* = \frac{n}{1 + \beta} \quad (1.66)$$

Where  $\beta = \varepsilon_{22}/\varepsilon_{11}$  is the strain path.  $n$  is the strain hardening component in Hollomon law.

As shown in Figure 1.27, if necking takes place as described by Hill's criterion, based on the von Mises yield function for isotropic materials, the characteristic angle  $\theta$  must satisfy the condition  $\Delta\varepsilon_{tt} = 0$ :

$$\Delta\varepsilon_{tt} = \Delta\varepsilon_{11} \sin^2 \theta + \Delta\varepsilon_{22} \cos^2 \theta$$

$$\theta = \arctan \sqrt{-\beta} \quad (1.67)$$

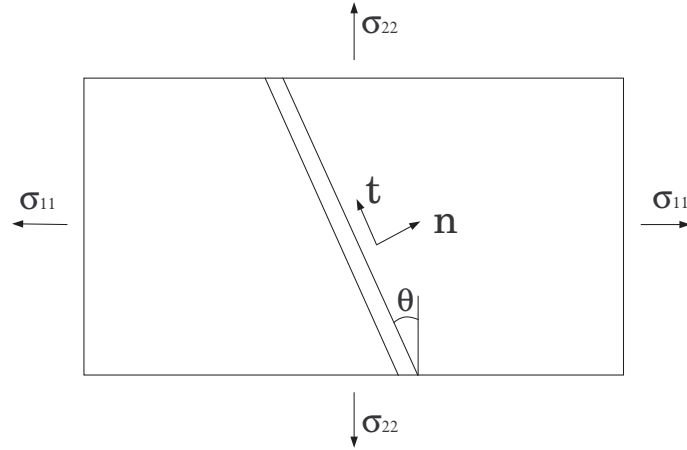


Figure 1.27: Schematic view of Hill's criterion

#### 1.4.1.2 Modified maximum force criterion (MMFC)

Swift generalized the Considère criterion in order to determine the limit strains in biaxial tension with the assumption that plastic instability occurs at a maximum load for proportional loading. Considère criterion can be extended to plane stress state ( $\sigma_{33} = 0$ ):

$$dF_1 = 0, \quad dF_2 = 0$$

As presented in the literature, Swift diffuse necking criterion is too conservative and it underestimates the forming limit strains significantly. Hora et al. (1996) intended to improve Swift criterion by considering that the onset of necking depends significantly on the strain path  $\beta$  [39]. The 'MMFC' criterion is expressed by:

$$\frac{\partial \sigma_{11}}{\partial \varepsilon_{11}} + \frac{\partial \sigma_{11}}{\partial \beta} \frac{\partial \beta}{\partial \varepsilon_{11}} = \sigma_{11} \quad (1.68)$$

With von Mises yield criterion and proportional loading, Hora's necking criterion can be expressed for the whole strain range:

$$\varepsilon_{11}^* = n + \frac{(2\Omega - 1)^2 (2 - \Omega)}{6(1 - \Omega + \Omega^2)}, \quad \Omega = \frac{\sigma_{22}}{\sigma_{11}} \quad (1.69)$$

#### 1.4.1.3 Marciniak and Kuczynski (M-K) model

The typical M-K model is defined with a pre-existing imperfection in the form of a long groove. The original M-K model introduced by Marciniak and Kuczynski [68] with the groove perpendicular to the principal stress  $\sigma_{11}$ , is shown in Figure 1.28(a). Later, Hutchinson et al. [41] extended M-K model to the negative strain paths based on a groove inclined at an angle  $\Psi_0$  with respect to the principal axis-2 (Figure 1.28(b)).

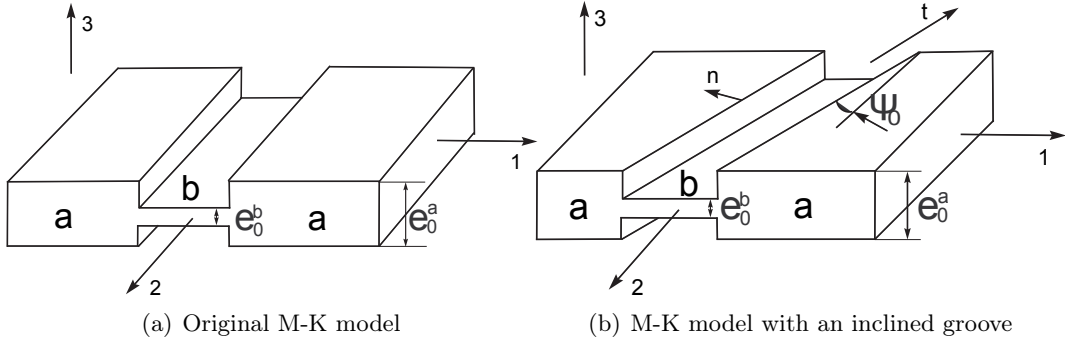


Figure 1.28: Representation of the M-K model

The pre-existing imperfection is characterized by an initial imperfection factor:

$$f_0 = \frac{e_0^b}{e_0^a} \quad (1.70)$$

Where  $e_0^a$ ,  $e_0^b$  are the initial sheet thicknesses in zone  $a$  and zone  $b$  (Figure 1.28).

The force equilibrium equations in the direction- $n$  in both zones are:

$$\sigma_{nn}^a e^a = \sigma_{nn}^b e^b, \quad \sigma_{nt}^a e^a = \sigma_{nt}^b e^b \quad (1.71)$$

Where  $e^a$ ,  $e^b$  are the current sheet thicknesses.

Strain in zone  $b$  and zone  $a$ , parallel to the groove, gives the compatibility condition:

$$\Delta \varepsilon_{tt}^a = \Delta \varepsilon_{tt}^b \quad (1.72)$$

With the consideration of the strain increments, the groove evolution is described by:

$$\tan(\Psi + \Delta\Psi) = \frac{1 + \Delta\varepsilon_{11}^a}{1 + \Delta\varepsilon_{22}^a} \tan\Psi \quad (1.73)$$

The imperfection parameter evolution,  $f$ , is expressed as:

$$f = \frac{e^b}{e^a} = f_0 \exp\left(\varepsilon_{33}^b + \Delta\varepsilon_{33}^b - \varepsilon_{33}^a - \Delta\varepsilon_{33}^a\right) \quad (1.74)$$

Under the assumption of proportional loading in zone  $a$  ( $\rho^a = \Delta\varepsilon_{22}^a / \Delta\varepsilon_{11}^a$ ), with the above compatibility condition, the strain increment in zone  $b$  can be determined. Due to the initial imperfection assumption, the strain evolution in zone  $b$  accelerates. When the strain ratio ( $\Delta\varepsilon^b / \Delta\varepsilon^a$ ) exceeds a certain value, the necking in zone  $b$  is assumed to happen and the corresponding strains ( $\varepsilon_{22}^a$ ,  $\varepsilon_{11}^a$ ) at this moment are retained as the limit strains. By changing the strain ratio ( $\rho^a$ ), the whole FLC can be obtained.

It is well known that in analytical M-K model, the initial imperfection value has a great influence when calculating the FLC as shown in Figure 1.29. The initial groove orientation influence on the FLC has been studied by many researchers. For the right side of the FLCs, the critical strains are obtained with the simplistic model  $\Psi_0 = 0$  [15][75]. For the left side of the FLCs, it is necessary to determine the critical groove angle. Zadpoor et al. [103] proposed three different approaches to calculate the FLDs in the negative minor strain ranges: (1)

direct determination of the critical angle using Hill's zero extension theory. (2) high resolution scanning of the angle space. (3) application of an optimization procedure to determine the critical angle.

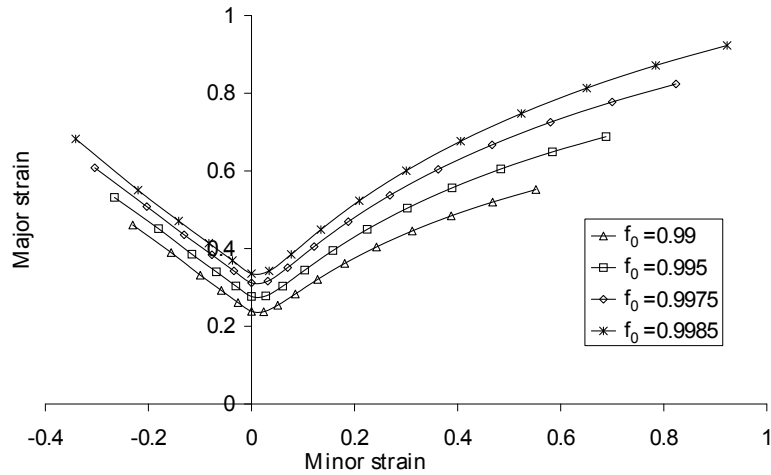


Figure 1.29: Effect of the initial imperfection factor  $f_0$  on the FLCs [105]

The comparison of predicted FLCs determined with different analytical models were carried out by Zhang [105] for a given material. The results are shown in Figure 1.30, it is shown that the FLCs obtained with different analytical models gave very different results, a great dispersion is observed. For  $FLC_0$  and the right hand of the  $FLC$ , the M-K model gives the most conservative prediction while for the left hand of the  $FLC$ , the M-K model predicts the highest formability.

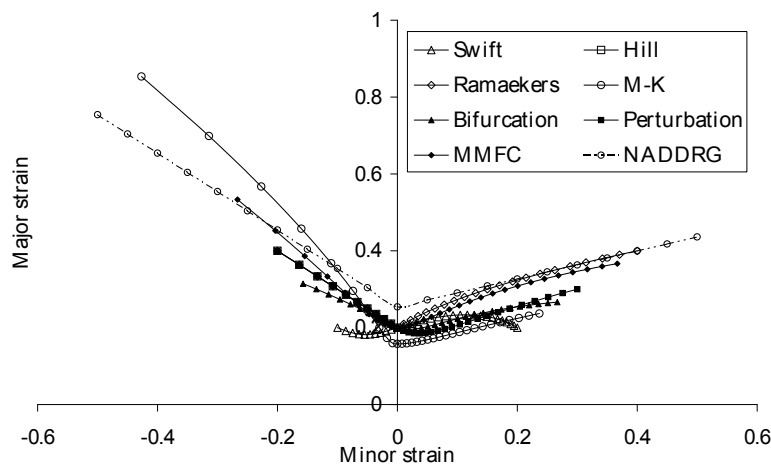


Figure 1.30: Comparison of FLCs with different analytical models [105]

The analytical M-K model has attracted lots of attentions. Based on the M-K analytical model, the influences of Hosford and BBC2000 yield function and groove orientation on the FLCs for AA5xxx alloys were studied in [30]. The results showed that the yield function affected only the right hand side of the FLCs and the critical angle for the left hand side of FLC occurred between  $30^\circ$  and  $50^\circ$  depending on yield function and material type. For the right hand side, the limit strain occurred at the angle of zero degree.

With the M-K model, a comprehensive study on the prediction of FLDs for AA3003-O

was carried out in [6]. Influence of different yield functions (BBC2000, BBC2002, BBC2003) and work hardening laws (Swift and Voce) on the FLC were analyzed. The results show that they both affect the prediction results and a coupling effect exists between the yield function and hardening model on the FLC, especially on the right hand side. The best predictive result was obtained with BBC2003 and Voce law.

### 1.4.2 Theoretical studies of temperature and strain rate sensitivity on FLCs

A general introduction of theoretical studies of the strain rate effects on FLCs is carried out in [105]. A brief review of the theoretical models with strain rate and temperature influence is presented in this part.

- Li and Chandra's perturbation analysis

Analytical closed form solutions based on a linear perturbation analysis were obtained to predict limit strains for rate sensitive materials in [59]. The equilibrium condition writes:

$$\left( \frac{n\dot{\bar{\varepsilon}}}{\omega} + m\bar{\varepsilon} \right) \frac{1}{g} = \bar{\varepsilon} \dot{\bar{\varepsilon}} \frac{1 + \beta}{\omega}$$

Under proportional loading, the limit strains can be obtained:

$$\begin{cases} \varepsilon_{11}^* = \frac{n}{1 + \beta - \xi m} & (\beta < 0) \\ \varepsilon_{11}^* = \frac{n(2 + \beta)^2}{4(1 + \beta + \beta^2)(1 + \beta) - \xi [3\beta^2 + m(2 + \beta)^2]} & (\beta > 0) \end{cases} \quad (1.75)$$

Where  $\xi$  can be determined from experimental data. The comparison between analytical predictions and experimental data for AA 6111 [32] showed that limit strains were enhanced by the increase of the material strain rate sensitivity index ( $m$ ).

- Ben Tahar's MMFC analysis

Ben Tahar [18] integrated the rate sensitivity into the MMFC criterion to study the strain rate effect:

$$\frac{n}{\bar{\varepsilon}} + m \frac{\dot{\bar{\varepsilon}}}{\bar{\varepsilon}} \leq g \left[ 1 + \frac{\frac{\partial f}{\partial \Omega} \frac{1}{f} \frac{\beta}{\Omega}}{\frac{\partial \Omega}{\partial \beta}} \right].$$

Under proportional loading, this criterion writes as:

$$\bar{\varepsilon}^* = \frac{n + \left( m \frac{g'(\beta)}{g} - \frac{\frac{\partial f}{\partial \Omega} \frac{1}{f} \frac{\beta}{\Omega}}{\frac{\partial \Omega}{\partial \beta}} \right) \beta}{g \left( 1 - m \frac{\dot{\bar{\varepsilon}}_1}{\bar{\varepsilon}_1^2} \right)}. \quad (1.76)$$

Through the two independent terms  $mg'(\beta)/g$  and  $m\dot{\bar{\varepsilon}}_1/\bar{\varepsilon}_1^2$  in Eq 1.76, the author has studied the strain rate sensitivity influence on FLCs. The results show that the former term

has a very little influence on FLCs except in biaxial zone, while the latter greatly improves the material formability.

- M-K model

For the analytical M-K model, due to its broad application, lots of work with rate sensitivity were carried out. For example, Nie and Lee [77] studied the rate influence on the FLC for anisotropic sheet metals with an isotropic hardening model. The result showed that increasing strain rate sensitivity raised the overall level of forming limits.

Based on the M-K theory, the empirical analytical expressions with strain rate sensitivity index ( $m$ ) (Eq 1.77) were proposed by Mesrar et al. [71] to predict localized necking. It was found that rate sensitivity shifted the level of FLCs upward, especially for the right hand side.

$$\begin{cases} \varepsilon_{11}^* = \frac{2 + \beta}{2g\sqrt{1 + \beta + \beta^2}} \left\{ n - \sqrt{2(1 - f_0)n} + \left[ m + \frac{5\beta^2}{(2 + \beta)^2} (P^2 - 1) \right] \ln \left( \frac{1}{1 - f_0} \right) \right\} & (\beta < 0) \\ \varepsilon_{11}^* = \frac{\sqrt{1 + 2R/(1 + R)\beta + \beta^2}}{g(1 + \beta)} \left\{ n - \sqrt{2(1 - f_0)n} + m \ln \left( \frac{1}{1 - f_0} \right) \right\} & (\beta > 0), \end{cases} \quad (1.77)$$

A comparison between the perturbation analysis and M-K model was carried out in [105] for a given material. As shown in Figure 1.31, although with the same tendency, very different predictions between the two models were observed.

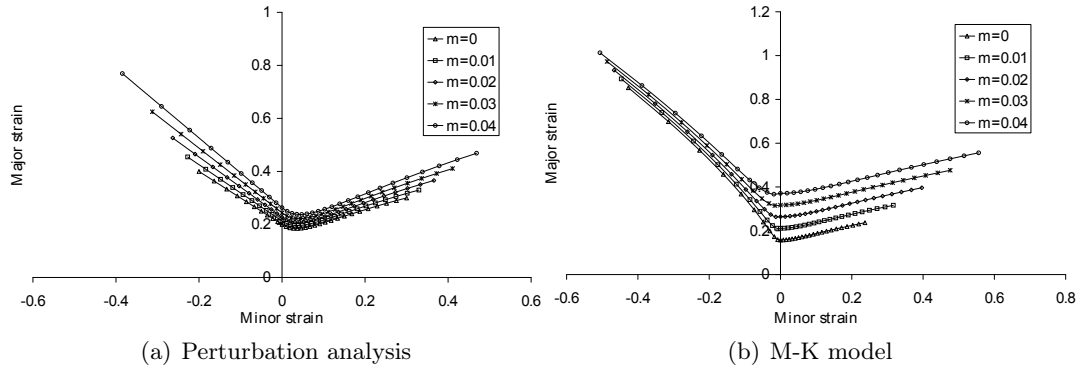


Figure 1.31: Comparison of rate sensitivity effect on FLCs between perturbation analysis and M-K model

The related researches above mostly focus on the strain rate sensitivity index ( $m$ ) influence. Recently, with the M-K model, the strain rate and temperature effects on the FLCs have been analyzed [49]. Modified KHL model and Barlat's yield function (YLD96) were used to predict FLCs at different strain rates ( $10^{-4}$ ,  $10^{-2}$  and  $10^0 s^{-1}$ ) and temperatures (23, 100 and 200°C) for AA5082-O. The results showed that a high strain rate improved the formability at 23°C, however, a low strain rate improved the formability at 200°C. Using Voce hardening model and constant imperfection value  $f_0$  in [4], the FLCs of AA5182-O from 25°C to 260°C are determined with analytical M-K model. The level of predicted FLCs has increased with temperature.

In the literature, for analytical models taking into account both temperature and strain rate effects on the FLCs, very few works can be found. The M-K model can be used to

determine the FLCs under different temperatures and strain rates through the implementation of advanced hardening models. But very few direct experimental comparisons are presented.

### 1.4.3 Numerical models

Analytical methods give rapid prediction of the FLCs, but it is a very difficult task to incorporate the advanced operating conditions like strain rate or temperature. Thanks to the development of numerical modeling methods as well as computational facilities, the finite element method (FEM) has been chosen by some authors to predict the FLCs. The main advantage of using a FE modeling is the possibility to implement different hardening laws and yield functions to describe the mechanical behavior of the sheet metal under different conditions.

#### 1.4.3.1 Finite element M-K model

With a two-dimensional model, a thin sheet is simulated by Narasimhan and Wagoner [74] to construct the right hand side of the FLDs. The deformation was simulated by imposing displacements at the nodes along the boundaries of the model. From this model, lots of factors such as material properties (work hardening index  $n$  and strain rate sensitivity index  $m$ ), failure criterion and defect geometry on the FLCs were analyzed.

Based on M-K theory, Zhang et al. [106] have constructed a 3D FE M-K model (Figure 1.32) with hexahedral elements. The initial imperfection is defined by the different thickness values in the necking and adjacent zones. With the boundaries displacement constraints, Ludwick hardening model and strain ratio increment criterion, the whole predicted FLC was determined for AA5086 at room temperature. Compared to experimental data, good prediction result was obtained.

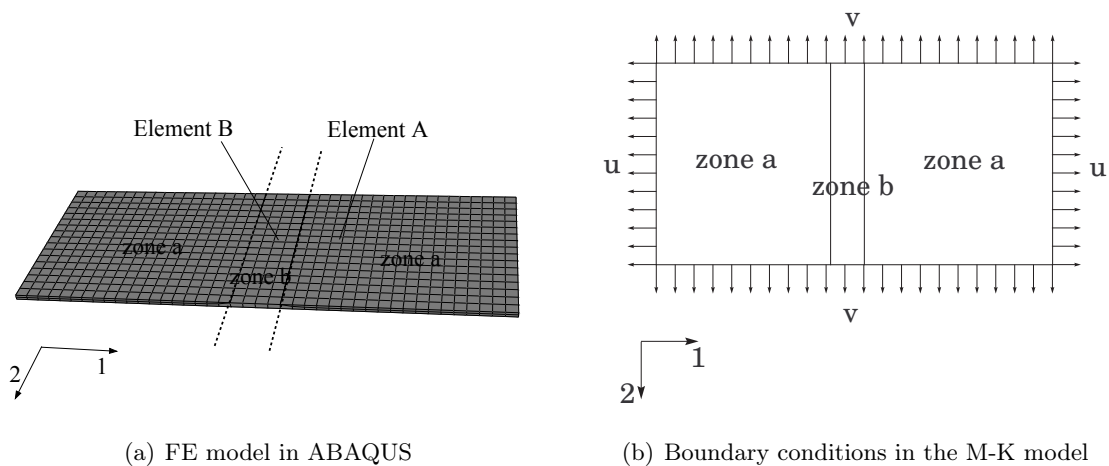


Figure 1.32: FE M-K model and corresponding boundary conditions [106]

#### 1.4.3.2 Simulation of conventional tests

The simulation of conventional tests have been also adopted to determine the FLDs for the sheet metal, such as Marciniak and Nakazima simulation tests.

The FE Marciniak test was selected in [81] to determine the FLD for two types of deep drawing steels, AA-3003 alloy and Ti-alloy with sheet thicknesses ranging from 0.5 mm to 1.23 mm in ABAQUS. Experimental determination of the FLD were also performed and good correlation between the FLDs obtained by both approaches was found. The simulation of Marciniak test was also carried out in [79] to study the relationship between the punch speed and the strain rate in the specimen. The right hand side of the FLC of a Nimonic C-263 alloy was investigated in [7] with a FE Marciniak test constructed with the explicit finite element code LSDYNA 3D. The simulation result coincided with the analytical FLC from a vertex theory using a power law and Hosford yield criterion [44].

The forming limits of AA5754-O sheets were studied in [44] through experimental and numerical investigations of Nakazima test. The simulation result well agreed with the experimental one. A FE model of Nakazima test setup was presented in [22]. The formability of an IF steel is studied using a thickness gradient criterion, a good agreement between the simulation and experimental results was observed.

The numerical determination of the FLCs for DC06 and DP600 with FE Nakazima model was accomplished in [69]. The influence of the punch diameter was evaluated. Compared to experimental results, the FEM data with punch diameter of 100 mm gave good agreement results. But the simulation results with punch diameter of 20 mm deviated from experimental data. The bending effect was pointed out as critical for an appropriate determination of the formability limits through Nakazima FEM simulations.

Besides the standard Marciniak and Nakazima tests, other conventional tests like hydraulic bulge test, Olsen and Erichsen test, limit dome height test and plane strain stretching test were also modeled with the FE method. One great disadvantage of these conventional simulation tests is the calibration of parameters like lubrication, contact conditions, blank-holder force or mesh size which can significantly affect the results.

Recently, a simulation of cruciform biaxial tension test was carried out in [109] to determine the FLCs. There is no friction, blank-holder force and lubrication effects in this model which can be an interesting alternative.

#### 1.4.4 Conclusions

Many FLC predictive models have been proposed, including mainly two different classes, analytical and numerical models. For analytical models, several prevalent models to predict the FLCs have been introduced but great dispersions can be observed. About the strain rate effect on the FLCs, most of these analytical models focus on the influence of strain rate sensitivity index ( $m$ ) and few works concern the study of the forming temperature influence. In the analytical or FE M-K model, the temperature and strain rate effects on the FLCs have been investigated through the implementation of advanced hardening models.

### 1.5 Conclusions

To optimize the sheet metal forming process, a reliable predictive model is essential. And the accuracy of the prediction result depends greatly on a precise characterization of the thermo-viscoplastic behavior of the sheet metal.

The formability of the aluminium alloys can generally be improved at elevated forming temperature. For the industrial production, the strain rate in different zones of a forming part can vary from quasi-static to about  $10s^{-1}$ . The strain rate effect on the formability of aluminium alloys can be neglected at ambient temperature, while this effect should be taken into account at elevated temperatures. In addition, as presented in the literature, the study of coupling effect of temperature and strain rate on the sheet metal formability still lacks, especially for aluminium alloys.

To determine the model parameters, reliable experimental database under different operating conditions is necessary. For the experimental determination of sheet metal flow stresses at different temperatures and strain rates, several methods have been presented and discussed. Due to its simplicity, the uniaxial tensile test is widely used and will be adopted in this work although the deformed strain is limited. For the experimental determination of FLCs, an existed Marciniak test setup developed in our laboratory is used to carry out the formability test at elevated temperatures.

Related researches show that the material constitutive models (hardening law and yield function) play an important role in determining the FLCs for analytical and numerical models. Two types of advanced hardening laws (phenomenological and physical based models) taking into account temperature and strain rate effects have been introduced in detail. Although physical based models are more attractive since they can introduce the microstructure evolutions, their applications are limited due to their high number of parameters and then complex calibration stages. Thanks to their simplicity, the phenomenological models are widely used. Among the proposed hardening models which are used to model the thermo-viscoplastic behavior of sheet metal, three distinct types can be clearly classified: power law, saturation and mixed models. Only a few models for each type are identified and used in Chapter 2 and Chapter 4.

The analytical and numerical models for determining FLCs and the related research works dealing with temperature and strain rate effects on aluminium alloy formability have been reviewed. Among these models, for the FLC predictions under different temperatures and strain rates, the M-K theory (analytical MK model and FE M-K model) seems to own the advantage and will be used in Chapter 4. Several related studies about temperature and strain rate effects on the FLCs have been carried out in the literature but usually without direct comparison with experimental results.



## Chapter 2

# Investigations on the thermo-elasto-viscoplastic hardening behavior of a 5086 aluminium alloy



*Le choix d'un modèle de loi d'érouissage peut considérablement affecter les résultats issus des simulations numériques de procédés de mise en forme des tôles. Ce choix est d'autant plus difficile lorsque l'identification de ces lois est réalisée à partir d'essais de traction uniaxiale classiques et donc sur une plage de déformation équivalente limitée, généralement inférieure à 20%. En effet, ces lois peuvent être utilisées à des niveaux de déformation bien plus élevés, surtout lorsqu'elles sont intégrées à des modèles prédictifs de courbes limites de formage pour lesquels des déformations supérieures à 50% peuvent être atteintes. La prise en compte des effets de la température et de la vitesse de déformation accentue un peu plus l'incertitude liée à l'utilisation de ces lois, compte tenu du grand nombre de modèles rhéologiques proposés dans la littérature.*

*La précédente étude bibliographique a livré un aperçu de ces modèles dont certains sont particulièrement adaptés à la modélisation du comportement thermo-viscoplastique des alliages d'aluminium. Parmi toutes ces lois, huit d'entre elles ont été choisies et classifiées suivant trois familles : lois de type puissance, de type saturante et de type mixte. L'identification de ces lois a été menée à partir d'essais de traction uniaxiale sur éprouvettes à section constante pour des vitesses d'essai de 1, 10 et 100 mm/s et pour des températures de 20, 150 et 200°C.*

*Les résultats expérimentaux montrent que l'alliage d'aluminium étudié est insensible à la vitesse de déformation à température ambiante. Une sensibilité à la vitesse est mise en évidence pour des températures de l'ordre de 200°C. Pour une déformation équivalente comprise entre 15 et 20%, les lois « saturantes » semblent être les plus aptes à modéliser le comportement du matériau pour les différentes conditions opératoires. Finalement, le tracé et la comparaison des différentes lois d'érouissage identifiées montrent une grande divergence de comportements pour des grandes déformations.*



## 2.1 Introduction

In sheet metal forming field, the characterization of flow stress is crucial for the process simulation. The hardening model which describes the sheet metal flow stress affects significantly the accuracy of simulation results (final sheet deformation, predicted punch force, forming limits...). Hardening laws are typically identified from tensile tests until a low level of strains, generally below 20%. With this test, a significant uncertainty remains on the identified law ability to describe the behavior of the material for high strain levels. This is the case when the hardening laws are used in predictive models of formability in which large strain ranges are reached (up to 50%).

In this chapter, uniaxial tensile tests with a constant section specimen are carried out at tensile speeds of 1, 10 and 100 mm/s and forming temperatures of 20, 150 and 200°C to determine the flow stresses of AA5086. Due to the constant section specimen, the stress-strain curves are obtained directly from the experiments and the temperature and strain rate effects on the flow stresses are discussed. Several hardening models introduced in Chapter 1 are chosen to correlate the material flow stresses under the tested temperatures and forming speeds. The parameters are identified and the predicted flow stresses for all the proposed hardening models are compared to experimental results and discussed.

## 2.2 Uniaxial tensile test of AA5086

### 2.2.1 Material

Aluminium-magnesium alloys (5xxx series) are widely used in automotive, aircraft and naval industries due to their high-strength to weight ratio, corrosion resistance, good workability and weldability characteristics. Its chemical components are shown in Table 2.1.

Table 2.1: Chemical components of AA5086 in weight percent (asm.matweb.com)

<i>Component</i>	<i>Wt.%</i>	<i>Component</i>	<i>Wt.%</i>	<i>Component</i>	<i>Wt.%</i>
Al	93 – 96.3	Mg	3.5 – 4.5	Si	<i>Max</i> 0.4
Cr	0.05 – 0.25	Mn	0.2 – 0.7	Ti	<i>Max</i> 0.15
Cu	<i>Max</i> 0.1	Other, each	<i>Max</i> 0.05	Zn	<i>Max</i> 0.25
Fe	<i>Max</i> 0.5	Other, total	<i>Max</i> 0.15		

### 2.2.2 Experimental setup

#### 2.2.2.1 Specimen

The geometry and dimensions of the tensile specimen are illustrated in Figure 2.1. The specimen has a strain gauge length ( $L_0$ ) of 80 mm, a thickness ( $t_0$ ) of 2 mm and a section width ( $W_0$ ) of 10 mm.

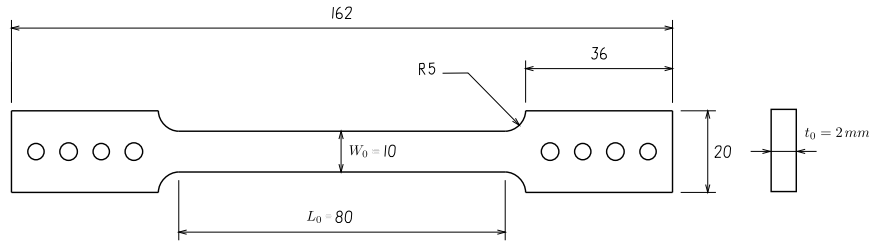


Figure 2.1: Geometry and dimensions of the tensile specimen (dimensions in mm)

All the tested specimens are machined along the rolling direction. A special grip system is used as shown in Figure 2.2. The heels and the specimen are clamped and the system allows a predetermined run in order to reach the desired test velocity.

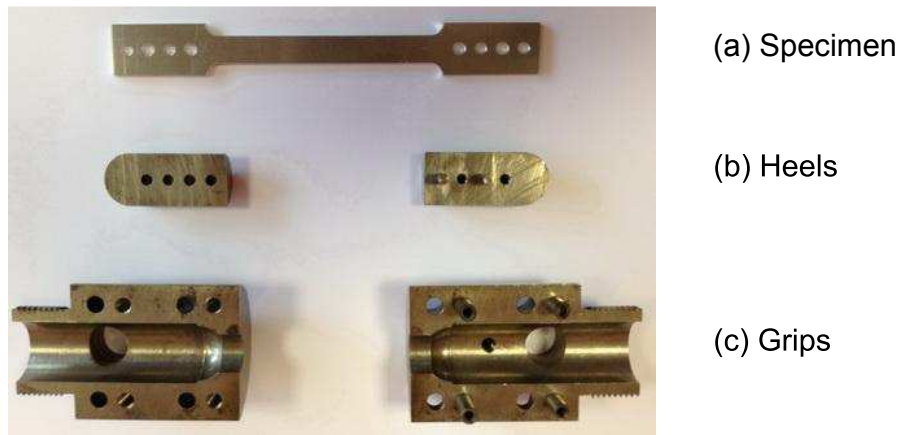


Figure 2.2: Grip system used in the tensile tests

### 2.2.2.2 Experimental equipments

The tests are performed under three temperatures (20, 150 and 200°C) and tensile speeds (1, 10 and 100 mm/s). They are carried out with a servo-hydraulic tensile testing machine equipped with a heating furnace. The heat is generated by wire-netting heating resistances. The validity of the temperature in the specimen is confirmed by a recorded data from an external thermocouple stuck on the tested specimen.

### 2.2.3 Experimental results

For each forming condition, two specimens are tested. The force-displacement curves for the different temperatures and tensile speeds are shown in Figure 2.3. With Eq 2.1, the strain-stress curves of AA5086 are determined as shown in Figure 2.4 and Figure 2.5. Due to the constant cross-section of the design specimen, the corresponding strain rate can also be calculated.

$$\begin{cases} \bar{\epsilon} = \ln(1 + \Delta L/L_0) \\ \bar{\sigma} = F \cdot (L_0 + \Delta L) / (A_0 \cdot L_0) \quad \text{with} \quad A_0 = t_0 \cdot W_0 \\ \dot{\bar{\epsilon}} = V/L_0 \end{cases} \quad (2.1)$$

$V$  is the uniaxial tensile speed.

## 2.2.4 Discussions

### 2.2.4.1 Temperature influence

Different strain hardening behaviors between ambient and high temperature on the flow stresses of AA5086 are observed. The flow stresses show a monotonic character with strain at ambient temperature while they show a saturation state at high strain and high temperature as shown in Figure 2.4(a) and 2.4(b).

It is shown in Figure 2.4 that, at the same tensile speed, the temperature has a negative influence on the material flow stresses. The flow stress temperature sensitivity is much more pronounced at low tensile speed than at high tensile speed. The stress reduction at high temperature can be explained by the thermally activated dislocation motion which is much more easier at high temperature. At high tensile speed, the time available for the dislocation to obtain the additional thermal energy is reduced, so the temperature sensitivity on the flow stress is weaker.

### 2.2.4.2 Strain rate influence

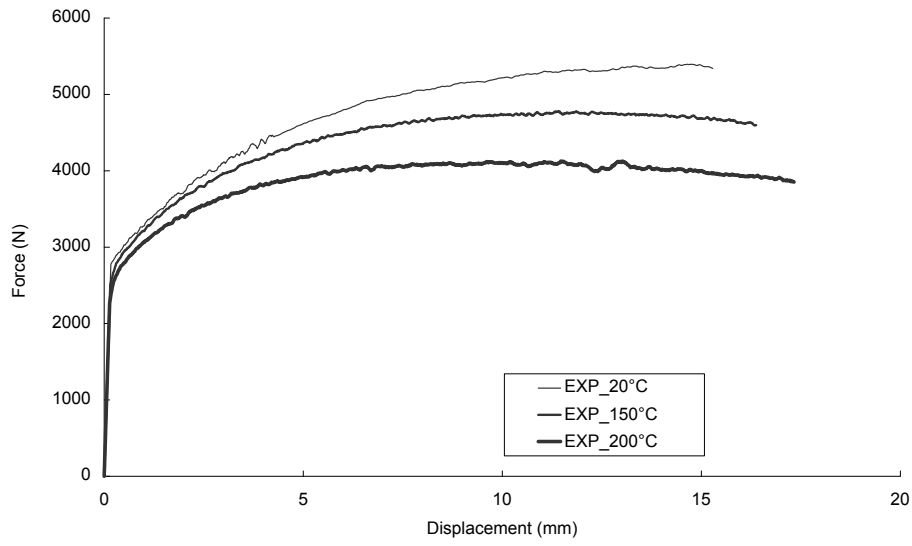
The strain rate influence on the flow stress is presented in Figure 2.5. There is almost no differences among the flow stresses between the different tensile speeds at 20°C and 150°C. At 200 °C, the results show a clear positive strain rate influence on the flow stress. In all, it can be concluded that the flow stress of AA5086 is insensitive to strain rate at ambient temperature while it is strain rate dependent at high temperature.

## 2.3 Identification methods

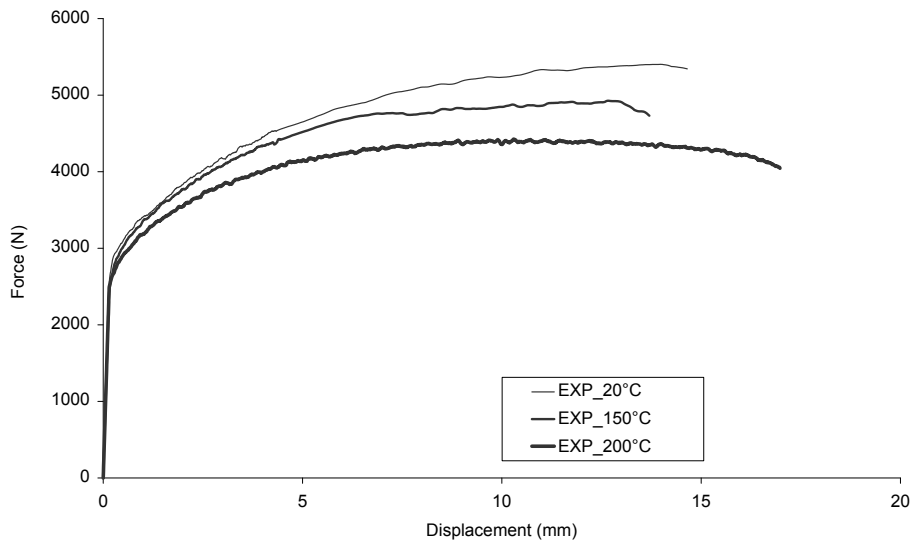
Two prevalent methods used in the literature to identify the fitting parameters are briefly introduced in this part.

### 2.3.1 Direct method

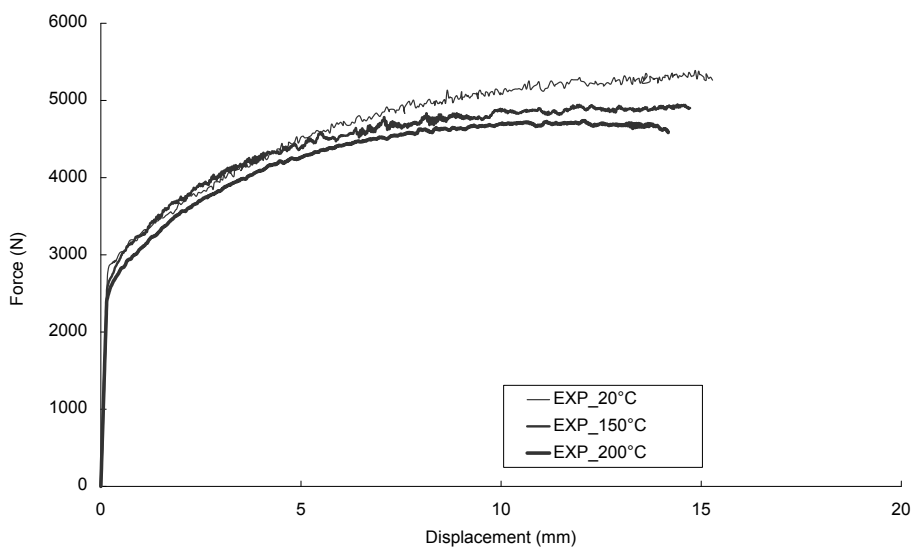
From experimental results, the stress-strain curves under different conditions ( $\bar{\sigma} = \bar{\sigma}(\bar{\epsilon})|_{\bar{\epsilon}, T}$ ,  $\bar{\sigma} = \bar{\sigma}(\dot{\bar{\epsilon}})|_{\bar{\epsilon}, T}$ ,  $\bar{\sigma} = \bar{\sigma}(T)|_{\bar{\epsilon}, \dot{\bar{\epsilon}}}$ ) are obtained. With the analytical equations of the hardening laws, the related fitting parameters can be determined directly. Taking the Norton - Hoff hardening model ( $\bar{\sigma} = K\bar{\epsilon}^n\dot{\bar{\epsilon}}^m$ ) as an example, as shown in Figure 2.6, the values of  $n$  and  $m$  can be determined according to the definition. This determination method is simple and fast but it can only be applied to models with low number of fitting parameters. Besides, this method decouples the combined effect of strain rate and temperature.



(a) 1 mm/s

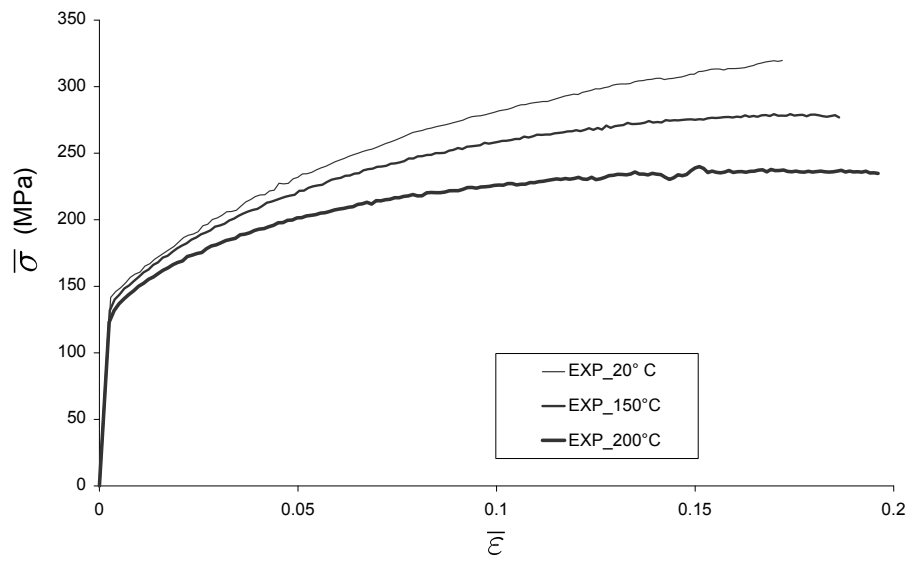


(b) 10 mm/s

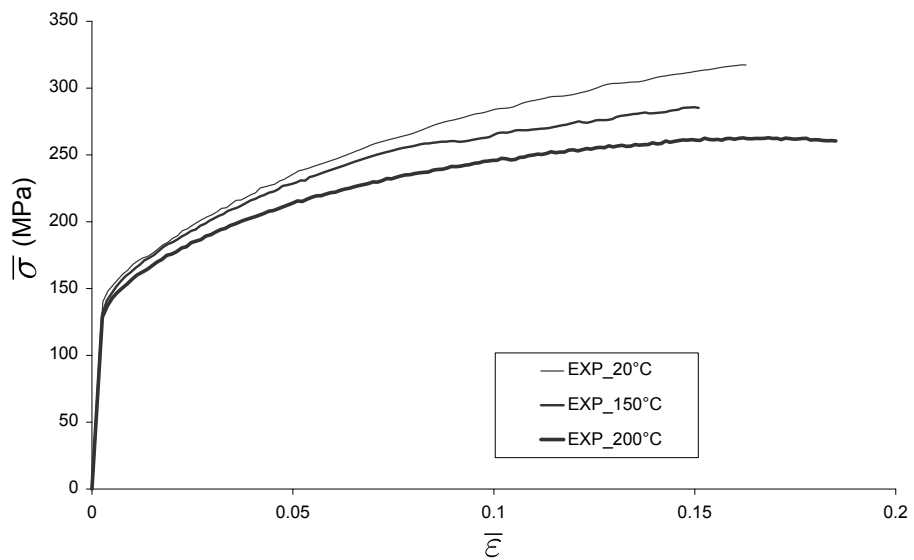


(c) 100 mm/s

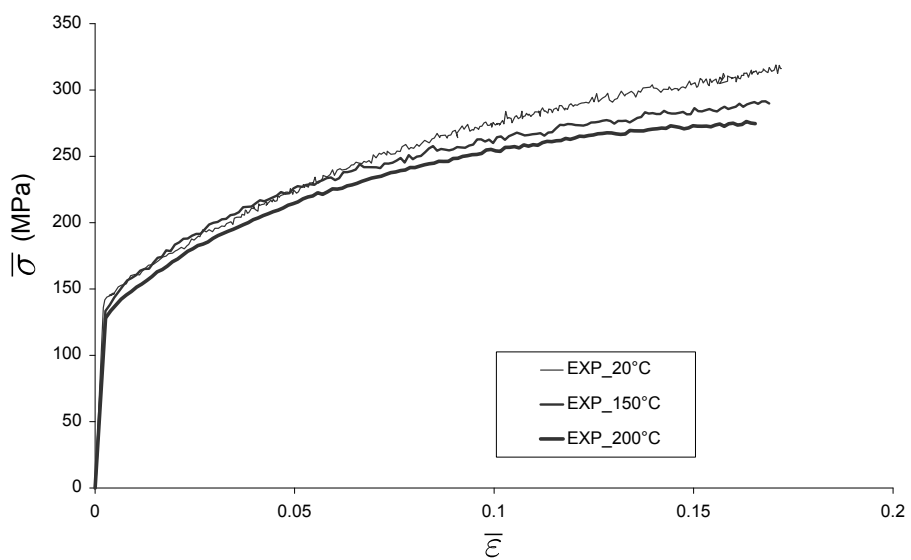
Figure 2.3: Force versus displacement curves at different temperatures for each tensile speed



(a) 1 mm/s

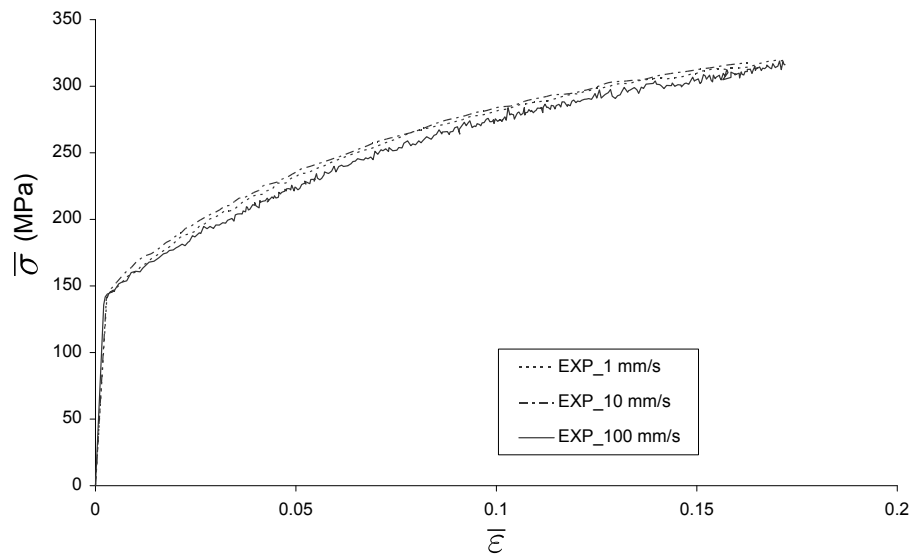


(b) 10 mm/s

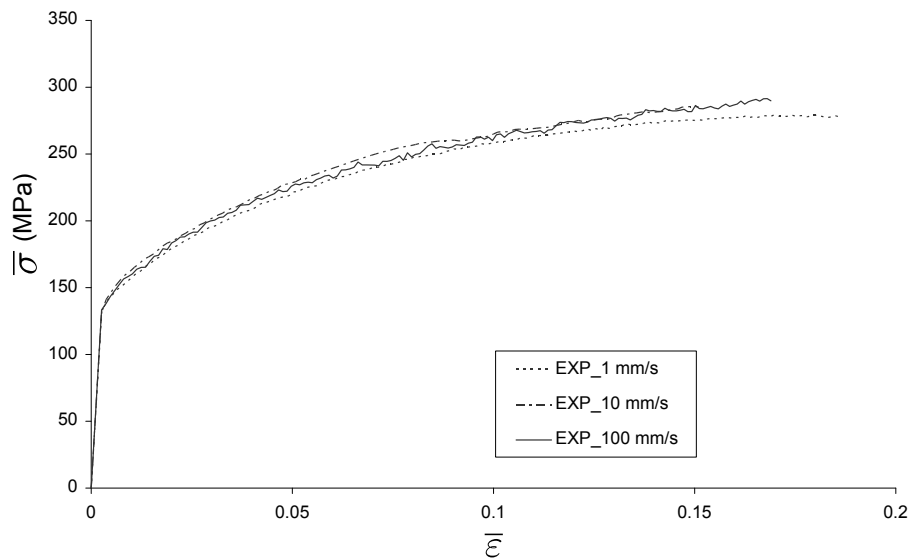


(c) 100 mm/s

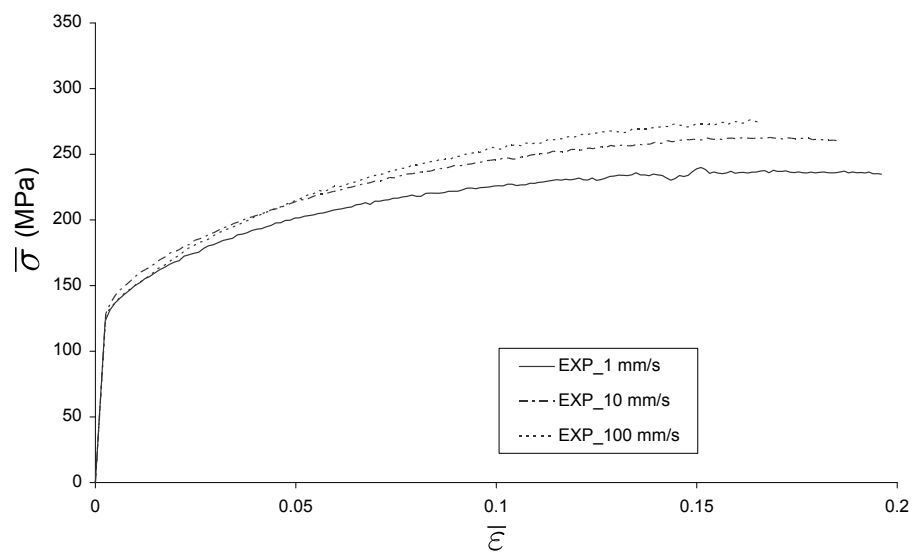
Figure 2.4: Temperature influence on the flow stresses at different tensile speeds



(a) 20°C



(b) 150°C



(c) 200°C

Figure 2.5: Tensile speed influence on the flow stresses at different temperatures

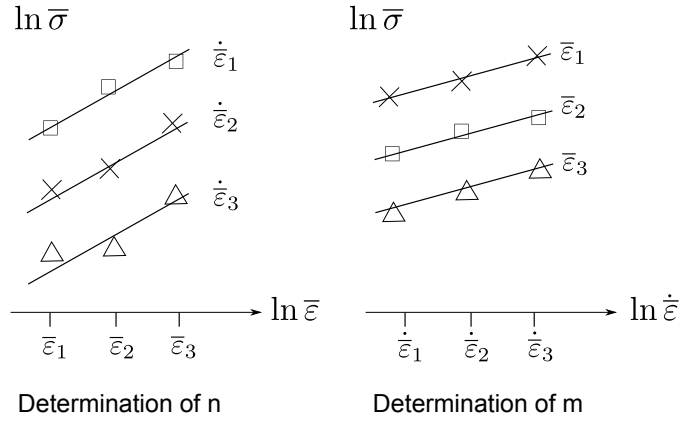


Figure 2.6: Parameter determination with direct method

### 2.3.2 Optimization method

A procedure of optimization associated with the minimization of a cost function (E) can be used to determine the parameters of the hardening law. The procedure is analytical or numerical (Table 2.2).

#### 2.3.2.1 Analytical

The analytical method combines the analytical equation and the strain-stress data available for an homogeneous tensile test. For an homogeneous specimen, the values  $\bar{\sigma}^{exp}$  versus  $\bar{\epsilon}^{exp}$  can be obtained from the experiments. For a set of parameter values, the analytical hardening equations  $\bar{\sigma}^{cal}$  are calculated, the mean absolute error can be expressed as:

$$E = \frac{\sum_{i=1}^N |(\bar{\sigma}_i^{exp} - \bar{\sigma}_i^{cal}) / \bar{\sigma}_i^{exp}|}{N} \quad (2.2)$$

$\bar{\sigma}_i^{exp}$  and  $\bar{\sigma}_i^{cal}$  denote the stresses obtained by experiment and calculated from constitutive equation at the  $i^{th}$  increment, respectively.  $N$  is the number of experimental measured strain points.

Table 2.2: Identification of rheological parameters [29]

	model	
	analytical	numerical
Experimental	$F^{exp}(\Delta L, V, T)$	$F^{exp}(\Delta L, V, T)$
$O^{exp}$	$\downarrow$ analytical model $\downarrow$ $\bar{\sigma}^{exp}(\bar{\epsilon}, \dot{\bar{\epsilon}}, T)$	
Calculation	$\bar{\sigma}^{cal}(P, \bar{\epsilon}, \dot{\bar{\epsilon}}, T)$	$\bar{\sigma}^{cal}(P, \bar{\epsilon}, \dot{\bar{\epsilon}}, T)$
$O^{cal}(P)$		$\downarrow$ numerical model $\downarrow$ $F^{cal}(P, \Delta L, V, T)$
E	$f[\bar{\sigma}^{exp}, \bar{\sigma}^{cal}(P)]$	$f[F^{exp}, F^{cal}(P)]$

### 2.3.2.2 Numerical

The numerical method is based on the FE model of the rheological test and on the direct measured data from experiments which are usually the force versus displacement curves for a tensile test. The parameter identification procedure to find a set of rheological parameters for a known constitutive equation can be formulated as an inverse problem. To determine the fitting parameters, the following elements are essential:

- Uniaxial tensile experimental data which can be the measured force, so with this method, the homogeneous specimen is not mandatory.
- A FE model of the uniaxial tensile test that provides the required output data.
- Optimization procedure which analyze the discrepancy between experimental input data and simulation output data.

With an inverse analysis method, the coupling effect between strain rate and temperature can be analyzed. The temperature variation inside the specimen caused by plastic strain deformation can also be taken into account. The high calculation cost is the main disadvantage.

The principle of the optimized method is presented in Figure 2.7. The final fitting parameters  $P$  are obtained when the cost function ( $E$ ) between the prediction values and the experimental ones reaches the defined minimum value.

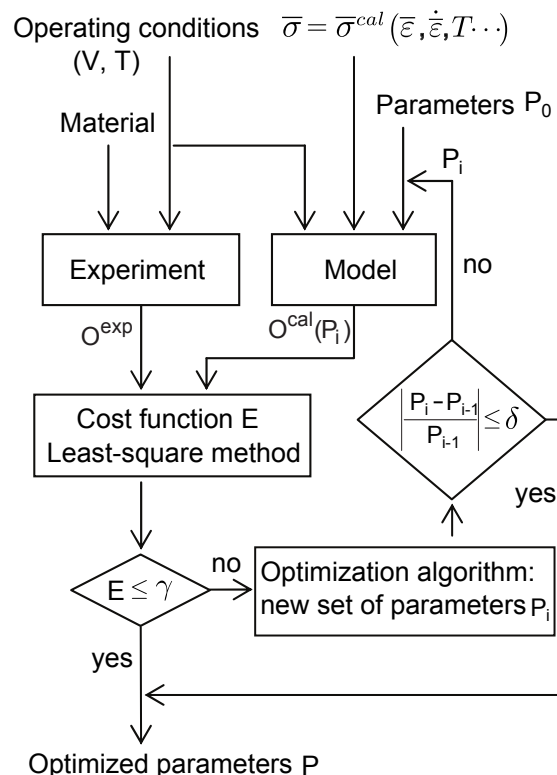


Figure 2.7: Principle of the optimization procedure [29]

## 2.4 Identification of the rheological parameters for different hardening models

In this work, the parameters (P) are determined with the optimization method through a gradient-based Matlab minimization function. With this method, the temperature increase generated by plastic deformation inside the specimen is not taken into account. Indeed, the tested speeds are not very high and the main purpose of this study is to quantify the hardening model influence on the FLCs.

### 2.4.1 Initial yield stresses of AA5086

Through the stress-strain curves, the initial yield stresses of AA5086 are determined, it is found that the initial yield stress is independent on strain rate, the values are presented in Table 2.3 at the three temperatures.

Table 2.3: Initial yield stresses of AA5086 at different temperatures

Temperature ( °C )	Yield stress ( MPa )
20	134.6
150	127.1
200	121.5

To describe the material flow stresses in the temperature range, it is necessary to know the evolution of initial yield stresses under different temperatures. Eq 2.3 is proposed to describe the initial yield stress  $\sigma_0$  in function of the temperature based on the evolution of modulus in RK model [87]. In Figure 2.8, the calculated values from 20°C to 200°C gives good matches with the measured ones.

$$\sigma_0(T) = \left\{ 1 - \frac{T}{T_m} \exp \left[ K \left( 1 - \frac{T_m}{T} \right) \right] \right\} \cdot \sigma_0(T_0) \quad (2.3)$$

Where  $\sigma_0$  is the initial yield stress at different temperatures,  $T$  is the current temperature,  $T_m = 627^\circ\text{C}$  is the melting temperature,  $\sigma_0(T_0)$  is the initial yield stress at ambient temperature ( $T_0$ ),  $K = 0.556$  is the fitting parameter.

### 2.4.2 Identified hardening models

For the choice of the hardening model, a compromise must be found between the accuracy of the model description and the number of fitting parameters. According to the different strain hardening characters, the selected models have been divided into different types as shown in Table 2.4. With the strain-stress data and determined initial yield stresses, the optimized fitting parameters for the selected hardening models are presented hereafter.

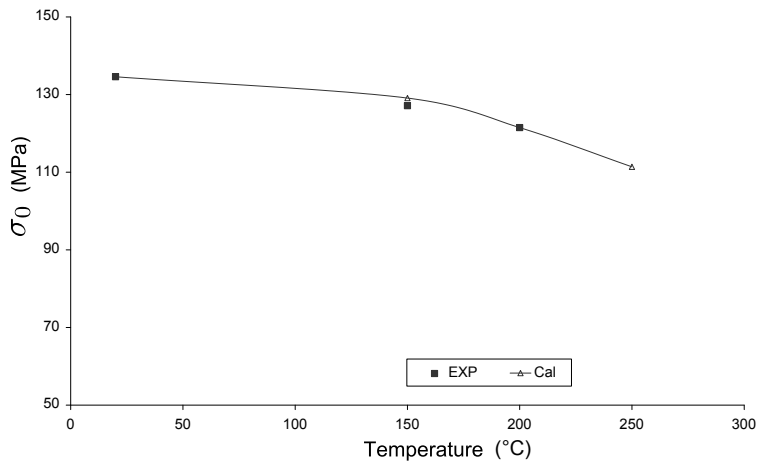


Figure 2.8: Evolution of the initial yield stresses for AA5086

Table 2.4: Overview of the different hardening models

Power laws	Saturation laws	Mixed law
Ludwick ; KHL ; ZA	Voce ; Bergström	H-V

Compared to the physical-based models, the empirical models have fewer identified parameters and their integration is easier into commercial FE softwares. But the original proposed models are usually only suitable in a limited range of temperature and strain rate. To make the model adapted under wide forming conditions, many modifications are proposed on the original models. One prevalent method used in the literature consists in modeling the fitting parameter evolutions according to the test temperature or strain rate as presented in [2]. In this work, the same method is adopted.

### 2.4.3 Power law hardening models

#### 2.4.3.1 Ludwick model

Ludwick hardening law is a simple and widely used empirical model for the description of material flow stresses in sheet metal forming field as shown in Eq 2.4.

$$\bar{\sigma} = \sigma_0 + K \bar{\varepsilon}_p^n \quad (2.4)$$

Where  $K$  and  $n$  are the fitting parameters used to describe the material strain hardening character.

#### Temperature influence

With Eq 2.4, the fitting parameters  $K$  and  $n$  under different temperatures and tensile speeds are determined as shown in Table 2.5. The correlation results between the prediction and experimental data are shown in Figure 2.9. Ludwick model gives a good description of the material flow stresses under each forming condition.

Table 2.5: The values of  $K$  and  $n$  under different temperatures and tensile speeds

Tensile speed (mm/s)	Temperature ( $^{\circ}C$ )	$K$ (MPa)	$n$
1	20	522	0.56
	150	353	0.444
	200	212	0.328
10	20	517	0.544
	150	399	0.46
	200	305	0.4014
100	20	481	0.525
	150	430	0.505
	200	409	0.495

For a given tensile speed, the strain rate influence is constant. The evolution of  $K$  and  $n$  according to temperature under each forming speed is shown in Figure 2.10. The results reveal that the parameters  $K$  and  $n$  decrease quasi linearly with temperature. The fitting parameters are modified into a linear expression and the model is rewritten as:

$$\bar{\sigma} = \sigma_0 + (K_0 - K_1 T) \bar{\varepsilon}_p^{(n_0 - n_1 T)} \quad (2.5)$$

### Strain rate sensitivity

The strain rate influence is incorporated by means of a multiplicative formulation. The term  $\dot{\varepsilon}^m$  is added to the original Ludwick model, as shown in Eq 2.6. With this model, the fitting parameters are optimized with experimental data for each temperature and under the three tensile speeds. The optimized parameters are shown in Table 2.6 and the correlation results are shown in Figure 2.11.

$$\bar{\sigma} = \sigma_0 + K \bar{\varepsilon}_p^n \dot{\varepsilon}_p^m \quad (2.6)$$

Table 2.6: Fitting values of  $K$ ,  $n$  and  $m$  for each temperature under the three tensile speeds

Temperature ( $^{\circ}C$ )	Tensile speed (mm/s)	$K$ (MPa)	$n$	$m$
20	1 / 10 / 100	504.5	0.5414	0.00001
150	1 / 10 / 100	384.9	0.4616	0.00624
200	1 / 10 / 100	335	0.4094	0.05502

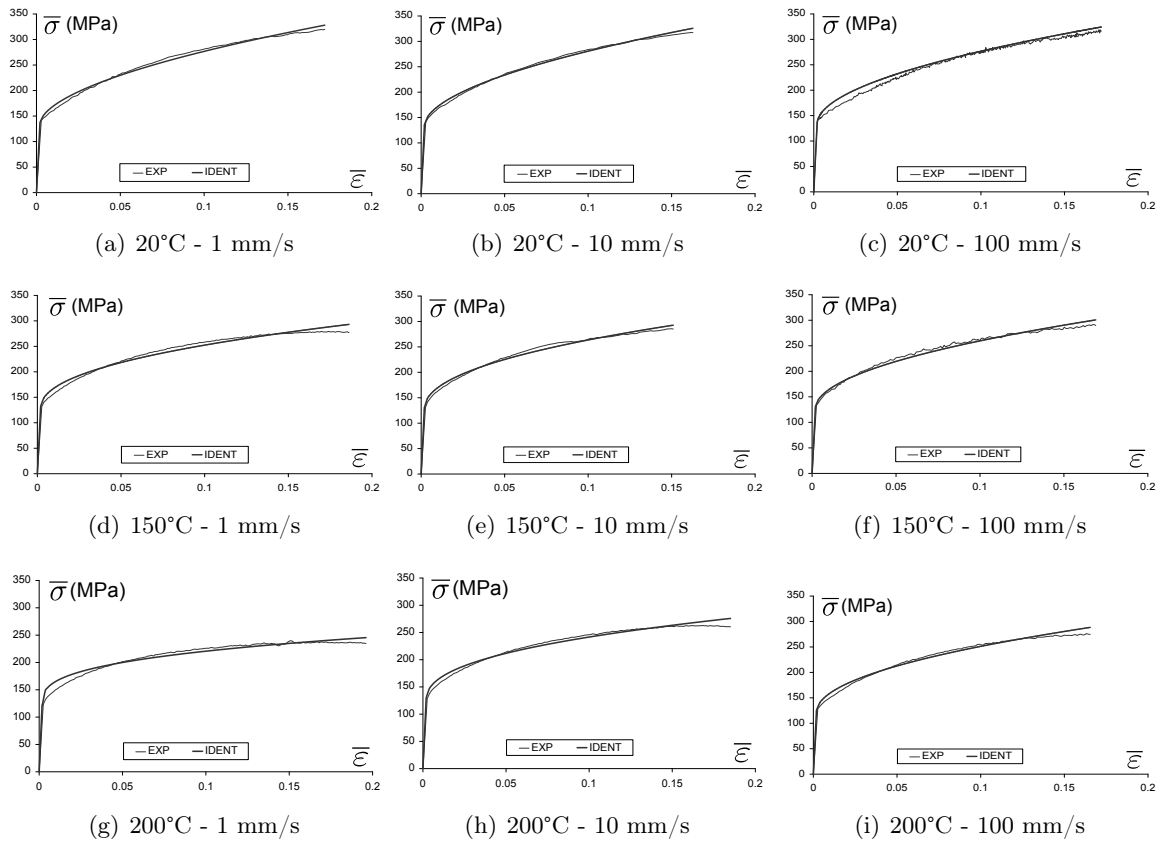


Figure 2.9: Identification results of the original Ludwick model

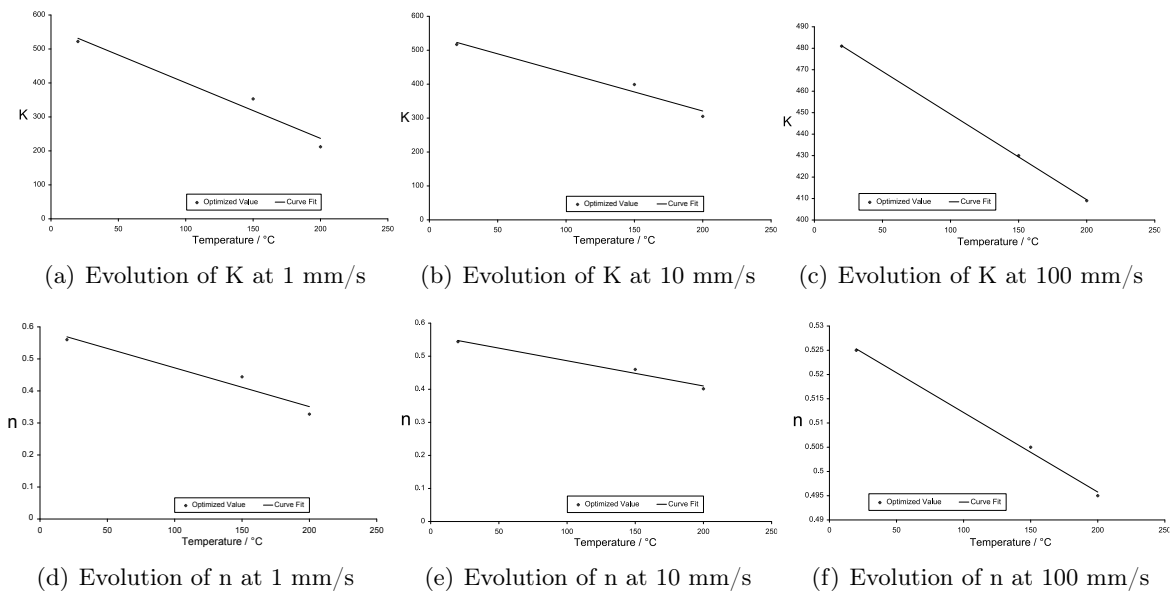


Figure 2.10: Evolution of  $K$  and  $n$  with temperature for Ludwick model

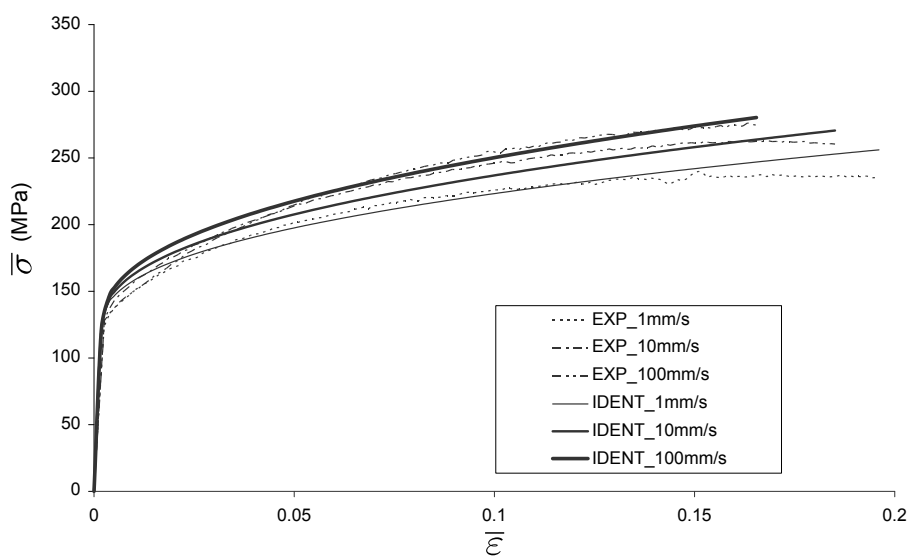
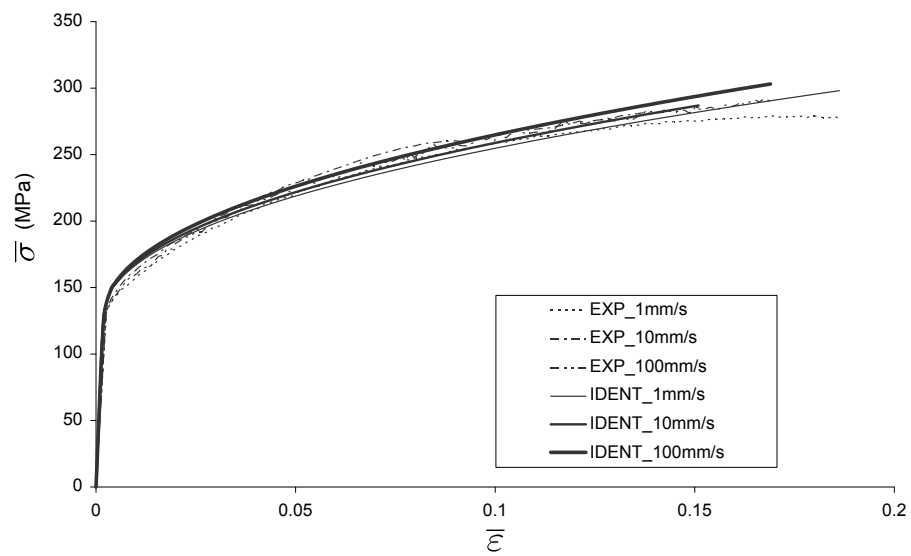
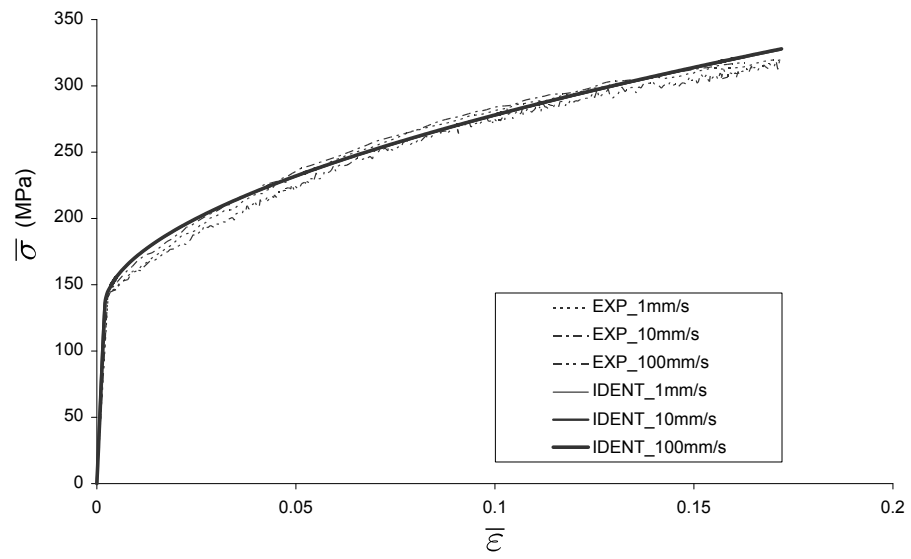


Figure 2.11: Prediction results with strain rate modified Ludwick model for each temperature

The linear evolution of  $K$  and  $n$  according to temperature for the modified strain rate Ludwick model is confirmed by Figure 2.12. Figure 2.13 shows that the strain rate sensitivity index  $m$  evolves exponentially with tested temperatures. The value of  $m$  is very small at ambient temperature which confirms that the material is strain rate insensitive for this condition. The values of  $m$  indicate a positive strain rate influence on the flow stresses at high temperature.

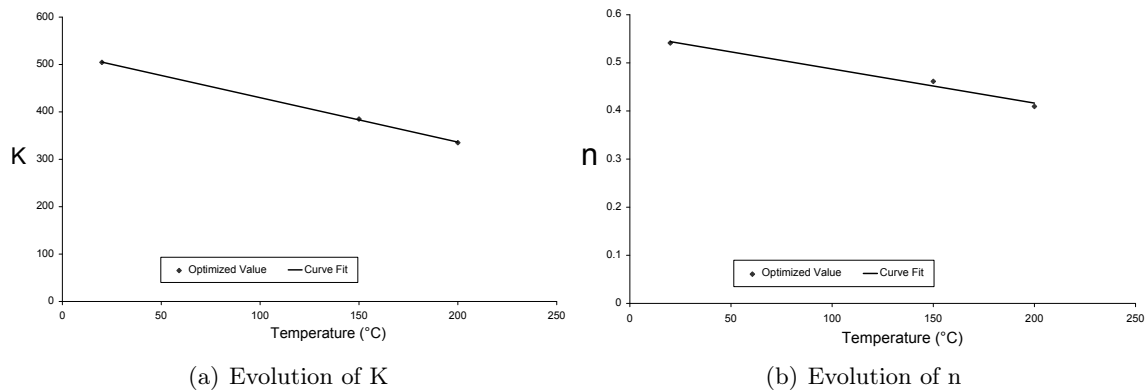


Figure 2.12: Evolution of  $K$  and  $n$  for Ludwick model with strain rate term

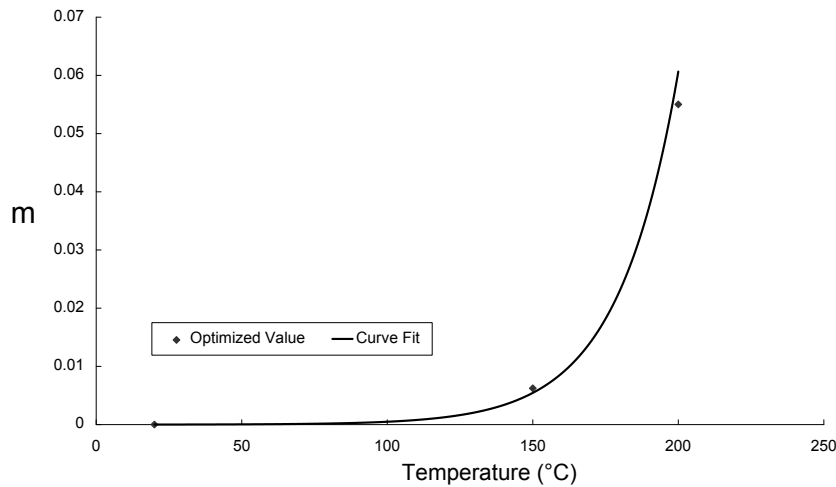


Figure 2.13: Strain rate sensitivity index  $m$  at different temperatures

### Final proposed model

With the parameter evolution results and the yield stress  $\sigma_0(T)$ , the final proposed Ludwick model incorporating temperature and strain rate influence is given by Eq 2.7. Considering all the experimental data, the optimized parameters and the correlation results are shown in Table 2.7 and Figure 2.15.

$$\bar{\sigma} = \sigma_0(T) + (K_0 - K_1T) \bar{\epsilon}_p^{(n_0 - n_1T)} \dot{\bar{\epsilon}}_p^{m_0 \exp(m_1T)} \quad (2.7)$$

Despite its simplistic formulation, it is shown in Figure 2.15 that the proposed Ludwick model gives a good correlation result with experimental data under all forming conditions. Within the temperature range, the proposed model gives the best correlation under 1 mm/s.

Under 100 mm/s for small strains, a little deviation is observed. The predicted flow stresses by Ludwick model are a little higher than experimental curves under all tested conditions at high strain levels. This is caused by the monotonic strain hardening character of the power law type. The flow stresses predicted by Ludwick model with strain levels up to 50% under different forming conditions are shown in Figure 2.14. The results show that the predicted flow stress presents a monotonic character even at high temperature and low strain rate.

Table 2.7: Optimized parameters of the final proposed Ludwick model

$K_0$ (MPa)	$K_1$ (MPa/°C)	$n_0$	$n_1$ (1/°C)	$m_0$	$m_1$ (1/°C)
537.41	0.9753	0.5667	0.0007207	0.00008811	0.0319

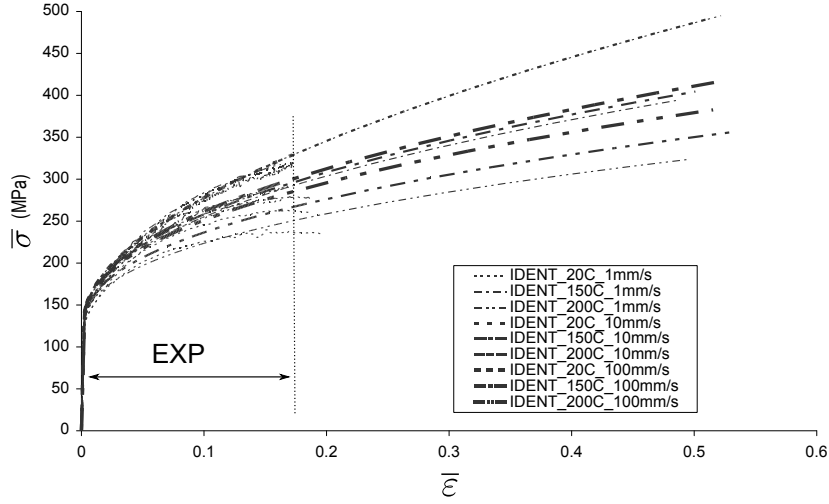


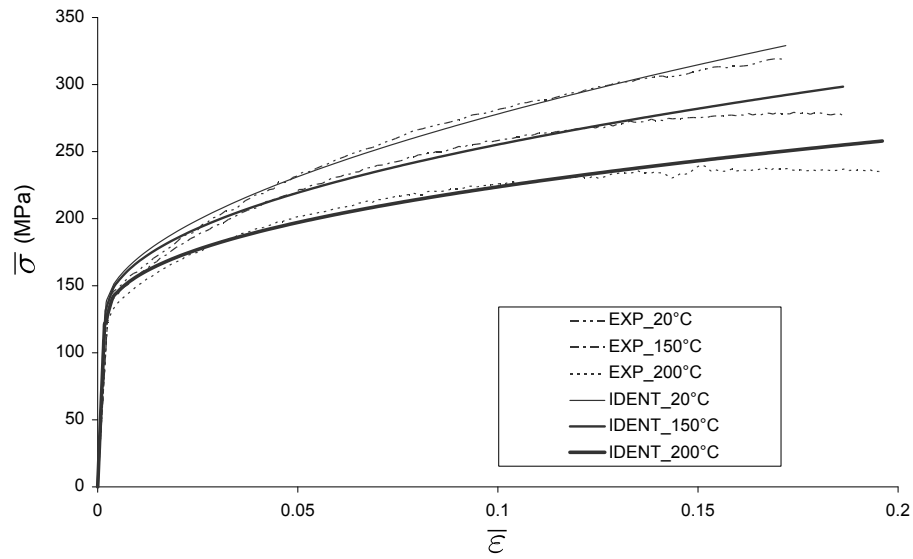
Figure 2.14: Correlation results of proposed Ludwick model with strain level up to 50%

### 2.4.3.2 KHL model

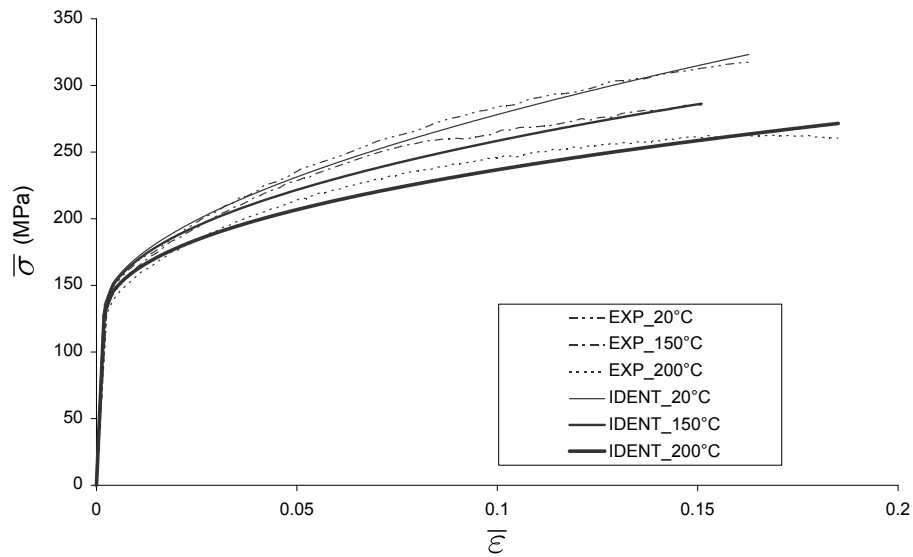
The KHL model presented in [49] and used to describe the flow stresses of AA5182-O (temperatures of 20, 100 and 200°C and strain rates of 0.0001, 0.01 and 1 s<sup>-1</sup>) is introduced in Eq 2.8.

$$\bar{\sigma} = \left( \sigma_0(T_0) \left( \frac{T_m - T}{T_m - T_r} \right)^{m_1} + B \left( 1 - \frac{\ln \dot{\bar{\epsilon}}_p}{\ln D_0} \right)^{n_1} \bar{\epsilon}_p^{n_0} \left( \frac{T_m - T}{T_m - T_r} \right)^{m_2} \right) \left( \frac{\dot{\bar{\epsilon}}_p}{\dot{\bar{\epsilon}}_0} \right)^C \quad (2.8)$$

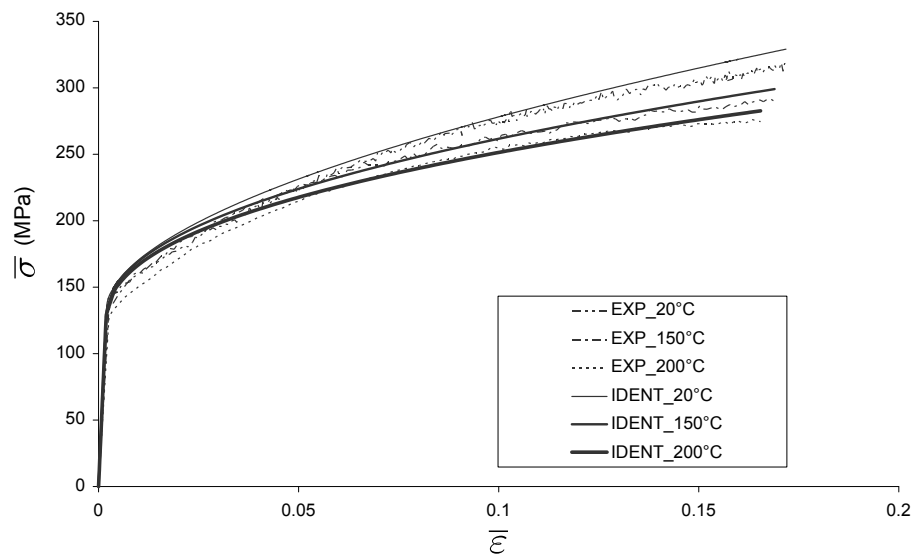
Where  $T_m = 627$  °C is the melting temperature,  $T_r = 20$ °C is the reference temperature,  $B$ ,  $n_1$ ,  $n_0$ ,  $c$ ,  $m_1$ ,  $m_2$  are the fitting material constants,  $\dot{\bar{\epsilon}}_0 = 1$  s<sup>-1</sup> and  $D_0$  is the maximum strain rate (fixed to 10<sup>6</sup> s<sup>-1</sup>). The initial yield stresses depicted by KHL model are expressed as  $\sigma_0(T_0) \left( \frac{T_m - T}{T_m - T_r} \right)^{m_1} \left( \frac{\dot{\bar{\epsilon}}_p}{\dot{\bar{\epsilon}}_0} \right)^C$  which means that the initial yield stress is affected by strain rate. This conflicts with the conclusion obtained from experimental results, so the decoupling of initial yield stress with strain rate is necessary.



(a) 1 mm/s



(b) 10 mm/s



(c) 100 mm/s

Figure 2.15: Correlation results of the proposed Ludwick model under different temperatures and strain rates

With the optimization results at each temperature and the three tensile speeds, the parameter evolutions of  $n_0$  and  $C$  are analyzed. Similar linear evolutions as described in the Ludwick model are found. The final proposed KHL model is shown in Eq 2.9.

$$\bar{\sigma} = \sigma_0(T) + B \left(1 - \frac{\ln \dot{\bar{\epsilon}}_p}{\ln D_0}\right)^{n_1} \bar{\epsilon}_p^{n_2 - n_3 T} \left(\frac{T_m - T}{T_m - T_r}\right)^m \left(\frac{\dot{\bar{\epsilon}}_p}{\dot{\bar{\epsilon}}_0}\right)^{C_0 \exp(C_1 T)} \quad (2.9)$$

The identification results are presented in Table 2.8 and Figure 2.17. The function  $\left(1 - \frac{\ln \dot{\bar{\epsilon}}}{\ln D_0}\right)^{n_1}$  is proposed in [50] to describe the flow stress increase at high strain rates ( $10^3 - 10^4 s^{-1}$ ). Considering the moderate level of tested strain rates, it is logical to find a small value for  $n_1$  and the term  $\left(1 - \frac{\ln \dot{\bar{\epsilon}}}{\ln D_0}\right)^{n_1}$  is close to 1 for the different strain rates. Compared to the parameter values for AA5182-O in [49], similar results are obtained for AA5086.

Table 2.8: The fitting parameters of proposed KHL model

$B$ (MPa)	$n_1$	$n_2$	$n_3$ (1/°C)	$m$	$C_0$	$C_1$ (1/°C)
510.4	0.1235	0.5706	0.0007557	1.1345	0.0004105	0.02506

The flow stresses predicted by the proposed KHL model with strain level up to 50% are shown in Figure 2.16. Similar to Ludwick model, the flow stresses from KHL model show a monotonic increasing character with strain.

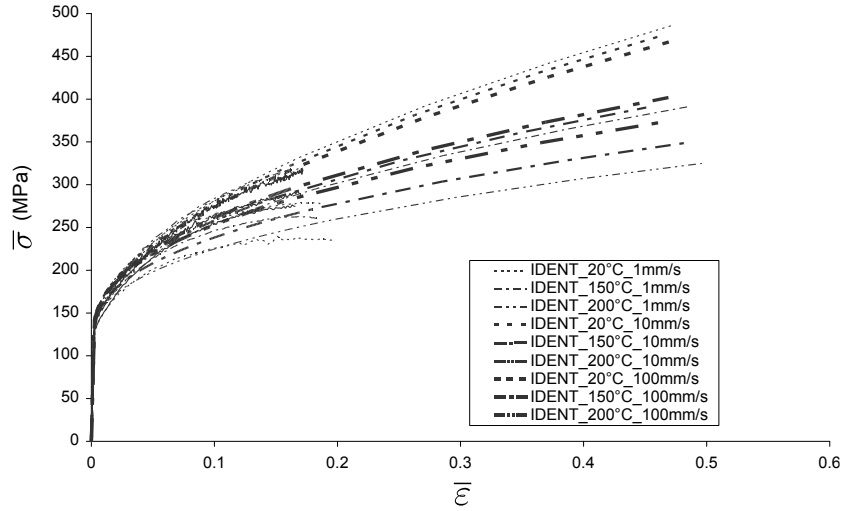
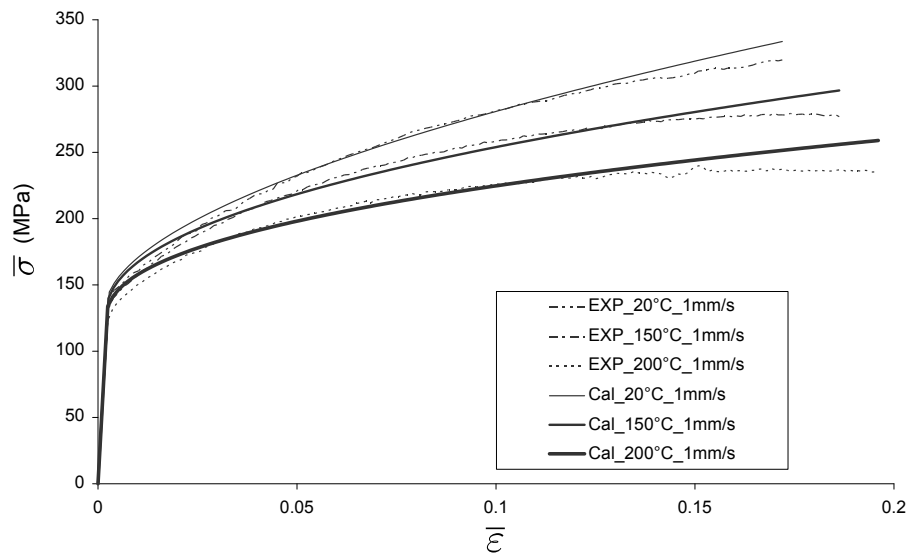
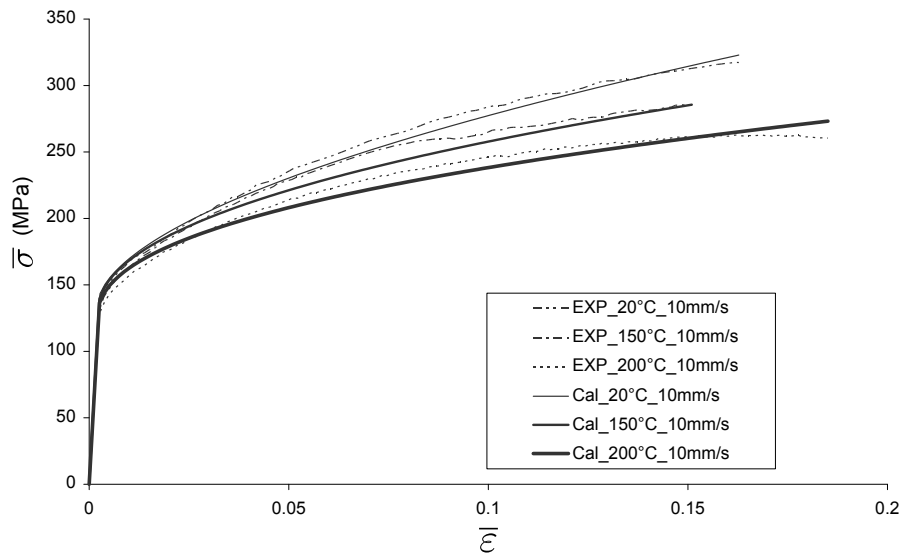


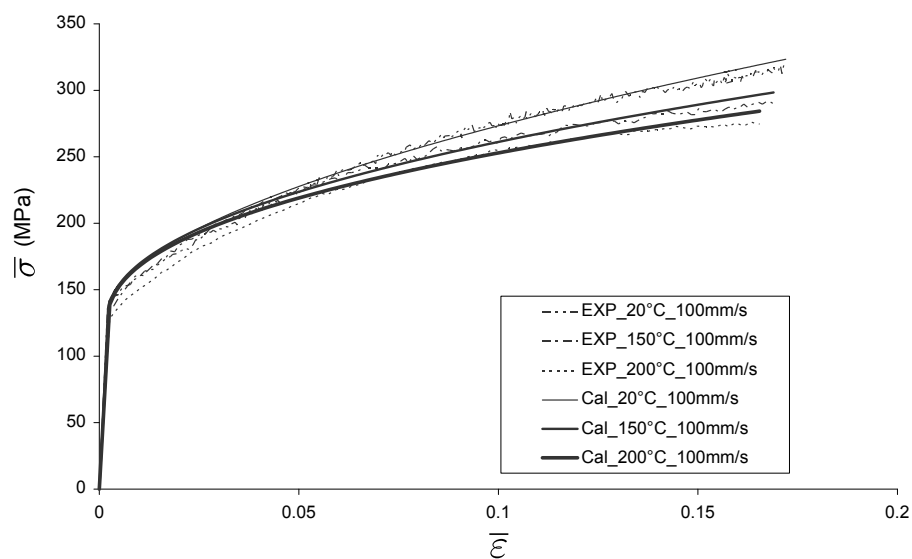
Figure 2.16: Correlation results of the proposed KHL model with strain levels up to 50%



(a) 1 mm/s



(b) 10 mm/s



(c) 100 mm/s

Figure 2.17: Correlation results of the proposed KHL model under different temperatures and strain rates

### 2.4.3.3 ZA model

The physical based ZA model for FCC material writes as:

$$\bar{\sigma} = \sigma_0 + C_1 \bar{\varepsilon}_p^{C_2} \exp(-C_3 T + C_4 T \ln(\dot{\bar{\varepsilon}}_p)) \quad (2.10)$$

$C_1$ ,  $C_2$ ,  $C_3$  and  $C_4$  are fitting parameters. In the literature, lots of modified ZA model have been proposed due to its simplicity and physical based character. In [90], for the study of an austenitic stainless steel (alloy D9), the authors proposed a modified ZA model including the coupling effects of temperature and strain. The parameter  $C_3$  is modified with a term of plastic strain. According to this proposal, the proposed ZA model in Eq 2.11 is used in this work.

$$\bar{\sigma} = \sigma_0(T) + K_1 \bar{\varepsilon}_p^n \exp(-(K_2 + K_3 T) \bar{\varepsilon}_p + K_4 \exp(K_5 T) \ln(\dot{\bar{\varepsilon}}_p)) \quad (2.11)$$

This formulation can be rewritten (Eq 2.12), it is an expression similar to Ludwick model with a softening function:  $\exp(-(K_2 + K_3 T) \bar{\varepsilon}_p)$ .

$$\bar{\sigma} = \sigma_0(T) + K_1 \bar{\varepsilon}_p^n \exp(-(K_2 + K_3 T) \bar{\varepsilon}_p) \dot{\bar{\varepsilon}}_p^{K_4 \exp(K_5 T)} \quad (2.12)$$

The identification results are presented in Table 2.9 and the correlation results are shown in Figure 2.19. Compared to Ludwick model, ZA model gives a better correlation with experimental results for strains close to 20%, especially at 1 mm/s. The flow stresses predicted by ZA model with strain level up to 50% are shown in Figure 2.18. The results show that this model give a marked softening for high strains.

Table 2.9: The fitting parameters of modified ZA model

$K_1$ ( MPa )	$K_2$	$K_3$ (1/°C)	$K_4$	$K_5$ (1/°C)	$n$
931.7	2.1342	0.007873	1.195E-06	0.05253	0.696

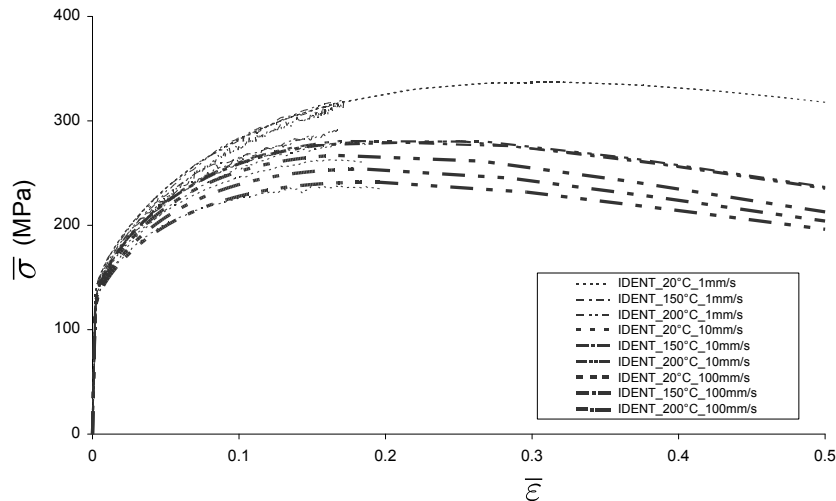
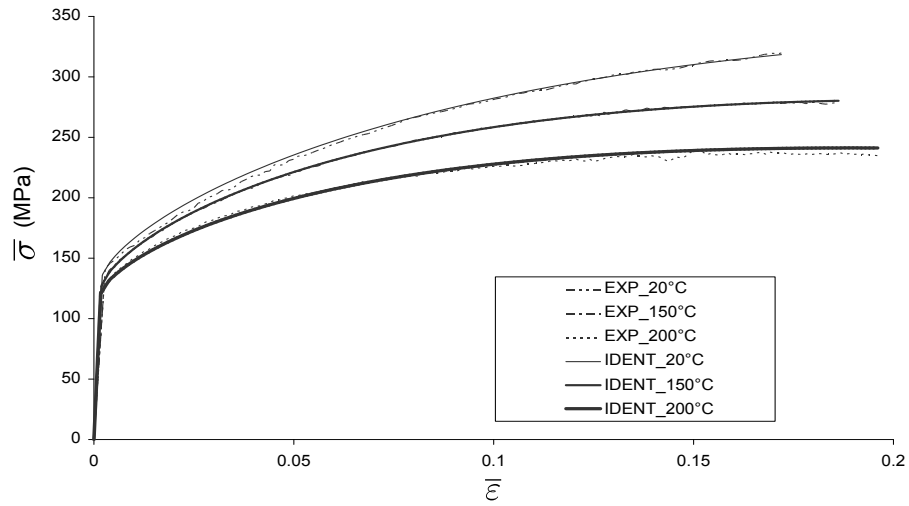
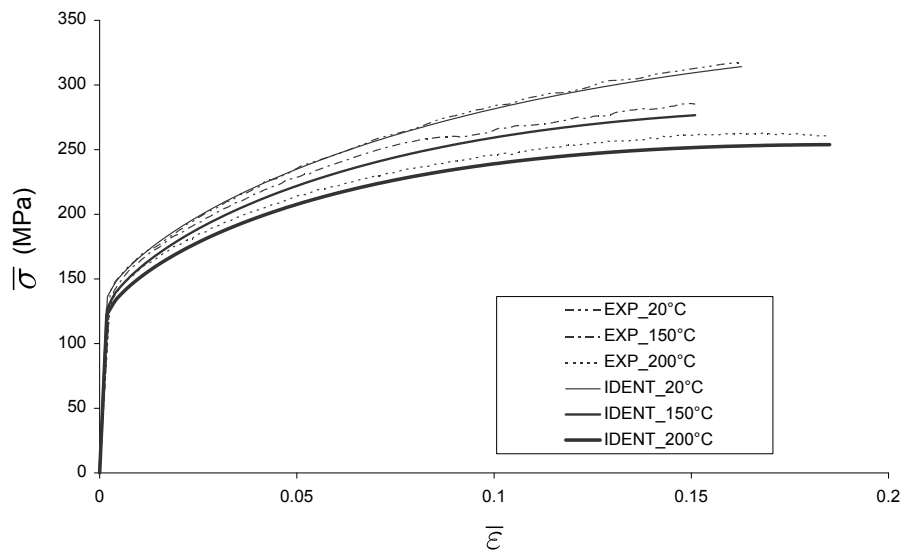


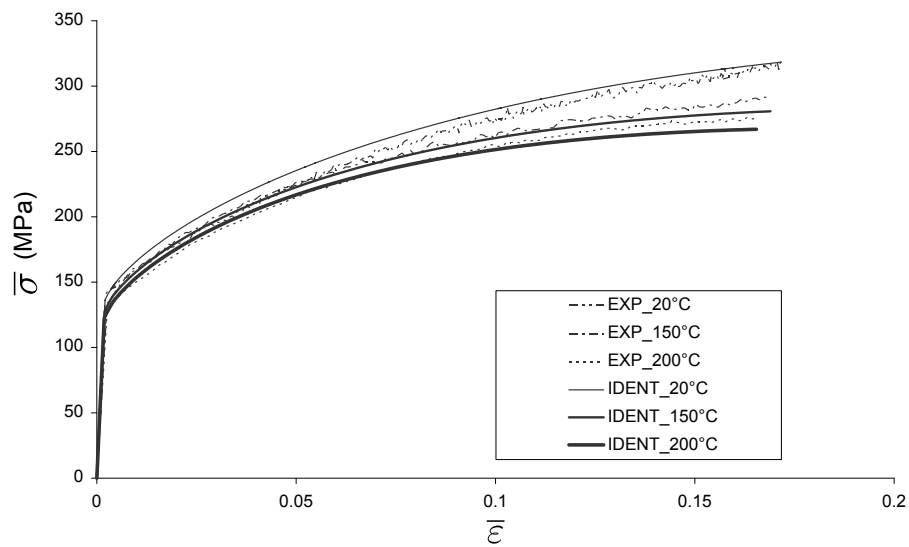
Figure 2.18: Correlation results of the proposed ZA model with strain levels up to 50%



(a) 1 mm/s



(b) 10 mm/s



(c) 100 mm/s

Figure 2.19: Correlation results of the proposed ZA model under different temperatures and strain rates

### 2.4.4 Saturation type hardening model

In the literature, it is widely accepted that the aluminium flow stresses present a saturation character at high strains. Due to the strain saturation character of Voce-type models, they are commonly used to describe the mechanical behaviors of aluminium alloys. In this part, three Voce models and a Bergström model are presented.

#### 2.4.4.1 Voce\_1 model ( $V_1$ model )

The original formula of  $V_1$  model is shown in Eq 2.13. With the same identification method adopted with Ludwick model, the fitting parameters under each forming condition are shown in Table 2.10 and their evolution are plotted in Figure 2.20. It is shown that the fitting parameters  $C_1$  and  $C_2$  can be expressed with an exponential term.

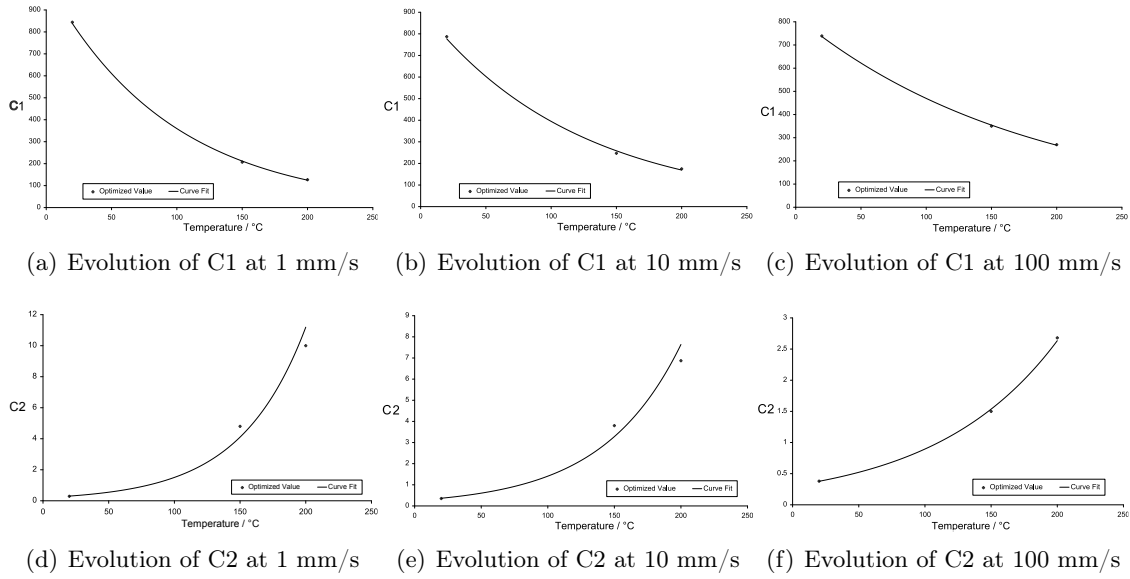
$$\bar{\sigma} = \sigma_0 + C_1 \sqrt{1 - \exp(-C_2 \bar{\epsilon}_p)} \quad (2.13)$$

The strain rate influence term  $\dot{\bar{\epsilon}}_p^m$  is adopted and  $m$  is also found to evolve exponentially with temperature. The final proposed  $V_1$  model is written in Eq 2.14. The optimized parameters are presented in Table 2.11 and the correlation results are shown in Figure 2.22.

$$\bar{\sigma} = \sigma_0(T) + K_1 \exp(-K_2 T) \sqrt{1 - \exp(-K_3 \exp(K_4 T) \bar{\epsilon}_p)} \dot{\bar{\epsilon}}_p^{m_0 \exp(m_1 T)} \quad (2.14)$$

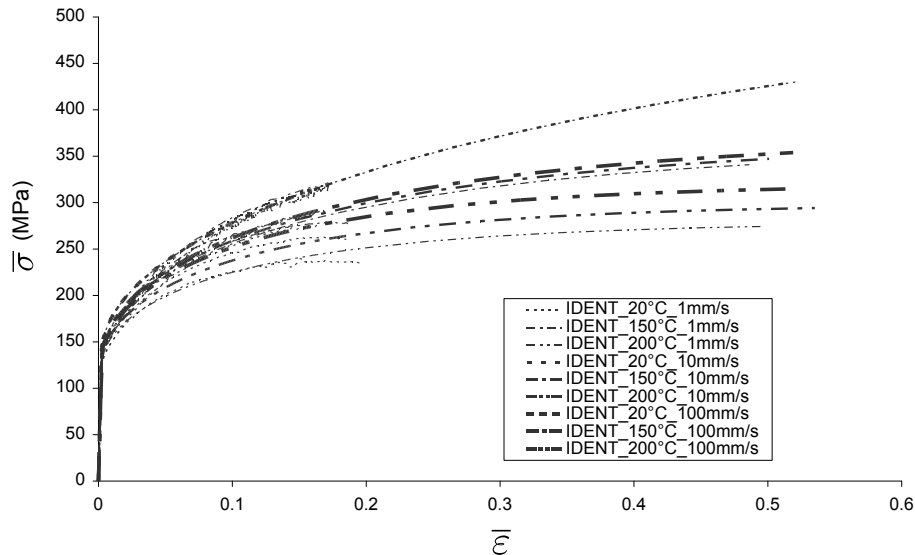
Table 2.10: The fitting values  $C_1$  and  $C_2$  under each forming condition

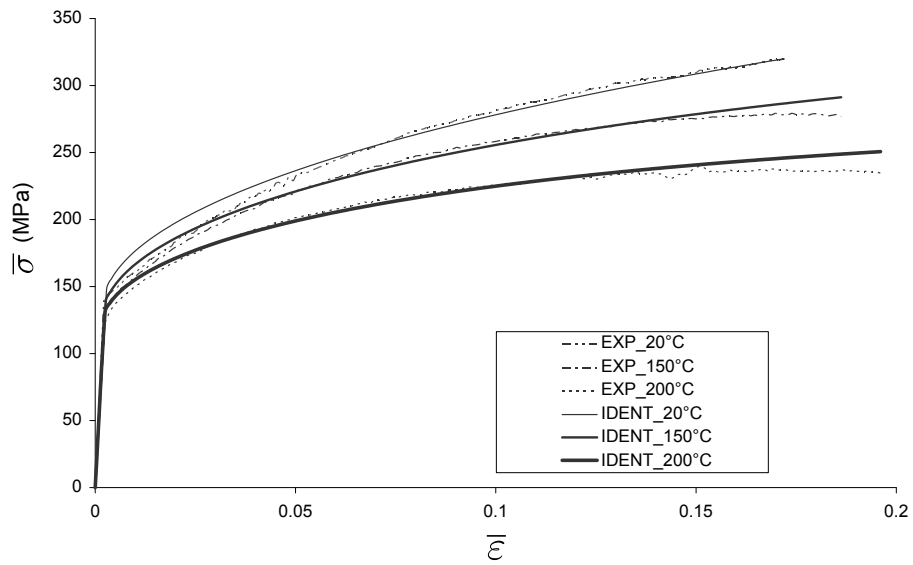
Tensile speed	Temperature ( °C )	$C_1$ ( MPa )	$C_2$
1 mm/s	20	844	0.29
	150	207	4.8
	200	127	10
10 mm/s	20	787	0.35
	150	247	3.8
	200	175	6.87
100 mm/s	20	739	0.38
	150	350	1.5
	200	270	2.68

Figure 2.20: Evolution of  $C_1$  and  $C_2$  with temperature under different tensile speedsTable 2.11: The fitting parameters of  $V_1$  model under all forming conditions

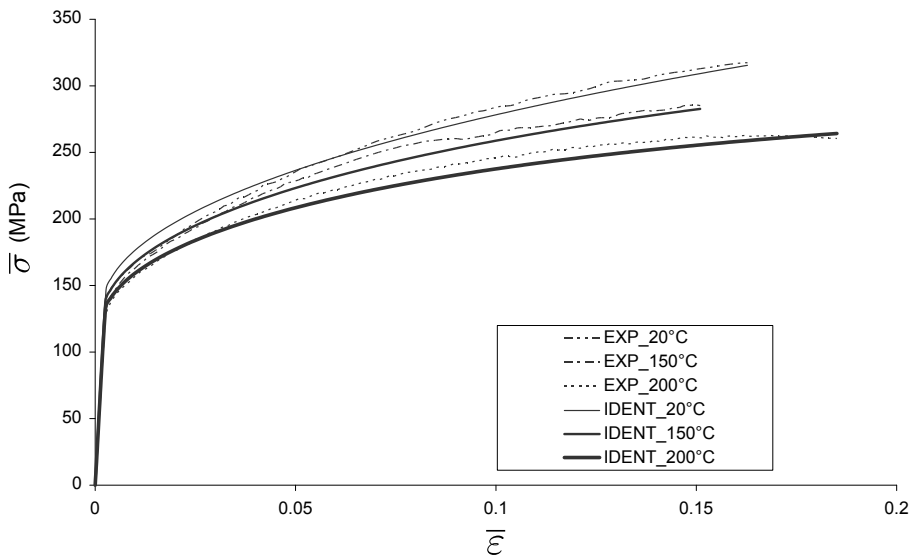
$K_1$ (MPa)	$K_2$ (1/°C)	$K_3$	$K_4$ (1/°C)	$m_0$	$m_1$ (1/°C)
485.96	0.004532	0.9434	0.00903	0.00009159	0.03153

In comparison with Ludwick model,  $V_1$  model also gives a good correlation. It also gives a higher evaluation under small strain compared to experimental curves, especially at 100 mm/s. The flow stresses predicted by  $V_1$  model with strain level up to 50% are shown in Figure 2.21. A slight saturation of the flow stresses is observed for high strain levels.

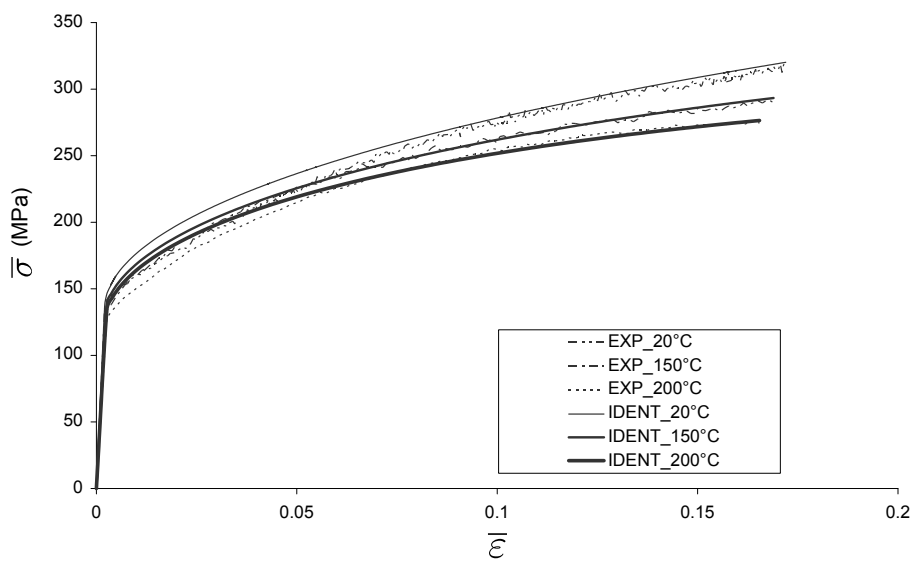
Figure 2.21: Correlation results of  $V_1$  model with strain levels up to 50%



(a) 1 mm/s



(b) 10 mm/s



(c) 100 mm/s

Figure 2.22: Correlation results of the proposed  $V_1$  model under different temperatures and strain rates

### 2.4.4.2 Voce\_2 model ( $V_2$ model )

The original  $V_2$  model is introduced and used by [9] to describe the strain-hardening curve of AA5182-O, it writes as:

$$\bar{\sigma} = \sigma_0 + C_1 (1 - \exp(-C_2 \bar{\epsilon}_p)) \quad (2.15)$$

With the optimized procedure, incorporating strain rate influence and analysis of the parameter evolutions, the final proposed  $V_2$  model is shown in Eq 2.16.

$$\bar{\sigma} = \sigma_0(T) + (K_1 - K_2 T) (1 - \exp(-(K_3 + K_4 T) \bar{\epsilon}_p)) \dot{\bar{\epsilon}}_p^{m_0 \exp(m_1 T)} \quad (2.16)$$

The identification results are shown in Table 2.12 and the correlation results are shown in Figure 2.24. The  $V_2$  model gives a good correlation result especially at high strain level. In comparison with the other models, this model gives a lower prediction at the beginning of plastic deformation. The flow stresses predicted by  $V_2$  model with strain level up to 50% are shown in Figure 2.23. When the strain passes 20%, a steady flow stress is observed for all the forming conditions.

Table 2.12: The fitting parameters of  $V_2$  model

$K_1$ (MPa)	$K_2$ (MPa/°C)	$K_3$	$K_4$ (1/°C)	$m_0$	$m_1$ (1/°C)
201.9	0.2457	13.4023	0.04473	0.0001514	0.02965

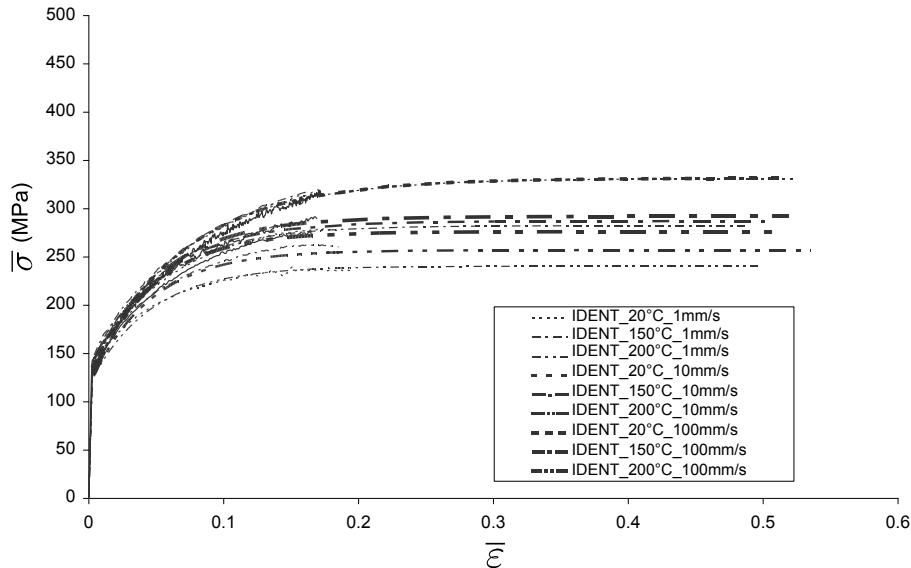


Figure 2.23: Correlation results of  $V_2$  model with strain levels up to 50%

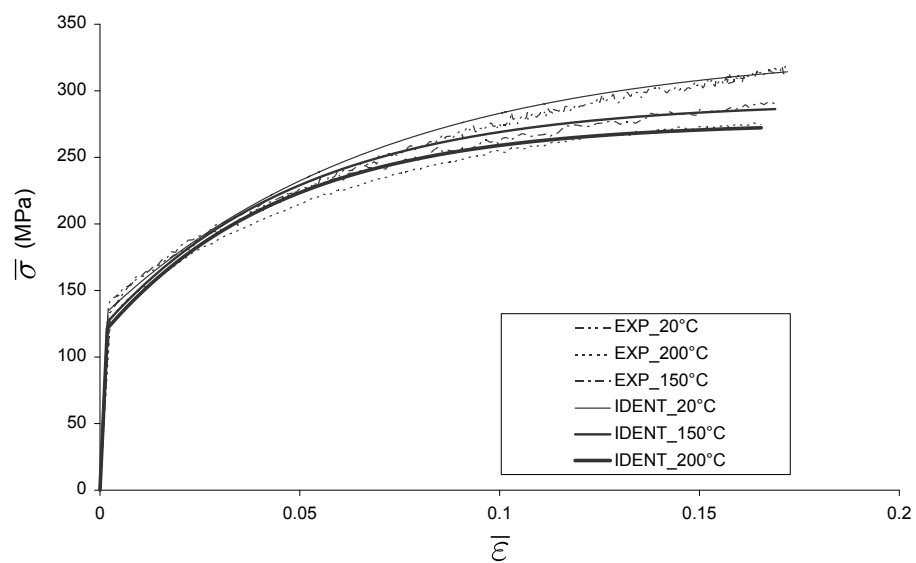
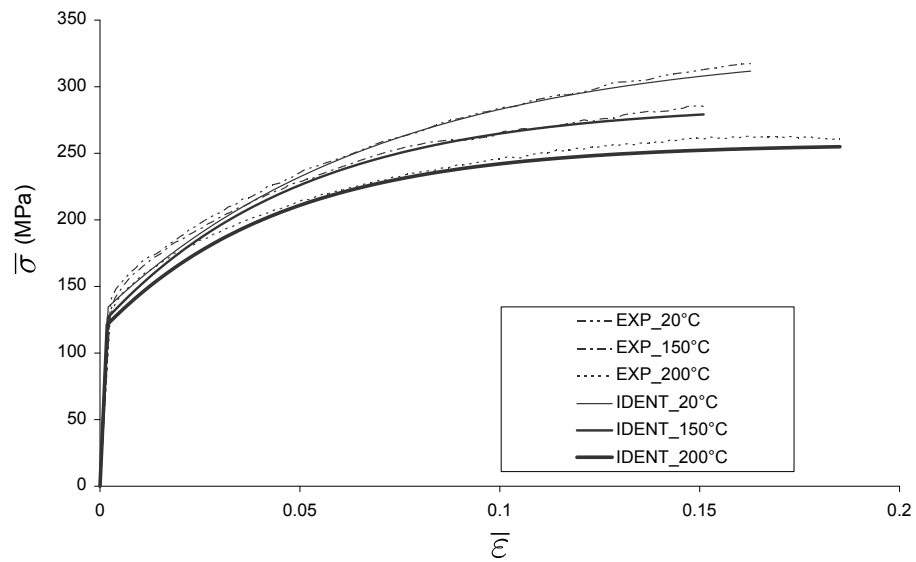
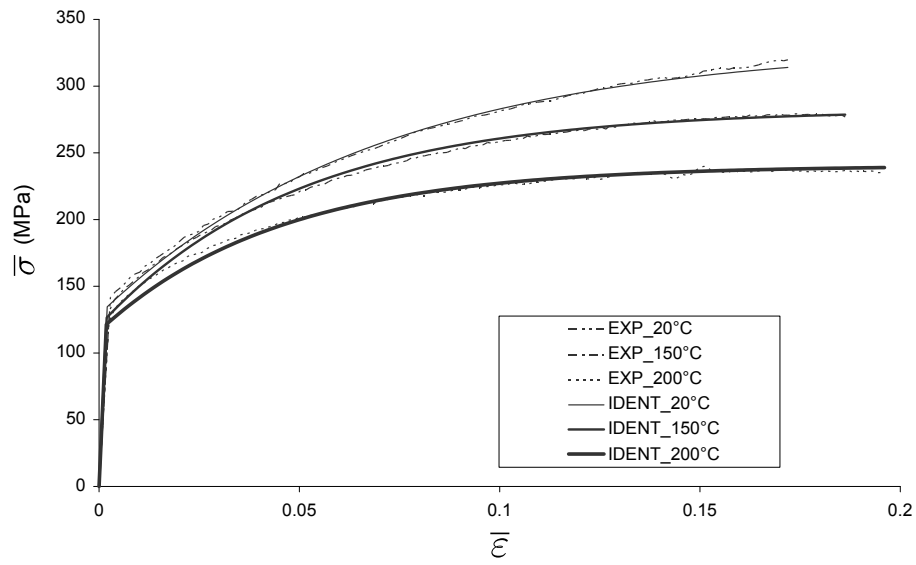


Figure 2.24: Correlation results of the proposed  $V_2$  model under different temperatures and strain rates

### 2.4.4.3 Voce\_3 model ( $V_3$ model)

Considering the high strain softening character of  $V_2$  model and the strong hardening of the power law model, it could be interesting to combine the two strain hardening characters. A power law strain term  $\bar{\epsilon}_p^{C_3}$  is inserted into  $V_2$  model, and the  $V_3$  model is obtained (Eq 2.17).

$$\bar{\sigma} = \sigma_0 + C_1 (1 - \exp(-C_2 \bar{\epsilon}_p^{C_3})) \quad (2.17)$$

The final proposed  $V_3$  model is given by Eq 2.18.

$$\bar{\sigma} = \sigma_0(T) + (K_1 - K_2 T) (1 - \exp(-K_3 \exp(K_4 T) \bar{\epsilon}_p^n)) \dot{\bar{\epsilon}}_p^{\frac{m_0 \exp(m_1 T)}{p}} \quad (2.18)$$

The identification results are shown in Table 2.13 and Figure 2.26. Different from  $V_1$  and  $V_2$  model, this model gives a good flow stresses description even at the beginning of plastic deformation. The flow stresses predicted by  $V_3$  model with strain level up to 50% are shown in Figure 2.25. A saturation stress state between  $V_1$  and  $V_2$  models at high strain level is observed.

Table 2.13: The fitting parameters of  $V_3$  model

$K_1$ ( MPa )	$K_2$ ( MPa /°C )	$K_3$	$K_4$ (1/°C)	$n$	$m_0$	$m_1$ (1/°C)
245.2	0.3932	5.6066	0.002781	0.7857	0.0003087	0.02562

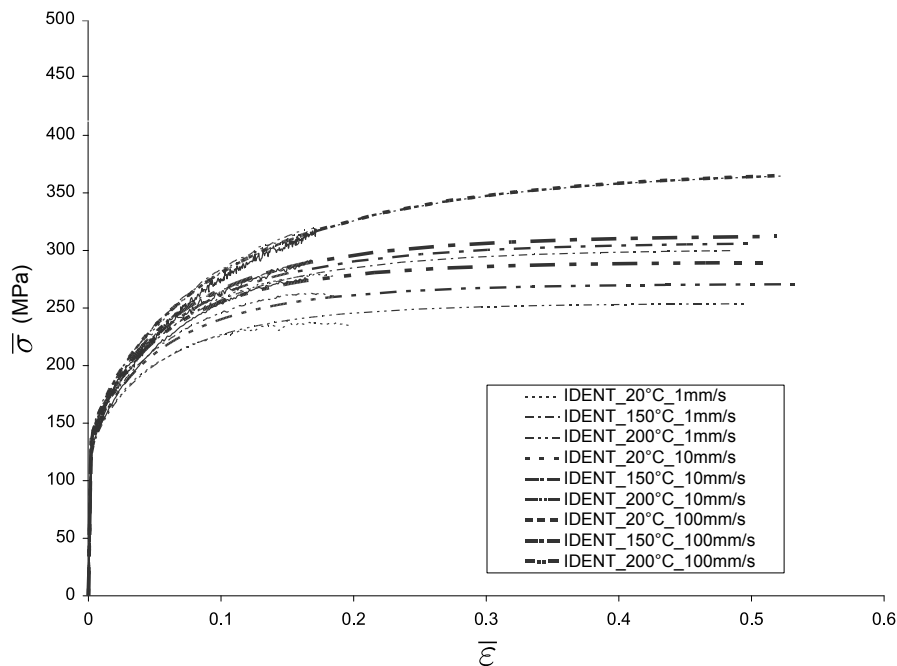
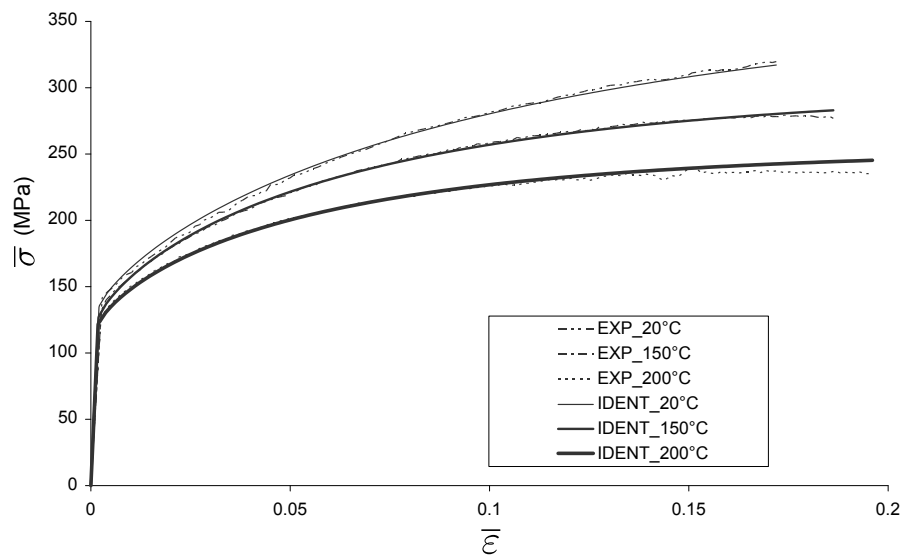
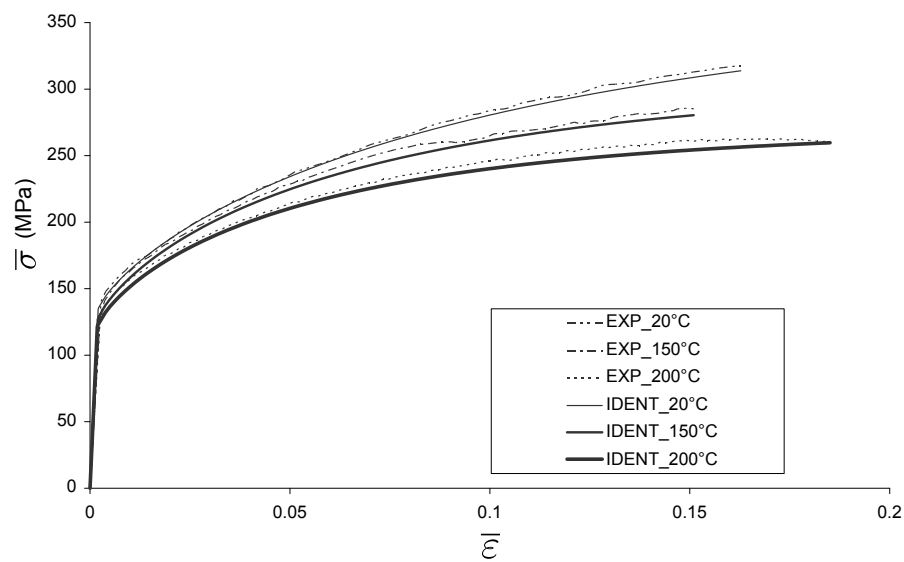


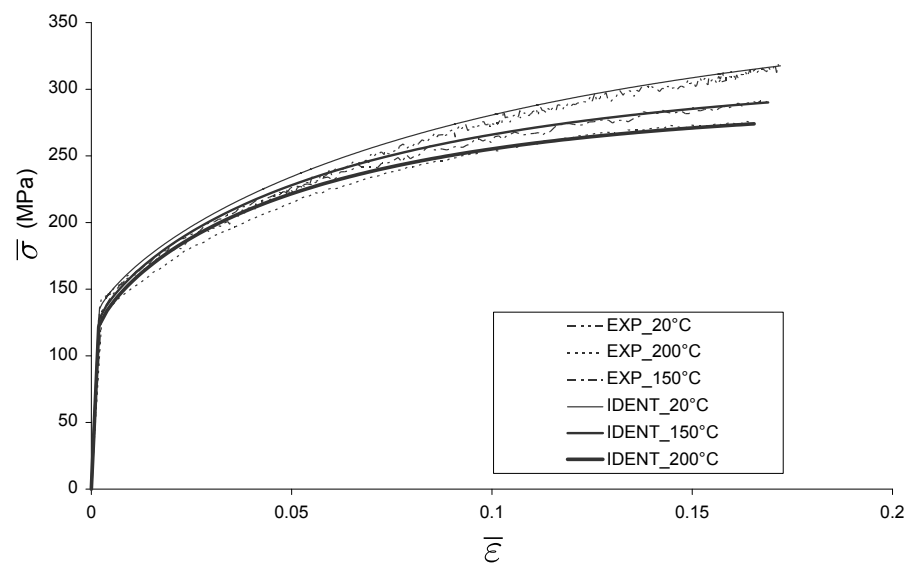
Figure 2.25: Correlation results of  $V_3$  model with strain levels up to 50%



(a) 1 mm/s



(b) 10 mm/s



(c) 100 mm/s

Figure 2.26: Correlation results of the proposed  $V_3$  model under different temperatures and strain rates

#### 2.4.4.4 Bergström model

Bergström model is also a kind of Voce type model. The extended Bergström model for AA5xxx [98] writes as:

$$\bar{\sigma} = \sigma_0 + C_1 \left[ C_2 \bar{\varepsilon}_p + (1 - \exp(-C_3 \bar{\varepsilon}_p))^{C_4} \right] \quad (2.19)$$

Where  $C_1$ ,  $C_2$ ,  $C_3$  and  $C_4$  are fitting parameters.  $C_2$  is the strain hardening parameter for large strain behavior.  $C_3$  is the strain hardening parameter for small strain behavior.

The identified parameter  $C_2$  is found to be close to 0 for each forming condition, so the function  $C_2 \bar{\varepsilon}_p$  can be neglected. Incorporating the evolutions of  $C_1$ ,  $C_3$ ,  $C_4$  and the strain rate sensitivity index  $m$ , the final proposed Bergström model is given by Eq 2.20. The identification results are shown in Table 2.14 and Figure 2.28. The flow stresses predicted by the proposed Bergström model with strain level up to 50% are shown in Figure 2.27. The results of this model and the ones from  $V_3$  are very close.

$$\bar{\sigma} = \sigma_0(T) + (K_1 - K_2 T) (1 - \exp(-(K_3 + K_4 T) \bar{\varepsilon}_p))^{(n_0 - n_1 T) \frac{\dot{\varepsilon}_p^{m_0} \exp(m_1 T)}{\bar{\varepsilon}_p}} \quad (2.20)$$

Table 2.14: The fitting parameters of the proposed Bergström model

$K_1$ ( MPa )	$K_2$ ( MPa/°C )	$K_3$	$K_4$ (1/°C)	$n_0$	$n_1$ (1/°C)	$m_0$	$m_1$ (1/°C)
223.86	0.2776	9.0706	0.01277	0.7927	0.0008054	0.0001789	0.02834

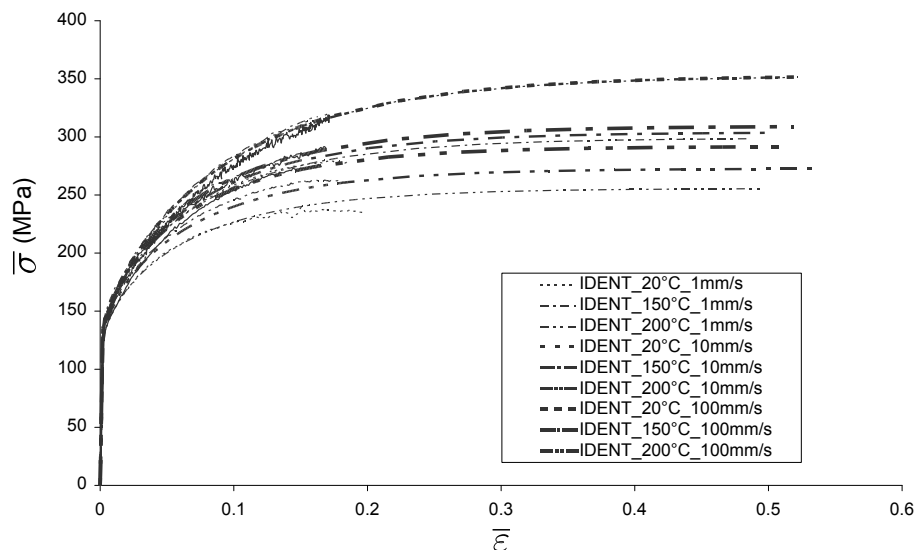
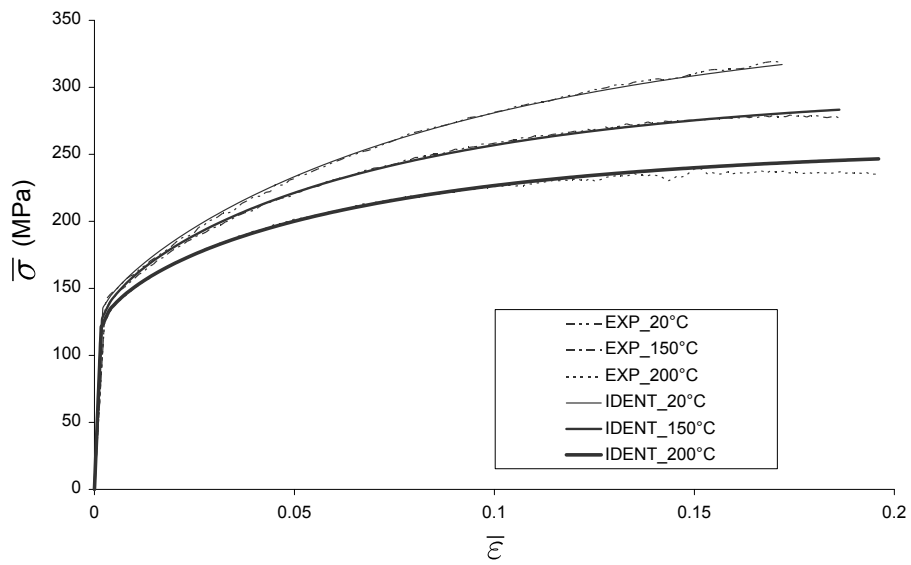
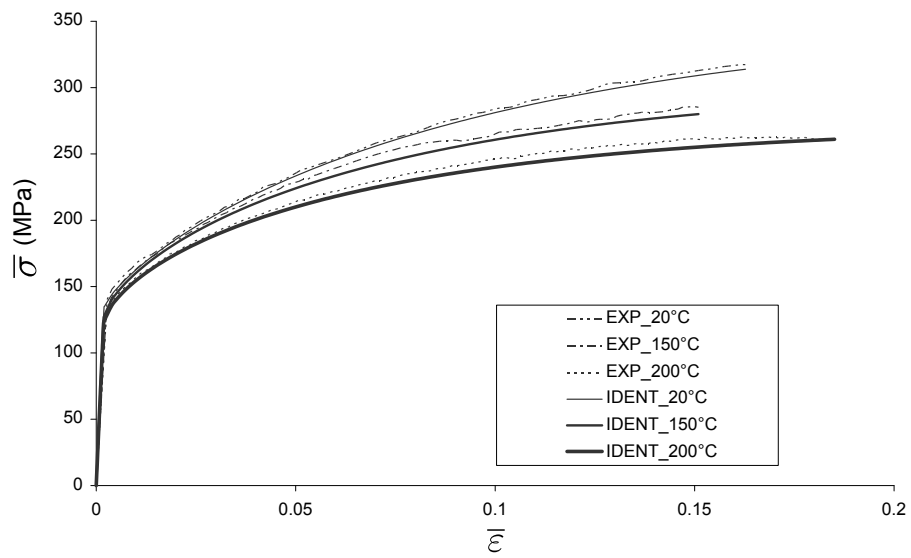


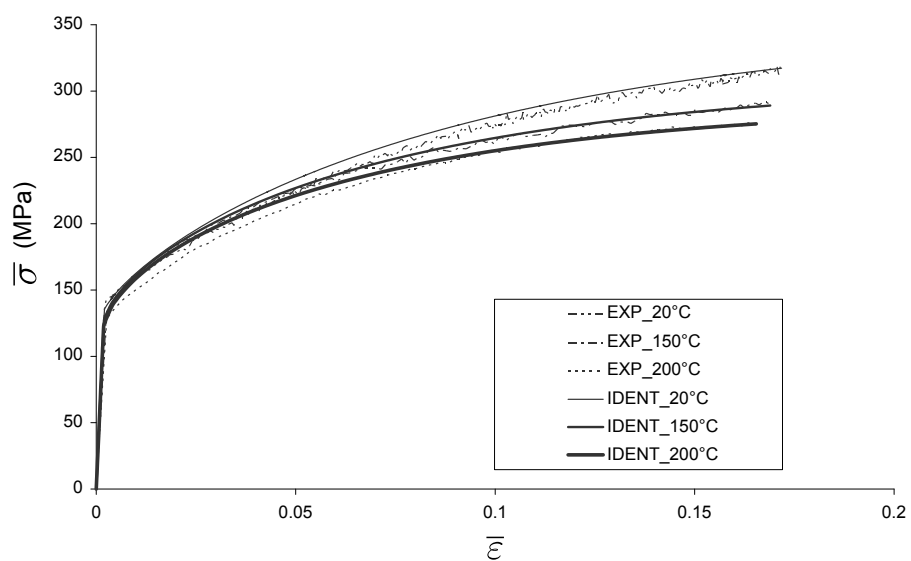
Figure 2.27: Correlation results of the proposed Bergström model with strain levels up to 50%



(a) 1 mm/s



(b) 10 mm/s



(c) 100 mm/s

Figure 2.28: Correlation results of the proposed *Bergström* model under different temperatures and strain rates

### 2.4.5 Mixed hardening model (H-V)

H-V model is described as a combination function of Hollomon and Voce model, the original formula is proposed by [95], and writes as:

$$\begin{cases} \bar{\sigma} = f(\bar{\epsilon}_p, T) \cdot v(\dot{\bar{\epsilon}}_p) \cdot h(T) \\ f(\bar{\epsilon}_p, T) = (\alpha(T) f_H + (1 - \alpha(T)) f_V) \end{cases} \quad (2.21)$$

Due to the temperature effect in function  $f(\bar{\epsilon}_p, T)$ , the identified result of  $h(T) = \exp(b/T)$  proposed in the original model is found to be close to 1 for each tensile speed. Taking into account strain rate term  $\dot{\bar{\epsilon}}_p^m$  and analyzing the evolution of  $m$  with forming temperature, the final proposed H-V model is simplified (Eq 2.22).

$$\begin{cases} \bar{\sigma} = \sigma_0(T) + (\alpha(T) f_H + (1 - \alpha(T)) f_V) \dot{\bar{\epsilon}}_p^{m_0 \exp(m_1 T)} \\ \alpha(T) = \alpha_1 - \alpha_2 (T - T_0) \\ f_H = K_1 \bar{\epsilon}_p^n \\ f_V = K_2 (1 - \exp(-K_3 \bar{\epsilon}_p)) \end{cases} \quad (2.22)$$

The identification results are presented in Table 2.15 and Figure 2.30. Compared to Ludwick model, this model gives a better description of flow stresses at the beginning of plastic deformation. The flow stresses predicted by proposed H-V model with strain level up to 50% are shown in Figure 2.29. An intermediate strain hardening character between the Power law type (Ludwick, KHL) and Saturation law type is observed.

Table 2.15: The fitting parameters of proposed H-V model

$\alpha_1$	$\alpha_2(1/^\circ\text{C})$	$K_1( \text{MPa} )$	$n$	$K_2( \text{MPa} )$	$K_3$	$m_0$	$m_1(1/^\circ\text{C})$
0.683	0.002533	633.11	0.6125	136.82	28.14	0.00009326	0.03192

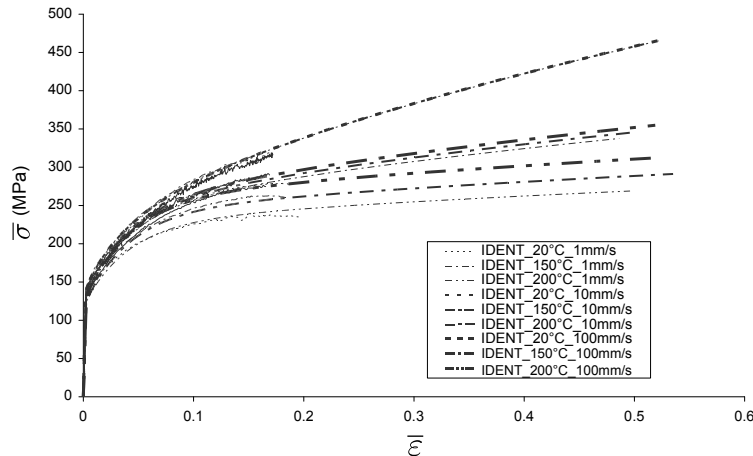
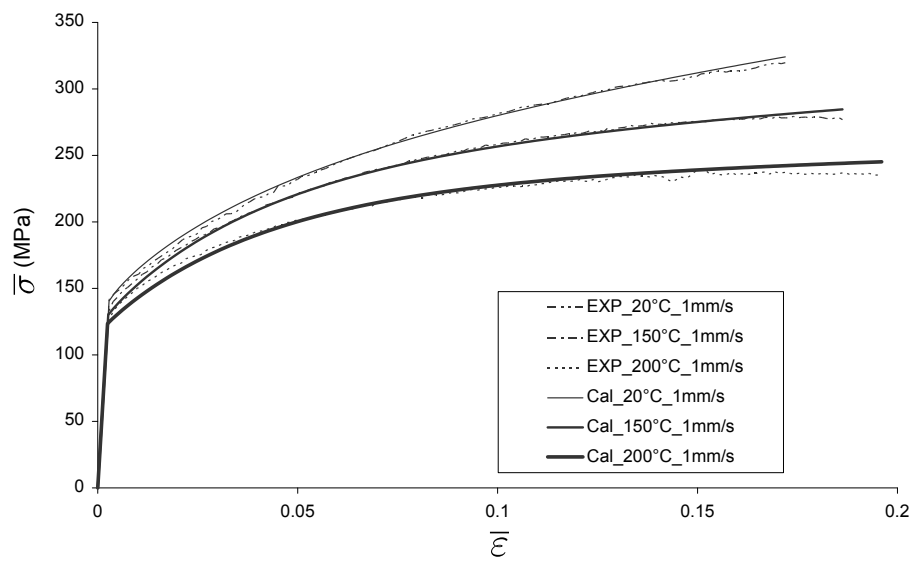
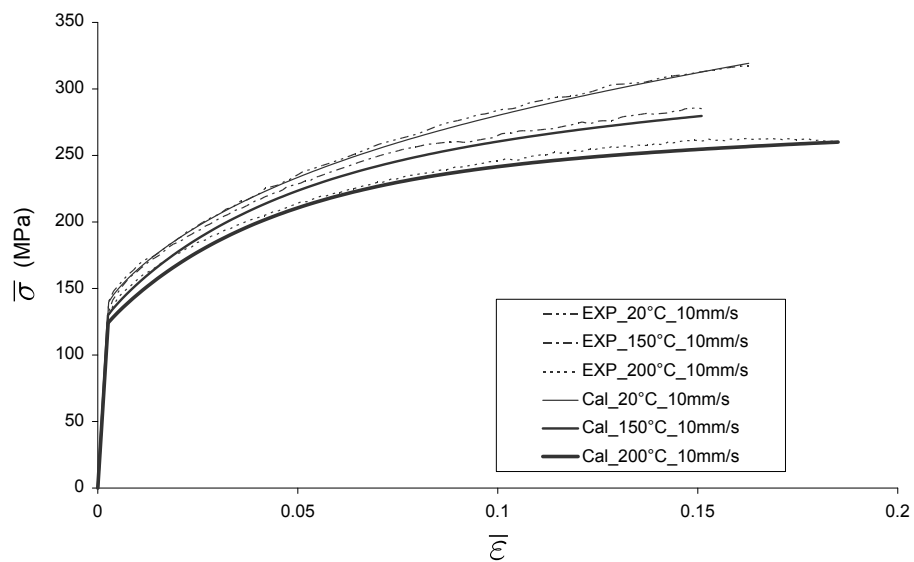


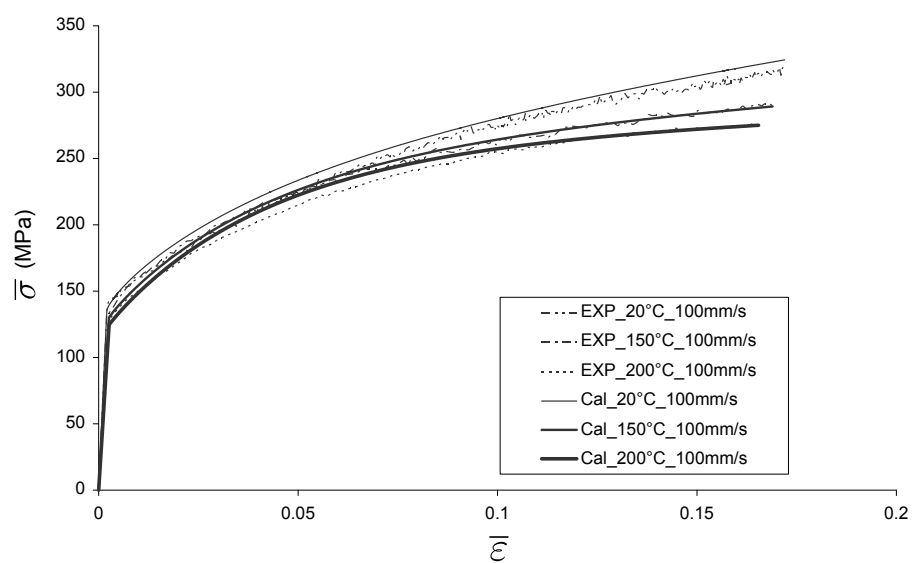
Figure 2.29: Correlation results of proposed H-V model with strain levels up to 50%



(a) 1 mm/s



(b) 10 mm/s



(c) 100 mm/s

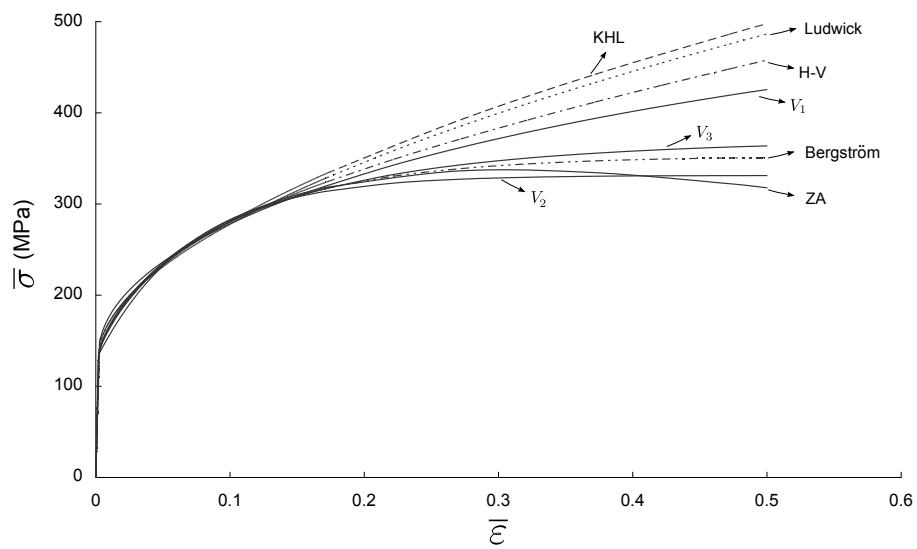
Figure 2.30: Correlation results of the proposed H-V model under different temperatures and strain rates

## 2.5 Conclusions

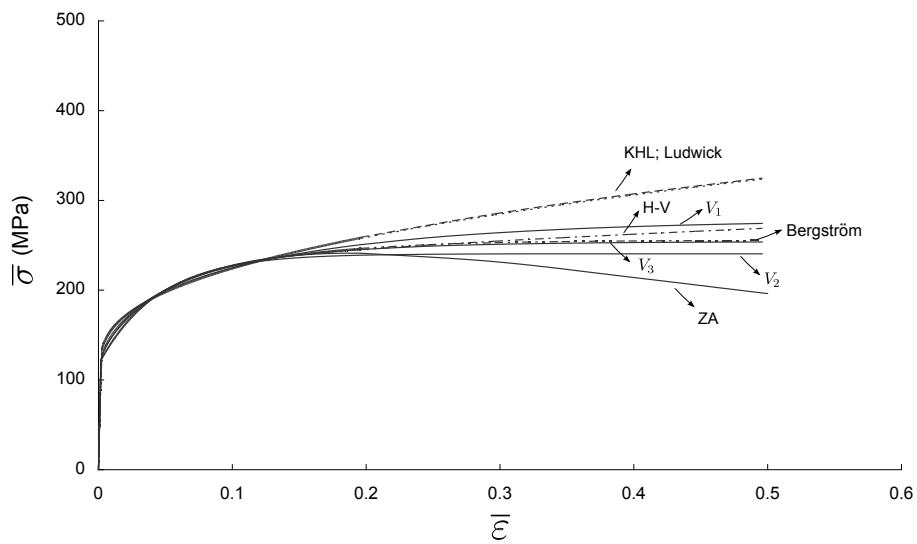
In this chapter, uniaxial tensile tests with constant section specimens are carried out under different forming speeds (1, 10 and 100 mm/s) and temperatures (20, 150 and 200°C). Flow stresses of AA5086 are directly obtained from the experimental results. From experimental observations, it is found that the material exhibits strain rate insensitivity at ambient temperature and 150°C, while it is strain rate sensitive at higher temperatures (up to 200°C). The stress level increases with increasing tensile speed. For a given tensile speed, the temperature has a negative influence on the material flow stress.

With stress-strain data, the optimized parameters are determined for eight models. The proposed models all give a reasonable description of the flow stresses within the measured strain range (below 18%). The saturation type hardening models give better correlation results at high strains, especially for high tensile speeds. For a strain level up to 50%, the hardening models previously identified exhibit very different extrapolations, as shown in Figure 2.31.

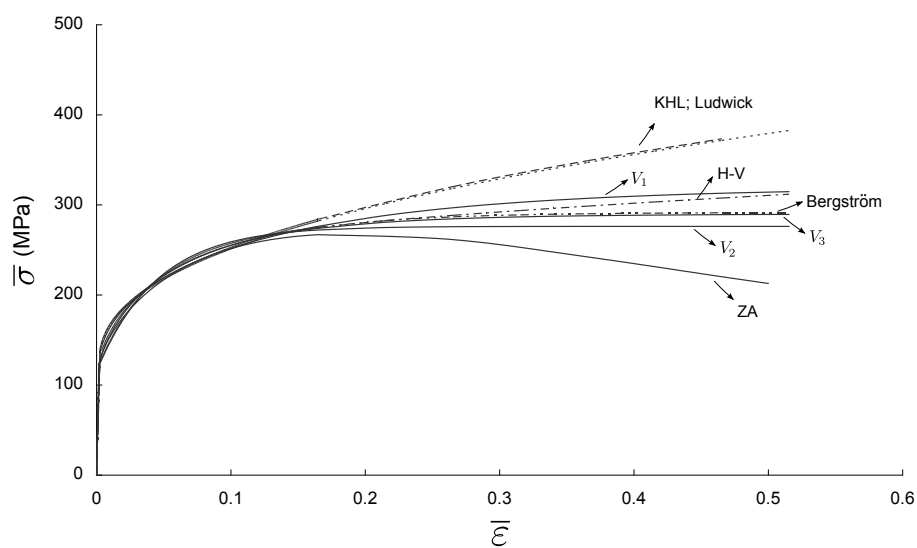
The tensile test is unable to characterize the material behavior at high strains. A clear uncertainty exists when the hardening modeling is required for the prediction of forming limit curves. The predictions of FLCs with the different hardening models and the correlation with experimental FLCs will give further information on the validity of these laws.



(a) 20°C at 1 mm/s



(b) 200°C at 1 mm/s



(c) 200°C at 100 mm/s

Figure 2.31: Flow stresses predicted by different hardening models with strain level up to 50%.



## Chapter 3

# Experimental investigations of sheet formability under different temperatures and strain rates



*La validation d'un modèle prédictif des courbes limite de formage intégrant les effets de la température et de la vitesse de déformation nécessite une base expérimentale suffisamment large et précise. Un dispositif de type Marciniak a été choisi pour caractériser la formabilité de l'alliage d'aluminium 5086 pour ces conditions opératoires. La mise en température des éprouvettes se fait par conduction, grâce à des cartouches chauffantes placées à l'intérieur des serre-flans. La mesure des déformations dans le plan de l'éprouvette est assurée tout au long de l'essai grâce à une caméra haute résolution couplée à un logiciel de corrélation d'images.*

*Lors de la caractérisation expérimentale de courbes limite de formage, le choix du critère permettant de détecter l'apparition de la striction est critique. Les valeurs des limites de formabilité sont en effet fortement dépendantes de ce choix. Plusieurs critères sont comparés et discutés, le critère spatial basé sur la norme ISO 12004-2 est finalement retenu de par sa robustesse et sa facilité d'utilisation.*

*Les essais ont été réalisés à température ambiante et pour des températures de 150 et 200°C. Trois vitesses de poinçon ont été retenues : 0.1, 1 et 10 mm/s, ces vitesses conduisent respectivement à des vitesses de déformation dans l'éprouvette de l'ordre de 0.02, 0.2 et 2 s<sup>-1</sup>. Les courbes limite de formage obtenues montrent un effet certain de la température et de la vitesse de déformation sur la formabilité du matériau étudié. Pour une vitesse donnée, l'augmentation de la température tend à améliorer la formabilité, cet effet est amplifié lorsque la vitesse de déformation décroît. Globalement, l'effet de la température et de la vitesse de déformation consiste en une « translation » des courbes limite de formage suivant l'axe des déformations majeures, leur forme générale étant peu modifiée quel que soit le chemin de déformation testé.*



### 3.1 Introduction

In the literature, several analytical and numerical models have been proposed to study the sheet formability of aluminium alloys. In order to verify their reliability, it is essential to get dependable experimental data. In the international standard ISO 12004-2 [1], Nakazima and Marciniak tests are proposed to determine the forming limit curves of sheet metal. It is shown in Figure 3.1 that two high-resolution cameras are required to capture the out-of-plane deformation for Nakazima test while only one camera is enough to measure the deformation of flat zone in Marciniak test.

Due to the in-plane deformation character of Marciniak test, the process of the image data is easier, especially under high forming speeds. Besides, for the Marciniak test, there is no contact and then friction between the punch and the central zone where the strain localization develops. Considering the reasons above, Marciniak test is chosen and used in this study.

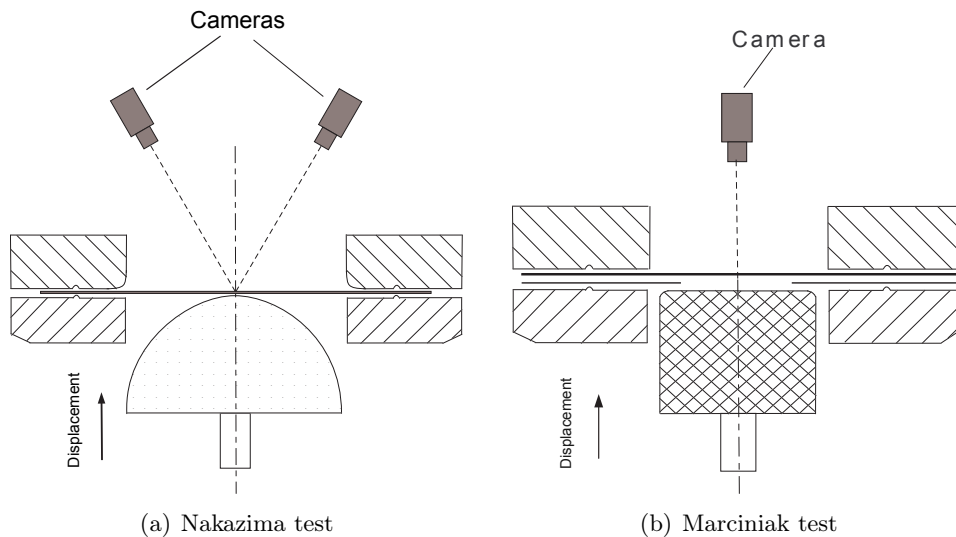


Figure 3.1: Comparison of Nakazima and Marciniak tests

In this work, an existing Marciniak device is modified to study the formability of AA5086 under different temperatures and forming speeds. The images of the specimen during the test are recorded and the digital image correlation (DIC) method is used to analyze the specimen deformation under the different forming conditions.

Several failure criteria are proposed and compared to determine the forming limit strains of AA5086. By choosing a proper failure criterion, the FLCs of AA5086 under the different forming conditions are obtained and the effects of temperature and strain rate on the sheet formability are discussed.

### 3.2 Experimental Marciniak test

To carry out the Marciniak tests under different temperatures and analyze the deformation of the specimen, the equipments adopted in this work are introduced hereafter.

### 3.2.1 Marciniak heating apparatus

The cross section of Marciniak test used in this work is shown in Figure 3.2, the part dimensions are shown in Table 3.1. The current Marciniak test setup is designed as a proportional model to the proposed dimensions in Standard ISO 12004-2, it is much more compact in order to facilitate the tests under high forming speeds.

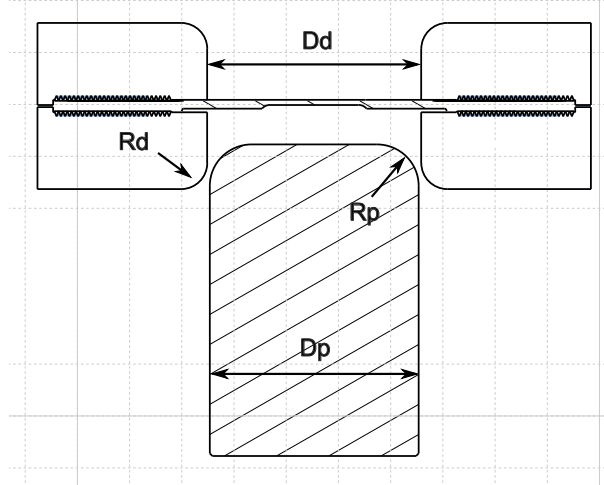


Figure 3.2: Cross section of Marciniak test

Table 3.1: Part dimensions of Marciniak test

Punch diameter $D_p$	Punch nose radius $R_p$	Die diameter $D_d$	Die radius $R_d$
40 mm	8 mm	43.8 mm	5 mm

A dedicated heating system is designed to study the temperature influence on the formability. As shown in Figure 3.3, eight heaters are plugged into the up and bottom blankholders, the specimen is heated by heat conduction. To improve heating efficiency, a sheet of mica is inserted between the die and the bottom-blankholder to reduce heat conduction with the die. Due to high heat conductivity of aluminium, the specimen temperature can be reduced when it is in contact with the punch. To ensure constant temperature in the specimen during the test, an additional heater is inserted into the punch. One heater in the blankholder and the heater in the punch are both associated with two thermocouples in order to ensure temperature regulation from two independent PID temperature controllers (respectively controller-2 and controller-1). To test the validity of the heating system, external thermocouples are stucked to the specimen and punch to measure the evolution of temperature.

For a given specimen, with the external stucked thermocouples, many temperature tests are carried out. Linear relationships between the setting values in the controllers and the temperatures in specimen and punch are obtained. For example, as shown in Figure 3.4, with setting values of 182°C in controller-1 and 172°C in controller-2, the desired temperature of 150°C in the specimen and the punch is obtained. It is confirmed by temperature tests that after being heated for a certain time, the temperature distributions in the specimen and the punch are homogeneous. This procedure has been validated for different specimens. The

setting values in the controllers and the final temperatures in the specimens as well as the heating time are shown in Table 3.2.

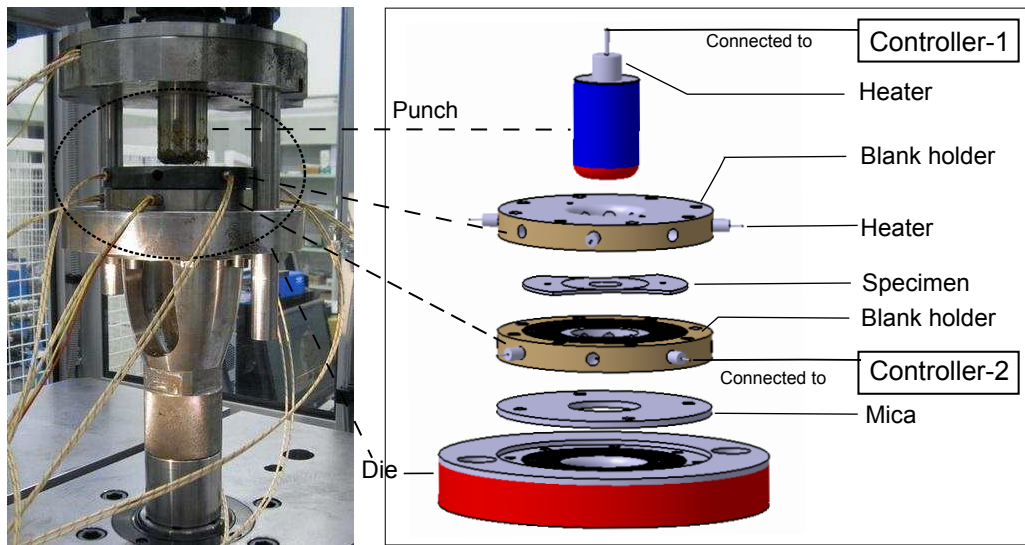


Figure 3.3: Marciniak heating apparatus

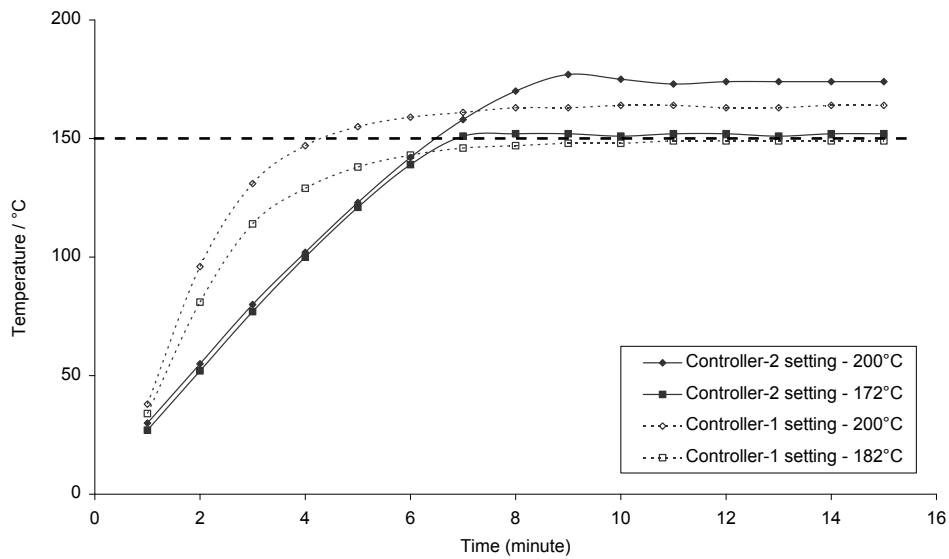


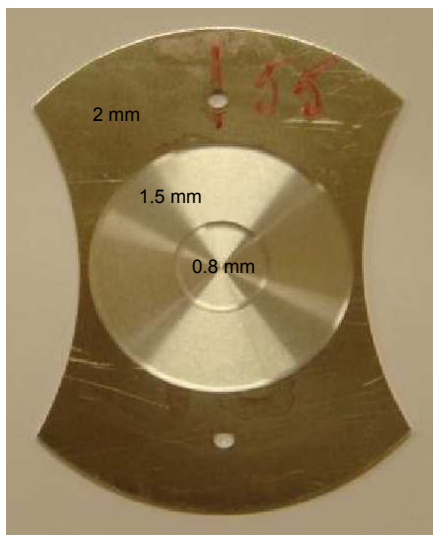
Figure 3.4: Temperature evolutions in the punch and specimen

### 3.2.2 Specimen geometry

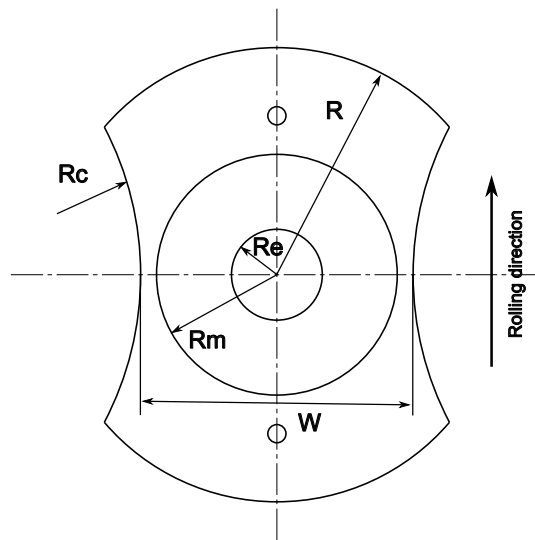
A typical specimen example and its geometries are shown in Figure 3.5. All the specimens are machined with the same orientation of the rolling direction (Figure 3.5(b)). The related dimensions are given in Table 3.3.

Table 3.2: Temperature parameters in the heating system

Controller-1 (°C)	Heating time (min)	Punch (°C)
182	8	150
245	12	200
Controller-2 (°C)	Heating time (min)	Specimen (°C)
172	8	150
231	12	200



(a) Typical specimen



(b) Specimen geometry

Figure 3.5: Typical specimen example

Table 3.3: Specimen dimensions of Marciniak test

W (mm)	10	20	30	40	45	48	50	52	55	58	60	80	100
R (mm)							50						
Rc (mm)							70						
Rm (mm)							26.5						
Re (mm)							10						

In Marciniak test, for a specimen with a constant width, a limit strain point corresponding to a fixed strain path on the FLC can be determined. By changing the specimen widths, different strain paths can be obtained. The whole FLC under different strain paths, from uniaxial stretching over plane strain condition to biaxial stretching is built as shown in Figure 3.6.

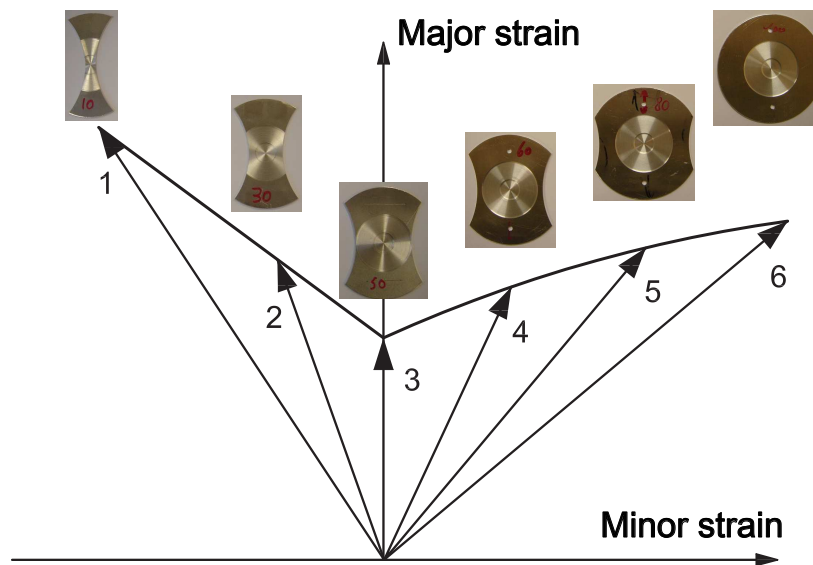


Figure 3.6: Different strain paths on the FLC

Different from ISO 12004-2, the specimen adopted in this work is designed with a non-uniform thickness (Figure 3.5(a)). The central part has a thickness of 0.8 mm, the adjacent part 1.5 mm and the clamping part is set to 2.0 mm. This design is used to ensure a strain localization in the central zone. For the same material (AA5086), Zidane [109] has shown a very few influence of the machining on the sheet metal formability.

During Marciniak test, lubrication is used to reduce frictions between the punch and die radius. Silicone grease is used when temperature passes 150°C. A temperature range up to 200°C is chosen in this work. As it will be seen, this temperature is sufficient to produce a noticeable effect on formability. Using the equipments above, Marciniak tests are carried out with a servo-hydraulic test machine (maximum load capacity of 250 kN) at temperatures of 20, 150 and 200°C and punch speeds of 0.1, 1 and 10 mm/s. The corresponding strain rates in the specimen for these forming speeds are about 0.02, 0.2 and 2 s<sup>-1</sup>.

### 3.2.3 Image acquisition system

The image acquisition system includes a high speed resolution camera, an optical mirror and an external illumination source. The schematic view of the system is shown in Figure 3.7 and the experimental system is shown in Figure 3.8. This distance between the mirror and the specimen is constant through the test.

In order to analyze the deformation with the recorded images, all the specimens are sprayed with a white paint as the background and black dots are sprayed on its surface. With this method, the specimen with a speckle pattern is generated as shown in Figure 3.9. It has been proved that all the paintings remain adherent during the tests below 200°C.

The high speed camera used in this work is a FASTCAM ultima APX-RS digital CMOS camera manufactured by Photron with a full mega pixel resolution (1024×1024 pixels) and frame rates from 50 to 3000 frames per second. The external cold light source is used to capture good specimen images and it does not affect specimen temperature during the test. The configuration parameters of CMOS camera are set according to the forming speed and

external illumination source as shown in Table 3.4.

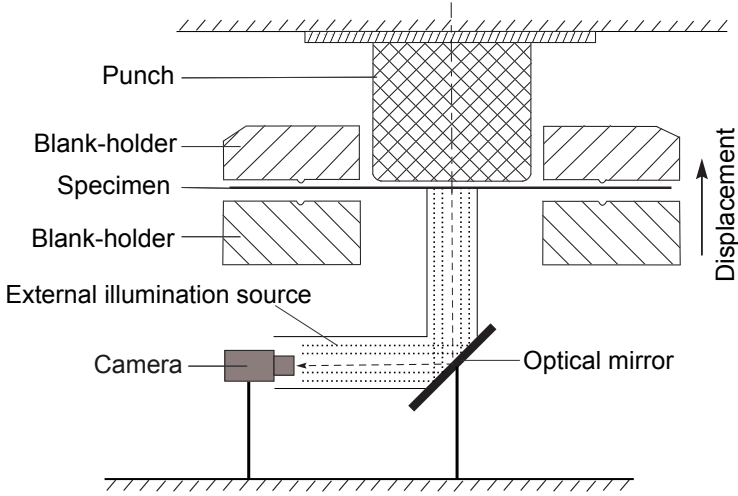


Figure 3.7: Schema of the acquisition system

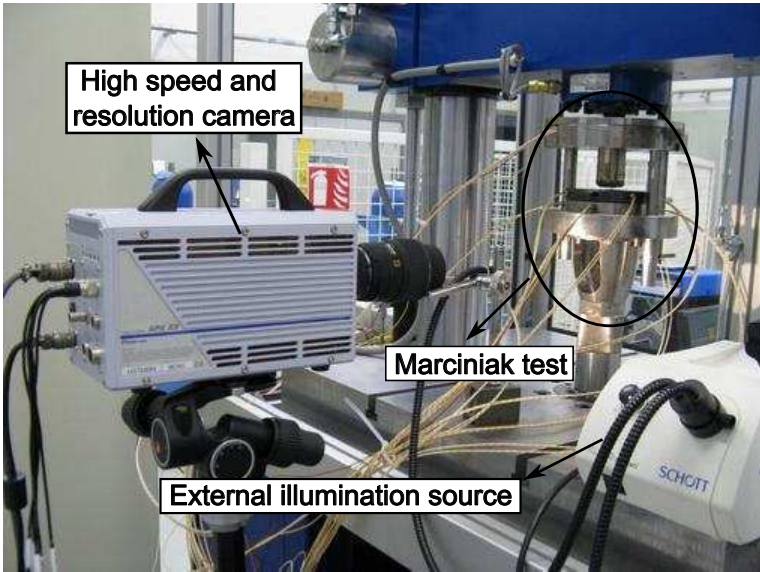


Figure 3.8: Experimental acquisition system

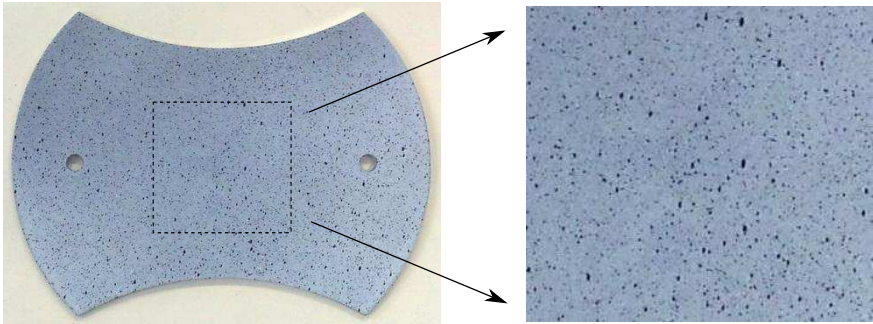


Figure 3.9: Specimen painted with a speckle pattern

Table 3.4: Configuration parameters in the CMOS camera

Punch speed (mm/s)	resolution (mm)	resolution (pixel)	shutter speed (image/s)
0.1	34.0×29.8	512×448	50
1	34.0×29.8	512×448	60
10	34.0×29.8	512×448	500

### 3.2.4 Strain analyzing

The schema of the DIC principle is shown in Figure 3.10. During Marciniak test, the captured zone with random pattern can be represented by a discrete function: the gray level (value between 0 and 255). The zone is divided into small squares called 'subsets' and these subsets are characterized by their unique gray level so that the system can recognize and locate a given subset in different images. With the reference and sequential deformed images, the displacement and trajectory fields can be determined by a correlation program.

The correlation analysis is carried out by the commercial digital imaging program software CORRELA 2006 developed by LMS at the University of Poitiers. Different zones on the image are defined to execute image correlation according to the use of different criteria to detect forming limits. Take the criterion ISO 12004-2 as an example (described hereafter), a rectangular section across the localization zone (containing the crack) is taken on the reference image as shown in Figure 3.11.

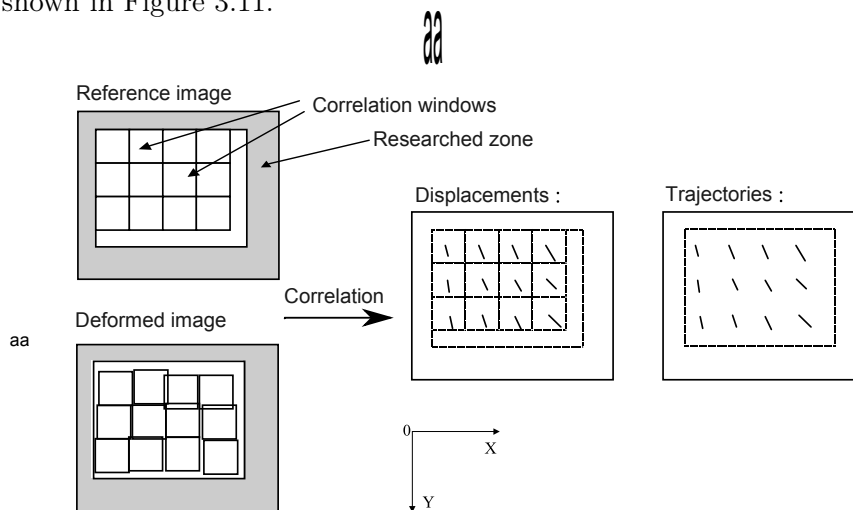


Figure 3.10: DIC principle

FFT (Fast Fourier Transform) correlation method and “Lagrange” strain equations for large strain calculation method are selected in CORRELA 2006. The subset dimensions are presented in Figure 3.12. L and H define the size of subset, D and E denote the distance between two sequential subsets in the X and Y direction.

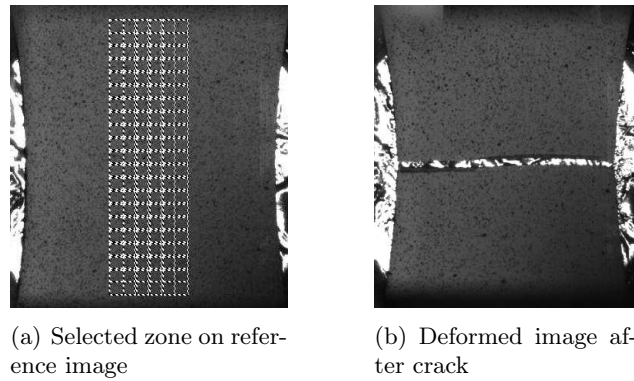


Figure 3.11: Selected zone for correlation analysis

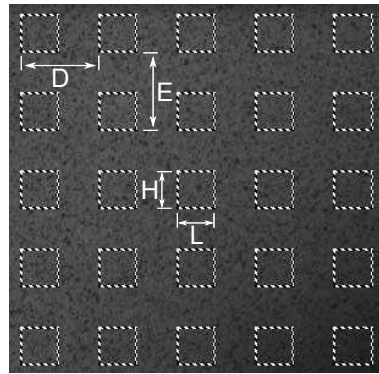


Figure 3.12: Subset dimensions

In Correla 2006, the geometries for strain calculation can be described by two ways: 'X' and 'L'. Figure 3.13 shows the geometry in 'X' which is used in current work. By setting different interval values, in-plane strains are calculated at the center of selected subsets.  $L$  and  $H$  are both set to 32 pixels (2.128 mm). In order to obtain more strain points with DIC method,  $D$  and  $E$  are both set to 4 pixels (0.266 mm). To smooth the strain values, the interval value is set to 8. With this configuration, the correlation results can provide the in-plane initial and current positions and the strains for each subset at different instant times.

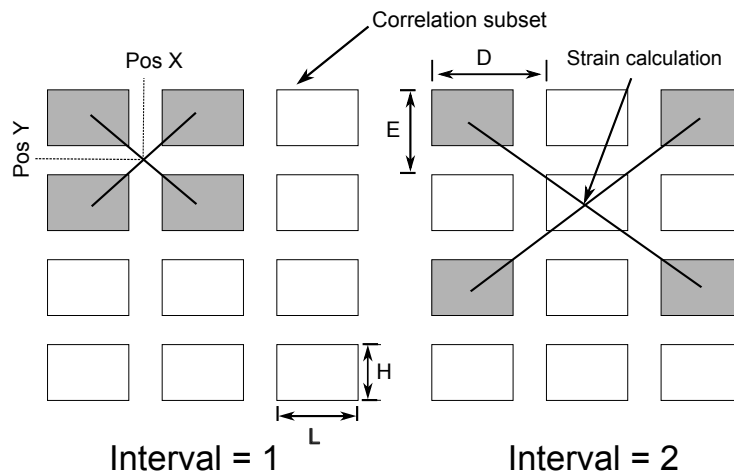


Figure 3.13: Geometry models for strain calculation

### 3.3 Failure criteria to determine the forming limit strains

For determining FLCs, the choice of the criterion to detect the onset of localized necking is critical. As briefly introduced in chapter 1, several temporal and spatial criteria have been proposed to determine the limit values from the measurement of local or global data. In this part, different failure criteria are compared and discussed for a given specimen (40 mm width at 150°C and 10 mm/s).

#### 3.3.1 Strain increment ratio

This criterion is widely used in the M-K theory, due to its simplistic definition. It is a temporal criterion based on the different strain evolutions in the necking and adjacent zones. Two points (one point B in necking zone and one point A in adjacent zone) on the specimen are chosen. After strain localization, the strain divergence between the two zones accelerates as shown in Figure 3.14. When major true strain increment ratio ( $\Delta\varepsilon_{Major}^B / \Delta\varepsilon_{Major}^A$ ) exceeds a certain value (7 is proposed by Zhang [105]), necking is assumed to occur and the corresponding major and minor strain of point B at this time is noted as one point on the FLC as presented in Figure 3.15.

Nevertheless, with this method, the positions of point A and B and the interval time value used to calculate strain increment ratio both affect the limit strain values. With the same selected points, the limit strain values determined with different interval times are shown in Table 3.5. With the increase of interval time, a weak forming limit value increase is observed. The limit strains with a  $\Delta t$  of 0.01 s gives the most conservative result. This interval time  $\Delta t = 0.01$  s is kept in the following comparisons.

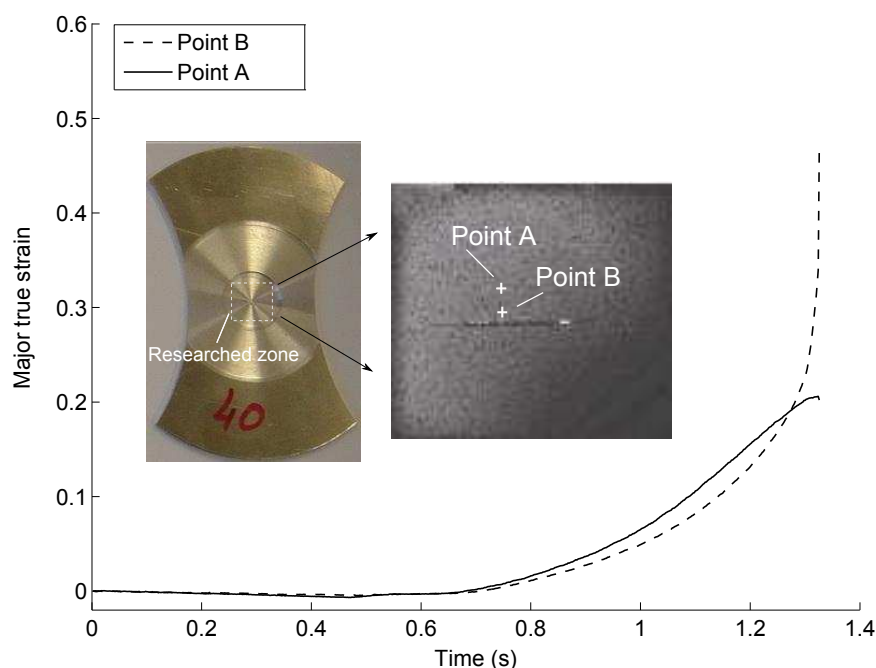


Figure 3.14: Major true strain evolution of different zones

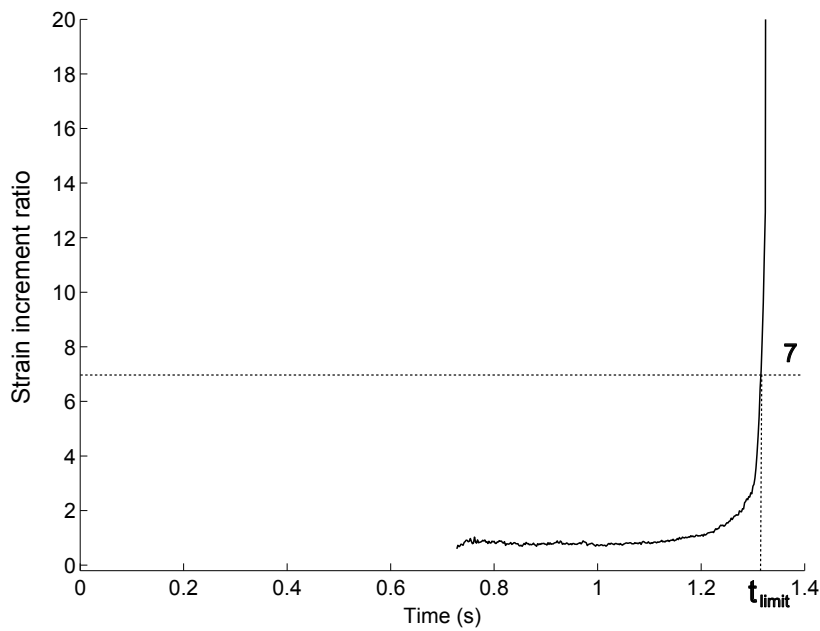


Figure 3.15: Strain increment ratio criterion

Table 3.5: Forming limit values with different interval times

Interval time (s)	$t_{limit}$ (s)	Major strain	Minor strain
0.01	1.307	0.2448	-0.0385
0.02	1.309	0.2566	-0.0395
0.03	1.312	0.2682	-0.0404
0.04	1.316	0.2856	-0.0405

### 3.3.2 ISO 12004-2 standard

This method is introduced in detail within the international standard ISO 12004-2, it is also called “cross section” or “position-dependent” measurement method. This spatial criterion is based on the strain distributions in the sample before the occurrence of a crack.

As shown in Figure 3.16, a relevant cross section containing the crack is chosen to analyze strain distribution. To allow a reproducible evaluation, three sections are selected and the sections should be perpendicular to the crack as much as possible. The position values  $X(m)$  and the strains ( $\varepsilon_{11}$ ,  $\varepsilon_{22}$ ) for each section point on the specimen surface can be obtained with DIC method.

The principle of ISO 12004-2 is that, with a fit window of selected principal strain values ( $\varepsilon_{22}$ ,  $\varepsilon_{11}$ ) on both sides of the necked area for a necked but not cracked specimen, a second order inverse polynomial function ( $f(x) = 1/(ax^2 + bx + c)$ ) is fitted to determine the limit strain values at the onset of necking. The crack position can be determined by the maximum value of the parabola.

With correlation data, the major strain distributions of selected sections on the specimen

before the occurrence of crack is shown in Figure 3.17, a bell-shape strain distribution curve is obtained. For these strain evolutions, a procedure of a second derivative is applied. The inner boundary of the fit window is defined by the point with the maximum peak of the second derivative at each side of the crack (Figure 3.18).

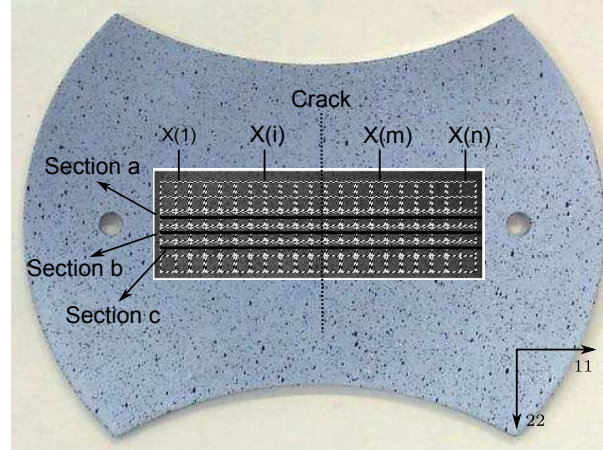


Figure 3.16: Cross sections proposed in ISO 12004-2

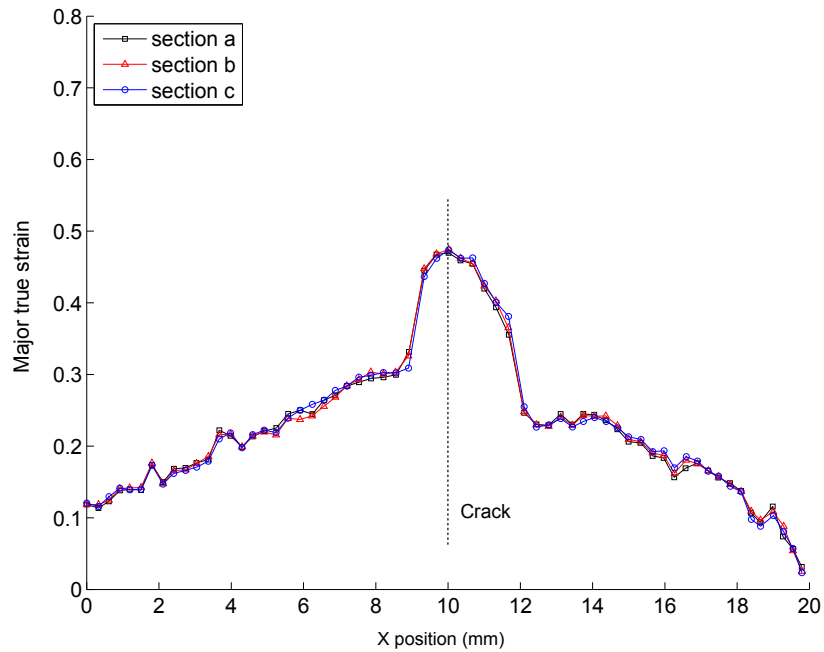


Figure 3.17: Profile of major strain distribution

To find the outer boundary of the fit window, ISO 12004-2 defines the fit window width  $W$  for each side in Eq 3.1.

$$\begin{cases} W = 4 [1 + (\bar{\varepsilon}_{22}/\bar{\varepsilon}_{11})] \\ \bar{\varepsilon}_{22} = 1/2(\varepsilon_{22,Bl} + \varepsilon_{22,Br}) \\ \bar{\varepsilon}_{11} = 1/2(\varepsilon_{11,Bl} + \varepsilon_{11,Br}) \end{cases} \quad (3.1)$$

Where  $(\varepsilon_{22}, \varepsilon_{11})$  are the principal strain values of inner point at each side,  $Bl$  stands for

left inner boundary and  $Br$  stands for right inner boundary (Figure 3.18)

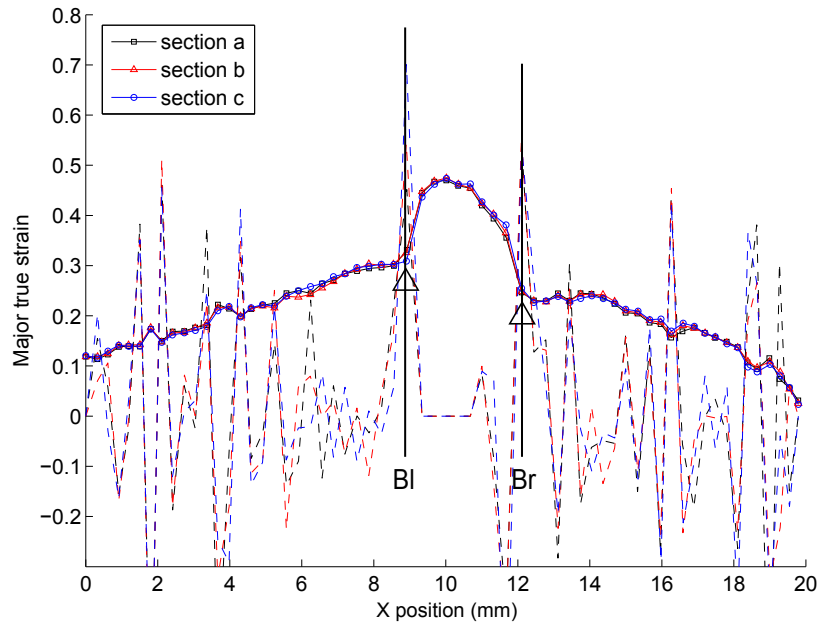


Figure 3.18: Determination of the inner boundary of the fit window

The thickness true strain is  $\varepsilon_{33} = -\varepsilon_{11} - \varepsilon_{22}$  based on the volume constancy. Making use of the inverse best-fit parabola ( $f(x) = 1/(ax^2 + bx + c)$ ) of the strain points over the defined fit window on each side of the bell-shape curve, the maximum of the inverse parabola are determined as the limit strains ( $\varepsilon_{11,limit}$ ,  $\varepsilon_{33,limit}$ ) as shown in Figure 3.19. The limit strain  $\varepsilon_{22,limit}$  is obtained by  $\varepsilon_{22,limit} = -\varepsilon_{11,limit} - \varepsilon_{33,limit}$ . For each section, one pair ( $\varepsilon_{11,limit}$ ,  $\varepsilon_{22,limit}$ ) can be obtained, the average value of the three sections is taken as one point of the FLC.

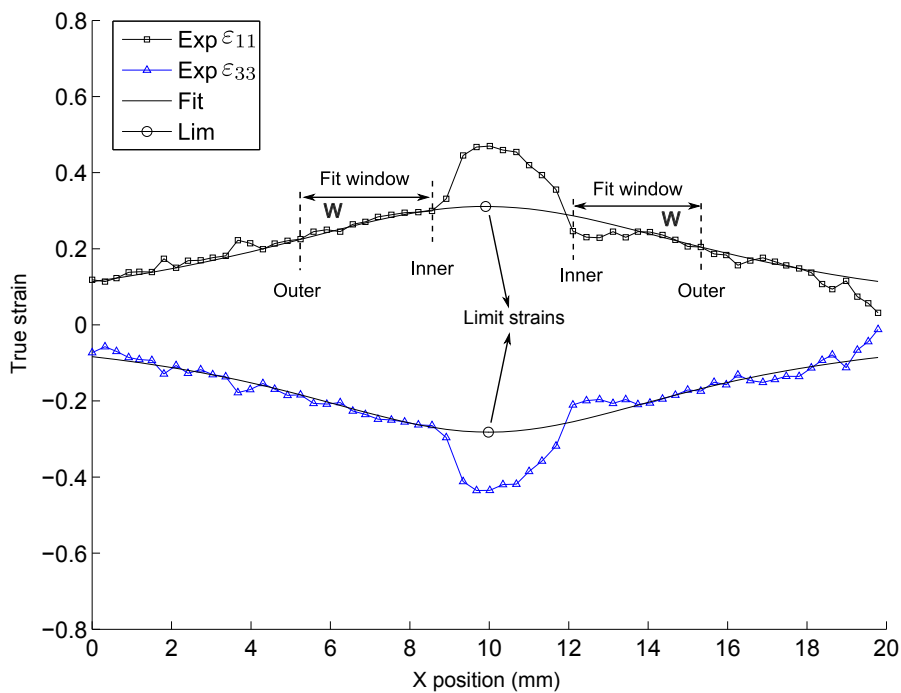


Figure 3.19: Example of inverse fit parabola to determine the limit strains

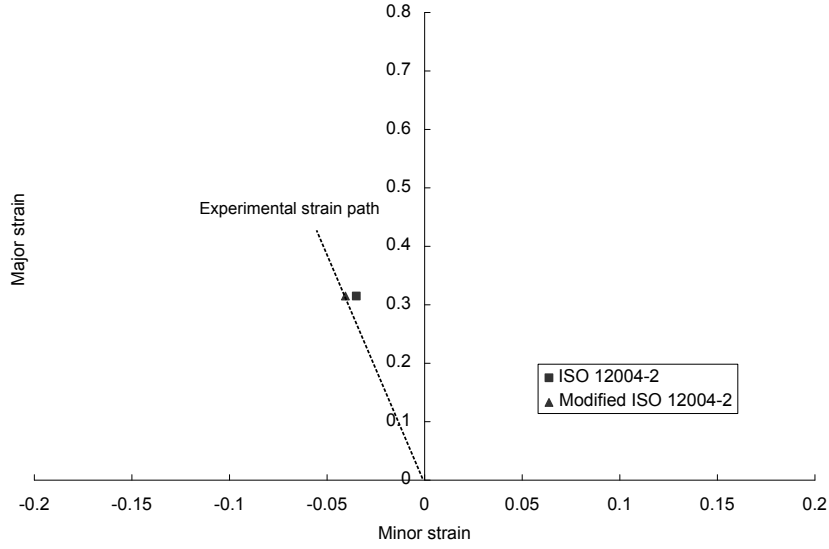


Figure 3.20: Limit points obtained with ISO 12004-2 and the modified method

Table 3.6: Limit strains obtained by ISO 12004-2 and modified method

Method	Major strain	Minor strain
ISO 12004-2	0.3149	-0.035
Modified ISO 12004-2	0.3149	-0.041

In ISO 12004-2, the fitting procedures of  $\varepsilon_{11}$  and  $\varepsilon_{33}$  are independent and  $\varepsilon_{33}$  is determined indirectly from the measured values of  $\varepsilon_{11}$  and  $\varepsilon_{22}$ . It is found that the determined strain path  $\beta = \varepsilon_{22,limit}/\varepsilon_{11,limit}$  does not always correspond to the measured strain path ( $\beta_{exp}$ ), especially around plane strain condition, when  $\varepsilon_{22}$  is small. To limit this data scatter, a modified strain path method is proposed. The limit strain  $\varepsilon_{22,limit}$  is determined directly by the measured strain path ( $\beta_{exp}$ ), with the relation  $\varepsilon_{22,limit} = \beta_{exp} \cdot \varepsilon_{11,limit}$ . The limit strains obtained by ISO 12004-2 and the modified strain path method are shown in Figure 3.20 and Table 3.6. For the following work, the modified method is kept.

### 3.3.3 Time dependent analysis method

It is introduced in ISO12004-2 that a “time dependent” method is under development. In the literature, a so-called time continuous evaluation method is proposed by [70]. This method is based upon a trend analysis of strain rate in the area of necking and subsequent cracking.

With the image before crack, the distribution of major strain is obtained as previously shown in Figure 3.17. The point with the highest major strain value is chosen to start the evaluation, a mean value of three sections as introduced in ISO 12004-2 is calculated to stabilize the measurement.

The different steps of this time-dependent method are shown in Figure 3.21. Major strain and major strain rate show a homogeneous evolution at the beginning of deformation. At the onset of necking, the two values both present a drastic increase. The evolution of the

acceleration of major strain is linear at the beginning of deformation (Figure 3.21(c)), followed by a drastic increase. A linear regression coefficient of the major strain acceleration is then calculated. With an ongoing homogeneous plastic deformation, the values of the linear regression coefficient start to increase, reaching a maximum value at the onset of necking. After necking, the acceleration of major strain increases drastically and the linear regression coefficient decreases. The maximum value of the linear regression coefficient curve indicates the time for the onset of necking (Figure 3.21(d)) and the corresponding major and minor strain values at this time are taken as one point of the FLC.

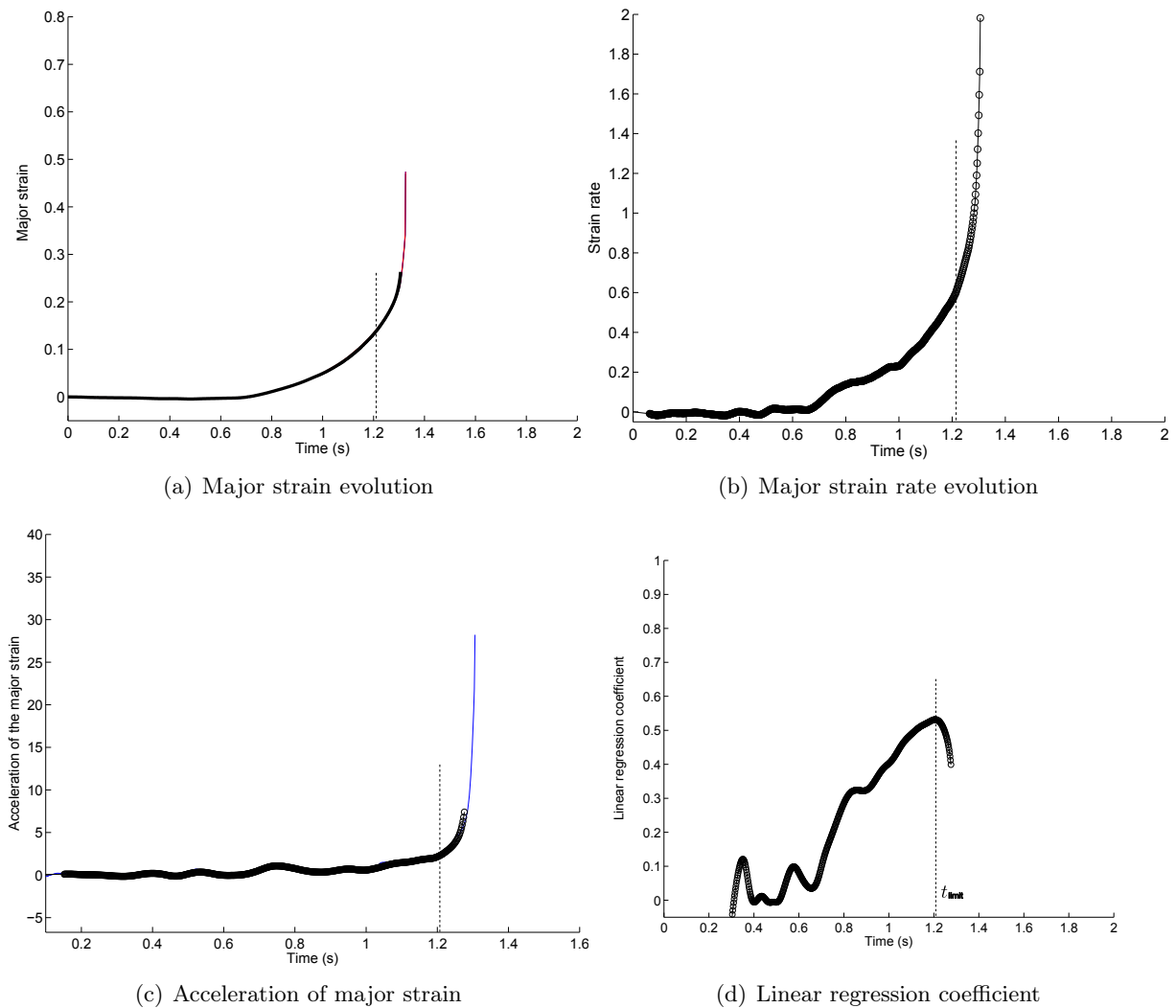


Figure 3.21: Time dependent method

### 3.3.4 Maximum punch force

During Marciniak test, the punch force is recorded by a conventional load cell with resistive strain gauges, as shown in Figure 3.22. Simultaneously the specimen deformation is recorded by the high speed camera. The punch force shows a sharp increase until its maximum value and abruptly decreases as soon as failure appears into the sheet. Hence, the force value can be used as a global criterion to determine the limit strain. The selected sections presented in ISO 12004-2 are chosen. The maximum strain values in the selected zones corresponding to time  $t_{limit}$  (the maximum force time) are obtained from the strains calculated by DIC method.

The average values of the three maximum strain values are noted as the limit strains.

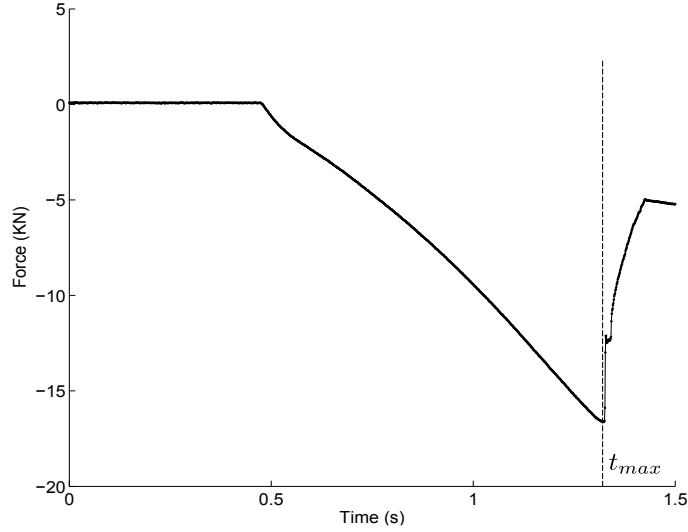


Figure 3.22: Force evolution during Marciniak test

### 3.3.5 Discussion

For the given specimen of 40 mm width, the limit strains and corresponding instants determined with the different failure criteria are summarized in Table 3.7. The results show that the limit strains are clearly dependent on the failure criteria. The time dependent criterion gives the smallest determined instant value and the force criterion gives the biggest. The equivalent strain distributions in the necking zone (Figure 3.14) corresponding to the different instants of Table 3.7 are shown in Figure 3.23. For time dependent analysis criterion, the strain localization is not clear, but for force criterion the onset of necking is clearly observed.

Table 3.7: Limit strain and corresponding instants with different criteria

Methods	t (s)	Major strain	Minor strain
Strain increment ratio	1.307	0.2448	-0.0385
ISO 12004-2	1.321	0.3149	-0.035
Time dependent	1.203	0.1344	-0.0293
Maximum Force	1.323	0.3174	-0.0405

The FLCs of AA5086 at 150°C and 10 mm/s determined with the different failure criteria are shown in Figure 3.24. Several conclusions can be drawn:

- The time dependent criterion gives very conservative results. As introduced in [70], this criterion is well adapted for material with a distinctive necking before cracking. For material AA5086, the criterion may detect the diffuse necking instead of the localized necking which leads to a conservative FLC result. After diffuse necking, the sheet metal continues to be deformed until the onset of localized necking.

- The strain increment ratio criterion gives too much scattered data in uniaxial and plane strain zones. For this criterion, only one point in the necking zone is chosen. The choices of point position, interval time  $\Delta t$  and strain increment critical value all affect the limit strain values.
- The global force criterion gives too high dispersion for some specimens. During Marciniak test, the punch force is affected by many factors such as lubrication conditions or blankholder force. Consequently, the maximum punch force seems unsuitable to determine the limit strains. It has also been shown in [82].
- The modified criterion from the standard ISO 12004 gives the most regular and repeatable data which proves its robustness. This criterion will be adopted to determine all the forming limit curves in the following of this work.

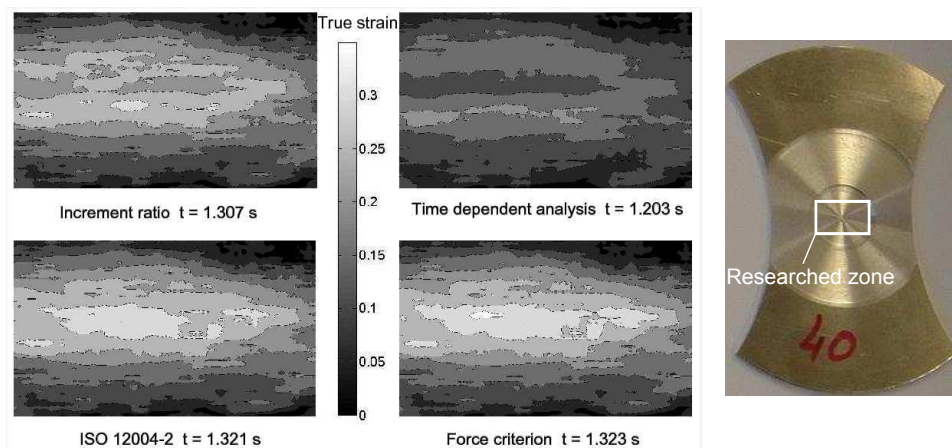


Figure 3.23: Equivalent strain distribution into the specimen at different critical times

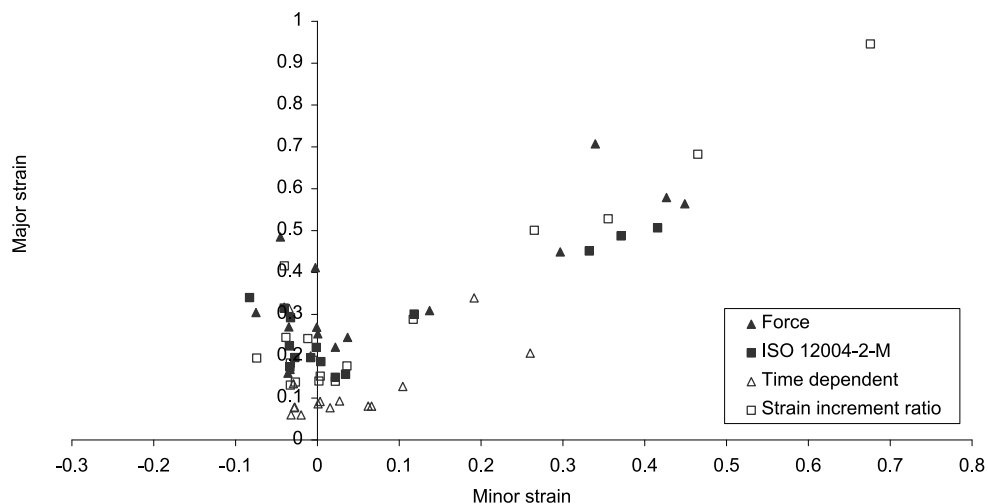


Figure 3.24: The FLCs of AA5086 at 150°C and 10 mm/s with different failure criteria

### 3.4 Temperature and strain rate influence on the formability of AA5086

The experimental FLCs determined from Marciniak test with criterion ISO 12004-2 are presented in Figure 3.25. It is demonstrated that temperature and strain rate significantly affect the sheet formability. To make the comparison easier between the different forming conditions, three typical points on the experimental FLCs corresponding to three different strain states of sheet forming (uniaxial, plane strain, biaxial) are chosen. The details of temperature and strain rate influence on the sheet formability of AA5086 are discussed hereafter.

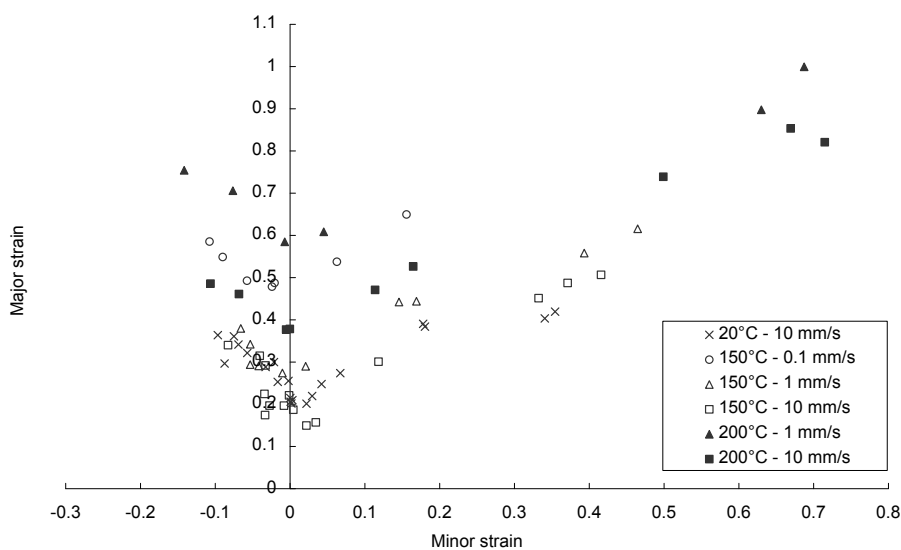


Figure 3.25: FLCs of AA5086 under different temperatures and strain rates

#### 3.4.1 Temperature effect

Figure 3.26 shows the limit major strain values for the three strain states at 10 mm/s and at different temperatures. There is almost no difference for the formability between 20°C and 150°C except a little increase for the biaxial state. When temperature grows up to 200°C, a significant formability increase is observed, especially for the biaxial state. The  $FLC_0$  (plane strain state) at 200°C shows an increment of about 80% compared to that at 20°C.

It has been introduced in [96, 72] that the formability is not sensitive to strain rate at room temperature for 5XXX series aluminium alloys and this conclusion has also been validated by Zhang [105]. In this work, the limit strains at 20°C under 10 mm/s are taken as the reference formability at ambient temperature for all the forming speeds. The major strains of the three typical strain states at 1 mm/s are shown in Figure 3.27. Comparing with the results at 10 mm/s, the limit strains at 1 mm/s present a higher temperature sensitivity at 150°C and 200°C. The  $FLC_0$  at 150°C shows an increment of 24%. At 200°C, significant increments of the limit strains are observed. The  $FLC_0$  at 200°C shows an increment of 181% compared to that at 20°C. Similar formability improvements at 200°C are also observed for the other two strain states.

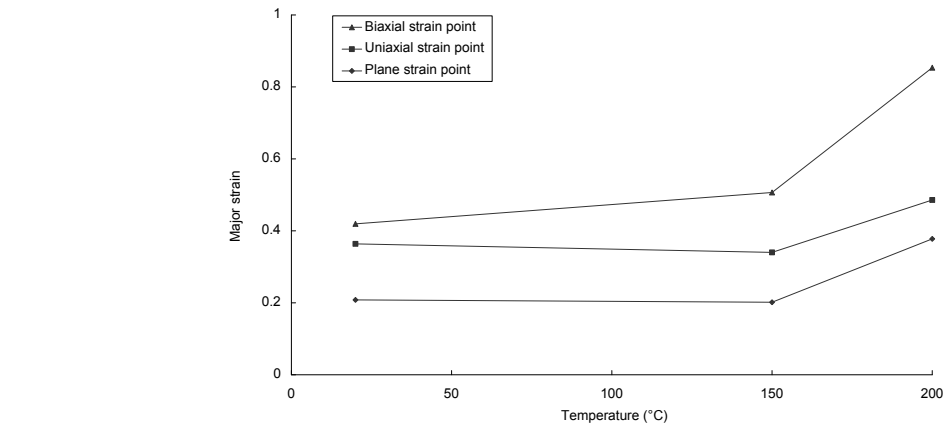


Figure 3.26: Limit major strains for the 3 typical strain states at different temperatures and 10 mm/s

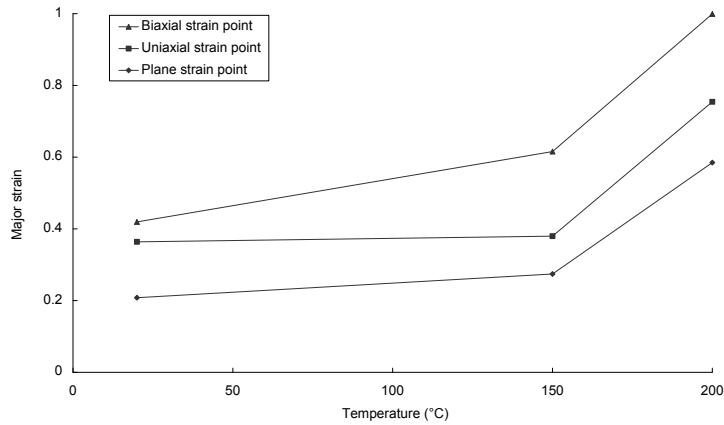


Figure 3.27: Limit major strains for the 3 typical strain states at different temperatures and 1 mm/s

The limit major strains at 0.1 mm/s are presented in Figure 3.28. In contrast with results presented for 1 mm/s and 10 mm/s strain rates, a marked temperature influence is observed at 150°C. The  $FLC_0$  increases about 86% from 20°C to 150°C at 0.1 mm/s.

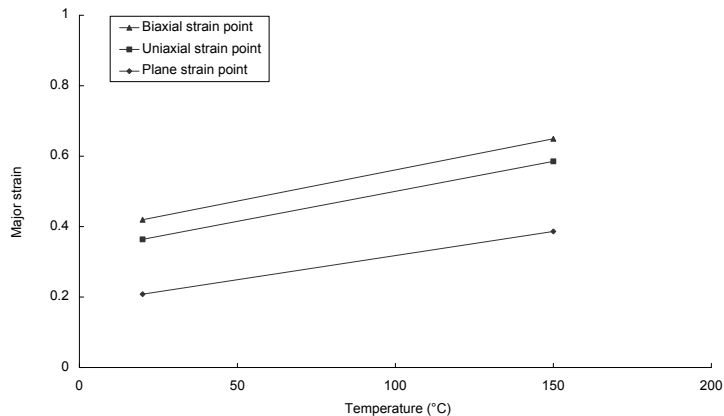


Figure 3.28: Limit major strains for the 3 typical strain states at different temperatures and 0.1 mm/s

To analyze the coupling effects of temperature and strain rate on AA5086 sheet formability, the values of  $FLC_0$  at different temperatures and strain rates are shown in Figure 3.29. It is shown that the formability improvements due to the temperature effects is more prominent at lower forming speeds. At 200°C, a drastic formability increment is found. The results prove that the strain rate plays an important role in determining the sheet formability. At 150°C and 0.1 mm/s, the experimental  $FLC_0$  is higher than the  $FLC_0$  at 200°C and 10 mm/s.

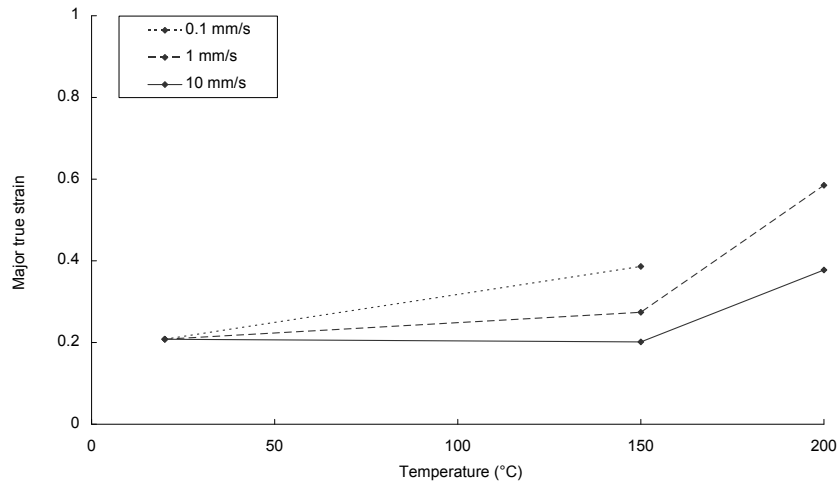


Figure 3.29:  $FLC_0$  at different temperatures and strain rates

An overview of the whole FLCs at different temperatures for each forming speed is shown in Figures 3.30 to 3.32. For the strain paths covered by experiments, the same results as presented previously are confirmed. A positive effect of temperature is observed on the formability of AA5086 which agrees with [96, 72]. The temperature influence is much more prominent under low forming speeds. Globally the level of FLCs is strongly modified, but the shape is not affected by the temperature.

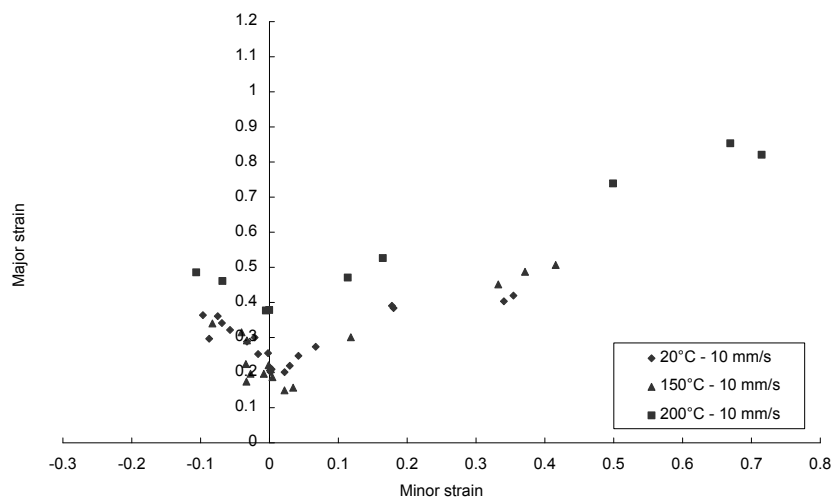


Figure 3.30: The FLCs of AA5086 at different temperatures for a forming speed of 10 mm/s

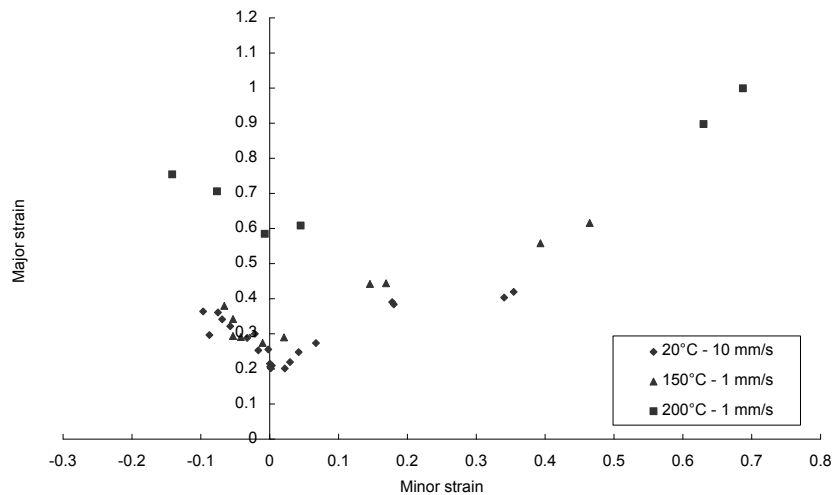


Figure 3.31: The FLCs of AA5086 at different temperatures for a forming speed of 1 mm/s

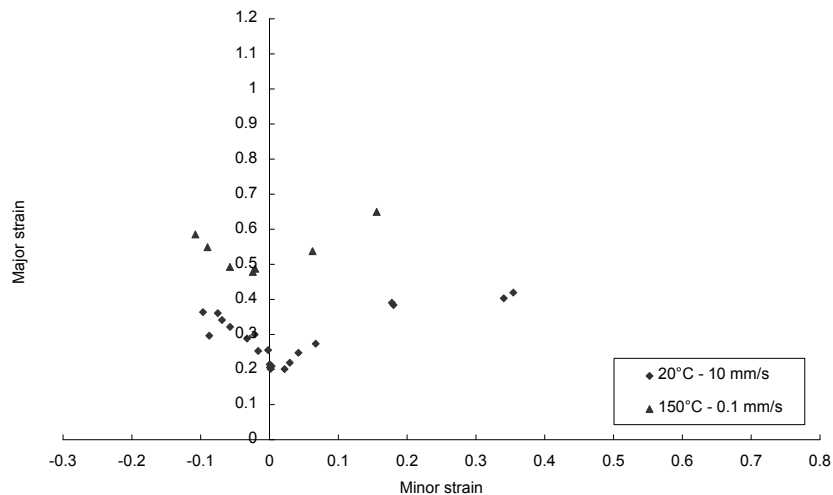


Figure 3.32: The FLCs of AA5086 at different temperatures for a forming speed of 0.1 mm/s

### 3.4.2 Strain rate effect

At 150°C, the limit major strains for the three typical strain states under the different forming speeds are shown in Figure 3.33. As seen before, the formability increases with decreasing forming speed. When the forming speed reduces from 10 mm/s to 1 mm/s and 0.1 mm/s, the  $FLC_0$  shows an increase amplitude of 35% and 92%, respectively. Figure 3.34 shows the limit major strain values for the different forming speeds at 200°C. When the forming speed decreases from 10 mm/s to 1 mm/s, a  $FLC_0$  increment about 55% is observed. The decrease of forming speed leads to a more important increase of the forming limits at 200°C compared to 150°C.

The whole FLCs at the different forming speeds for each temperature are shown in Figure 3.35 and Figure 3.36. The forming speed affects greatly the sheet metal formability, especially at high temperatures. In this case, the high forming speed can compensate the temperature positive effect. It is also found that at 200°C, a little weak strain rate sensitivity is observed for biaxial strain state points. With the forming speed reduced from 10 mm/s to 1 mm/s, the formability increase is lower for biaxial strain state point compared to the uniaxial and plane

strain state points. Similar observation is found by [79] for the FLCs of AZ31 based on failure limit strains. This may be caused by the shear fracture which decreases the formability in the biaxial stretch forming region as explained for the same phenomenon for austenitic steel sheets [56].

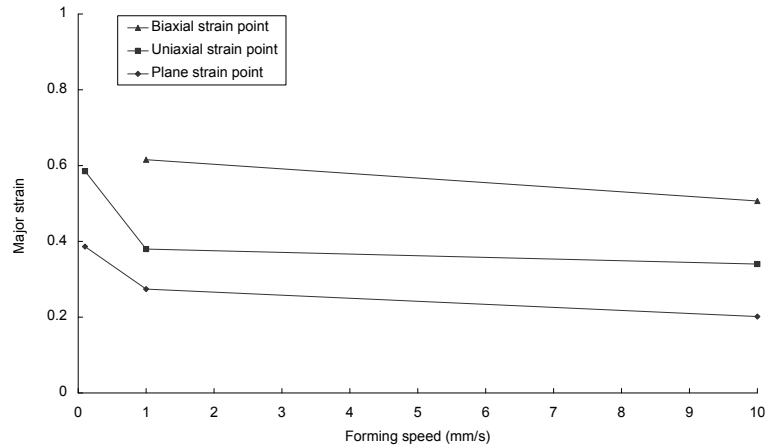


Figure 3.33: Limit major strains of 3 typical strain states for different strain rates at 150°C

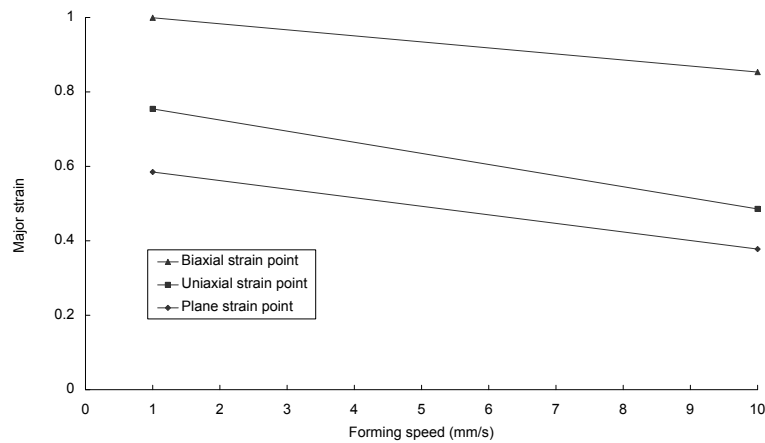


Figure 3.34: Limit major strains of 3 typical strain states for different strain rates at 200°C

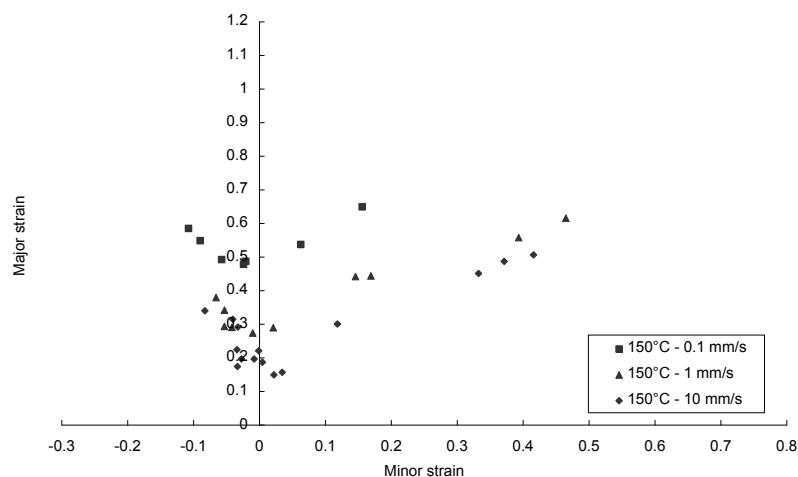


Figure 3.35: Strain rate influence on the formability of AA5086 at 150°C

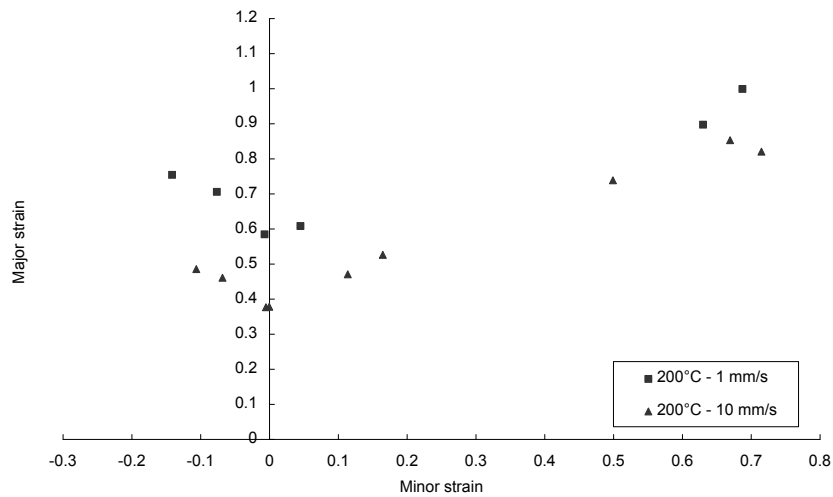


Figure 3.36: Strain rate influence on the formability of AA5086 at 200°C

### 3.5 Conclusions

In this chapter, a heating system for an existing Marciniak setup is designed. With this heating system, a constant temperature can be obtained in the specimen during the test. By means of the modified Marciniak setup and the on-line measurement method, the sheet metal AA5086 formability under different temperatures (20, 150, 200°C) and punch speeds (0.1, 1, 10 mm/s) is studied.

To determine the FLCs, different failure criteria are compared and discussed. The ISO 12004-2 criterion gives the most regular and robust results compared to the strain increment ratio, time-dependent and maximum punch force criteria. The FLCs of AA5086 under different temperatures and forming speeds are finally determined with this criterion. The results show that the sheet metal AA5086 formability increases with increasing temperature and decreasing forming speed.

The positive effect of temperature on formability can be compensated by the increase of forming speed. As an example, the  $FLC_0$  at 150°C and 0.1 mm/s is higher than the one at 200°C and 10 mm/s. Globally, temperature and strain rate affect the level of FLCs, the shape is slightly modified for all the strain paths.

## Chapter 4

# Numerical predictions of AA5086 sheet formability



Dans ce chapitre, deux modèles éléments finis (EF), le modèle du test d'emboutissage de Marciniak et le modèle M-K sont définis dans l'environnement du code de calcul ABAQUS. Dans ces deux modélisations, différentes lois d'érouissage ont pu être facilement implémentées par le sous-programme utilisateur « Uhard ». L'objectif est d'évaluer la capacité de ces modèles à prédire les limites de formabilité de l'alliage d'aluminium AA5086 obtenues expérimentalement au chapitre 3 pour différentes conditions opératoires de température et de vitesse.

Dans un premier temps, la capacité du modèle EF du test d'emboutissage de Marciniak à prédire les CLF a été testée puisque reflétant naturellement l'opération de mise en forme réalisée au chapitre précédent. Les CLF obtenues pour deux lois d'érouissage, une loi de Ludwick, rigidifiante, et une loi de Voce saturante sont comparées aux CLF expérimentales. La loi de Voce ne permet pas de traduire l'influence positive de la température sur la formabilité, contrairement à la loi de Ludwick. Toutefois les formabilités obtenues avec cette dernière surestiment largement les formabilités expérimentales.

Par la suite, une modélisation éléments finis du modèle M-K est proposée. L'influence des paramètres (taille et orientation) du défaut géométrique initial, de la loi d'érouissage et du critère de plasticité sur le tracé des CLF numériques est évaluée. Le modèle EF de type M-K permet d'obtenir des tendances similaires à celles mentionnées dans la littérature à partir d'un modèle analytique M-K. La difficulté dans l'utilisation de ce modèle réside d'une part dans la calibration du défaut initial et d'autre part dans le choix d'une formulation adéquate de la loi d'érouissage et du critère de plasticité. Différentes stratégies de calibration du défaut initial sont envisagées : (i) calibration sur trois points caractéristiques du DLF (traction uniaxiale, déformation plane et biaxial), (ii) calibration sur le  $CLF_0$  expérimental pour chaque condition opératoire, (iii) calibration d'une valeur unique du défaut pour l'ensemble des conditions opératoires. En ce qui concerne les lois d'érouissage, l'ensemble des lois identifiées dans le second chapitre a été testé et certaines formulations ont semblé particulièrement inadaptées pour prédire la formabilité du matériau pour certaines conditions.



## 4.1 Introduction

For the FLCs prediction, many analytical models have been proposed as introduced in Chapter 1. But the difficulty to implement advanced hardening models describing the mechanical responses of materials at different temperatures and strain rates limits the interest of these analytical models. In contrast, these implementations are easy in FE numerical models.

In this chapter, two finite element models, FE Marciniak model and FE M-K model, are introduced. Through the ABAQUS user-defined subroutine Uhard, different hardening models can be implemented. The FE Marciniak model is very close to the experimental procedure, so it seems natural to evaluate its response under the proposed forming conditions. A FE modeling of the well known geometrical M-K model is also proposed. The influences of the model inherent characteristics (initial imperfection value  $f_0$ , initial groove orientation  $\psi_0$ , the yield function and hardening law) on the FLCs are studied. By means of the experimental database established in the previous chapter, different strategies of calibration of the initial imperfection defect  $f_0$  are investigated.

With the proposed  $f_0$  calibration method, FLCs are determined at different strain rates and temperatures with different hardening models. By means of comparisons with experimental data, the validity of the FE M-K model and the influence of hardening law on the FLCs are discussed.

## 4.2 Simulation of Marciniak test

### 4.2.1 FE Marciniak model

Corresponding to the experimental device presented in chapter 3, the FE Marciniak model consists in three parts: a rigid cylindrical punch with a flat bottom, a rigid die and a deformable specimen. Due to symmetry, only a quarter part of the geometrical model is considered, as shown in Figure 4.1.

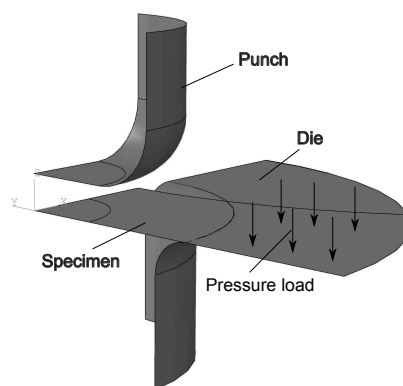


Figure 4.1: FE Marciniak test model in ABAQUS

The die remains fixed during the simulation process and the blank-holder is simulated by a pressure load directly applied on the specimen. The pressure load is set to a large value of 100 KN to prevent sliding between the blank and the die or the blank-holder.

### 4.2.1.1 Modeling

The modeled specimen shape is the same like the experimental one (Figure 4.2); Three different thickness zones are defined, they are noted as ZT0.8, ZT1.5 and ZT2.0 depending on the thickness of the sheet in the concerned zone.

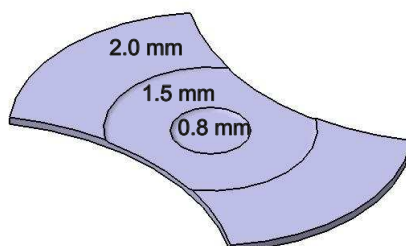


Figure 4.2: Example of a specimen shape

During sheet forming process, lubrication is a critical process factor which affects the forming force and the flow of material. In FE Marciniak model, the friction conditions are defined by contact interactions between the surfaces of different parts. Coulomb's friction law is considered here and the friction coefficients between the different parts are set in Table 4.1.

Table 4.1: Friction coefficients in contact interactions of the FE model of Marciniak test

Interaction	Friction coefficient
Punch-ZT1.5 and ZT2.0	0.05
Die-specimen	0.1

To reduce the computation time, a fine mesh in the central zone and a coarse mesh in the clamped zone are chosen. Shell linear elements S4R are adopted. The specimen mesh is shown in Figure 4.3.

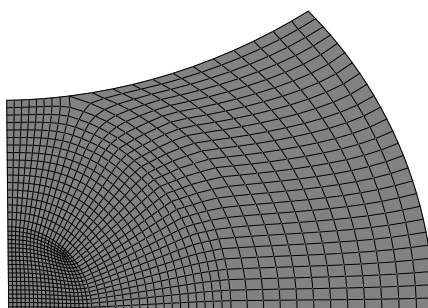


Figure 4.3: Specimen mesh in the FE model of the Marciniak test

### 4.2.2 FLCs with FE Marciniak model

In Figure 4.4, like in the experimental method, elements in the central zone of the specimen mesh are used to determine the FLC. Compared to experimental results, the strains present a

much more regular distribution (Figure 4.5). The inverse fit parabola of the simulated strains defined clearly the limit strains.

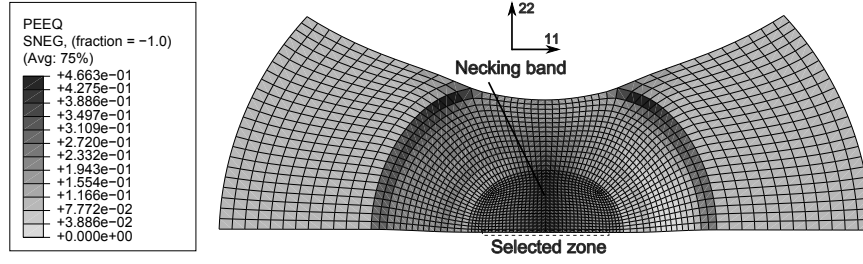


Figure 4.4: Selected zone of the ISO 12004-2 criterion in the FE Marciniak model

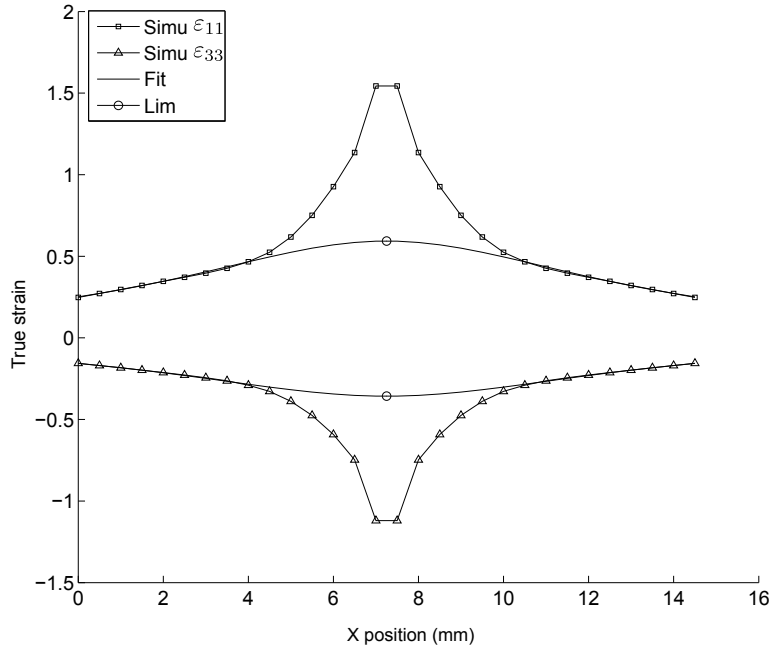


Figure 4.5: Example of inverse fit parabola for FE Marciniak

In the literature, the Ludwick and Voce models are often used to determine the FLCs. In this part, they are also adopted. The formulations identified in Chapter 2 are recalled below.

Ludwick model:

$$\bar{\sigma} = \sigma_0(T) + (K_0 - K_1 T) \bar{\varepsilon}_p^{(n_0 - n_1 T)} \dot{\bar{\varepsilon}}_p^{m_0 \exp(m_1 T)} \quad (4.1)$$

Voce\_1 model:

$$\bar{\sigma} = \sigma_0(T) + K_1 \exp(-K_2 T) \sqrt{1 - \exp(-K_3 \exp(K_4 T) \bar{\varepsilon}_p)} \dot{\bar{\varepsilon}}_p^{m_0 \exp(m_1 T)} \quad (4.2)$$

With Ludwick model, the predicted FLCs at 20°C and 200°C for 10 mm/s are shown in Figure 4.6. The results show a small temperature influence on the FLCs between 20°C and 200°C, with high strain predictions compared to experiment ones. The predicted FLCs shape is rather good especially for the left hand side. Using the Voce\_1 hardening law in the FE model of the Marciniak test leads to the determined FLCs shown in Figure 4.7.

The predicted FLC gives a better prediction at 20°C than the Ludwick law, but no clear temperature influence is found between 20°C and 200°C.

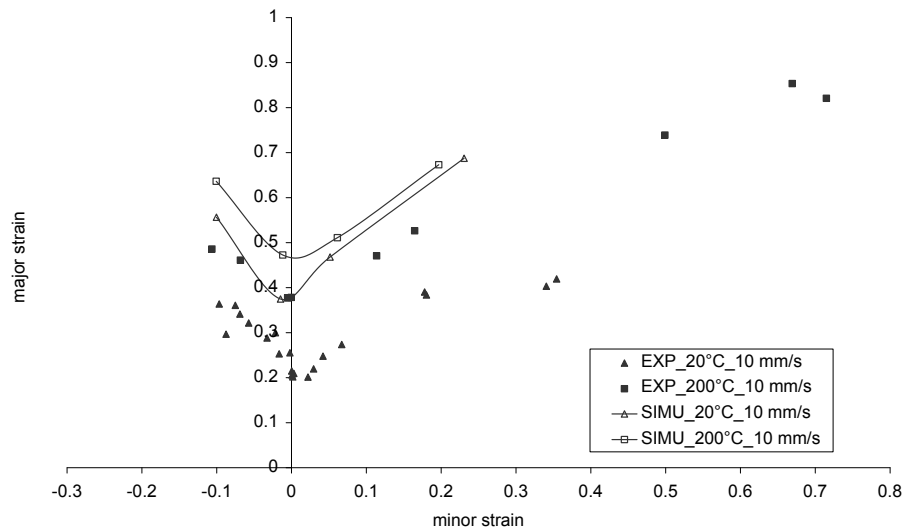


Figure 4.6: Predicted FLCs obtained by Ludwick model with ISO 12004-2

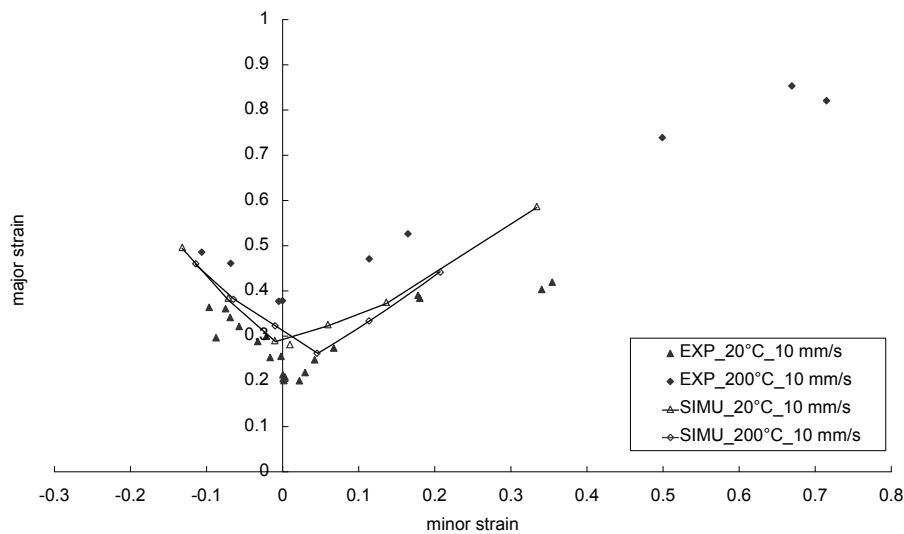


Figure 4.7: Predicted FLCs obtained by Voce\_1 model with ISO 12004-2

To investigate the strain rate influence, the FLCs are determined by ISO 12004-2 with Ludwick model at 200°C under different forming speeds. As shown in Figure 4.8, a weak positive strain rate influence on the formability is found. But the predicted results are far from the experimental ones.

### 4.2.3 Conclusions

Through the FE Marciniak model, the forming limit points are determined with ISO 12004-2. Compared to experimental results, several conclusions are obtained:

- The standard ISO 12004-2 can be adopted in the FE model and gives a direct predicted FLCs which can be compared with experimental results.

- The two tested hardening models give very different FLCs results at the tested temperatures. For the temperature, Ludwick model gives a better prediction compared to Voce\_1 model.
- With Ludwick model, positive temperature and strain rate sensitivities on the FLCs can be obtained. For the strain rate, these results are in contradiction with the experimental ones.
- In the FE Marciniak model, for some specimens (especially for large width specimens), it is difficult to obtain the strain localization condition in the central zone.

The FE Marciniak model is shown to be inadequate for determining the whole FLCs for different temperatures and strain rates. Hereafter, the application of a FE M-K model is discussed.

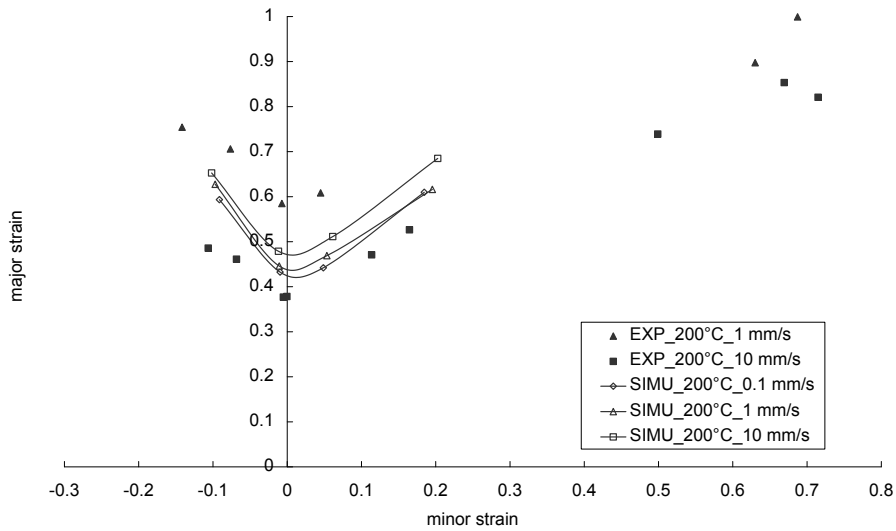


Figure 4.8: Predicted FLCs with Ludwick model under different strain rates

### 4.3 Simulation of M-K model

As introduced in chapter 1, the FE M-K model has already been used to determine the FLCs. The validity of this predictive model has been confirmed by Banabic [13] for FLCs construction on the right hand side. In this part, the FE M-K model is firstly introduced and the influence of factors such as the initial imperfection value  $f_0$ , the groove orientation  $\psi_0$  and hardening law are discussed.

#### 4.3.1 Presentation of the FE M-K model

Due to symmetry character of the model, only one eighth part (one half in the thickness part and one fourth in the plane part) of the entire geometrical M-K model is used as shown in Figure 4.9. Like analytical M-K model, the characteristic of the FE M-K model is also defined by the initial thickness imperfection, the initial value of  $f_0$  is defined as  $f_0 = t_b / t_a$ ,  $t_b$  and  $t_a$  are the thicknesses of zone b and zone a, respectively. In current model,  $t_a$  is set to 1 mm, changing the values of  $t_b$ , different initial imperfections  $f_0$  can be obtained.

In this model, different strain states can be covered by imposing different ratios of displacements in the directions 1 and 2. The displacement in direction 1 is fixed to 60 mm and different displacement in direction 2 from -6 to 20 mm are used in this simulation.

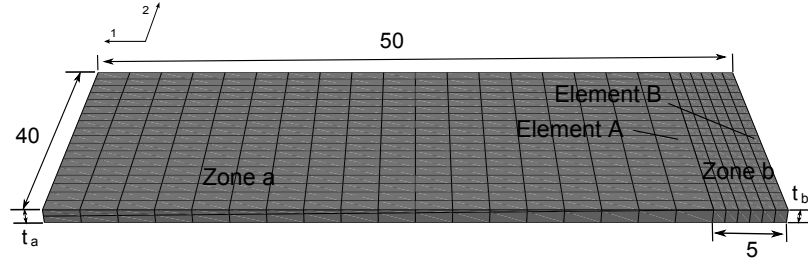


Figure 4.9: FE MK model in ABAQUS (dimensions in mm)

Compared to FE Marciniak model, the FE M-K model is more simple (from a geometry point of view and there is no contact interaction). Consequently, the CPU TIME consumed is lower. The model is meshed by hexahedral elements with fine mesh in zone b. Due to initial imperfection assumption, strain localization can be obtained easily in zone b as shown in Figure 4.10. The failure criterion adopted in FE M-K model is the equivalent plastic strain increment ratio ( $\Delta\bar{\epsilon}_p^b/\Delta\bar{\epsilon}_p^a$ ). Element A (in zone a) and element B (in zone b) in Figure 4.9 are chosen to calculate this strain increment ratio.

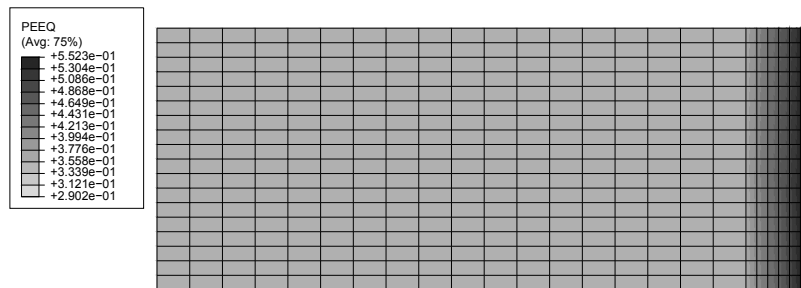


Figure 4.10: Equivalent plastic strain (PEEQ) distribution in different zones of the FE M-K model

Imposing different ratios of displacement in the directions 1 and 2 in FE M-K model, the different limit strain points on the FLC can be determined. Through ABAQUS user-defined Uhard subroutine, the different hardening models can be implemented. Different initial temperatures corresponding to the experimental ones are defined for the whole model. By adjusting the total calculation time in the FE M-K model, the simulated strain rate is set to values close to the experimental ones.

### 4.3.2 Influence factors of the FE M-K model

In analytical M-K model, the influence factors on the FLCs have been discussed in the literature and the results are widely accepted. In this part, these related factors are investigated for the FE M-K model.

### 4.3.2.1 Initial imperfection value $f_0$

The influence of  $f_0$  in analytical M-K model on the FLCs has been studied by many authors. It is pointed out that high values of  $f_0$  increase the FLC. With the proposed Ludwick model, the influence of  $f_0$  on the FLCs in the FE M-K model is studied. Similar results to analytical M-K model are obtained as shown in Figure 4.11, where one can see it, the FE M-K is also quite sensitive to  $f_0$ .

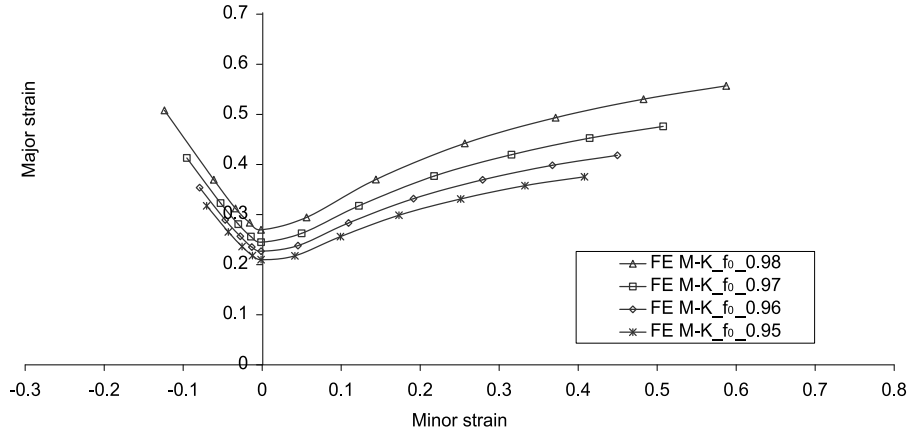


Figure 4.11: Influence of  $f_0$  on the FLCs in the FE M-K model

The definition of the  $f_0$  value of the initial imperfection will be a crucial stage of the calibration procedure of the FE M-K model to determine the FLCs.

### 4.3.2.2 Initial inclined groove orientation $\psi_0$

Concerning the influence of the initial groove orientation value  $\psi_0$ , it is reviewed that for the right side (RHS) of the FLCs, the critical minimum strains are obtained with  $\psi_0 = 0$  with the analytical M-K model. For the left side (LHS) of the FLCs, it is necessary to determine the critical angle that gives the minimum limit strain values [30][93][103]. As presented in Figure 4.12, the FE M-K model with an inclined groove is constructed. By means of a same initial imperfection value  $f_0 = 0.98$  and the Ludwick hardening model, the FLCs are determined with different angles  $\psi_0$ .

It is shown in Figure 4.13 that when the groove orientation is small ( $\psi_0 < 10^\circ$ ), there is almost no groove orientation influence on the FLCs. With the increasing of  $\psi_0$ , the FLCs are shifted up. For the RHS of FLCs, the results coincide with the ones from the analytical model, the critical limit strains occur at angle of zero degree. For the LHS of FLCs, different results are obtained, compared to analytical M-K model. But it is still the zero degree model that gives the minimum limit strains. This result is in accordance with the necking band orientation observed in Marciniak tests with the small width specimens. As shown in Figure 4.14, the crack positions are all perpendicular to the rolling direction for different width specimens. For the following, all simulations will be carried out with the FE M-K model of  $\psi_0 = 0$ .

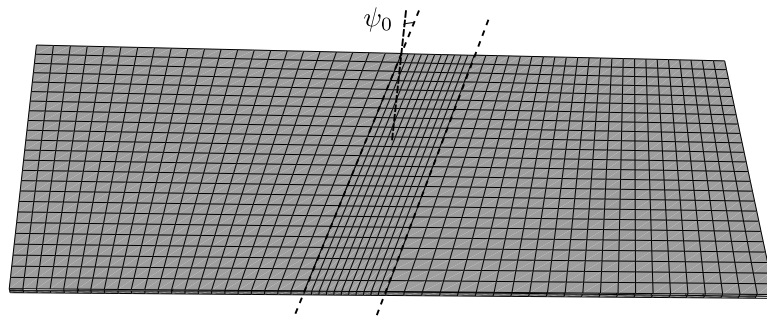


Figure 4.12: FE M-K model with an initial inclined groove

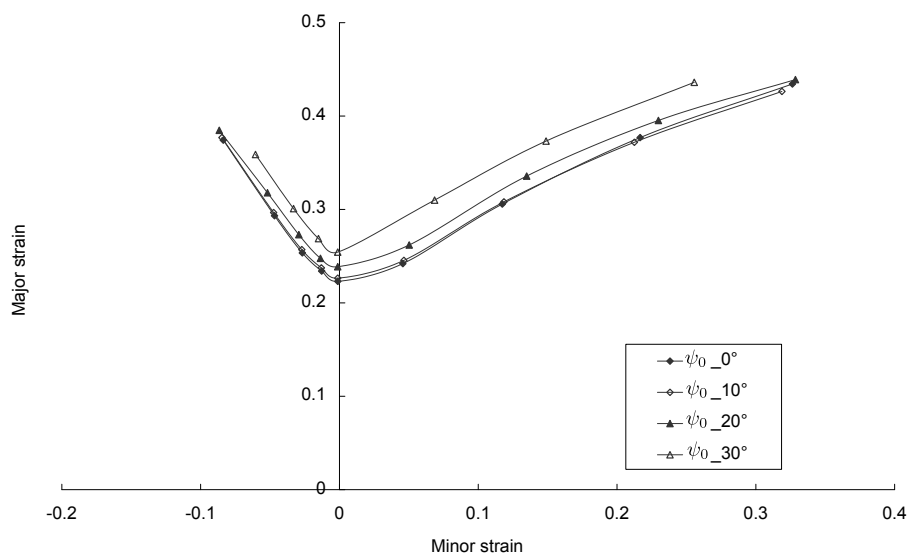


Figure 4.13: FLCs obtained with different initial inclined grooves in FE M-K model

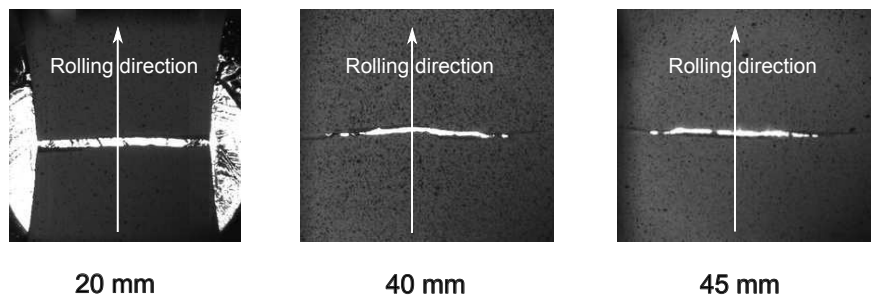


Figure 4.14: Crack in experimental specimens

#### 4.3.2.3 Hardening law

The role of strain-hardening laws in the prediction of forming limit curves is discussed by [94]. It is found that the Voce equation has yielded better limit strains for copper and its alloys compared to the classically adopted Hollomon equation for materials such as deep drawing steels. The hardening models of Voce, power-law and Tian-Zhang are used by [5] to construct the FLCs for AA3105 and AA8011 aluminium alloys, significant influences of the hardening

models are observed. In [25], Swift hardening law and Voce equation are used to determine the FLCs for aluminium alloy AA6016-T4 based on M-K theory, a successful correlation is observed between the experimental FLCs and the computed limit strains when Yld96 yield criterion and Voce equation are adopted.

In FE M-K model with initial imperfection  $f_0 = 0.98$ , the FLCs are obtained by the proposed Ludwick and the Voce\_1 hardening model as shown in Figure 4.15. It is shown that the levels of FLCs are strongly influenced by the hardening model. The Ludwick model gives higher predictions for all strain paths compared to Voce\_1 hardening model. Hence, for the use of FE M-K model, specific care must be taken to choose an appropriate hardening law.

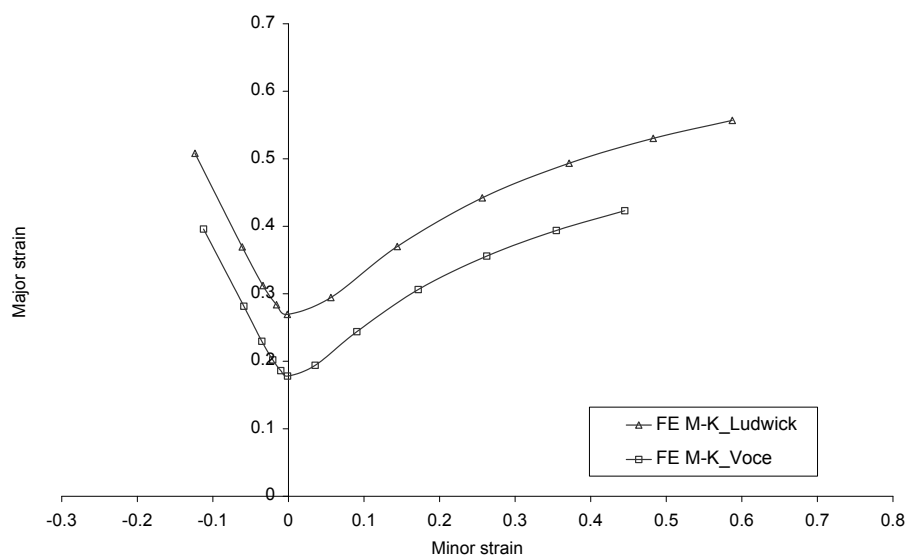


Figure 4.15: Hardening law influence on the FLCs in FE M-K model

#### 4.3.2.4 Yield function

The yield function has been proved to be important for determining the FLCs in analytical M-K model. In the work of Vegter and van Den Boogaard [99], three different yield functions (Vegter, Hill'90, Yld2000) are implemented into analytical M-K model using the same Bergström hardening model to predict the FLCs. The results show that the LHS of the FLCs and the  $FLC_0$  do not depend on the yield criterion while the different yield functions lead to significant differences in the prediction of the RHS.

By implementing two simple yield functions, von Mises and Hill'48, the FLCs are determined with Ludwick hardening model and constant  $f_0 = 0.98$ . The parameters of Hill'48 yield function for AA5086 are given in Table 4.2.

Table 4.2: The parameters of Hill'48 yield function for AA5086

F	G	H	L	M	N
0.7	0.636	0.363	1.5	1.5	1.494

The same conclusions already given for analytical M-K model are obtained as shown in

Figure 4.16. There is no influence for the left hand side of the FLCs and  $FLC_0$ . For the right hand side, the von Mises yield function gives a more conservative prediction compared to Hill'48. As explained in Chapter 1, the Hill'48 criterion is not well adapted for aluminium alloys, also, in the following predictions, the conservative isotropic von Mises criterion is kept.

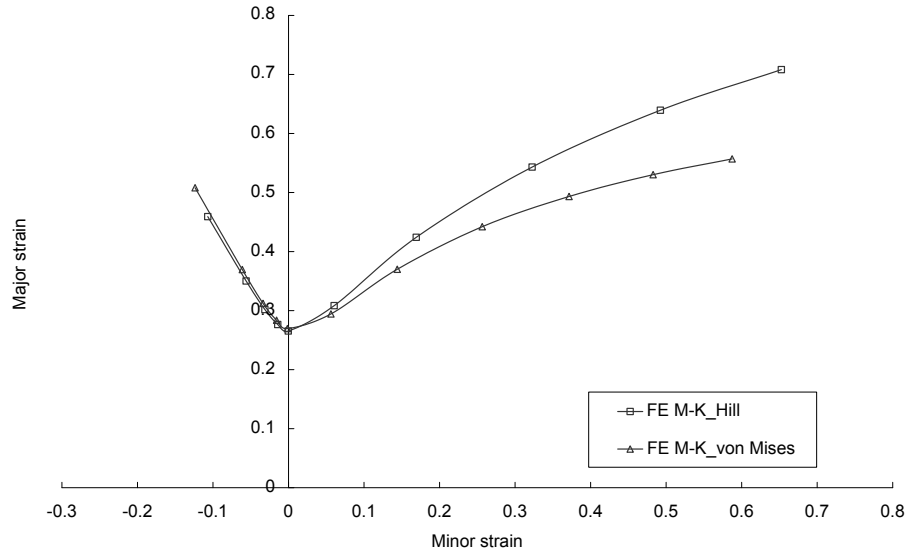


Figure 4.16: Yield function influence on the FLCs in FE M-K model

## 4.4 Determination of FLCs through FE M-K model

In M-K theory, two methods exist for the choice of imperfection value  $f_0$ . One is calculating  $f_0$  from a microstructure analysis, as presented in [17]. The other widely used method is to make the best fit between the prediction results and experimental ones.

Up to now, in the literature, there is no guideline for the choice of  $f_0$ , especially for the use of M-K model under different strain rates and temperatures. In this work, a geometric  $f_0$  calibration method is adopted. The validation of FE M-K as a predictive model for determining FLCs under different forming conditions is carried out in the following parts.

### 4.4.1 Strategies to calibrate $f_0$

The geometric calibration of  $f_0$  can be formulated as an inverse analysis problem. Three typical points (uniaxial tension (UT), plane strain tension (PT), biaxial tension (BT)) on the FLCs can be easily obtained through experimental investigations. The limit strain values of each point can be used as input experimental data. In this part, with different input experimental data (UT, PT or BT), different calibration strategies are compared.

Based on the optimization algorithm presented in Chapter 2, an inverse procedure is developed in the optimization software ModeFRONTIER as shown in Figure 4.17. As introduced previously, setting different boundary displacement (BD) conditions in the FE M-K model (direction 1 and direction 2 in Figure 4.9), the simulated limit strains with different strain paths can be obtained. Comparing the input experimental values and the simulated ones, by means of a minimum cost function in Matlab, the best fit value of  $f_0$  can be determined.

In the following parts, the comparison of the prediction results and experimental data using different input data are presented.

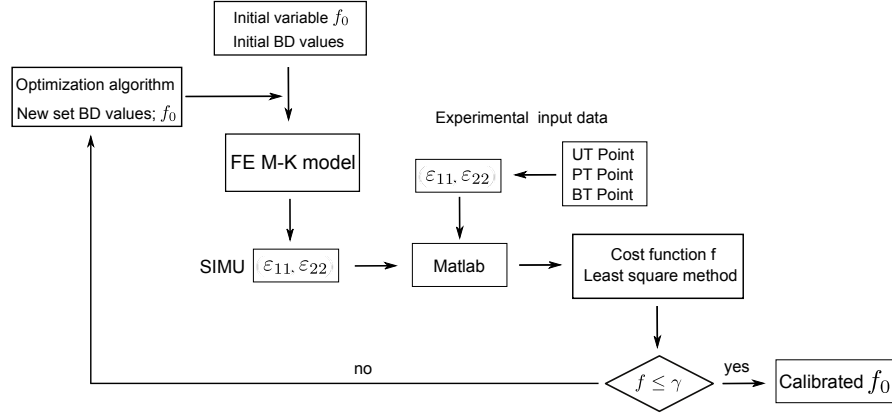


Figure 4.17: Imperfection value  $f_0$  calibration method

#### 4.4.1.1 Calibration at 20°C and 10 mm/s

Under the forming condition at 20°C and 10 mm/s, the three experimental points (triangular mark in Figure 4.18) and the calibrated initial imperfection  $f_0$  by Ludwick hardening model are shown in Table 4.3. The results show that the calibrated  $f_0$  from biaxial point gives the highest value and the other two points give almost the same value. With the calibrated  $f_0$ , the comparison of determined FLCs by Ludwick model and the experimental results are shown in Figure 4.18. The FLCs obtained with different calibration methods are noted as  $FLC_{uniaxial}$ ,  $FLC_{plane}$  and  $FLC_{biaxial}$  for convenience. The  $FLC_{uniaxial}$  and  $FLC_{plane}$  give a little conservative prediction for the RHS and a good prediction around plane strain region. The  $FLC_{biaxial}$  gives an overestimation around plane strain zone.

Table 4.3: Experimental points and calibrated  $f_0$  at 20°C and 10 mm/s

EXP_Points	Major strain	Minor strain	Calibrated $f_0$
Uniaxial (UT)	0.3638	-0.0966	0.9505
Plane strain (PT)	0.2081	0.001408	0.9507
Biaxial (BT)	0.4195	0.3543	0.968

As presented in Figure 4.16, the RHS of the FLC is influenced by the yield function. Hence the calibration results from biaxial point (BT) is coupling with the yield function. The high calibration value of  $f_0$  for BT is probably due to the conservative von Mises yield function, which leads to the overestimation in the plane strain area. It could be interesting to use a more appropriate yield function to verify that the calibration method from biaxial point (BT) can also lead to a good  $FLC_0$  prediction.

#### 4.4.1.2 Calibration at 200°C and 10 mm/s

At 200°C and 10 mm/s, with Ludwick model, the calibration results are shown in Table 4.4. The biaxial point still gives the highest  $f_0$  value. At 200°C and 10 mm/s, the calibration FLCs are shown in Figure 4.19. The  $FLC_{biaxial}$  gives higher evaluation for the LHS of FLC and  $FLC_0$ . The  $FLC_{uniaxial}$  gives lower evaluation for the whole FLC, while the  $FLC_{plane}$  gives a good correlation for the LHS and plane strain condition and a little conservative evaluation for the RHS, especially under equi-biaxial tension state.

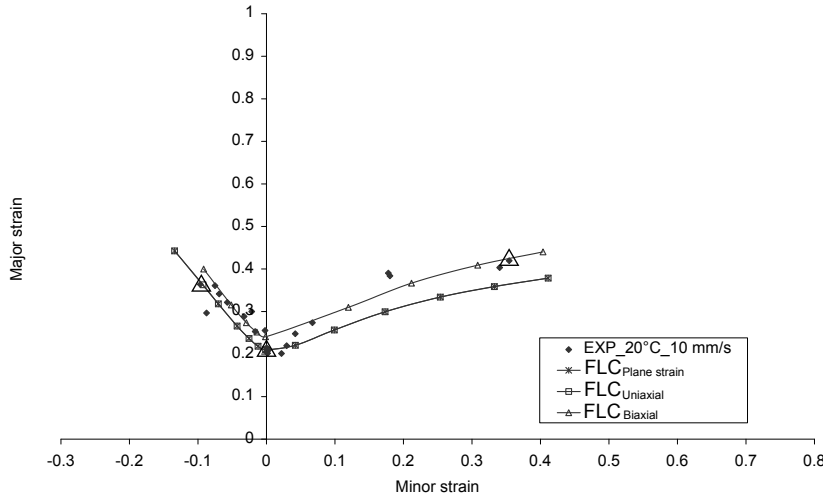


Figure 4.18: Comparison of different  $f_0$  calibration methods at 20°C and 10 mm/s

Table 4.4: Experimental points and calibrated  $f_0$  at 200°C and 10 mm/s

EXP_Points	Major strain	Minor strain	Calibrated $f_0$
Uniaxial	0.4857	-0.1064	0.9857
Plane strain	0.3777	-0.002778	0.9927
Biaxial	0.8207	0.7148	0.9961

#### 4.4.1.3 Conclusions

The calibration method from biaxial point gives the higher imperfection value  $f_0$  which is caused by the yield function. With a more appropriate yield function, this method could also give a satisfying prediction. For the calibration method from the uniaxial point, the choice of the point is crucial. Although it is not affected by yield function, the variations between the different experimental points can leads to significant different prediction results.

For the calibration method from plane strain point, it seems easier to choose the experimental point value. This choice is insensitive to the yield function which simplifies the calibration stage. The comparison of the results show that the plane strain calibration method show correct results at two temperatures. Also, the  $f_0$  calibration method from plane strain point is adopted in the following of this work. One point has to be emphasized is that the calibrated values  $f_0$  are not constant for different forming conditions for the three methods.

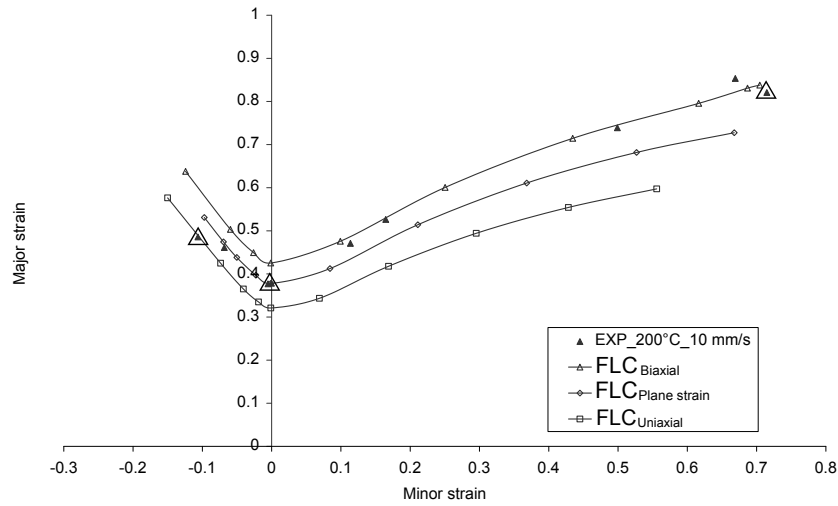


Figure 4.19: Comparison of different  $f_0$  calibration methods at 200°C and 10 mm/s

#### 4.4.2 FLCs with $f_0$ calibrated from each forming condition

The  $FLC_0$  experimental values are given in Table 4.5 for the different operating conditions. With these data, the initial imperfection value  $f_0$  can be calibrated for different hardening models.

Table 4.5: Experimental values of  $FLC_0$  under different forming conditions

Temperature ( °C)	Forming speed (mm/s)	Major strain
20	10	0.2081
150	0.1	0.3862
150	1	0.2741
150	10	0.2016
200	1	0.5849
200	10	0.3777

##### 4.4.2.1 Predicted FLCs from power law type hardening model

**Predicted FLCs from Ludwick model** Through experimental  $FLC_0$ , the calibrated  $f_0$  with Ludwick model for different conditions are shown in Table 4.6, including the error between the calibrated  $FLC_0$  and the experimental ones.

Observed from Table 4.6, the calibrated  $f_0$  values vary a lot for the different forming conditions. For a given forming speed, the calibrated  $f_0$  value increases with the temperature. On the contrary, for a given temperature, the calibrated  $f_0$  value increases with decreasing forming speed.

Table 4.6: Calibrated  $f_0$  with Ludwick model

Temperature ( °C)	Forming speed (mm/s)	Calibrated $f_0$	Error
20	10	0.9507	1.1%
150	10	0.97	2%
200	10	0.9927	0.05%
150	1	0.99	5.3%
200	1	0.99985	0.75%
150	0.1	0.99985	0.03%

With Ludwick model and the  $f_0$  calibrated at each forming condition, the predicted FLCs are shown in Figure 4.21. Good formability predictions are obtained over the whole temperature and strain rate ranges, especially for the LHS of the FLCs. A little conservative prediction in the RHS of the FLCs, especially under biaxial strain state is observed with von Mises yield function. As shown in Figure 4.21(c), under the condition of 1 mm/s and 200°C, it is very difficult to determine the limit strain values at high strain levels. This may be caused by the high calibrated  $f_0$  which leads to some difficulties to achieve the onset of necking.

With Hill'48 yield function and Ludwick model, the predicted FLC at 20°C is shown in Figure 4.20. It is shown that for Ludwick model, the predicted FLCs with Hill'48 yield function give a good correlation result for the RHS compared to the one with von Mises.

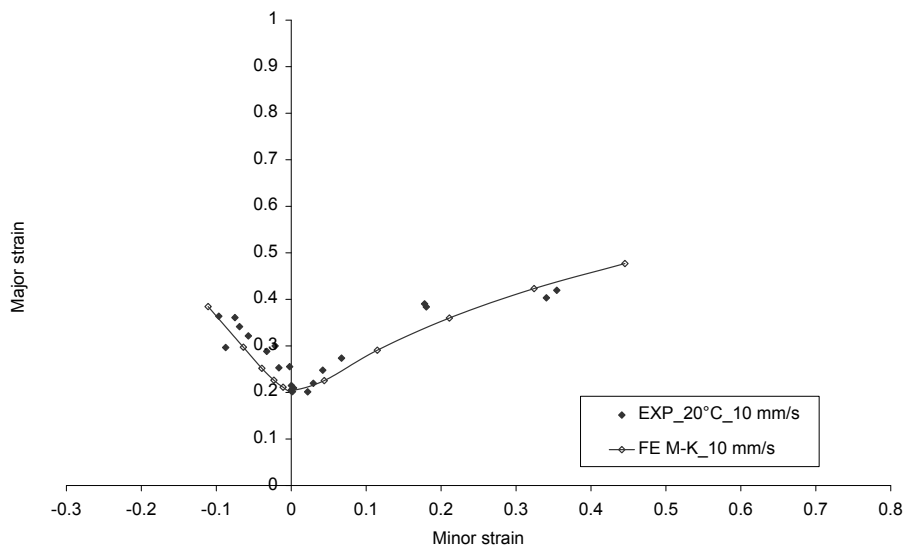
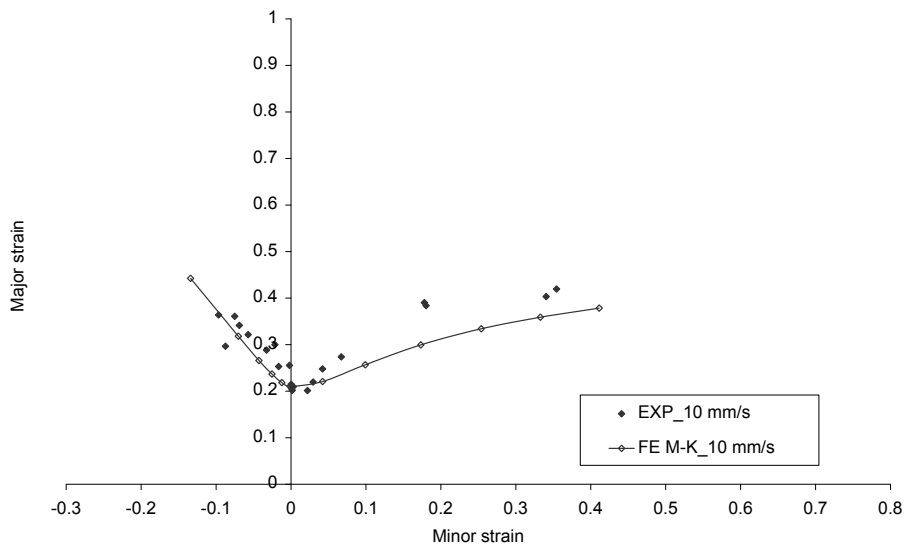
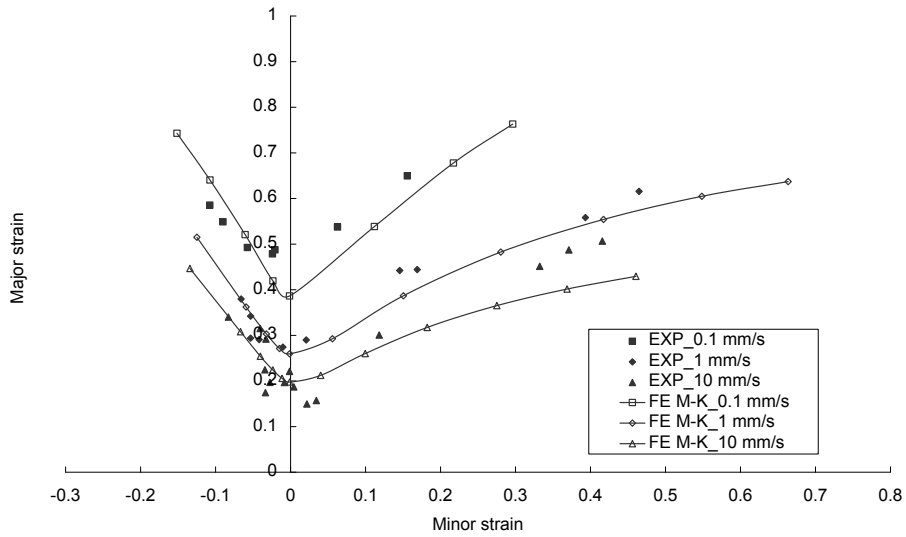


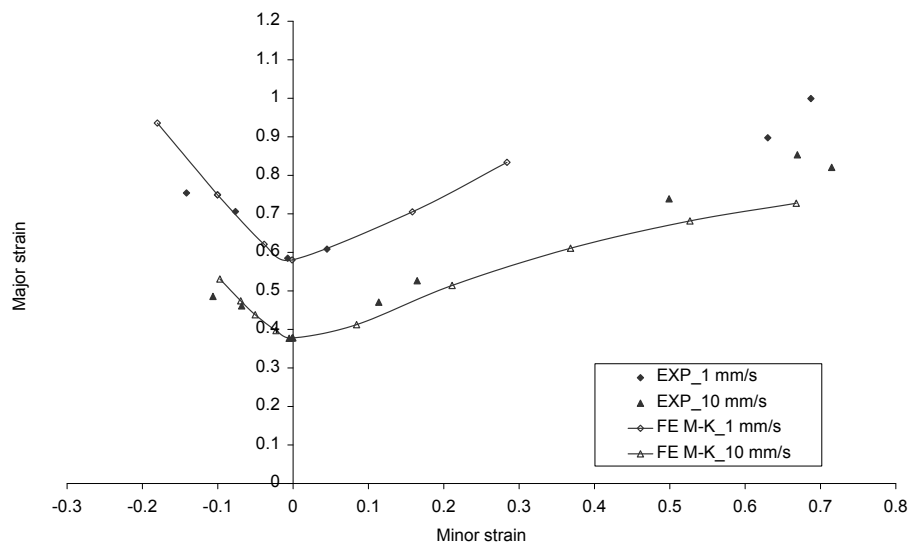
Figure 4.20: Predicted FLCs with Hill'48 yield function and Ludwick model



(a) Predicted FLC at 20°C



(b) Predicted FLCs at 150°C



(c) Predicted FLCs at 200°C

Figure 4.21: Predicted FLCs with Ludwick model

**Predicted FLCs from KHL model**

$$\bar{\sigma} = \sigma_0(T) + B \left( 1 - \frac{\ln \dot{\bar{\epsilon}}_p}{\ln D_0} \right)^{n_1} \bar{\epsilon}_p^{n_2 - n_3 T} \left( \frac{T_m - T}{T_m - T_r} \right)^m \left( \frac{\dot{\bar{\epsilon}}_p}{\dot{\bar{\epsilon}}_0} \right)^{C_0 \exp(C_1 T)} \quad (4.3)$$

The  $f_0$  calibration results with KHL model are shown in Table 4.7. The determined FLCs are shown in Figure 4.22. It is found that the FLCs prediction results by KHL model are similar to the results obtained by Ludwick model.

Table 4.7: Calibrated  $f_0$  with KHL model

Temperature ( °C)	Forming speed (mm/s)	Calibrated $f_0$	Error
20	10	0.985	3.2%
150	10	0.97	3.7%
200	10	0.9925	0.82%
150	1	0.99	1.4%
200	1	0.9999	1.7%
150	0.1	0.9996	0.5%

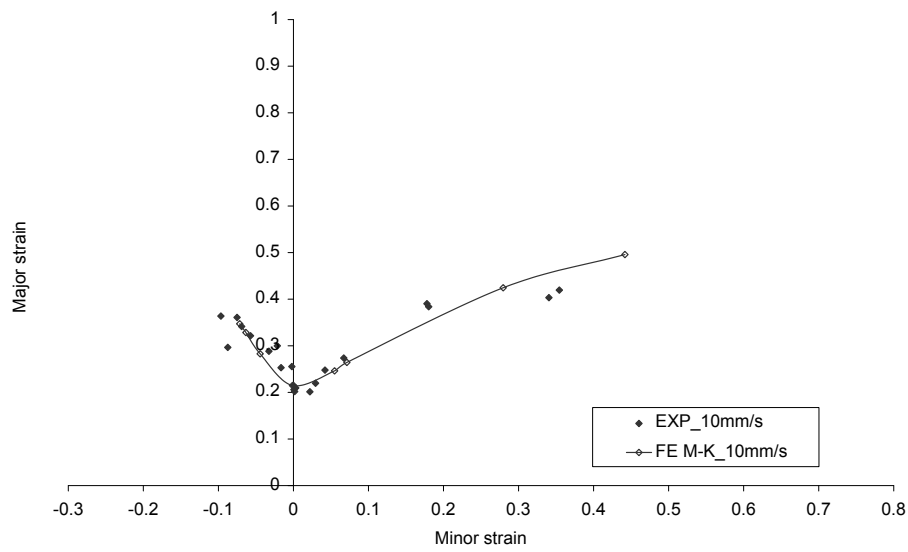
**Predicted FLCs from ZA model**

$$\bar{\sigma} = \sigma_0(T) + K_1 \bar{\epsilon}_p^n \exp(-(K_2 + K_3 T) \bar{\epsilon}_p) \dot{\bar{\epsilon}}_p^{K_4 \exp(K_5 T)} \quad (4.4)$$

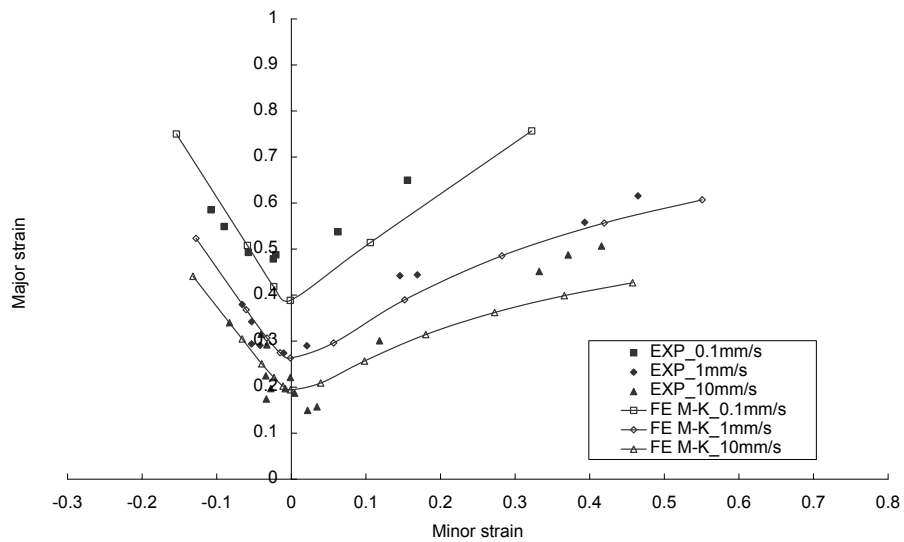
The  $f_0$  calibration results with ZA model are shown in Table 4.8. Great error values were found for all conditions even with a very high value of  $f_0$ . The determined FLCs are shown in Figure 4.23. It is found that the FLCs prediction results by ZA model gives too low prediction results. At large strain levels, for RHS, the predicted FLC at 20°C is even higher than the FLC at 200°C. This can be explained by an overestimation of the softening effect of this model at high strain level.

Table 4.8: Calibrated  $f_0$  with ZA model

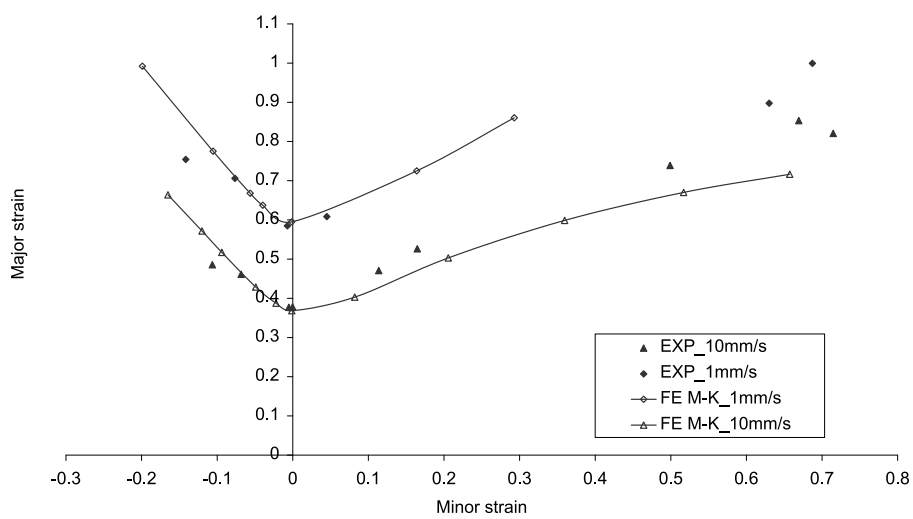
Temperature ( °C)	Forming speed (mm/s)	Calibrated $f_0$	Error
20	10	0.99995	20%
150	10	0.99995	35%
200	10	0.99995	50%
150	1	0.99995	52%
200	1	0.99995	68%
150	0.1	0.99995	66%



(a) Predicted FLC at 20°C



(b) Predicted FLCs at 150°C



(c) Predicted FLCs at 200°C

Figure 4.22: Predicted FLCs with KHL model

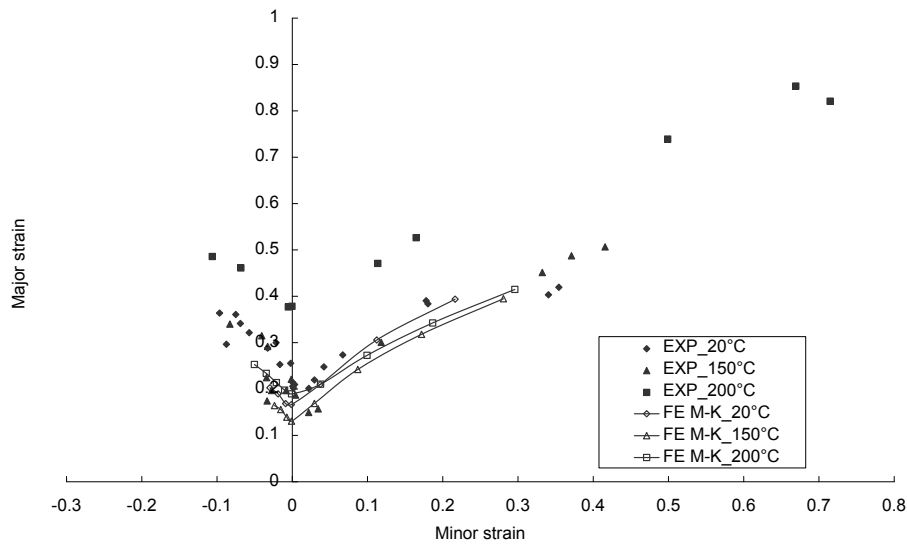


Figure 4.23: Predicted FLCs with ZA model under 10 mm/s

#### 4.4.2.2 Predicted FLCs from saturation type hardening model

**Predicted FLCs by Voce\_1 model** The calibrated  $f_0$  with Voce\_1 model are shown in Table 4.9. Big discrepancies are found between predicted  $FLC_0$  and measured ones at 150°C and 0.1 mm/s, and at 200°C and 1 mm/s even the  $f_0$  value is set to 0.99999. The  $f_0$  calibration results indicate that this hardening model cannot predict the formabilities at these two forming conditions.

Table 4.9: Calibrated  $f_0$  with Voce\_1 model

Temperature ( °C)	Forming speed (mm/s)	Calibrated $f_0$	Error
20	10	0.9908	1.8%
150	10	0.997	0.05%
200	10	0.99999	3%
150	1	0.99999	6%
200	1	0.99999	36%
150	0.1	0.99999	48%

At 10 mm/s, the predicted FLCs are presented in Figure 4.24, good matches between predicted and experimental FLCs are observed except slight overestimation for the equi-biaxial zone. For the RHS, the predicted FLCs at 150°C is a little higher than that at 20°C, prominent in equi-biaxial zone, which coincides with experimental results.

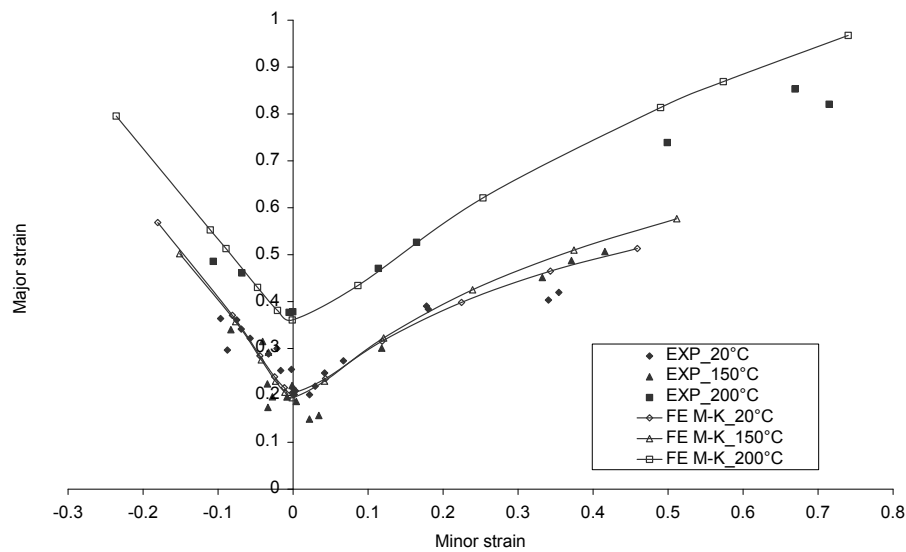


Figure 4.24: Predicted FLCs by Voce\_1 model under 10 mm/s

The predicted FLCs with Ludwick model at 10 mm/s are shown in Figure 4.25. With von Mises yield function, the Voce\_1 model gives a better prediction than Ludwick model for the RHS at 10 mm/s. The comparison of the predicted FLCs obtained with Voce\_1 and Ludwick hardening laws and the same von Mises yield function at 10 mm/s shows that the two laws give satisfying results. The trend of the Ludwick law is to underestimate the experimental results while the Voce\_1 law leads to overestimate these results. It can be explained by the two different character of these laws for large strains, one is power type and the other presents a saturation stress state.

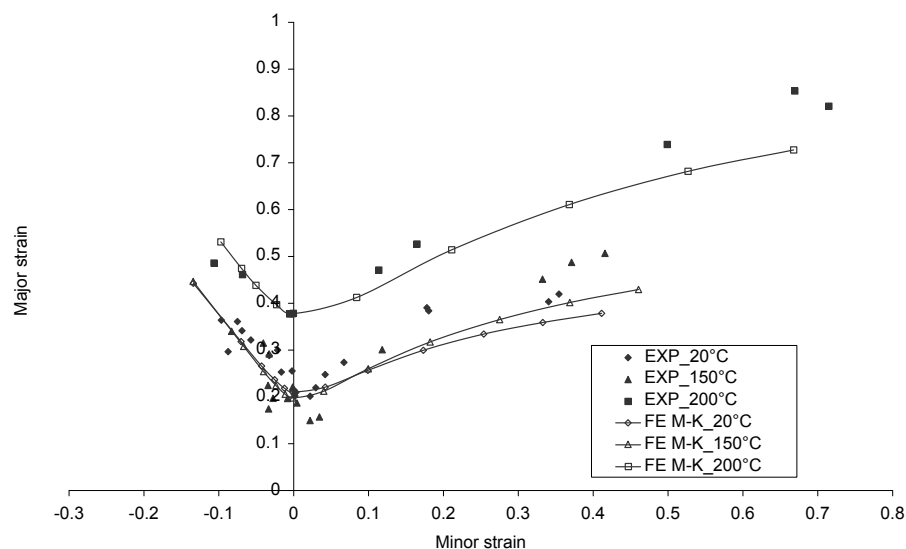


Figure 4.25: Predicted FLCs by Ludwick model under 10 mm/s

The predicted FLC with Voce\_1 model and Hill'48 yield function at 20°C is shown in Figure 4.26. With Hill'48 yield function, Ludwick model gives better RHS of FLC prediction than Voce\_1 model. It can be concluded that the yield function influence on the FLCs is strongly coupling with the hardening model.

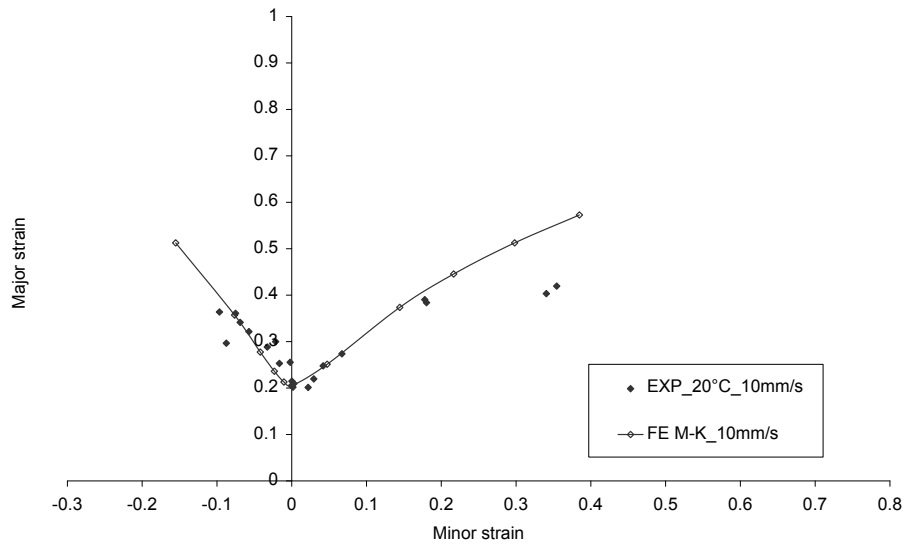


Figure 4.26: Predicted FLCs with Hill'48 yield function and Voce\_1 model

### Predicted FLCs by Voce\_2 model

$$\bar{\sigma} = \sigma_0(T) + (K_1 - K_2T) (1 - \exp(-(K_3 + K_4T)\bar{\epsilon}_p)) \dot{\bar{\epsilon}}_p^{m_0 \exp(m_1T)} \quad (4.5)$$

The calibrated  $f_0$  with Voce\_2 model are shown in Table 4.10. The results show that it is difficult to find suitable values of  $f_0$  with this model. Even at 20°C and 10 mm/s, with high values of  $f_0$ , the gap error is high up to 27%.

Table 4.10: Calibrated  $f_0$  with Voce\_2 model

Temperature ( °C)	Forming speed (mm/s)	Calibrated $f_0$	Gap Error ( $\bar{\epsilon}_{major}$ )
20	10	0.99995	27%
150	10	0.99995	27%
200	10	0.99995	32%
150	1	0.99995	46%
200	1	0.99995	58%
150	0.1	0.99995	70%

### Predicted FLCs by Voce\_3 model

$$\bar{\sigma} = \sigma_0(T) + (K_1 - K_2T) (1 - \exp(-K_3 \exp(K_4T)\bar{\epsilon}_p^n)) \dot{\bar{\epsilon}}_p^{m_0 \exp(m_1T)} \quad (4.6)$$

With Voce\_3 model, similar results as Voce\_2 model are obtained. The calibrated values of  $f_0$  are shown in Table 4.11. The predicted FLCs with the calibrated values of  $f_0$  at 10 mm/s are shown in Figure 4.27.

Table 4.11: Calibrated  $f_0$  with Voce\_3 model

Temperature ( °C)	Forming speed (mm/s)	Calibrated $f_0$	Gap Error ( $\bar{\varepsilon}_{major}$ )
20	10	0.99995	15%
150	10	0.99995	5%
200	10	0.99995	24%
150	1	0.99995	31%
200	1	0.99995	53%
150	0.1	0.99995	61%

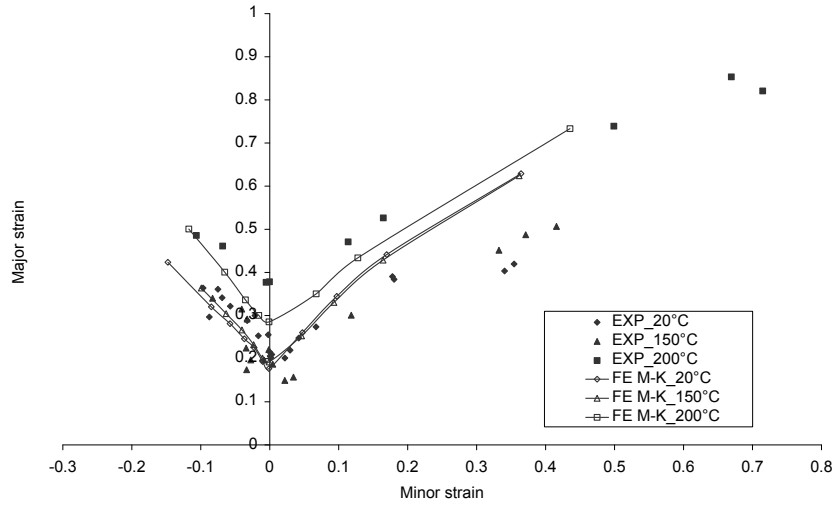


Figure 4.27: Predicted FLCs by Voce\_3 model at 10 mm/s

#### Predicted FLCs by Bergström model

$$\bar{\sigma} = \sigma_0(T) + (K_1 - K_2 T) (1 - \exp(-(K_3 + K_4 T)\bar{\varepsilon}_p))^{(n_0 - n_1 T) \frac{m_0 \exp(m_1 T)}{\bar{\varepsilon}_p}} \quad (4.7)$$

The calibrated values of  $f_0$  with Bergström model are shown in Table 4.12. Similar results like Voce\_2 and Voce\_3 models are observed.

#### 4.4.2.3 Predicted FLCs by mixed type hardening model (H-V)

$$\begin{cases} \bar{\sigma} = f(\bar{\varepsilon}_p, T) \cdot v(\dot{\bar{\varepsilon}}_p) \cdot h(T) \\ f(\bar{\varepsilon}_p, T) = (\alpha(T) f_H + (1 - \alpha(T)) f_V) \end{cases} \quad (4.8)$$

The calibrated values of  $f_0$  with H-V model are shown in Table 4.13. Large discrepancies are found for the conditions of forming speeds at 0.1 mm/s and 1 mm/s. The predicted FLCs at 10 mm/s are shown in Figure 4.28. The predicted FLC at 20°C gives a good evaluation. At 200°C, the predicted FLC overestimated the limit strains in the equi-biaxial zone. At 150°C, high overestimation for the RHS is found, similar as the result presented in Voce\_3 model.

Table 4.12: Calibrated  $f_0$  with Bergström model

Temperature ( °C)	Forming speed (mm/s)	Calibrated $f_0$	Error ( $\bar{\epsilon}_{major}$ )
20	10	0.99995	21%
150	10	0.99995	4.4%
200	10	0.99995	23.5%
150	0.1	0.99995	63%
150	1	0.99995	34%
200	1	0.99995	52.4%

Table 4.13: Calibrated  $f_0$  with H-V model

Temperature ( °C)	Forming speed (mm/s)	Calibrated $f_0$	Gap Error ( $\bar{\epsilon}_{major}$ )
20	10	0.975	3%
150	10	0.999	1.6%
200	10	0.99995	6.8%
150	1	0.99995	13%
200	1	0.99995	43%
150	0.1	0.99995	51%

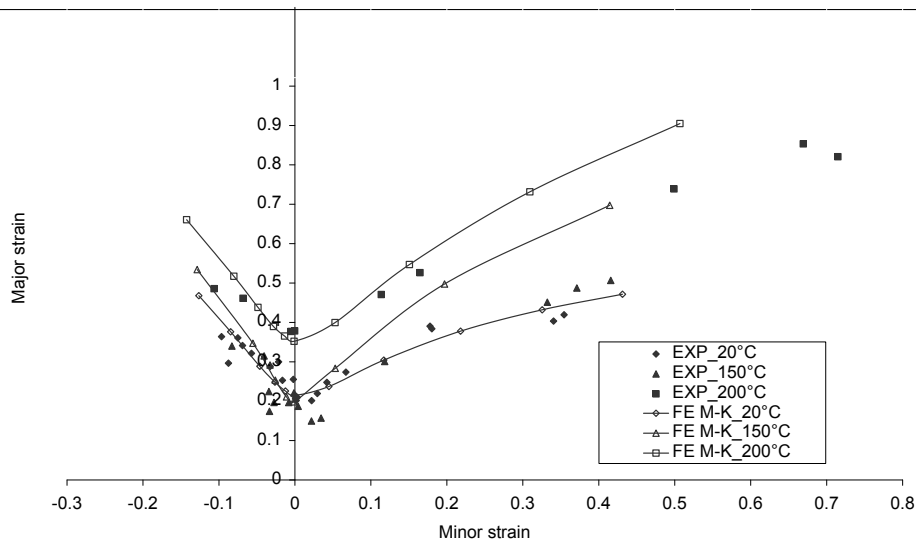


Figure 4.28: Predicted FLCs by H-V model at 10 mm/s

#### 4.4.2.4 Conclusions

Although all the proposed hardening models give globally good descriptions of the flow stresses, they strongly affect the predicted FLCs. The power type hardening models, Ludwick

and KHL models, give a good formability prediction over the whole temperature and strain rate ranges. Due to the high softening stress prediction at high strain levels, the ZA model gives a very low FLC prediction even with a very high  $f_0$  value.

For the saturation type hardening models, only the Voce\_1 hardening model gives a good FLCs prediction over the temperature range at 10 mm/s. For the high values of experimental  $FLC_0$ , it is impossible to find a suitable value of  $f_0$  for all the saturation type models. This behavior can be explained by an overestimation of the saturation phenomenon on the flow stress which can be a consequence of imprecision in the extrapolation of the hardening law at large strains for the Voce type models. For mixed model (H-V), a rather good correlation is observed at 10 mm/s and at 20°C and 200°C.

#### 4.4.3 Predicted FLCs with a constant calibrated $f_0$

As shown above, with  $f_0$  calibration for each forming condition, the FE M-K model is proved to be an effective model to predict the FLCs depending on the choice of hardening model and yield function. But in the literature, the value  $f_0$  is usually defined as a constant fitting value. In [17], the authors give a value of  $f_0$  equals to 0.996 from the framework of microstructure. But most works are carried out at room temperature and constant forming speed which can not give a guideline for the  $f_0$  choice under different temperatures and strain rates. Very few works concern the calibration of the M-K model for temperatures and strain rates.

As presented in chapter 1, for the application of the analytical M-K model at different temperatures, a constant  $f_0$  value equals to 0.996 is adopted in [4] with a Voce hardening model for the FLCs prediction of AA5182-O between 25°C and 260°C. In [49], the FLCs were obtained by analytical M-K model at different temperatures but imperfection  $f_0$  value was not mentioned. Moreover, the two above mentioned research results have not been validated by experimental data.

In the following parts, the FLCs determined by the FE M-K model with a constant value of  $f_0$  are presented. Three typical hardening models (Ludwick, Voce\_1 and H-V) are used in this part. Comparisons between experimental and numerical FLCs are discussed.

##### 4.4.3.1 Temperature influence on the FLCs with a constant $f_0$

The predicted FLCs determined with  $f_0 = 0.996$  by Ludwick model at 10 mm/s are shown in Figure 4.29. The determined FLCs show a good tendency of the temperature sensitivity. But the predicted FLCs deviate from experimental results, especially at 20°C and 150°C. An overestimation of all the predicted  $FLC_0$  values are found compared to experimental results.

To study the imperfection  $f_0$  value influence on the FLCs over the temperature range, the predicted  $FLC_0$  with different hardening models and different values of  $f_0$  at different temperatures under 10 mm/s are presented in Figure 4.31. For the three types of hardening models, the predicted  $FLC_0$  at 150°C give the lowest values whatever the  $f_0$  value is. For a  $f_0$  value higher than 0.996, a drastic  $FLC_0$  increase is found for the three hardening models and the three temperatures. As shown in Figure 4.31(c), for H-V model, with a same  $f_0$  value, the predicted  $FLC_0$  at 200°C is always lower than the one at 20°C.

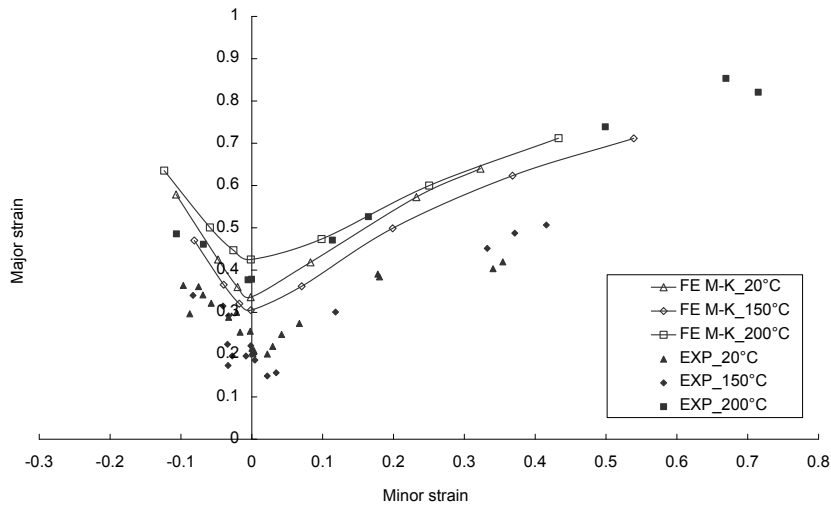


Figure 4.29: Predicted FLCs by Ludwick model with  $f_0 = 0.996$  at 10 mm/s

With the calibrated  $f_0$  values (0.9507, 0.97, 0.9927) according to the experimental data at 20, 150 and 200°C, and at 10 mm/s, the  $FLC_0$  can be determined at various temperatures (from 20 to 200°C). The results from Ludwick model are shown in Figure 4.30. With calibrated  $f_0$  values at 20 and 150°C, too conservative predictions are observed for the  $FLC_0$  value of 200°C. With the calibrated  $f_0$  at 200°C, a good temperature sensitivity is found, but the predicted  $FLC_0$  values are clearly higher than the experimental ones at 20 and 150°C.

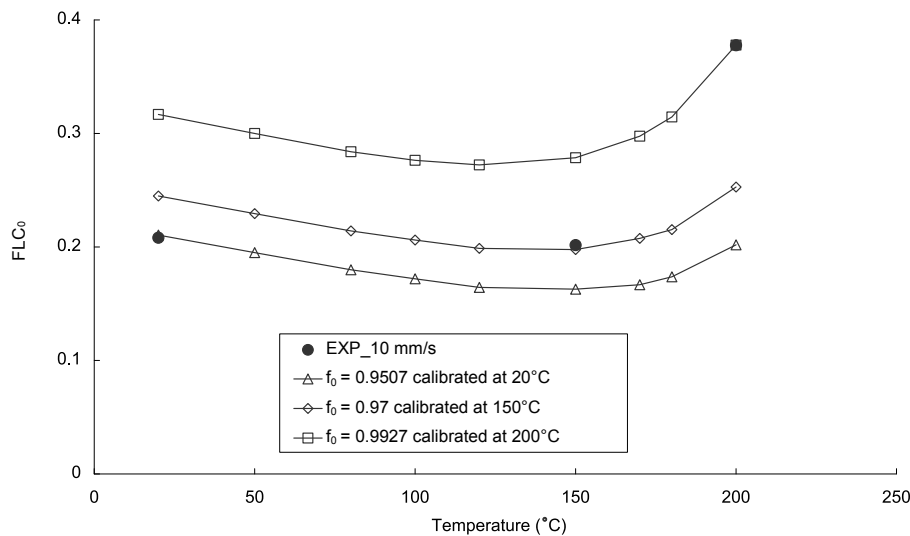
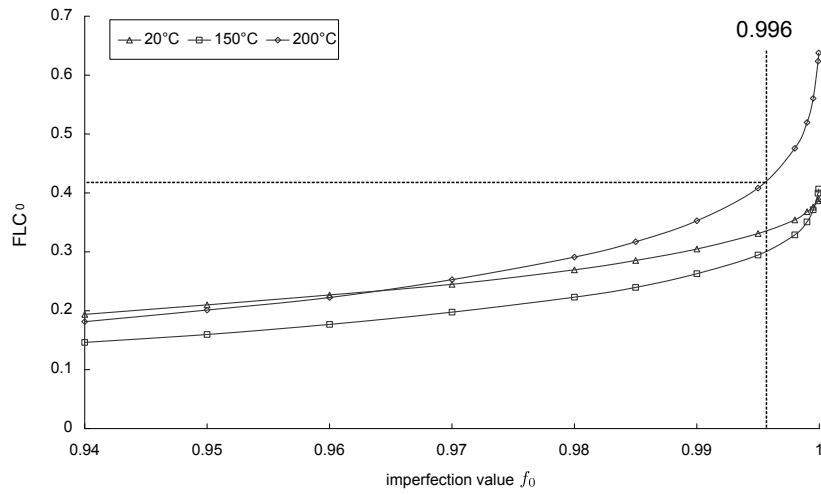
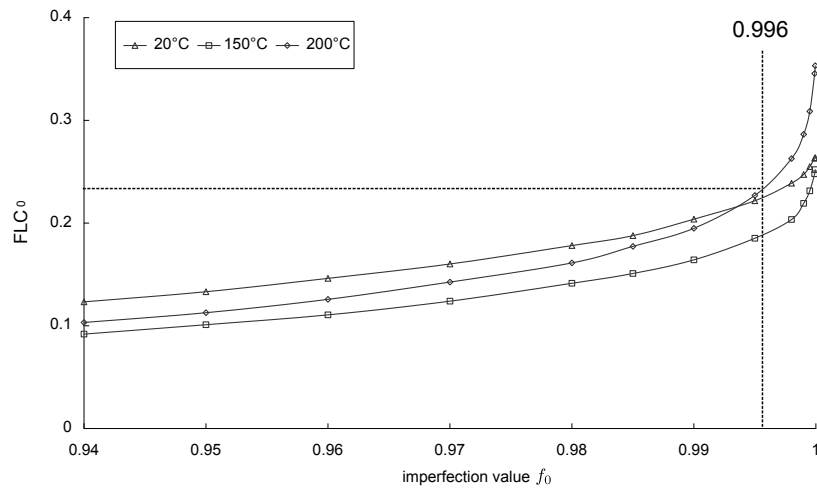


Figure 4.30:  $FLC_0$  by Ludwick model with  $f_0$  calibrated at different temperatures and at 10 mm/s

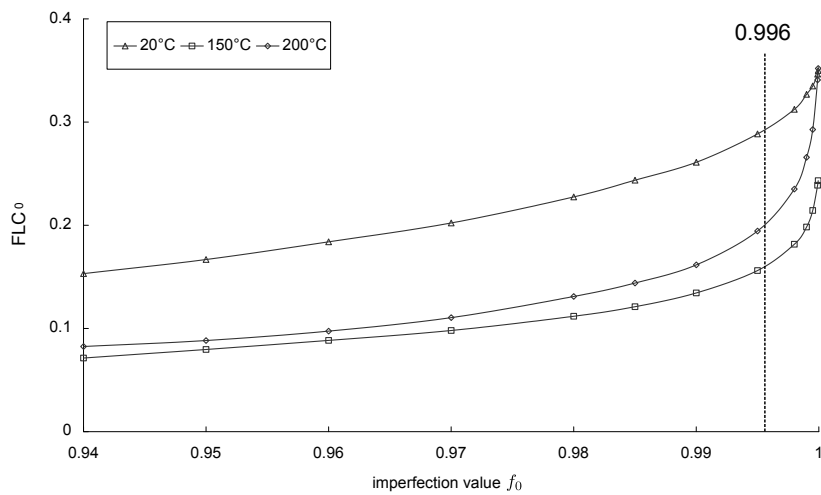
Same procedures are applied to the calibrated  $f_0$  values at the forming speed of 1 mm/s (Figure 4.32). The result with  $f_0$  calibrated at 200°C give a more important trend of the temperature influence.



(a) Ludwick model



(b) Voce\_1 model



(c) H-V model

Figure 4.31:  $FLC_0$  for different  $f_0$  values at 10 mm/s

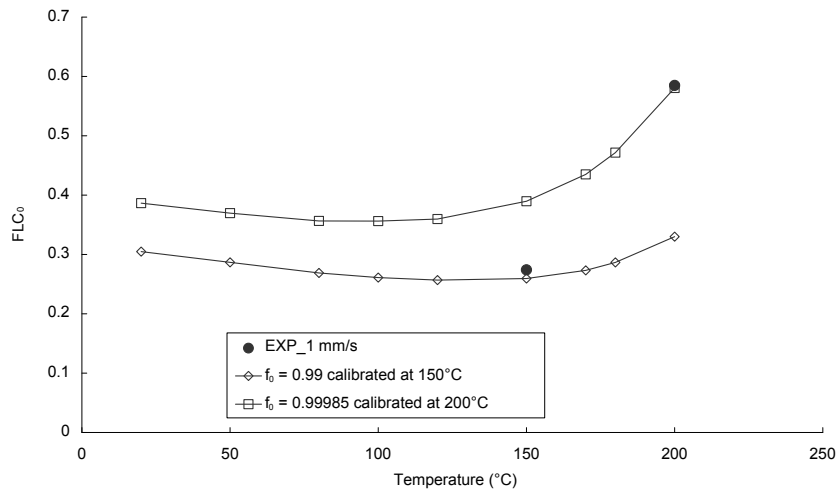


Figure 4.32:  $FLC_0$  by Ludwick model with  $f_0$  calibrated at different temperatures and at 1 mm/s

From the comparison between Figure 4.30 and Figure 4.32, a similar temperature influence tendency on the  $FLC_0$  prediction is found. At a constant forming speed, the predicted formability decreases with increasing temperature until about 120°C. The lowest predicted formability is observed between 120 and 150°C. When the temperature exceeds 150°C, the predicted formability begins to increase. This tendency is much more clear with the  $f_0$  value calibrated at high temperature.

#### 4.4.3.2 Strain rate influence on the FLCs with constant $f_0$

At 150°C, the predicted  $FLC_0$  with different values of  $f_0$  under different forming speeds from Ludwick and Voce\_1 model are shown in Figure 4.33 and Figure 4.34. The results show that there is no strain rate influence on the predicted  $FLC_0$  at 150°C whatever the values of  $f_0$  are adopted. This prediction is in contradiction with the experimental observed formability strain rate sensitivity phenomenon at 150°C.

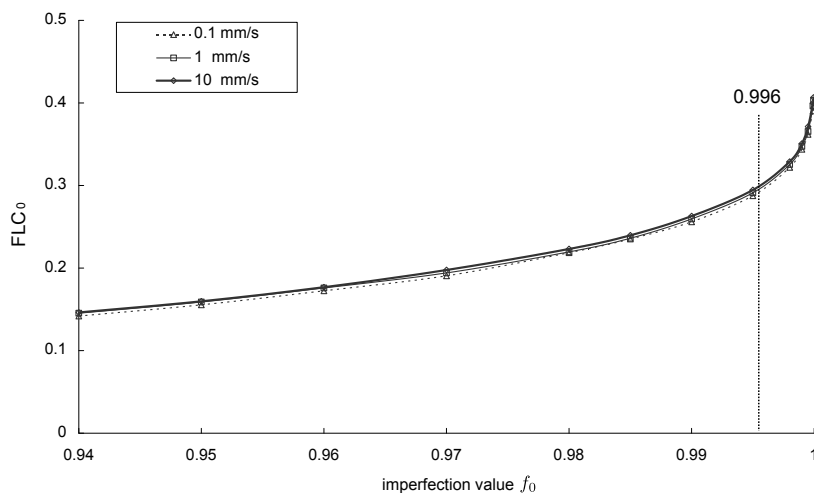


Figure 4.33:  $FLC_0$  with different values of  $f_0$  from Ludwick model at 150°C

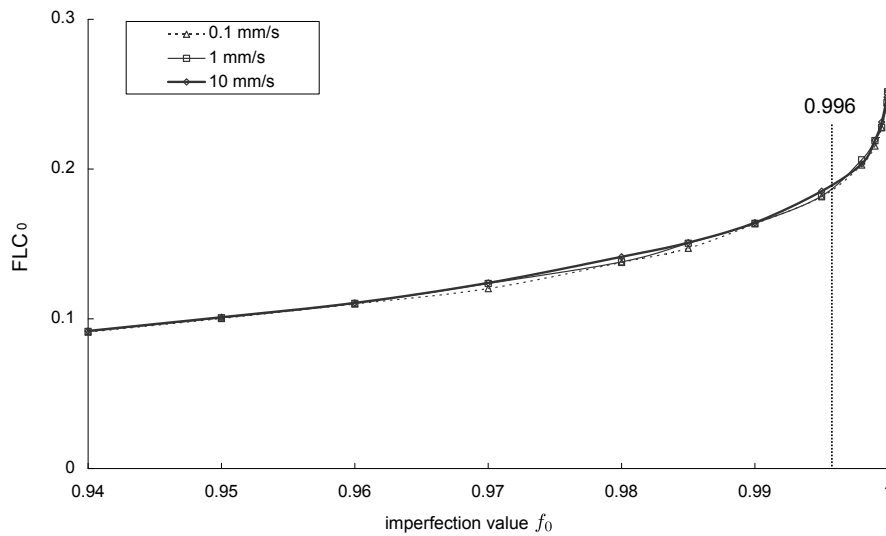


Figure 4.34:  $FLC_0$  with different values of  $f_0$  from Voce\_1 model at 150°C

The predicted  $FLC_0$  with different values of  $f_0$  at 200°C are shown in Figure 4.35. A strain rate influence on the  $FLC_0$  can be observed at 200°C which can be explained by the strain rate sensitivity index ( $m = m_0 \exp(m_1 T)$ ) at 200°C. Unfortunately, contrary to experimental results, a weak positive strain rate influence is found for all the  $f_0$  values.

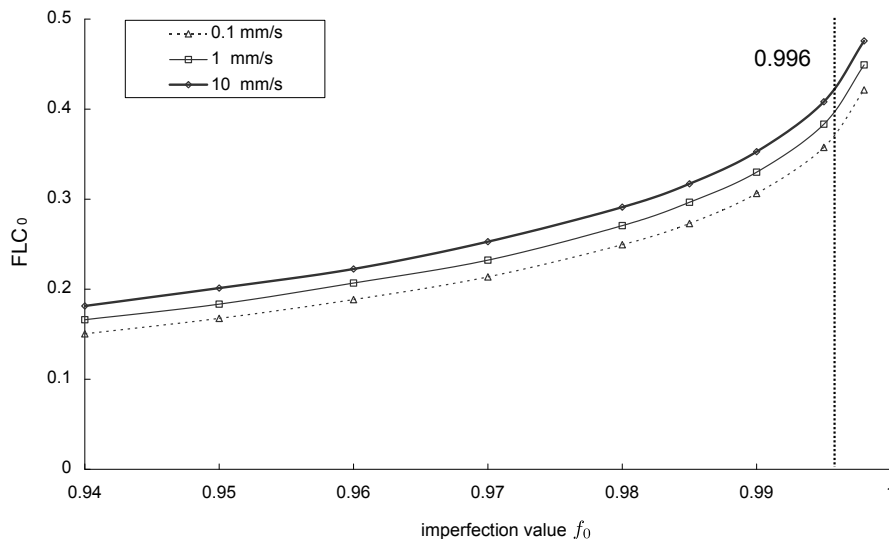


Figure 4.35:  $FLC_0$  with different values of  $f_0$  by Ludwick model at 200°C

With the calibrated  $f_0$  values (0.99985, 0.99, 0.97) according to experimental data (0.1, 1 and 10 mm/s, at 150°C), the  $FLC_0$  from Ludwick model at different forming speeds (0.1, 1 and 10 mm/s) are shown in Figure 4.36. As in Figure 4.33, no strain rate sensitivity is observed.

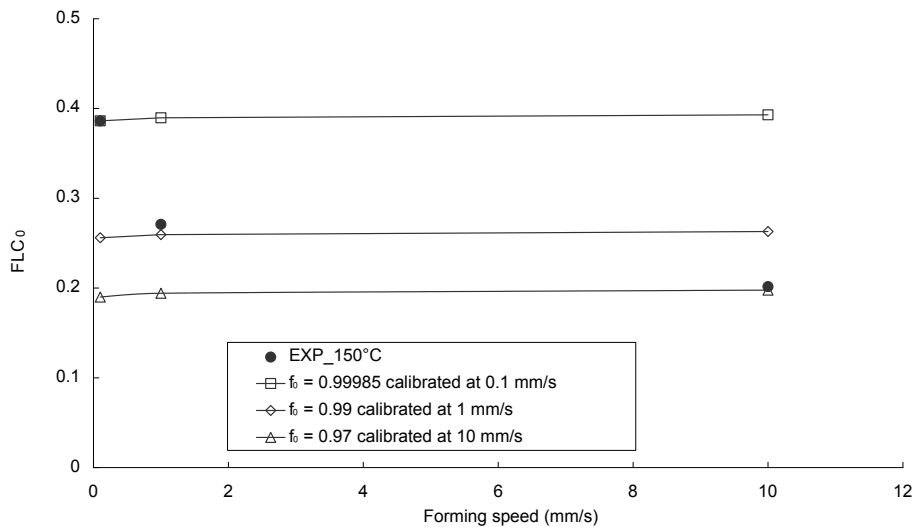


Figure 4.36:  $FLC_0$  from Ludwick model with different calibrated  $f_0$  at different forming speeds and at 150°C

The same procedure is applied to experimental data at 200°C. As shown in Figure 4.35, a weak positive strain rate effect is observed which is in contrast with the experimental result.

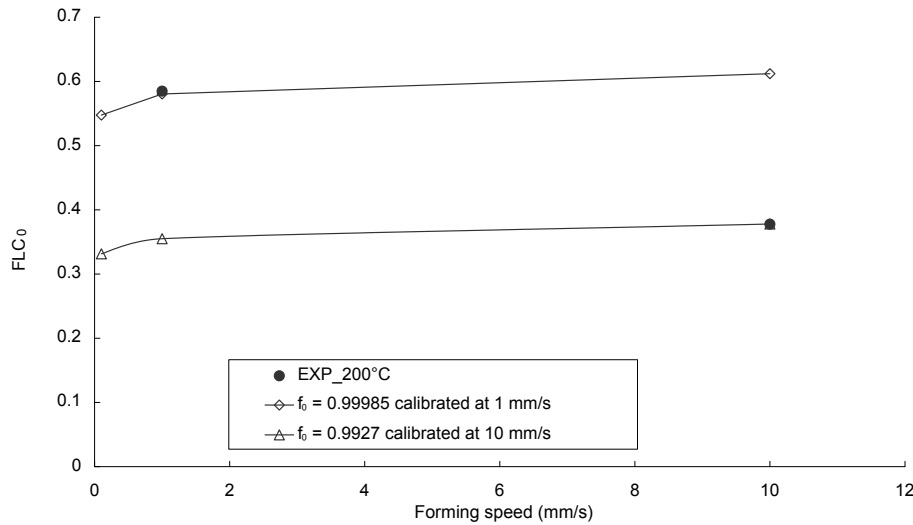


Figure 4.37:  $FLC_0$  from Ludwick model with different calibrated  $f_0$  at different forming speeds and at 200°C

#### 4.4.3.3 Conclusions

The temperature and strain rate influences on the formability have been carried out with the FE M-K model and a constant initial imperfection value  $f_0$ . With an appropriate hardening model, a good temperature influence tendency can be obtained but the predicted results deviate from experimental ones. The predicted  $FLC_0$  is shown to be strain rate independent at 150°C and strain rate dependent with a weak positive sensitivity at 200°C. While the strain rate is proved to have a negative influence on the experimental formability at 150 and 200°C. In conclusion, it seems unsuitable to adopt a constant initial imperfection value whatever the choice of the hardening law.

## 4.5 Conclusions

In this chapter, the formability of an AA5086 sheet metal under different temperatures and strain rates has been investigated numerically with the FE Marciniak and FE M-K models. From these numerical investigations, the following conclusions are obtained:

- It is shown that the FE Marciniak model is inadequate for determining the FLCs under different temperatures and strain rates.
- As the analytical M-K model, the FE M-K model is very sensitive to the initial imperfection value  $f_0$ , the yield function (for the RHS) and the hardening law. The FE M-K model allows to easily implement complex thermo-elastoviscoplastic behavior. Large values of  $f_0$  increase the FLCs levels.
- The calibration of the initial imperfection from experimental plane strain point seems to be the more efficient strategy. When the initial imperfection  $f_0$  value is calibrated on each forming condition, the FE M-K model can be an efficient tool for predicting sheet metal formability.
- For a given  $f_0$  value, the FE M-K model can predict the positive temperature effect while it is almost insensitive to the strain rate.
- Different types of hardening models have been used in the FE M-K model to determine the FLCs. The power law type hardening model (Ludwick and KHL) gives the best formability prediction over the tested temperature and strain rate ranges compared to experimental data whereas the saturation and mixed types hardening models do not agree with experimental observations.

# Conclusions and perspectives

---

L'objectif principal de ce travail consistait à apporter une contribution à l'étude des effets de conditions opératoires, en l'occurrence la température et la vitesse de déformation, sur la formabilité de tôles d'alliage d'aluminium 5086. Pour remplir cet objectif, une campagne expérimentale de tracé de Courbes Limites de Formage (CLF) complètes et l'étude d'un modèle prédictif ont été menées.

Une campagne d'essai a été réalisée sur cet alliage d'aluminium à partir d'un montage de type Marciniak. Ce montage s'est avéré assez efficace pour tracer des courbes limites de formage (CLF) complètes sur une plage de température allant de l'ambient jusqu'à 200°C et sur une plage de vitesse de déformation allant du quasi-statique jusqu'à 2s<sup>-1</sup>. Ces essais ont clairement mis en évidence un effet positif de la température et un effet négatif de la vitesse de déformation sur la formabilité de cet alliage. L'effet de la vitesse de déformation est relativement marqué sur cette gamme modérée de température puisque une augmentation des vitesses de mise en forme peut compenser le gain de formabilité provenant d'une augmentation de la température de chauffe de la tôle. La qualité finale du produit est donc directement liée au choix de ces conditions opératoires. Ce choix peut être réalisé à partir d'une optimisation numérique du procédé si le comportement rhéologique et les limites de formabilité du matériau sont connus avec une précision suffisante.

La revue bibliographique a montré que la prise en compte de la température et de la vitesse de déformation dans les modèles prédictifs des CLF est à ce jour relativement limitée. Peu de modèles proposent une corrélation directe avec des résultats de caractérisation expérimentale des limites de formabilité. L'objectif était donc de voir si un modèle était capable de prédire ces effets et surtout de corréliser les précédents résultats expérimentaux. Le modèle proposé consiste en la simulation par la méthode des éléments finis du modèle géométrique de Marciniak et Kuczynski (M-K). Les résultats de ce modèle sont très sensibles à la modélisation du comportement rhéologique du matériau et à la calibration du défaut géométrique pilotant l'apparition de la striction.

Grâce à des essais de traction uniaxiale réalisés pour les mêmes conditions opératoires que celles des essais de formabilité de Marciniak, plusieurs familles de lois d'écrouissage ont été identifiées. Ces lois conduisent à des comportements très différents pour des grandes déformations. Le niveau modéré de déformation atteint par l'essai de traction simple ne permettant pas de choisir la loi la plus adaptée.

L'introduction de ces lois dans le modèle conduit à des prédictions très différentes de la formabilité du matériau pour une valeur donnée du défaut géométrique. L'utilisation du point expérimental de la CLF pour des conditions de déformation plane permet un bon calibrage du défaut et surtout une très bonne description de la CLF complète par rapport aux résultats expérimentaux. La procédure de calibration a été effectuée pour toutes les lois et il est démontré que la valeur du défaut géométrique ne pouvait pas rester constante quelles que soient les conditions opératoires étudiées. Néanmoins, l'utilisation d'un seul point expérimental permet un tracé relativement précis des CLF en température et en vitesse de déformation lorsque des lois de type puissance sont utilisées (Ludwick, KHL). Certaines lois se sont avérées incapables de prédire la formabilité du matériau pour certaines conditions. Finalement, pour une valeur de défaut donnée, le modèle M-K permet de représenter l'effet positif de la température sur la formabilité. Par contre, pour un même défaut, le modèle est assez peu sensible à l'effet de la vitesse de déformation. Après une phase de calibration, le modèle M-K peut donc permettre la prédiction de CLF pour différentes conditions opératoires, il resterait à donner un sens un peu plus physique à la valeur du défaut géométrique afin de justifier son évolution avec la température et/ou la vitesse de déformation.

Suite à ces travaux, plusieurs perspectives de recherche peuvent être envisagées afin d'améliorer la prédiction des CLF.

- *Ce travail a montré que l'utilisation d'un seul point de la CLF expérimentale, en déformation plane, permettait de recalculer correctement les prédictions du modèle quel que soit l'état de déformation considéré. Il serait alors intéressant de mener une campagne expérimentale sur une plage de température et de vitesse plus large et plus complète à partir d'une seule géométrie d'éprouvette afin de bien identifier les effets couplés de ces conditions.*
- *Les prédictions du modèle M-K sont très sensibles au choix de la loi d'écrouissage et du critère de plasticité caractérisant le matériau. Compte tenu de cette grande sensibilité, le modèle prédictif des CLF pourrait être intégré dans une boucle d'identification des paramètres rhéologiques du matériau et permettre ainsi une bonne définition de son comportement pour des grandes déformations.*
- *Enfin, le choix de la valeur du défaut géométrique reste un frein à l'utilisation du modèle M-K. Récemment, un nouveau modèle basé sur une forme cruciforme a été proposé par l'équipe, il a été validé à température ambiante et en quasi-statique. Il permet de décrire la courbe limite de formage sans phase de calibration. L'intégration des différentes lois identifiées dans ce modèle permettra peut-être de fournir une solution alternative à l'utilisation du modèle M-K pour les conditions opératoires étudiées.*

# Conclusions and perspectives

---

The main objective of this work was to study the temperature and strain rate effects on the formability of AA5086 sheet. With this object, experimental investigations on the FLCs and study of a predictive model have been performed.

An existing Marciniak test setup has been used to experimentally evaluate the formability of this aluminium alloy sheet. With this device, whole FLCs from ambient temperature up to 200°C and over a strain rate range from quasi-static to  $2s^{-1}$  have been plotted. From these experimental tests, positive temperature and negative strain rate effects on the formability have been observed. Although the studied temperature range is limited, the strain rate sensitivity plays an important role on the formability of this AA5086 on the tested temperature range. The formability improvement due to the temperature effect can be compensated by the increase of the forming speed. The quality of the final part greatly depends on the operating conditions. Also, the parameters of the forming process could be optimized numerically if both accurate rheological behavior and forming limit strains of the studied material are available.

The literature review has showed that the predictive models to determine the FLCs taking into account temperature and strain rate effect were relatively rare and that few models propose a direct comparison with experimental results. Hence, the objective of this work was to verify the validity of a model to predict temperature and strain rate effects on the FLC and to give a good correlation with experimental results. A Finite Element M-K model based on the Marciniak and Kuzynski theory is proposed. These model predictions are very sensitive to the initial imperfection value which causes the onset of necking and it also greatly depends on the modeling of the rheological behavior of the material.

Uniaxial tensile tests have been performed at different temperatures and tensile speeds corresponding to the same forming conditions as Marciniak tests. With this database, several types of hardening models have been identified. These models give very different flow stress predictions for large strains. Due to the limited strain level reached in the uniaxial tensile test, the choice of the more appropriate hardening model is not a simple task.

For a given  $f_0$  imperfection value, the FE M-K model gives very different predictions for the identified hardening models. With the calibrated  $f_0$  imperfection value from experimental data corresponding to the plane strain condition, a good correlation is obtained between the whole predicted and experimental FLCs. The  $f_0$  imperfection values have been calibrated with all the proposed hardening models and the results show that the  $f_0$  value can not remain constant for the different forming conditions. Nevertheless, the  $f_0$  calibration from a single experimental point corresponding to the  $FLC_0$  gives relatively precise FLCs predictions at different temperatures and strain rates for the power law type models (Ludwick and KHL). Some hardening models seem to be unsuitable to predict the AA5086 formability under different forming conditions. Finally, for a given imperfection  $f_0$  value, the FE M-K model can predict the positive temperature effect on the formability while it is almost insensitive to the strain rate. Also after a calibration stage, the FE M-K model could be used as an effective tool to predict the FLCs for different operating conditions. A physical signification

of the evolution of imperfection value according to temperature and/or strain rate could be justified.

According to this work, several perspectives may be envisaged to improve the FLC prediction.

- This work has proved that with the single experimental  $FLC_0$  point, the FE M-K model succeed in predicting the FLC for the whole strain paths. It could be interesting to determine the formability with a single specimen, over a wider range of temperature and strain rate, to well identify the coupling effect of temperature and strain rate.
- The predictions of the FE M-K model are very sensitive to the hardening model and yield function. Due to this high sensitivity, this predictive model could be integrated into the material rheological parameter identification procedure to obtain a good definition of the material rheological behavior for large strains.
- Finally, the choice of the initial imperfection value is still a difficulty for the use of the FE M-K model. Recently, a new FE model based on a cruciform shape has been proposed in our group to determine the FLC without the calibration stage. This model has been validated at ambient temperature and for quasi-static conditions. The integration of the identified hardening laws in this model may provide an alternative to the use of the FE M-K model.



# Bibliography

- [1] International standard ISO 12004-2: 2008 metallic materials - sheet and strip - determination of forming-limit curves - part 2: Determination of forming-limit curves in the laboratory, 2008.
- [2] N. Abedrabbo, F. Pourboghrat, and J. Carsley. Forming of aluminum alloys at elevated temperatures - part 1: Material characterization. *International Journal of Plasticity*, 22(2):314 – 341, 2006.
- [3] N. Abedrabbo, F. Pourboghrat, and J. Carsley. Forming of aluminum alloys at elevated temperatures - part 2: Numerical modeling and experimental verification. *International Journal of Plasticity*, 22(2):342 – 373, 2006.
- [4] N. Abedrabbo, F. Pourboghrat, and J. Carsley. Forming of AA5182-o and AA5754-o at elevated temperatures using coupled thermo-mechanical finite element models. *International Journal of Plasticity*, 23(5):841 – 875, 2007.
- [5] M. Aghaie-Khafri and R. Mahmudi. Predicting of plastic instability and forming limit diagrams. *International Journal of Mechanical Sciences*, 46(9):1289 – 1306, 2004.
- [6] S. Ahmadi, A. Eivani, and A. Akbarzadeh. An experimental and theoretical study on the prediction of forming limit diagrams using new bbc yield criteria and m-k analysis. *Computational Materials Science*, 44(4):1272 – 1280, 2009.
- [7] K. Ankamma, P. R. Reddy, S. Nagarjuna, G. C. M. Reddy, M. Komaraiah, and N. E. Prasad. Numerical simulation for determination of limit strains of a cold rolled and solution treated nimonic C-263 alloy sheet. *The Bulletin of Materials Science*, 34:515 – 524, 2011.
- [8] H. Aretz. Numerical restrictions of the modified maximum force criterion for prediction of forming limits in sheet metal forming. *Modelling and Simulation in Materials Science and Engineering*, 12:677 – 692, 2004.
- [9] H. Aretz. An extension of Hill’s localized necking model. *International Journal of Engineering Science*, 48:312 – 331, 2010.
- [10] D. Bae and A. Ghosh. A planar simple shear test and flow behavior in a superplastic Al-Mg alloy. *Metallurgical and Materials Transactions A*, 34A:2465 – 2471, 2003.
- [11] D. Banabic. *Sheet Metal Forming Processes: Constitutive Modelling and Numerical Simulation*. Springer, 2010.

- 
- [12] D. Banabic, H. Aretz, D. S. Comsa, and L. Paraianu. An improved analytical description of orthotropy in metallic sheets. *International Journal of Plasticity*, 21(3):493 – 512, 2005.
- [13] D. Banabic, H. Aretz, L. Paraianu, and P. Jurco. Application of various FLD modelling approaches. *Modelling and Simulation in Materials Science and Engineering*, 13:759 – 769, 2005.
- [14] D. Banabic, S. Comsa, P. Jurco, G. Cosovici, L. Paraianu, and D. Julean. FLD theoretical model using a new anisotropic yield criterion. *Journal of Materials Processing Technology*, 157-158:23–27, 2004.
- [15] D. Banabic and E. Dannenmann. Prediction of the influence of yield locus on the limit strains in sheet metals. *Journal of Materials Processing Technology*, 109(1-2):9 – 12, 2001.
- [16] D. Banabic and K. Siegert. Anisotropy and formability of AA5182-o aluminium alloy sheets. *CIRP Annals - Manufacturing Technology*, 53:219 – 222, 2004.
- [17] F. Barlat and O. Richmond. Modelling macroscopic imperfections for the prediction of flow localization and fracture. *Fatigue and fracture of engineering materials and structures*, 26:311 – 321, 2003.
- [18] M. Ben Tahar. *Contribution à l'étude et la simulation du procédé d'hydroformage*. PhD thesis, École des Mines de Paris, 2005.
- [19] Y. Bergström. Dislocation model for the stress-strain behaviour of polycrystalline alpha-iron with special emphasis on the variation of the densities of mobile and immobile dislocations. *Materials Science and Engineering*, 5:193 – 200, 1969.
- [20] Y. Bergström. The plastic deformation of metals - a dislocation model and its applicability. *Reviews on Powder Metallurgy and Physical Ceramics*, 2:105 – 115, 1983.
- [21] E. Billur and M. Koç. A comparative study on hydraulic bulge testing and analysis methods. In *Proceedings of the 2008 international manufacturing science and engineering conference (MSEC2008)*, Evanston, IL, USA., 2008.
- [22] H. Bo, L. Zhong-qin, L. Shu-hui, and Y. Zhong-qi. Prediction of forming limit in virtual sheet metal forming based on thickness gradient criterion. In *Numisheet 2008, Interlaken, Switzerland*, 2008.
- [23] S. Bodner and P. Y. Constitutive equations for elastic-viscoplastic strain-hardening materials. *Journal of Applied Mechanics*, pages 385 – 389, 1975.
- [24] N. Bonora and P. Milella. Constitutive modeling for ductile behavior incorporating strain rate, temperature, and damage mechanics. *International Journal of Impact Engineering*, 26:53 – 64, 2001.

- [25] M. C. Butuc, J. J. Gracio, and A. B. da Rocha. A theoretical study on forming limit diagrams prediction. *Journal of Materials Processing Technology*, 142(3):714 – 724, 2003.
- [26] S. Chen, C. Huang, C. Wang, and Z. Duan. Mechanical properties and constitutive relationships of 30CrMnSiA steel heated at high rate. *Materials Science and Engineering A*, pages 105 – 108, 2008.
- [27] A. B. da Rocha, F. Barlat, and J. Jalinier. Prediction of the forming limit diagrams of anisotropic sheets in linear and non-linear loading. *Materials Science and Engineering*, 68:151–164, 1984 - 1985.
- [28] S. Diot. *Caractérisation expérimentale et numérique du comportement dynamique des matériaux*. PhD thesis, Institut National des Sciences Appliquées de Rennes, 2003.
- [29] S. Diot, D. Guines, A. Gavras, and E. Ragneau. Minimization of friction influence on the evaluation of rheological parameters from compression test: Application to a forging steel behavior identification. *Journal of Engineering Materials and Technology*, 131, 2009.
- [30] M. Ganjani and A. Assempour. An improved analytical approach for determination of forming limit diagrams considering the effects of yield functions. *Journal of Materials Processing Technology*, 182(1-3):598 – 607, 2007.
- [31] A. Gavras, B. Davoodi, and E. Ragneau. A study of material constitutive behaviour at elevated temperature from compressive SPHB test using an inverse analysis method. *Journal de Physique IV*, 134:661 – 666, 2006.
- [32] A. Graf and W. Hosford. The influence of strain-path changes on forming limit diagrams of Al 6111 T4. *International Journal of Mechanical Sciences*, 36:897–910, 1994.
- [33] D. E. Green, K. W. Neale, S. R. MacEwen, A. Makinde, and R. Perrin. Experimental investigation of the biaxial behaviour of an aluminum sheet. *International Journal of Plasticity*, 20(8-9):1677 – 1706, 2004.
- [34] Z. Gronostajski. The constitutive equations for FEM analysis. *Journal of Materials Processing Technology*, 106(1-3):40 – 44, 2000.
- [35] W.-G. Guo and S. Nemat-Nasser. Flow stress of Nitronic-50 stainless steel over a wide range of strain rates and temperatures. *Mechanics of Materials*, 38(11):1090 – 1103, 2006.
- [36] G. Gutscher, H.-C. Wu, G. Ngaile, and T. Altan. Determination of flow stress for sheet metal forming using the viscous pressure bulge (VPB) test. *Journal of Materials Processing Technology*, 146(1):1 – 7, 2004.
- [37] R. Hill. On discontinuous plastic states, with special reference to localized necking in thin sheets. *Journal of the Mechanics and Physics of Solids*, 1:19–30, 1952.

- [38] K. Ho, J. Lin, and T. Dean. Constitutive modelling of primary creep for age forming an aluminium alloy. *Journal of Materials Processing Technology*, 153 - 154:122 – 127, 2004.
- [39] P. Hora, L. Tong, and J. Reissner. Mathematical prediction of FLC using macroscopic instability criteria combined with microstructural crack propagation models. *In Proceeding of palsticity 03*, pages 364 – 366, 2003.
- [40] S. Huang and A. Khan. Modeling the mechanical behavior of 1100-0 aluminum at different strain rates by the Bodner-Partom model. *International Journal of Plasticity*, 8:501–517, 1992.
- [41] J. Hutchinson, K. Neale, and A. Needleman. Mechanics of sheet metal forming. *New York / London, Plenum Press*, pages 269 – 285, 1978.
- [42] H.Vegter, C. ten Horn, and M. Abspoel. Modeling of the forming limit curve by MK analysis and FE simulations. *NUMISHEET*, 2008.
- [43] P.-P. Jeunechamps, K. Ho, J. Lin, J.-P. Ponthot, and T. Dean. A closed form technique to predict springback in creep age-forming. *International Journal of Mechanical Sciences*, 48(6):621 – 629, 2006.
- [44] M. Jie, C. Cheng, L. Chan, C. Chow, and C. Tang. Experimental and theoretical analysis on formability of aluminum tailor-welded blanks. *Journal of Engineering Materials and Technology*, 129:151, 2007.
- [45] G. Johnson and W. Cook. A constitutive model and data for metals subjected to large strains, high strain rates, and high temperatures. *Proceedings of the 7th International Symposium on Ballistics*, 1983.
- [46] W. Johnston, W. Pollock, and D. Dawicke. Biaxial testing of 2195 aluminium alloy using cruciform specimen. *Analytical Services and Materials, Inc.Hampton, Virginia*, 2002.
- [47] R. Kapoor and S. Nemat-Nasser. Comparison between high strain-rate and low strain-rate deformation of tantalum. *Metallurgical and Materials Transactions A*, 31 A:815 – 823, 1999.
- [48] A. Karafillis and M. Boyce. A general anisotropic yield criterion using bounds and a transformation weighting tensor. *Journal of the Mechanics and Physics of Solids*, 41:1859 – 1886, 1993.
- [49] A. S. Khan and M. Baig. Anisotropic responses, constitutive modeling and the effects of strain-rate and temperature on the formability of an aluminum alloy. *International Journal of Plasticity*, 27:522 – 538, 2011.
- [50] A. S. Khan and S. Huang. Experimental and theoretical study of mechanical behavior of 1100 aluminum in the strain rate range 10<sup>-5</sup>-10<sup>4</sup>s<sup>-1</sup>. *International Journal of Plasticity*, 8(4):397 – 424, 1992.

- [51] A. S. Khan and R. Liang. Behaviors of three BCC metal over a wide range of strain rates and temperatures: experiments and modeling. *International Journal of Plasticity*, 15(10):1089 – 1109, 1999.
- [52] S. Kim, H. Huh, H. Bok, and M. Moon. Forming limit diagram of auto-body steel sheets for high-speed sheet metal forming. *Journal of Materials Processing Technology*, 211(5):851 – 862, 2011. Special Issue: Impulse Forming.
- [53] J. Klepaczko. Thermally activated flow and strain rate history effects for some polycrystalline FCC metals. *Materials Sci and Engng*, 18:121 – 135, 1975.
- [54] J. Klepaczko. A practical stress-strain-strain rate-temperature constitutive relations of the power form. *J. Mech. Working technology*, 15:25 – 39, 1987.
- [55] U. Kocks, A. Argon, and M. Ashby. Thermodynamics and kinematics of slip. *Progress in Materials Science, Pergamon Press, New York*, 19, 1975.
- [56] A. Korhonen and T. Manninen. Forming and fracture limits of austenitic stainless steel sheets. *Materials Science and Engineering: A*, 488(1–2):157 – 166, 2008.
- [57] D. Li and A. Ghosh. Tensile deformation behavior of aluminum alloys at warm forming temperatures. *Materials Science and Engineering: A*, 352(1-2):279 – 286, 2003.
- [58] D. Li and A. K. Ghosh. Biaxial warm forming behavior of aluminum sheet alloys. *Journal of Materials Processing Technology*, 145(3):281 – 293, 2004.
- [59] M. Li and A. Chandra. Influence of strain-rate sensitivity on necking and instability in sheet metal forming. *Journal of materials processing technology*, 96:133–138, 1999.
- [60] R. Liang and A. S. Khan. A critical review of experimental results and constitutive models for BCC and FCC metals over a wide range of strain rates and temperatures. *International Journal of Plasticity*, 15:963 – 980, 1999.
- [61] Y. Lin, M.-S. Chen, and J. Zhong. Prediction of 42crmo steel flow stress at high temperature and strain rate. *Mechanics Research Communications*, 35(3):142 – 150, 2008.
- [62] Y. Lin and X.-M. Chen. A combined Johnson-Cook and Zerilli-Armstrong model for hot compressed typical high-strength alloy steel. *Computational Materials Science*, 49(3):628 – 633, 2010.
- [63] Y. Lin, Y.-C. Xia, X.-M. Chen, and M.-S. Chen. Constitutive descriptions for hot compressed 2124-t851 aluminum alloy over a wide range of temperature and strain rate. *Computational Materials Science*, 50(1):227 – 233, 2010.
- [64] Z. Liu. *Numerical and experimental study of AZ31-O magnesium alloy warm sheet forming*. PhD thesis, École nationale supérieure des mines de Paris, 2012.
- [65] C. MacGregor and J. Fisher. A velocity modified temperature for the plastic flow of metals. *Journal of Applied Mechanics*, 13:11 – 16, 1946.

- [66] S. Mahabunphachai and M. Koç. Investigations on forming of aluminum 5052 and 6061 sheet alloys at warm temperatures. *Materials and Design*, 31(5):2422 – 2434, 2010.
- [67] W. Mailer and K. POhandt. New experiments for determining yield loci of sheet metal. *Journal of Materials Processing Technology*, 60:643 – 648, 1996.
- [68] Z. Marciniak and K. Kuczynski. Limit strains in the processes of stretch-forming sheet metal. *International Journal of Mechanical Sciences*, 9(9):609 – 620, 1967.
- [69] A. Martinez Lopez and A. Boogaard van den. Formability limit curves under stretch-bending. In *15th International Deep Drawing Research Group Conference, IDDRG, Bilbao, Spain*, 2011.
- [70] M. Merklein, A. Kuppert, and M. Geiger. Time dependent determination of forming limit diagrams. *CIRP Annals - Manufacturing Technology*, 59(1):295 – 298, 2010.
- [71] R. Mesrar, S. Fromentin, R. Makkouk, M. Martiny, and G. Ferron. Limits to ductility of metal sheets subjected to complex strain-paths. *International Journal of Plasticity*, 14:391–411, 1998.
- [72] T. Naka, G. Torikai, R. Hino, and F. Yoshida. The effects of temperature and forming speed on the forming limit diagram for type 5083 aluminum-magnesium alloy sheet. *Journal of Materials Processing Technology*, 113(1-3):648 – 653, 2001.
- [73] T. Naka, T. Uemori, R. Hino, M. Kohzu, K. Higashi, and F. Yoshida. Effects of strain rate, temperature and sheet thickness on yield locus of AZ31 magnesium alloy sheet. *Journal of Materials Processing Technology*, 201(1-3):395 – 400, 2008.
- [74] K. Narasimhan and R. Wagoner. Finite element modeling simulation of in-plane forming limit diagrams of sheets containing finite defects. *Metallurgical and Materials Transactions A*, 22A:2655–2665, 1990.
- [75] C. J. Neil and S. R. Agnew. Crystal plasticity-based forming limit prediction for non-cubic metals: Application to Mg alloy AZ31B. *International Journal of Plasticity*, 25(3):379 – 398, 2009.
- [76] S. Nemat-Nasser and J. Isaacs. Direct measurement of isothermal flow stress of metals at elevated temperatures and high strain rates with application to Ta and TaW alloys. *Acta Materialia*, 45(3):907 – 919, 1997.
- [77] Q. Nie and D. Lee. The effect of rate-sensitivity on history dependent forming limit of anisotropic sheet metals. *Journal of Materials Shaping Technology*, 9:233–240, 1991.
- [78] V. Nohajová, K. Masláková, M. Štamborská, and Z. Bobovský. Brief description and application of bonder-partom model. In *Modelling of mechanical and mechatronic systems*, 2011.
- [79] G. Palumbo, D. Sorgente, and L. Tricarico. A numerical and experimental investigation of AZ31 formability at elevated temperatures using a constant strain rate test. *Materials and Design*, 31(3):1308 – 1316, 2010.

- [80] G. Palumbo and L. Tricarico. Numerical and experimental investigations on the warm deep drawing process of circular aluminum alloy specimens. *Journal of Materials Processing Technology*, 184(1-3):115 – 123, 2007.
- [81] T. Pepelnjak and K. Kuzman. Numerical determination of the forming limit diagrams. *Journal of Achievements in Materials and Manufacturing Engineering*, 20:375 – 378, 2007.
- [82] A. Petek, T. Pepelnjak, and K. Kuzman. An improved method for determining forming limit diagram in the digital environments. *Journal of Mechanical Engineering*, 51:330 – 345, 2005.
- [83] R. Picu, G. Vincze, F. Ozturk, J. Gracio, F. Barlat, and A. Maniatty. Strain rate sensitivity of the commercial aluminum alloy AA5182-O. *Materials Science and Engineering A*, 390(1-2):334 – 343, 2005.
- [84] S. M. Rehlaender. *Plane strain compression testing of aluminium alloy 6061 at elevated temperatures*. PhD thesis, The university of british columbia, 1994.
- [85] A. Rusinek and J. R. Klepaczko. Shear testing of a sheet steel at wide range of strain rates and a constitutive relation with strain-rate and temperature dependence of the flow stress. *International Journal of Plasticity*, 17(1):87 – 115, 2001.
- [86] A. Rusinek and J. Rodríguez-Martínez. Thermo-viscoplastic constitutive relation for aluminium alloys, modeling of negative strain rate sensitivity and viscous drag effects. *Materials and Design*, 30(10):4377 – 4390, 2009.
- [87] A. Rusinek, J. Rodríguez-Martínez, and A. Arias. A thermo-viscoplastic constitutive model for FCC metals with application to OFHC copper. *International Journal of Mechanical Sciences*, 52(2):120 – 135, 2010.
- [88] A. Rusinek, R. Zaera, and J. Klepaczko. Constitutive relations in 3-D for a wide range of strain rates and temperatures - application to mild steels. *International Journal of Solids and Structures*, 44(17):5611 – 5634, 2007.
- [89] A. Rusinek, R. Zaera, J. Klepaczko, and R. Cheriguene. Analysis of inertia and scale effects on dynamic neck formation during tension of sheet steel. *Acta Materialia*, 53(20):5387 – 5400, 2005.
- [90] D. Samantaray, S. Mandal, U. Borah, A. Bhaduri, and P. Sivaprasad. A thermo-viscoplastic constitutive model to predict elevated-temperature flow behaviour in a titanium-modified austenitic stainless steel. *Materials Science and Engineering: A*, 526(1-2):1 – 6, 2009.
- [91] M. Seth. *High velocity formability and factors affecting it*. PhD thesis, The Ohio State University, 2006.
- [92] H. Shin and J.-B. Kim. A phenomenological constitutive equation to describe various flow stress behaviors of materials in wide strain rate and temperature regimes. *Journal of Engineering Materials and Technology*, 132, 2010.

- [93] J. Signorelli, M. Bertinetti, and P. Turner. Predictions of forming limit diagrams using a rate-dependent polycrystal self-consistent plasticity model. *International Journal of Plasticity*, 25(1):1 – 25, 2009.
- [94] W. Sing and K. Rao. Role of strain-hardening laws in the prediction of forming limit curves. *Journal of Materials Processing Technology*, 63(1-3):105 – 110, 1997.
- [95] J. H. Sung, J. H. Kim, and R. Wagoner. A plastic constitutive equation incorporating strain, strain-rate, and temperature. *International Journal of Plasticity*, 26(12):1746 – 1771, 2010.
- [96] S. Toros, F. Ozturk, and I. Kacar. Review of warm forming of aluminum-magnesium alloys. *Journal of Materials Processing Technology*, 207(1-3):1 – 12, 2008.
- [97] A. van den Boogaard and P. Bolt. A material model for warm forming of aluminium sheet. In *VII International conference on computational plasticity, COMPLAS*, 2003.
- [98] H. Vegter, C. H. ten Horn, Y. An, E. H. Atzema, H. H. Pijlman, T. H. van den Boogaard, and H. Huétink. Characterization and modelling of the plastic material behaviour and its application in sheet metal forming simulation. *VII International Conference on Computational Plasticity, Barcelona*, 2003.
- [99] H. Vegter and A. van den Boogaard. A plane stress yield function for anisotropic sheet material by interpolation of biaxial stress states. *International Journal of Plasticity*, 22(3):557 – 580, 2006.
- [100] G. Z. Voyiadjis and F. H. Abed. Microstructural based models for bcc and fcc metals with temperature and strain rate dependency. *Mechanics of Materials*, 37(2-3):355 – 378, 2005.
- [101] H. Wang, M. Wan, Y. Yan, and X. Wu. The biaxial stress-strain curves of sheet metals. *Applied Mechanics and Materials*, 44 - 47:2519 – 2523, 2011.
- [102] L. Wang, M. Strangwood, D. Balint, J. Lin, and T. Dean. Formability and failure mechanisms of AA2024 under hot forming conditions. *Materials Science and Engineering: A*, 528(6):2648 – 2656, 2011.
- [103] A. A. Zadpoor, J. Sinke, and R. Benedictus. Optimization of computation procedures for full-model strain path dependent analysis of forming limits. In *International Deep Drawing Research Group*, 2008.
- [104] F. Zerli and R. Armstrong. Dislocation-mechanics-based constitutive relations for material dynamics calculation. *J. Appl. Phys.*, 5:1816 – 1825, 1987.
- [105] C. Zhang. *Etude de l'effet de la sensibilité à la vitesse de déformation sur la formabilité de tôle en alliage d'aluminium*. PhD thesis, Institut National des Sciences Appliquées de Rennes, 2008.

- 
- [106] C. Zhang, L. Leotoing, G. Zhao, D. Guines, and E. Ragneau. A methodology for evaluating sheet formability combining the tensile test with the M–K model. *Materials Science and Engineering: A*, 528(1):480 – 485, 2010.
- [107] C. Zhang, L. Leotoing, G. Zhao, D. Guines, and E. Ragneau. A comparative study of different necking criteria for numerical and experimental prediction of FLCs. *Journal of Materials Engineering and Performance*, 20:1036–1042, 2011. 10.1007/s11665-010-9729-7.
- [108] S. Zhang, M. Harada, K. Ozaki, and M. Sakane. Multiaxial creep-fatigue life using cruciform specimen. *International Journal of Fatigue*, 29(5):852 – 859, 2007.
- [109] I. Zidane. *Développement d'un banc d'essai de traction biaxiale pour la caractérisation de la formabilité et du comportement élastoplastique de tôles métalliques*. PhD thesis, Institut National des Sciences Appliquées de Rennes, 2009.

## AVIS DU JURY SUR LA REPRODUCTION DE LA THESE SOUTENUE

**Titre de la thèse:**

Caractérisation expérimentale et prédiction de la formabilité d' un alliage d'aluminium en fonction de la température et de la vitesse de déformation

**Nom Prénom de l'auteur : CHU XING RONG**

**Membres du jury :**

- Madame THUILLIER Sandrine
- Monsieur RAGNEAU ERIC
- Monsieur LEOTOING Lionel
- Monsieur GUINES Dominique
- Monsieur RACINEUX Guillaume
- Madame BOUVIER Salima
- Madame MASSONI Elisabeth

Président du jury : *S. Thuillier*

Date de la soutenance : 20 Février 2013

Reproduction de la these soutenue

- Thèse pouvant être reproduite en l'état  
 Thèse pouvant être reproduite après corrections suggérées

Fait à Rennes, le 20 Février 2013

Signature du président de jury

*S. Thuillier*

Le Directeur,

*M'hamed DRISSI*



M'hamed DRISSI

## Résumé

Les procédés de mise en forme de tôles minces sont très largement répandus dans l'industrie. Néanmoins, l'utilisation de ces procédés est limitée par le niveau de formabilité du matériau formé, notamment dans le cas des alliages d'aluminium. Afin d'améliorer ces limites de formabilité, des procédés de mise en forme à chaud peuvent être envisagés.

L'objectif de cette thèse est d'étudier à l'aide d'approches expérimentale et numérique l'effet de la température et de la vitesse de déformation sur la formabilité des tôles en alliage d'aluminium AA5086 et de proposer une modélisation capable de prédire ces effets. Une campagne d'essais a été réalisée sur ce matériau à partir d'un essai d'emboutissage de type Marciniak. Des courbes limites de formage (CLF) ont été établies sur une plage de température allant de l'ambiant jusqu'à 200°C et pour des vitesses de déformation allant de quasi-statique à 2s<sup>-1</sup>. Des effets, positif de la température et négatif de la vitesse de déformation sur la formabilité ont été mis en évidence.

La prise en compte des effets de la température et de la vitesse de déformation dans les modèles prédictifs des CLF, qu'ils soient analytiques ou numériques, est à ce jour très limitée. Dans ce travail, un modèle numérique prédictif basé sur la simulation par éléments finis du modèle géométrique de Marciniak et Kuczynski (M-K) est proposé. Les déformations limites obtenues avec de ce modèle sont très sensibles à la description du comportement thermo-viscoplastique du matériau et à la calibration du défaut géométrique pilotant l'apparition de la striction dans le modèle M-K.

Des essais de traction uniaxiale réalisés dans les mêmes conditions opératoires que les essais de mise en forme de Marciniak ont permis d'identifier des lois d'érouissage de nature très différentes (rigidifiante, saturante ou mixte). Ces lois conduisent à des prédictions très différentes de la formabilité du matériau pour une valeur donnée du défaut géométrique du modèle EF M-K. Différentes stratégies de calibration de la taille de ce défaut initial ont été envisagées. L'utilisation du point expérimental de la CLF correspondant à des conditions de déformation plane permet de calibrer de manière satisfaisante la valeur de ce défaut. Cette procédure de calibration a été appliquée pour l'ensemble des lois identifiées. Les lois de nature rigidifiante de type Ludwick se sont montrées les plus efficaces alors que les lois saturante de type Voce se sont avérées incapables de prédire la formabilité du matériau pour certaines conditions opératoires. Finalement, il est démontré qu'une valeur constante du défaut géométrique ne peut être retenue pour l'ensemble des conditions opératoires étudiées même si le modèle M-K s'est avéré assez efficace pour représenter l'effet de la température plutôt que celui de la vitesse de déformation.

## Abstract

Sheet metal forming processes are widely used in industry. Nevertheless, the use of these processes is limited by the formability of the considered material, in particular in the case of the aluminium alloys. To improve the formability, warm forming processes can be considered.

The objective of this work is to study by means of both experimental and numerical approaches, the effects of temperature and strain rate on the formability of AA5086 aluminium alloy sheets and to propose a modeling suitable to predict these effects. Experimental tests have been carried out on this material by means of the Marciniak stamping experimental device. Forming limit curves (FLCs) have been established on a temperature range going from ambient temperature to 200°C and on a strain rate range going from quasi-static up to 2s<sup>-1</sup>. A positive effect of the temperature and a negative effect of the strain rate on the formability limits were highlighted.

To date, very few predictive models of the FLCs taking into account temperature and strain rate effects are proposed in the literature. In this work, in order to predict the experimental temperature and strain rate sensitivities, a predictive model based on the finite element simulation of the Marciniak and Kuczynski (M-K) geometrical model is proposed. The limit strains obtained with this model are very sensitive to the description of the thermo-viscoplastic behaviour modeling and to the calibration of the initial geometrical imperfection controlling the onset of the necking.

Thanks to tensile tests carried out for the same operating conditions that those of Marciniak forming tests, several types (power law, saturation and mixed) of hardening laws have been identified. These hardening laws have been implemented in the FE M-K model to obtain numerical limit strains. Very different formability limits have been observed for a given value of the geometrical defect. Several strategies for the calibration of this initial imperfection size have been tested. The use of the experimental point of the FLC<sub>0</sub> corresponding to plane strain condition allows a good calibration of the initial imperfection value. This calibration procedure was carried out for all hardening laws. It is shown that the power law type models such as Ludwick law are more efficient while saturation laws such as Voce law are unable to predict the material formability for some conditions. Finally, it is shown that a constant value of the geometrical defect cannot be used to the whole operating conditions studied even if FE M-K model is shown to be efficient to represent the temperature effect rather than strain rate one